Fall 2020

Studying the effects of various process parameters on early age hydration of single- and multi-phase cementitious systems

Rachel Cook

Department: Materials Science and Engineering

Recommended Citation

Cook, Rachel, "Studying the effects of various process parameters on early age hydration of single- and multi-phase cementitious systems" (2020). *Doctoral Dissertations*. 2943.
https://scholarsmine.mst.edu/doctoral_dissertations/2943

STUDYING THE EFFECTS OF VARIOUS PROCESS PARAMETERS ON EARLY AGE HYDRATION OF SINGLE- AND MULTI-PHASE CEMENTITIOUS SYSTEMS

by

Rachel Elizabeth Cook

A DISSERTATION

Presented to the Graduate Faculty of the

MISSOURI UNIVERSITY OF SCIENCE AND TECHNOLOGY

In Partial Fulfillment of the Requirements for the Degree

DOCTOR OF PHILOSOPHY

in

CERAMIC ENGINEERING

2020

Approved by:

Aditya Kumar, Advisor
Hongyan Ma, Co-Advisor
Jeffrey D. Smith
Ronald J. O'Malley
Monday U. Okoronkwo

PUBLICATION DISSERTATION OPTION

This dissertation consists of the following seven articles, formatted in the style used by the Missouri University of Science and Technology. The details regarding reuse permissions of the previously published works that are included in this dissertation are contained in Appendix B.

Paper I, found on pages 17–61, has been published in *ACS Omega* in May, 2018.

Paper II, found on pages 62-88 has been submitted to the *Journal of the American Ceramic Society*.

Paper III, found on pages 89-130, has been published in *SN Applied Sciences* in January, 2019 by Springer Nature.

Paper IV, found on pages 131-175 has been published in the *Journal of the American Ceramic Society* in November, 2019.

Paper V, found on pages 176-222 has been published in the *Journal of Materials in Civil Engineering* in November, 2019.

Paper VI, found on pages 223-260 has been published in *Engineering Reports* in June, 2020.

Paper VII, found on pages 261-305 has been prepared for submission for publication.

ABSTRACT

The hydration of multi-phase ordinary Portland cement (OPC) and its pure phase derivatives, such as tricalcium silicate (C_3S) and belite (β-C_2S), are studied in the context varying process parameters — for instance, variable water content, water activity, superplasticizer structure and dose, and mineral additive type and particle size. These parameters are studied by means of physical experiments and numerical/computational techniques, such as: thermodynamic estimations; numerical kinetic-based modelling; and artificial intelligence techniques like machine learning (ML) models. In the past decade, numerical kinetic modeling has greatly improved in terms of fitting experimental, isothermal calorimetry to kinetic-based modelling based the evolving understanding of hydration processes. However, there are remaining points of contention within literature, that could potentially take an additional decade to resolve. The dissertation work utilizes the numeric kinetic-based, phase boundary nucleation and growth (pBNG) model but also introduces ML models as a technique to predict the heat-evolution — which, is related to other fresh properties, such as rheological, microstructural, and mechanical properties — of a paste system by utilizing underlying nonlinear time-dependent composition-property relationships.

ACKNOWLEDGMENTS

I would like to express appreciation to all of my professional mentors that have helped guide me to this point. I would like to thank, first and foremost, my advisor Dr. Aditya Kumar for his support, guidance, and patience through the process of working towards my PhD these past four years. Through his guidance, I have become a more proficient researcher, writer, and critical thinker, which will have an overall lasting, positive impact on my career. Additionally, I would like to convey my gratitude towards the other members of my dissertation committee — my co-advisor, Dr. Hongyan Ma; Dr. Jeffrey Smith; Dr. Ronald O'Malley; and Dr. Monday Okoronkwo — for serving as mentors, taking the time to review my work, and their insightful and valuable input through this process. I would also like to thank my undergraduate thesis advisor, Dr. Yiquan Wu, for encouraging me to pursue graduate school after working under his guidance in a research setting.

I would like to express appreciation for my family for their love and support over the years. I would like to thank: my parents, Mary Ann and Albert Cook, for their continued care throughout my childhood and education; my siblings A.J., Josh, Bryson, Lilly, and Angelina for their support and enduring friendship through my time in graduate school; and my grandparents, Laura and Al Cook, for their mentorship, guidance, gift of timeless, cherished memories, and being there to support me when I needed it most. Lastly, I would like to thank my partner, Evan Schwind, for his incessant encouragement, love, and friendship.

TABLE OF CONTENTS

Page

PUBLICATION DISSERTATION OPTION iii

ABSTRACT iv

ACKNOWLEDGMENTS v

LIST OF ILLUSTRATIONS xiii

LIST OF TABLES xxi

SECTION

1. INTRODUCTION 1

1.1. GENERAL BACKGROUND AND RESEARCH OBJECTIVES 1

1.2. THE STUDY OF SINGLE- & MULTI-CEMENTITIOUS PHASES 2

1.3. PROCESS PARAMETERS OF INTEREST 3

1.3.1. Water. 3

1.3.1.1. Water-to-cement ratio. 4

1.3.1.2. Water activity (a_H). 4

1.3.2. Superplasticizers. 5

1.3.3. Mineral Additives. 7

1.4. HYDRATION IN THE CONTEXT OF ISOTHERMAL CALORIMETRY 9

1.5. A REVIEW OF NUMERICAL KINETIC-BASED MODELS IN THE CONTEXT OF CEMENT HYDRATION 12

1.6. ORGANIZATION OF DISSERTATION 15

PAPER

I. ELUCIDATING THE EFFECT OF WATER-TO-CEMENT RATIO ON THE HYDRATION OF CEMENT 17

ABSTRACT 17

1. INTRODUCTION 18

2. MATERIALS AND METHODS 23

2.1. MATERIALS 23

2.2. METHODS 24

2.2.1. Experimental Work. 24

2.2.2. Phase Boundary Nucleation and Growth (pBNG) Model. 25

3. RESULTS AND DISCUSSION 32

4. CONCLUSIONS 52

ACKNOWLEDGEMENTS 53

REFERENCES 54

II. INFLUENCE OF WATER ACTIVITY ON BELITE (β-C_2S) HYDRATION 62

ABSTRACT 62

1. INTRODUCTION 63

1.1. β-C_2S HYDRATION REACTIONS 65

1.2. PREVIOUS WATER ACTIVITY (a_H) STUDIES 66

2. METHODS AND MATERIALS 68

2.1. β-C_2S SYNTHESIS AND PHYSICAL TECHNIQUES 68

2.2. A THERMODYNAMIC ANALYSIS: ESTIMATIONS OF ACTIVITIES (a_x), CRITICAL WATER ACTIVITY (a_H), AND SOLUBILITY PRODUCT CONSTANT (KC_2S) 70

2.2.1. Isopropanol (a_{IPA}) and Water Activity (a_H) Calculations. 70

2.2.2. Solubility Product Constant (K_{C2S}) And Critical Water Activity (a_H) Calculations. 71

3. RESULTS AND DISCUSSION 73

4. SUMMARY AND CONCLUSIONS 78

ACKNOWLEDGEMENTS 80

REFERENCES 80

III. MECHANISMS OF TRICALCIUM SILICATE HYDRATION IN THE PRESENCE OF POLYCARBOXYLATE POLYMERS 89

ABSTRACT 89

1. INTRODUCTION 90

2. MATERIALS AND METHODS 96

2.1. MATERIALS 96

2.2. METHODS 98

2.2.1. Experimental Methods. 98

2.2.2. Phase Boundary Nucleation and Growth (pBNG) Model. 100

3. RESULTS AND DISCUSSION 105

4. CONCLUSIONS 121

ACKNOWLEDGEMENTS 123

REFERENCES 123

IV. INFLUENCE OF SIZE-CLASSIFIED AND SLIGHTLY SOLUBLE MINERAL ADDITIVES ON HYDRATION OF TRICALCIUM SILICATE 131

ABSTRACT 131

1. INTRODUCTION 132

2. MATERIALS AND METHODS 137

2.1. MATERIALS AND SIZE CLASSIFICATION OF FILLERS 137

2.2. METHODS 141

2.2.1. Experimental Methods. 141

2.2.2. Phase Boundary Nucleation and Growth (pBNG) Modeling.............. 142

3. RESULTS AND DISCUSSION 145

3.1. EXPERIMENTAL RESULTS 145

3.2. PHASE BOUNDARY NUCLEATION AND GROWTH (PBNG) SIMULATIONS 158

4. SUMMARY AND CONCLUSIONS 168

ACKNOWLEDGEMENTS 170

REFERENCES 170

V. PREDICTION OF COMPRESSIVE STRENGTH OF CONCRETE: CRITICAL COMPARISOM OF PERFORMANCE OF A HYBRID MACHINE LEARNING MODEL WITH STANDALONE MODELS 176

ABSTRACT 176

1. INTRODUCTION 177

2. MACHINE LEARNING MODELS 183

2.1. MULTILAYER PERCEPTRON ARTIFICIAL NEURAL NETWORK (MLP-ANN) 183

2.2. SUPPORT VECTOR MACHINE (SVM) 185

2.3. M5PRIME MODEL TREE ALGORITHM (M5P) 187

2.4. RANDOM FORESTS (RF) 189

2.5. THE HYBRID RANDOM FORESTS – FIREFLY ALGORITHM MODEL (RF-FFA) 192

2.5.1. The Firefly Algorithm (FFA). 192

2.5.2. The Hybrid Model (RF-FFA). 194

3. DATA COLLECTION AND PERFORMANCE EVALUATION OF MACHINE LEARNING MODELS 196

  3.1. DATA COLLECTION 196

  3.2. EVALUATION OF PREDICTION PERFORMANCE OF ML MODELS 198

4. RESULTS AND DISCUSSION 200

  4.1. HIGHLY NONLINEAR AND PERIODIC TRIGONOMETRIC FUNCTIONS 200

  4.2. COMPRESSIVE STRENGTH OF CONCRETE: DATASET-1 205

  4.3. COMPRESSIVE STRENGTH OF CONCRETE: DATASET-2 210

5. CONCLUSIONS 213

ACKNOWLEDGEMENTS 215

REFERENCES 215

VI. PREDICTION OF FLOTATION EFFICIENCY OF METAL SULFIDES USING AN ORIGINAL HYBRID MACHINE LEARNING MODEL 223

ABSTRACT 223

1. INTRODUCTION 224

  1.1. BACKGROUND 224

  1.2. MACHINE LEARNING MODELS 229

    1.2.1. Standalone ML Models. 229

    1.2.2. The Hybrid Random Forests — Firefly Algorithm (RF-FFA) Model. 231

2. MATERIALS AND PHYSICAL EXPERIMENTS 233

  2.1. MATERIALS 233

  2.2. CHARACTERIZATION OF FLOTATION FEED 234

  2.3. BATCH FLOTATION EXPERIMENTS 235

3. DATABASE DEVELOPMENT AND EVALUATION OF ML MODEL PREDICTION PERFORMANCE 237

3.1. DATABASE DEVELOPMENT 237

3.2. EVALUATION OF ML MODELS PREDICTION PERFORMANCE 238

4. RESULTS AND DISCUSSION 239

4.1. BULK FLOTATION OF GALENA AND CHALCOPYRITE 239

4.2. PREDICTIONS: MACHINE LEARNING MODELS 242

5. CONCLUSIONS 252

ACKNOWLEDGEMENTS 254

REFERENCES 254

VII. MACHINE LEARNING FOR HIGH-FIDELITY PREDICTION OF CEMENT HYDRATION KINETICS IN BLENDED SYSTEMS 261

ABSTRACT 261

1. INTRODUCTION 262

2. MATERIALS AND METHODS 268

2.1. MATERIALS 268

2.2. METHODS 272

2.2.1. Experimental Methods. 272

2.2.2. Database Collection and Assessment of Prediction Accuracy of ML Model 273

3. RESULTS 276

3.1. EXPERIMENTAL ISOTHERMAL CALORIMETRY OF [OPC + MINERAL ADDITIVE] SYSTEMS 276

3.2. HEAT EVOLUTION PREDICTION OF [OPC + MINERAL ADDITIVE] SYSTEMS 280

3.3. OPTIMIZATION OF [OPC + MINERAL ADDITIVE] MIXTURE DESIGN 287

4. CONCLUSIONS AND FUTURE WORK 291

ACKNOWLEDGEMENTS 293

REFERENCES 294

SECTION

2. CONCLUSIONS AND RECOMMENDATIONS FOR FUTURE WORK 306

2.1. SUMMARY AND CONCLUSIONS OF DISSERATION WORK 306

2.2. RECOMMENDATIONS FOR FUTURE WORK 309

APPENDICES

A. CURRICULUM VITAE 311

B. REUSE PERMISSIONS 315

BIBLIOGRAPHY 318

VITA 330

LIST OF ILLUSTRATIONS

SECTION Page

Figure 1.1. Early hydration of cement is often described in four periods that correspond to observable regime changes in heat flow rate as a function of time, which is measured using isothermal calorimetry. 10

PAPER I

Figure 1. The PSDs of the “as-received” (coarse) and ground (fine) cement as measured using SLS methods. 33

Figure 2. Isothermal microcalorimetry based determinations of (a) heat flow rates, and (b) cumulative heat release of pastes prepared using the coarse cement at different w/c. (c) shows the repeatability of heat flow rate determinations for a representative system. 34

Figure 3. Isothermal microcalorimetry based determinations of (a) heat flow rates, and (b) cumulative heat release of pastes prepared using the fine cement at different w/c. (c) Comparison of heat flow rates of pastes prepared at equivalent w/c using cements of different fineness. 36

Figure 4. (a) Portlandite mass contents (as mass percent of the binder) and (b) degree of hydration of cement (α) after 24 h of hydration in pastes prepared at different w/c, as determined from DTG analyses. (c) Comparison between α as calculated from microcalorimetry and DTG methods. 36

Figure 5. (a) Correlation between capillary porosity and degree of hydration (α) in pastes prepared at different w/c. 37

Figure 6. Representative set of simulated and measured hydration rates ($d\alpha/dt$) of cement in pastes prepared at different w/c. 39

Figure 7. Parameters derived from the simulations: (a) reactive paste fraction (p_f) and (b) water-to-cement ratio within the reaction vessel (w/c_{-RV}) as functions of the w/c. (c) Comparison between the average spacing between cement particle surfaces within the reaction vessel (y-axis) vis-à-vis the average spacing between them when they are assumed to remain suspended (x-axis) 41

Figure 8. 3D virtual microstructures showing the packing of particles at the time of mixing (i.e., without sedimentation of particles) in pastes prepared at: (a) w/c = 0.45, and (b) w/c = 10. (c) shows the effects of sedimentation of particles in a paste prepared at w/c = 10. 44

Figure 9. Outward growth rate of the product (G_{out}) as function of: (a) time, and (b) degree of hydration of the coarse cement. 47

Figure 10. Outward growth rate of the product (G_{out}) as a function of w/c when: (a) $\alpha = 0.10$, (b) $\alpha = 0.20$, and (c) $\alpha = 0.30$. 47

Figure 11. Estimated temporal evolution of the supersaturation of C-S-H (β_{CSH}) in pastes prepared using: (a) the coarse cement at different w/c, (b) the coarse and fine cements at w/c = 3, and (c) the coarse and fine cements at w/c = 10. 49

Figure 12. (a) Electrical conductivity and (b) pH of the pore solution of pastes prepared using the coarse cement at different w/c. Because of the large difference in magnitudes of solution's electrical conductivity, re-scaled subplots for the two curves are included within (a). (c) Heat flow rates of pastes, prepared using the coarse cement at w/c = 10, measured without (static) and with in-situ stirring. 51

PAPER II

Figure 1. Select isothermal microcalorimetry based determinations of the time dependent (a) heat flow rate; and (b) cumulative heat released of [β-C_2S + H + IPA] suspensions prepared at varying replacement levels (wt.$\%_{IPA}$) of water, with a liquid-to-solid ratio = 10 used in this study. 74

Figure 2. Select XRD results of [β-C_2S + H + IPA] systems are shown as representation of the measured raw intensity of the 29.375 ± 1.000 °2θ peak by (a) IPA replacement level and (b) the occurance of the peak with respect to °2θ. 76

Figure 3. The solubility product constant of β-C_2S (K_{C2S}), calculated using solubility values for CSH_4 and C_2SH_7 from literature [45,69], is shown as a function of water activity (a_H) as calculated from Equations 7 and 8, and related to IPA replacement level using the van Laar equations (Equations 5 and 6), which is graphically represented by the inset plot and included for the reader's reference. 78

PAPER III

Figure 1. (a) The cumulative (primary y-axis) and differential (secondary y-axis) particle size distribution (PSD) of C_3S. The largest relative uncertainty in the median diameter (d_{50}, µm) of C_3S, based on six replicate measurements, was on the order of ±6%. (b) Schematic representation of the comb-shaped architecture of PCE, wherein n is the number of repeating units, P is the side chain length, and C/E represents the carboxylate-to-ether ratio. 97

Figure 2. Isothermal microcalorimetry based determinations of time-dependent (a) heat flow rate and (b) cumulative heat release of C_3S pastes provisioned with PCE-1 at different dosages (C_{PCE}). 105

Figure 3. Isothermal microcalorimetry based determinations of time-dependent (a) heat flow rate and (b) cumulative heat release of C_3S pastes provisioned with different PCEs (i.e., PCE-1, PCE-2, and PCE-3) at equivalent dosage (C_{PCE}) of 1.25%. 108

Figure 4. The calorimetric parameters: (a) inverse of time to the main hydration peak, (b) heat flow rate at the main hydration peak, and (c) slope of the acceleration regime, extracted from heat evolution profiles, and plotted against PCE dosage. 108

Figure 5. (a) Isothermal microcalorimetry based determinations of time-dependent degree of reaction (α) of C_3S, (b) DTG traces showing differential mass loss profiles, and (c) mass contents of portlandite (CH: as $\%_{mass}$ of the binder) as determined from analyses of DTG traces, in [C_3S + PCE] pastes at 24 h. 110

Figure 6. The calorimetric parameters: (a) inverse of time to the main hydration peak, (b) heat flow rate at the main hydration peak, and (c) slope of the acceleration regime extracted from the calorimetry profiles, and plotted against the composite architectural parameter of the PCE (P_{PCE}: calculated using Equation 11). 114

Figure 7. Representative set of simulated and measured reaction rates (dα/dt; primary y-axis) and degree of reaction (α; secondary y-axis) for C_3S pastes prepared with varying PCE architectures and dosages of: (a) 0.000% PCE, (b) 1.250% PCE-1, and (c) 1.250% PCE-3. 115

Figure 8. Parameters derived from pBNG simulations: (a) nucleation density of the product ($I_{density}$), and (b) total number of super product nuclei formed per gram of C_3S (N_{nuc}: calculated from Equation 7), plotted against PCE dosage (C_{PCE}). 116

Figure 9. Parameters derived from pBNG simulations: (a) nucleation density of the product ($I_{density}$), and (b) total number of super product nuclei formed per gram of C_3S (N_{nuc}), plotted against the composite architectural parameter of PCE (P_{PCE}: calculated from Equation 11). 118

Figure 10. The temporal evolution of outward growth rate of the product (G_{out}), as obtained from pBNG simulations, for: (a) pastes prepared with PCE-1 at different dosages, (b) pastes prepared with PCE-3 at different dosages, and (c) pastes prepared with different PCEs at a fixed dosage of 0.625%. 119

Figure 11. The outward growth rate of the product, as obtained from pBNG simulations, at (a) t = 12 h, and (b) t = 72 h. 120

Figure 12. Measured heat flow rates of [C_3S + 2.5% PCE] pastes, prepared with (a) PCE-1, and (b) PCE-3. Results corresponding to both immediate and delayed (i.e., by 5-min) addition of PCE are shown. 121

PAPER IV

Figure 1. Cumulative PSDs of (a) C_3S; and (b) *as received* fillers: quartz, limestone, rutile, and corundum. 139

Figure 2. Cumulative PSDs of quartz, limestone, rutile and corundum, corresponding to: (a) *fine*; (b) *intermediate*; and (c) *coarse* size-classes. 140

Figure 3. Isothermal microcalorimetry based determinations of the time-dependent (a) heat flow rate; and (b) cumulative heat released of [C_3S + silica fume (SF)] pastes over a 24 h period [7]. 146

Figure 4. Isothermal microcalorimetry based determinations of the time-dependent (a) heat flow rate; and (b) cumulative heat released of [C_3S + filler] pastes prepared at 30% replacement level of C_3S by *as received* PSDs of silica fume, quartz, limestone, rutile, and corundum. 146

Figure 5. (a) Isothermal microcalorimetry based determinations of degree of reaction (α) of C_3S; (b) DTG traces showing differential mass loss profiles; and (c) mass contents of portlandite (CH: as $\%_{mass}$ of the binder) as determined from analyses of DTG traces, in [C_3S + 30% *as received* filler] pastes at 24 h. 148

Figure 6. Isothermal microcalorimetry based determinations of the time-dependent (a) heat flow rate; and (b) cumulative heat released of [C_3S + *area matched* filler] pastes prepared using *as received* PSDs of quartz, limestone, rutile, and corundum as fillers. 151

Figure 7. Isothermal microcalorimetry based determinations of heat evolution profiles of [C_3S + *area matched* filler] pastes prepared using: (a) *coarse* size-class; and (b) *fine* size-class PSDs of fillers (i.e., quartz, limestone, rutile, and corundum). 152

Figure 8. Calorimetric parameters: (a) inverse of time to the main hydration peak; (b) slope of the acceleration regime; and (c) heat flow at the main hydration peak, extracted from heat evolution profiles of *area matched* binary pastes. 156

Figure 9. pBNG simulation parameters: (a) reactive area fraction of the filler (a_{filler}); (b) product nucleation density ($I_{density}$); and (c) total number of supercritical product nuclei (N_{nuc}), obtained from numerical-reproduction of experimentally-measured reaction-rate profiles of *area matched* binary pastes. 163

Figure 10. The temporal evolution of outward growth rate of the product ($G_{out}(t)$), as obtained from pBNG simulations, for: [C_3S + *area matched* filler] pastes prepared with (a) *as received*, (b) *coarse*, and (c) *fine* size-classes. 164

Figure 11. pBNG simulation parameter (i.e., N_{nuc}: total number of supercritical nuclei of C-S-H formed per gram of C_3S) compared against experimentally-derived calorimetric parameters: (a) slope of the acceleration regime; and (b) inverse of time to the main hydration peak. 167

Figure 12. Isothermal microcalorimetry based determinations of the time-dependent: (a) heat flow rate; and (b) cumulative heat released of plain and [C_3S + corundum] pastes prepared using different PSDs and replacement levels of corundum. 167

PAPER V

Figure 1. Predictions made by ML models: (a) MLP-ANN; (b) SVM; (c) M5P; (d) RF; and (e) RF-FFA compared against actual values of the trigonometric function, $F_1(x)$ (Equation 17). 202

Figure 2. Predictions made by ML models: (a) MLP-ANN; (b) SVM; (c) M5P; (d) RF; and (e) RF-FFA compared against actual values of the trigonometric function, $F_2(x)$ (Equation 18). 204

Figure 3. Predictions made by ML models: (a) MLP-ANN; (b) SVM; (c) M5P; (d) RF; and (e) RF-FFA compared against actual compressive strength of concretes (drawn from Dataset-1). 207

Figure 4. Predictions made by ML models: (a) MLP-ANN; (b) SVM; (c) M5P; (d) RF; and (e) RF-FFA compared against actual compressive strength of concretes (drawn from Dataset-2). 212

PAPER VI

Figure 1. (a) MLA image showing mineral association in the flotation feed and (b) Mineralogical composition of sulfides-containing flotation feed in different size fractions. 235

Figure 2. Influence of process variables on the flotation behavior of galena and chalcopyrite from a complex sulfide ore of MVT (a)* effect of pulp's pH and (b)† Effect of pyrite's depressant dosage. 241

Figure 3. Predictions made by ML models: (a) multilayer perceptron artificial neural network (MLP-ANN); (b) support vector machine (SVM); (c) M5Prime model tree algorithm (M5P); (d) random forest (RF); and (e) RF-FFA compared against measured values of Pb-grade (drawn from the dataset described in Section 2.1.). 243

Figure 4. Predictions made by ML models: (a) multilayer perceptron artificial neural network (MLP-ANN); (b) support vector machine (SVM); (c) M5Prime model tree algorithm (M5P); (d) random forest (RF); and (e) RF-FFA compared against actual values of Pb-recovery (drawn from the dataset described in Section 2.1.). 244

Figure 5. Predictions made by ML models: (a) multilayer perceptron artificial neural network (MLP-ANN); (b) support vector machine (SVM); (c) M5Prime model tree algorithm (M5P); (d) random forest (RF); and (e) RF-FFA compared against actual values of Cu-grade (drawn from the dataset described in Section 3.1.). 245

Figure 6. Predictions made by ML models: (a) multilayer perceptron artificial neural network (MLP-ANN); (b) support vector machine (SVM); (c) M5Prime model tree algorithm (M5P); (d) random forest (RF); and (e) RF-FFA compared against actual values of Cu-recovery (drawn from the dataset described in Section 3.1). 249

Figure 7. Predictions of: (a) Pb-grade; and (b) Pb-recovery produced by the RF-FFA model using training sets consisting of 75%, or 60% or 40%, or 80% of total data-records. 250

PAPER VII

Figure 1. The cumulative particle size distributions (PSDs) of (a) ordinary Portland cement (OPC); and (b) varying distributions of limestone, that is, Limestone-1; Limestone-2; and Limestone-3 which correspondingly have SSAs of 4673.81 $cm^2. g^{-1}$; 1697.49 $cm^2. g^{-1}$; and 1239.88 $cm^2. g^{-1}$, respectively. 270

Figure 2. Isothermal calorimetry determinations of time-dependent (a) heat flow rate of [OPC + quartz] systems at replacement levels varying from 0 wt.% to 60 wt.%, and (b) heat flow rate and (c) cumulative heat release of [OPC + 1-additive] systems at identical 20 wt.% replacements of limestone; quartz; silica fume; and metakaolin. 277

Figure 3. Isothermal calorimetry determinations of time-dependent 2-additive systems, that is, (a) heat flow rate and (b) cumulative heat released of [OPC + metakaolin + limestone] systems as replacement levels ranging from 0% to 60% with respect to each additive in the system; and (c) heat flow rate and (d) cumulative heat released of [OPC + quartz + silica fume] systems as replacement levels ranging from 0% to 30% with respect to each additive in the system. 278

Figure 4. Grid-search method used to optimize hyper-parameters (*number of trees in the forest*; and *number of splits in each tree*) of the RF model to improve its prediction performance against: (a) cumulative heat flow, as evaluated by MAPE; (b) cumulative heat flow, as evaluated by R^2; (c) heat flow rate, as evaluated by MAPE; and (d) heat flow rate, as evaluated by R^2. 282

Figure 5. Statistical parameters describing errors in prediction of cumulative heat release of pastes over a 24-hour period in the testing database: (a) Person correlation coefficient (R); (b) coefficient of determination (R^2); (c) root mean squared error (RMSE); (d) mean absolute percentage error (MAPE); and (e) mean absolute error (MAE) as functions of time. 283

Figure 6. Statistical parameters describing errors in prediction of heat flow rate of pastes over a 24-hour period in the testing database: (a) Person correlation coefficient (R); (b) coefficient of determination (R^2); (c) root mean squared error (RMSE); (d) mean absolute percentage error (MAPE); and (e) mean absolute error (MAE) as functions of time. 284

Figure 7. The RF model's predictions of: (a) cumulative heat and (b) heat flow rate of [OPC + silica fume]; (c) cumulative heat and (d) heat flow rate of [OPC + limestone]; (e) cumulative heat and (f) heat flow rate of [OPC + silica fume + limestone]; and (g) cumulative heat and (h) heat flow rate of [OPC + metakaolin + limestone] compared against experimental measurements. 286

Figure 8. Isothermal calorimetry profiles of (a) [OPC + limestone]; (b) [OPC + quartz]; and (c) [OPC + metakaolin]. 289

LIST OF TABLES

PAPER III Page

Table 1. Architectural parameters of the three PCEs – as determined from multi-detection size exclusion chromatography (SEC), high-performance liquid chromatography (HPLC), and potentiometric titration techniques [23,40]. 98

PAPER IV

Table 1. Median diameters (d_{v50}) and specific surface areas (SSAs) of *as received*, *fine*, *intermediate*, and *coarse* size-classes of each filler (quartz, limestone, rutile, and corundum). 140

PAPER V

Table 1. A summary of statistical parameters pertaining to each of the 9 attributes (8 input and 1 output) of Dataset-1. 196

Table 2. A summary of statistical parameters pertaining to each of the 6 attributes (5 input and 1 output) of Dataset-2. 197

Table 3. Prediction performance of ML models, measured on the basis of the test set developed using Equation 17. 203

Table 4. Prediction performance of ML models, measured on the basis of the test set developed using Equation 18. 205

Table 5. Prediction performance of ML models, measured on the basis of the test set of Dataset-1. 208

Table 6. Prediction performance of ML models, measured on the basis of the test set of Dataset-2. 213

PAPER VI

Table 1. Statistical parameters relevant to the 12 attributes (8 inputs and 4 outputs) of the database. 237

Table 2. Statistical parameters pertaining ML models' predictions of Pb-grade. 245

Table 3. Statistical parameters pertaining ML models' predictions of Pb-recovery. 246

Table 4. Statistical parameters pertaining ML models' predictions of Cu-grade. 248

Table 5. Statistical parameters pertaining ML models' predictions of Cu-recovery. 248

Table 6. Statistical parameters pertaining RF-FFA model's predictions of Pb-grade in relation to the percentage of data-records used in the training set. 250

Table 7. Statistical parameters pertaining RF-FFA model's predictions of Pb-recovery in relation to the percentage of data-records used in the training set. 251

PAPER VII

Table 1. The median diameters (d_{v50}) and specific surface areas (SSAs) detailing particle size distributions (PSDs) corresponding to the type I/II ordinary Portland cement (OPC); quartz limestone; metakaolin; and silica fume* that were utilized in training and later testing of the ML algorithms. 271

Table 2. Median diameters (d_{v50}) and specific surface areas (SSAs) of quartz; limestone; and metakaolin. 272

Table 3. Summary of four statistical parameters related to each of the 10 attributes (8 inputs and 2 outputs) of the training database. 275

Table 4. Summary of four statistical parameters related to each of the 10 attributes (8 inputs and 2 outputs) of the testing database. 276

Table 5. Prediction performance of ML models, measured on the basis of the cumulative heat release and heat flow rate of cement pastes in the testing database. 283

Table 6. Optimization results of six 1-additive systems compared against actual values of additive type, additive replacement level, and additive SSA. 290

SECTION

1. INTRODUCTION

1.1. GENERAL BACKGROUND AND RESEARCH OBJECTIVES

Concrete is the most widely used material internationally for construction purposes [1], with more than 4.1 billion tons produced last year in the United States alone [2]. Despite concrete production's contributions to anthropogenic CO_2 emission totals globally, concrete is an essential building material, especially to developing countries where its mineral precursors are rea**(a_H)** dily available and relatively inexpensive [1]. Therefore, research that seeks to gain improved understanding of cementitious systems and further limit the carbon footprint of concrete and its components remains of importance [3].

This body of research seeks to do just that by studying the hydration reaction — which, is related to other fresh properties, such as rheological, microstructural, and mechanical properties — of OPC systems and its pure phase derivatives by employing physical and advanced numerical techniques to ultimately elucidate understanding and predict the consequent early-age properties of hydration. The work contained in this dissertation specifically seeks to do this by exploring the effects of: water-to-cement ratio; water activity; the molecular architecture of the superplasticizer polycarboxylate ether (PCE); size-classified fillers; and mineral additives generally on the hydration of cementitious systems. The effects of these various parameters are investigated via physical experiments and computational work in a series of studies and are introduced briefly in the following Sub-Section, 1.6.

1.2. THE STUDY OF SINGLE- & MULTI-CEMENTITIOUS PHASES

OPC-based systems (i.e., pastes; mortars; and concretes) are complicated ceramic or ceramic composite systems, that typically consist of copious anhydrous reactant and hydrated product phases at a given moment in time [4]. An anhydrous OPC powder normally consists of tricalcium silicate, dicalcium silicate, tricalcium aluminate, tetracalcium aluminoferrite (commofnly written as C_3S, C_2S, C_3A, and C_4AF, respectively in cement chemistry notation, where C = CaO; S = SiO_2; A = Al_2O_3; F= Fe_2O_3; and H = H_2O), and blended with one of the calcium sulfate hydrate states (anhydrite, hemihydrate, and/or gypsum) [4]. However, though true, this is a simplified depiction of the system. For example, an OPC system is often further complicated due to the presence of impurities which are commonly introduced before the pre-calcination process (i.e., during the initial mix process) in the aforementioned anhydrous phases, which can have various effects on crystallinity and therefore hydration rates. Additionally, it is not unusual for a commercial cement to contain additional phase components, such as free CaO [5].

Since OPC is such a complex system, pure phase derivatives are often studied to provide insight and improve understanding of the fundamental physiochemical processes that occur during the hydration process of OPC-based systems. Two such pure phase derivatives that are relevant to the work contained within this dissertation document are C_3S and β-C_2S. C_3S and β-C_2S comprise approximately 50-to-70% and 15-to-30% of

OPC by weight [6]. During hydration of both phases, portlandite (CH) and calcium silicate hydrate (C-S-H) form in the contiguous solution (i.e., homogeneously) and on the surfaces of the cement particulates (i.e., heterogeneously), respectively. C-S-H, sometimes referred to as the "glue" phase, is often attributed as the most important phase in OPC systems [7–9]. These hydration products are known to form for both C_3S and β-C_2S, however, they are thought to form at different rates.

1.3. PROCESS PARAMETERS OF INTEREST

Section 1.2. introduces a few of the many complexities present in cementitious systems. This section elaborates on the section above by briefly introduces relevant process parameters that are also commonly varied in a given cementitious system. To give context, a given hydraulic concrete system can contain — but is not limited to — the following components: coarse aggregate (i.e., generally gravel that is greater than approximately 4.75 mm in diameter), fine aggregate (i.e., generally sand that is less than 4.75 mm in diameter), anhydrous cement powder, water, chemical additives (e.g., superplasticizers), and ground mineral additives (e.g., filler and pozzolanic materials) [10]. The effects of water, mineral additives, and superplasticizers on hydration are explored within individual studies contained in this dissertation document and therefore are given focus in the following sub-sections to supply the essential background information, necessary to understand the work within this thesis.

1.3.1. Water. Water content is a crucial parameter for a given hydraulic cementitious system. Too much water will increase permeability and therefore have an inverse effect on mechanical properties, while an insufficient amount of water will limit the degree of reaction [11,12]. Since the introduction of lignosulfonates as a chemical admixture, an early iteration of a superplasticizer-type dispersant in the 1930s [13], researchers have tried to limit the amount of water in cementitious systems in pursuit of a dense, impermeable final product. However, as the accepted water-to-cement ratio has decreased, the compatibility relationship between superplasticizer and cement binder has become more prominent [14]. Superplasticizers and the aforementioned compatibility relationship are briefly discussed in Section 1.3.2.

1.3.1.1. Water-to-cement ratio. Previously, in the context of relevant kinetic numerical models, it was assumed that an increased water-to-cement ratio provided increased volume space for hydration products to nucleate and grow until the majority of the water present is incorporated into the hydrate network [15–17]. However, the literature [15–17] has demonstrated that the early periods of cement hydration are generally unaffected by varying water-to-cement ratios in more dilute systems. Of course, below a certain threshold (i.e., below approximately a water to cement ratio of 0.42 on a weight basis), a low relative amount of water within the system will eventually effect hydration rates at later periods of cement hydration, when self-desiccation ultimately ensues [18,19]. The effect of water-to-cement in more dilute (i.e., above the critical threshold) cementitious systems is explored and discussed further context of numerical kinetic models in Paper I.

1.3.1.2. Water activity (a_H). The term water activity (a_H) describes the chemical potential (i.e., the rate of change of free energy experienced by the system) of the water present to undergo thermodynamic processes. a_H — in a basic sense — is a property of water. The importance of which extends to any and all systems that contain water, including but not limited to hydraulic cementitious systems [19–21].

To better understand the effect of a_H on a given cementitious system, a thermodynamic analysis can be conducted by adapting methods established by Oey et al. [20] and utilized by Lapeyre et al. [21] These researchers [20,21] introduced the idea of experimentally manipulating a_H of the cementitious system of interest by varying replacements of water with near pure isopropyl alcohol (IPA). IPA was selected as a solvent replacement for water because of its outstanding miscibility with water, its inertness (i.e., its lack of reactivity with a cement binder compared to water), and its relatively smaller molecular size compared to water [22–24]. Further, using this approach, these researchers [20,21] were able to determine the critical a_H threshold required for the overall hydration reaction of the studied cementitious systems to proceed, that is, a critical threshold of $a_H \geq 0.70$ and ≥ 0.45 for C_3S [20] and $C_3A/C\$$ [21] systems, respectively.

This information provides insight that enables improved understanding of cementitious systems containing C_3S and $C_3A/C\$$ in their anhydrous forms. Paper II further enhances this understanding by employing the aforementioned thermodynamic approach on a standalone belite (β-C_2S) system.

1.3.2. Superplasticizers. Superplasticizers are polymeric dispersants used in OPC-based systems to improve rheological properties [13]. The incorporations of superplasticizers in a mix design can have benefits beyond rheology, that is, the integration of a superplasticizer reduces the amount of water required in an OPC-based mix, consequently leading to lower porosity and improved mechanical properties in the fully hydrated matrix [25,26].

There are several superplasticizers that have been introduced to concrete technologists over the years. To name a few modern superplasticizers: polynaphthalene sulfonates (PNS); polymamine sulfonates (PMS); polyethylene oxide (PEG) phosphonates; polycarboxylate ether (PCE); etc. Superplasticizers can have varying effects on hydration depending on the selected superplasticizer's molecular structure and composition; the cementitious system of interest; and the mode of addition. For example, PNS are generally negatively-charged linear polymers that have relatively low molecular weights, however the optimal molecular weight for PNS are dependent on the type of cement. PNS are reportedly more effective for systems requiring relatively high alkalinity (i.e., 13.6 pH) [27,28] — such as is required for alkali activated cements, for example, since they are chemically stable in such conditions [13,27,28]. This is explained by the correlation between the increased presence of alkali, increased concentration of SO_4^{2-} ions, and the PNS adsorption on aluminate phases [13,29]. This is in agreement with Nakakimi and Yamada's [30] findings, that is, the incompatibility relationship is associated with the type and amount of gypsum in a cementitious system. However, when PNS super-plasticizing effects were directly compared to PCE for a traditional cement system by Zhang and Kong [31], PCE demonstrated superior plasticizing capabilities but also greater decelerating effects on hydration rates, despite PNS demonstrating superior adsorption capabilities at approximately equivalent dosages. The varying performance between these superplasticizers can by and large be attributed to the superplasticizers' molecular structures. The following paragraph briefly discusses PCE and its parameters that are relevant to this dissertation.

PCE — first synthesized in Japan in the 1980s and has been extensively researched since then — is a well-known class of comb-shaped, polymer-based dispersants. PCE's comb-shaped architecture is comprised of an anionic backbone (i.e., polyacrylic acid or polymethacrylic acid) with side-chains (i.e., polyethylene glycol) attached to the backbone. These side-chains serve as steric repellents by protruding towards other cement particles and PCE molecules in the contiguous solution, effectively dispersing the system [32–38]. As mentioned above, the addition of PCE in a traditional cement system can also have a decelerating effect on cement hydration [32,33,38–41]. That is, PCE molecules function via electrostatically by attaching to the cement particles' positively charged surfaces and consequently impeding dissolution and nucleation of C-S-H [33,34,37,40,41]. PCE's molecular structure is thought to substantially influence the degree to which PCE adsorbs onto surfaces of cement and inhibit early hydration [33–35,42,43]. Further, with increasing dosage, PCE's retarding effect on cement hydration is observed to become more pronounced until the point at which the system is saturated with respect to PCE [43,44]. Paper III explores the combined effects of PCE's dose and molecular structure on the hydration of C_3S.

1.3.3. Mineral Additives. As production of OPC increases internationally [2,4,45,46], intensified stress is being placed on cement chemists to find replacement production procedures and resources to lessen CO_2 emissions resulting from OPC manufacturing [45,47–49]. That is, during the firing process of OPC — where the crushed and ground mineral precursors of OPC (i.e., argillaceous minerals containing silicates and aluminosilcate clay materials and calcium carbonate, typically in the form of calcite) are heated to approximately 1550°C [or lower, depending on impurity content] to form the anhydrous phases briefly discussed in Section 1.2.. At approximately 900°C calcium carbonate or rather $CaCO_3$ decomposes, causing the emission of CO_2. A potential solution, currently being extensively explored and optimized by researchers to mitigate CO_2 emissions, is partial replacement of OPC with CO_2-efficient mineral additives such as filler and pozzolanic materials. The following paragraph briefly define filler material behavior and provide examples of said materials.

A mineral additive, in the context of hydraulic cement systems and the work within this dissertation, can be referred to as a filler material when it exhibits a phenomena referred to within literature as the *filler effect* due to the alterations of hydration reaction rates [4,17,50–53] that accompany the replacement of cement with a filler material. More specifically, filler materials characteristically accelerate [4,17,51] early-age hydration (i.e., 0-to-24 hours after water is initially introduced to the anhydrous cementitious powder) chemical processes, leading to faster setting times and development of mechanical properties. This enhancement in hydration reaction rates is often attributed to the augmentation of total solid surface area that occurs when filler materials are used to replace cementitious powder. This in turn increases the number of surface sites available for the aforementioned hydration product, C-S-H — the "glue" phase — to nucleate and grow upon heterogeneously. Typical fillers materials include, but are not limited to: limestone (crystalline $CaCO_3$); quartz (crystalline SiO_2), silica fume (amorphous SiO_2); polymorphs of TiO_2 (i.e., rutile and anatase); metakaolin (amorphous-like $Al_2Si_2O_7$); and corundum (crystalline Al_2O_3) [52–59]. Paper IV compares the reaction performance of filler materials in [C_3S + filler] systems.

1.4. HYDRATION IN THE CONTEXT OF ISOTHERMAL CALORIMETRY

There are numerous physical techniques that can be employed to observe the hydration reaction progression for a given cementitious system. Other techniques are also often used to glean understanding regarding underlying kinetic mechanisms, but such techniques are outside of the scope of this work and are described in more detail here [60].

In the most basic sense, calorimetry is the measurement of heat [either absorbed or emitted] of a given system. Common calorimetry techniques — which, are discussed in more detail in this reference [60] in the context of cementitious systems for the interested reader — include differential scanning calorimetry (DSC) and adiabatic, semi-adiabatic, and isothermal calorimetry. With that stated, isothermal calorimetry — a technique that observes the heat evolution of a given sample at a constant temperature as it varies with time — is of interest to introduce in the context of cement hydration due to prominence and reoccurring utilization throughout the studies contained in this dissertation document.

Isothermal calorimetry is a useful tool when studying hydration reactions of cementitious materials. This technique is used to both qualitatively and quantitively observe the heat emitted and/or absorbed (i.e., exo-/endo-thermic) during chemical processes as a function of time. The physically obtained data can be expressed as the heat flow rate and/or the cumulative heat emitted as a function of time at a constant temperature. The heat flow rate is useful in understanding reaction kinetics, while the cumulative heat can be analyzed to obtain enthalpy, activation energy, and other thermodynamic parameters. The heat flow measured during the hydration process acts as a unique signature and can be used to better understand the underlying kinetic mechanisms in different cementitious systems. Early hydration can be categorized into four characteristic time-periods using the heat flow signatures (as seen in Figure 1.1.).

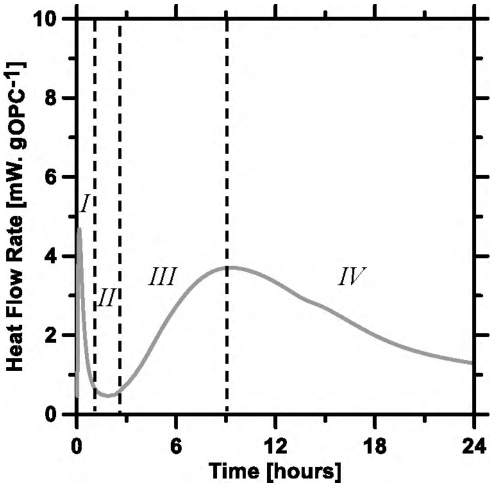

Figure 1.1. Early hydration of cement is often described in four periods that correspond to observable regime changes in heat flow rate as a function of time, which is measured using isothermal calorimetry. The four stages of early hydration are often referred to in the literature as: the (I) *initial period*; (II) *induction period*; (III) *acceleration period*; and (IV) *deceleration period.* The heat flow emitted over the course of the entire hydration reaction, with respect to each, unique cementitious system, can serve as a characteristic heat-evolution "fingerprint", yielding information about underlying kinetic mechanisms.

These are stated in literature as the (I) *initial period*; (II) *induction period*; (III) *acceleration period*; and (IV) *deceleration period* [3]. Within the first half hour or so from when the anhydrous cementitious powders come in contact with water (i.e., the *initial period*), particle surfaces are wetted and the consequent rapid dissolution and precipitation of hydration products leads to the *induction period*, where after rapid dissolution and precipitation, the pore solution is suddenly in a state of undersaturation. Two mechanisms have been proposed as the *induction period's* controlling process: a metastable barrier or a dissolution-precipitation step-regime, with the later having more supporting experimental evidence, which is summarized in these references [8,61]. The *induction period* is commonly thought to be rate-limited by a dissolution-precipitation step-regime until the pore solution becomes supersaturated and a mass nucleation event occurs (~ 4 h after hydration has been initiated), signaling the end of the *induction period* and the beginning of the *acceleration period*. The *acceleration period* — like the *induction period* — is also commonly described by its rate-limiting step, that is, the growth of the precipitated nuclei. At approximately 12 h of hydration, when the main hydration peak reaches a maximum heat flow rate, the *deceleration period* — a period of decreasing reaction rates, which is indicative of another change in the rate-limiting step — begins. The initiation of the *deceleration period* is somewhat debated within the literature, with most thinking this fourth period of hydration is initiated or, rather, rate-limited by one of three mechanisms: impingement, limited ion-diffusion — which is only thought to occur after all reactive surface sites are filled —, or limited dissolution [15,62–68]. There is some evidence in the literature against impingent and ion-diffusion as the rate-limiting steps during the *deceleration period*. It should be stated that the literature was, at one point, in agreement that impingement — both lateral and perpendicular — was the underlying mechanism that led the transition from the *acceleration* to the *deceleration period*, until several published micrographs were brought to the forefront, showing, the C-S-H in a “loosely packed” state (that is, not at an observable state of impingement) at 12 h of hydration [69–71], approximately at the time of occurrence of the main hydration peak.

1.5. A REVIEW OF NUMERICAL KINETIC-BASED MODELS IN THE CONTEXT OF CEMENT HYDRATION

As eluded to above, experimental isothermal calorimetry, heat-evolution results can be used to observe kinetic phenomena in cementitious systems, which are used to predict hydration and microstructural development of cement systems, typically by numerical kinetic models described in the literature [3,61,72–74]. The following text briefly summarizes kinetic models as they have been applied to cementitious systems in the past. The most famous numerical kinetic work established in the past century was by William A. Johnson and Robert F. Mehl [75], Melvin Avrami [76–78], and Andrey N. Kolmogorov [79], whose collective work is commonly denoted as JMAK kinetics. However, JMAK kinetics yielded relatively poor fits for cementitious systems [80–87], largely due to the mismatched assumptions established for JMAK compared to hydration of cement. That is, JMAK kinetics operated under the assumption of random nucleation occurring homogeneously over the total untransformed material of the given system and growth occurs independently and an isotropic fashion. However, as stated above, C-S-H grows heterogeneously in a needle-like manner [88–90]. As a result, Cahn's boundary nucleation and growth (pBNG) model, which assumes a constant nucleation rate and constant, isoptropic growth rate, where, nuclei form on in a random, heterogeneous fashion was adopted to model cementitious hydration [16]. Cahn's later work [91] and work by Villa and Rios [92] has served as inspiration for the more recent confined growth models that have been used to predict hydration for cementitious systems, which are discussed in a later paragraph [3].

Several follow-up studies [16,17,93–97] have been published in the literature that expand upon the work of Cahn [98] adapted by Thomas [16], and are sometimes referred to as phase boundary nucleation and growth (pBNG) models within the literature. In these models [16,17,93–97], a single product (encompassing both calcium silicate hydrate and calcium hydroxide) of constant density is assumed to form on cement particulate boundaries at a given nucleation event. As the product grows outward, pore space is consumed, both lateral and perpendicular impingement is assumed to occur and thought to lead to the *deceleration period*. Numerical models, based on these assumptions and diffusion-limited kinetics at later ages, have been used to fit the hydration rates of cementitious systems with some success [16,17,34,40,93–97]. However, Bullard [64] and Bullard et al. [65] presented simulated evidence, that impingement might not be the mechanisms triggering the switch between the *acceleration* to *deceleration period*, that is, there is evidence of perpendicular, but not lateral impingement — supported by micrographs [69–71], as stated above —, leading to doubt in the ion-diffusion layer theory and backing of limited dissolution as the rate-limiting step during the *deceleration period* in the literature [66,99,100].

Further literature, sought to challenge the limitation of BNG models in the context of current knowledge of hydration of cementitious systems. For instance, Cahn's older work is limited by the assumptions of static interfaces and isotropic growth rates (albeit, in various geometries, similar to JMAK kinetics), however adaptations of Cahn's more recent work [91] has allowed for confined growth, that is, a designated zone in time and space in the cited studies [73,101–106] is allotted for the calcium silicate hydrate phase to grow once nucleated. It's known that as the cement hydration reaction progresses, dissolution causes the boundary of the reacting cement particles to move inward and consequently, the formation of hydrates can occur outside and also, after some time, inside of the original grain boundary (as can be viewed via micrographs here [70] and described here [107]). As a result, confined growth models have been adapted to model the unsymmetrical fashion in which the calcium silicate hydrate phase has been observed to grow into and out towards the pore solution of the original anhydrous boundary, pre-wetting, but also adapted in studies where the focus is placed on the structure formation of the calcium silicate hydrate phase. The later models are often referred to as sheet or needle growth models in the literature and are referenced here [73,101–103,106]. Though confined growth, has become a prevalent approach to modeling cement hydration kinetics, other researchers champion a modified version of the pBNG approach[4,38,41,50,72,108]. In this model, the lateral and outward growth rates are temporally varied to relate the evolution in saturation of the pore solution with C-S-H's evolving growth rates. This model also employs a 2-step optimization procedure, which optimizes functional forms of the outward growth rate, allowing for an evolving outward growth rate as a function of time. The modified pBNG model takes a slightly different approach to the confined growth models, but both are in agreement with dissolution as the rate-limiting step during the *deceleration period*.

The previous text is not meant to interject that one model or group of models vs. others is right or wrong or, further, that specifics of various mechanistic-based hydration theories are correct or incorrect, rather the text is meant to highlight the ambiguity in the true kinetically rate-limiting steps at various points during the cement hydration process and the consequently developed numerical kinetic models. Models such as these, seek to understand the basic, underlying mechanisms behind a reaction, in this case the hydration or setting process of a cementitious system, and though progress has been made in the past decade, there is most likely over another decade or more of work to be completed until this work can be scaled in terms of holistic, in-field performance, that is, before kinetic models can be directly linked to fresh properties.

1.6. ORGANIZATION OF DISSERTATION

The introduction (i.e., Section 1.) outlining relevant background information pertaining to the research objectives (i.e., Sections 1.1.) has been given to provide the necessary context for readers unfamiliar with the dissertation topic. This thesis document is comprised of seven papers that have already been published, submitted, or prepared for publication.

Paper I through IV explores hydration of OPC, β-C_2S, and C_3S by means of physical experiments in conjunction with either a numerical-based kinetic or thermodynamic approach.

- Paper I provides an explanation as to why hydration rates of an OPC system are negligibly effected by varying water-to-cement ratios in dilute systems by utilizing isothermal calorimetry techniques and the modified pBNG model.
- Paper II serves as a re-exploration of the hydration of β-C_2S with modern techniques, while also providing values for thermodynamic parameters — water

activity (a_H) and solubility product constant of β-C_2S (K_{C_2S}) — for the first time, using an established thermodynamic approach.

- Paper III explores the combined effect of varying PCE molecular structure and dosages — referred to within the paper as the composite architectural parameter (P_{PCE}) — on C_3S hydration rates through physical and the kinetic-based pBNG model.
- Paper IV investigates the effect of various sized-classified filler types — limestone, quartz, rutile, and corundum — on early C_3S hydration through physical and the kinetic-based pBNG model.

Paper V through VII take a slightly different approach compared to the above papers. The above papers approach the research objectives with a traditional thermo-kinetic fundamental approach, while the below papers take a more “engineering” approach. More specifically, the above papers investigate the effect of a varying parameter in simple systems to elucidate understanding of fundamental mechanisms. As a system becomes increasingly complicated (i.e., to the degree that a given OPC-based system is complicated), execution of a thermo-kinetic model becomes increasingly difficult. Therefore, to obtain rapid and reliable predictions for systems with multiple components, an alternative computational technique is proposed — machine learning (ML), an artificially intelligent technique, ideal for the multivariable systems that are focused on in Papers V through VII.

PAPER

I. ELUCIDATING THE EFFECT OF WATER-TO-CEMENT RATIO ON THE HYDRATION OF CEMENT

Margarita Hernandez[1], Jonathan Lapeyre[2], Rachel Cook[2], Aditya Kumar[2], and Dimitri Feys[1]

1. Department of Civil, Architectural, and Environmental Engineering, Missouri University of Science and Technology (S&T), Rolla, MO 65409, USA.

2. Department of Materials Science and Engineering, Missouri University of Science and Technology (S&T), Rolla, MO 65409, USA.

ABSTRACT

The hydration of cement is often modeled as a phase boundary nucleation and growth (pBNG) process. Classical pBNG models, based on the use of isotropic and constant growth rate of the main hydrate, that is, calcium−silicate−hydrate (C−S−H), are unable to explain the lack of any significant effect of the water-to-cement (w/c) ratio on the hydration kinetics of cement. This paper presents a modified form of the pBNG model, in which the anisotropic growth of C−S−H is allowed to vary in relation to the nonlinear evolution of its supersaturation in solution. Results show that once the supercritical C−S− H nuclei form, their growth remains confined within a region in proximity to the cement particles. This is hypothesized to be a manifestation of the sedimentation of cement particles, which imposes a space constraint for C−S−H growth.

In pastes wherein the sedimentation of cement particles is disrupted, the hydration kinetics are no longer unresponsive to changes in w/c. Unlike C–S–H, the ions in solution are not confined, and hence, the supersaturation-dependent growth rate of C–S–H diminishes monotonically with increasing w/c. Overall, the outcomes of this work highlight important aspects that need to be considered in employing pBNG models for simulating hydration of cement-based systems.

Keywords: Cement; Hydration; Kinetics; Nucleation and Growth; Supersaturation.

1. INTRODUCTION

The reaction between cement and water, that is, hydration, involves dissolution of the anhydrous phases concomitant with precipitation of the hydration products (subsequently referred to as hydrates). Extensive research has been devoted to study the kinetics of cement hydration, as it principally dictates the development of the microstructure and the consequent evolution of both fresh (e.g., workability and time of set) and hardened properties (e.g., the rate/extent of strength development) of concrete. [1–3] It is widely accepted [1,2,4–6] that the early stage of cement hydration is driven by the nucleation and growth [7–10] of the main hydration product, that is, calcium–silicate–hydrate [1,5,11–13] (C–S–H, as per cement chemistry notation: C = CaO, S = SiO_2, H = H_2O, A = Al_2O_3, and F = Fe_2O_3); although, it is worth mentioning that in some studies, [14,15] it has been argued that kinetics of cement hydration is controlled by dissolution of the phases present in cement. In a typical plain cement paste (i.e., cement + water), C–S–H nucleates heterogeneously on the solid-phase boundaries, that is, surfaces of cement particles, and therefore, the mechanism of its formation is usually termed as phase boundary nucleation and growth (pBNG). As hydration progresses, the percolation of the overlapping layers of C−S− H binds the paste cohesively and leads to setting and subsequent development of mechanical properties. [5,11,16,17] Akin to pBNG processes occurring in metallic systems (e.g., solidification of metal), [18,19] the temporal evolution of cement hydration rate, as monitored using isothermal calorimetry techniques, comprises a characteristic reaction rate peak (i.e., the main hydration peak) up to which the rate of reaction accelerates and beyond which it declines. [1,13]

Several numerical models based on the pBNG mechanism have been developed to reproduce the experimental measurements of cement hydration rates. [5,6,11,12,16,20,21] In these models, a single product of constant density is assumed to form heterogeneously on solid phase boundaries at a given nucleation event, and its subsequent growth into the contiguous capillary pore space is treated as the rate-controlling mechanism. As the product fills up the capillary pore space, impingements between product nuclei, growing on the same or adjacent anhydrous particles, become increasingly dominant and ultimately cause a deceleration in the overall hydration rate. Numerical models, based on this premise and some additional assumptions (e.g., spherical or needlelike geometry of the product, diffusion-limited kinetics at later ages, and timedependent growth of C−S−H) have successfully been used to fit the hydration rates of cementitious systems. [5,6,12,16,20–24] These fits are typically obtained by iteratively varying relevant pBNG parameters (e.g., nucleation site frequency and product growth rate) to minimize the deviation between numerical and experimental hydration rates. However, as pointed out, [6,22,25] the parameters derived from such a fitting can be misleading as some underlying assumptions of the classical pBNG mechanism do not necessarily represent the physics of C−S−H nucleation and growth accurately. More specifically, the assumptions of (a) isotropic (i.e., spherical) growth of the product does not represent the experimentally observed needlelike geometry of C−S−H growth at early ages, [26–28] (b) the constant rate of product growth does not comply with the time-dependent variation of its supersaturation in the solution, [13,22,27,29,30] and (c) unconstrained formation of the product throughout the capillary pore space fails to explain the lack of any significant effect of the water-to-cement ratio (w/c mass basis) on the hydration kinetics of cement. [16,31,32] The last point is the main focus of this study and is described in further detail below.

Past studies [12,16,31] have shown that the early age (i.e., up to 24 h) hydration kinetics of cement are broadly unaffected by the w/c of the system. However, in pBNG models, [6,16,25,32] an increase in w/c implies a decrease in the area of the substrate per unit volume of the paste, which in turn affects the rate of formation of C−S−H and thus the overall hydration kinetics. Specifically, with increasing w/c, whereas impingements between C−S−H nuclei growing on the same particle remain broadly unaffected (i.e., assuming the same nucleation density of C−S−H), impingements between C−S−H layers growing on adjacent cement particles are fewer because of larger spacing between them. As a result, pBNG models predict a dependency of the hydration rate on w/c, unlike what is observed in experiments. [12,16,31] These contradictions between experimentally observed hydration rates and predictions of the pBNG model, including ones that involve the implementation of the nucleation and densifying growth theory (i.e., time-dependent densification of C−S−H), [5,16,33] are highlighted in the work of Kirby and Biernacki.

[31] In a recent study, Masoero et al. [34] proposed a reaction zone hypothesis to reconcile the aforementioned contradictions. The authors proposed that during the early hydration period, C−S−H grows exclusively within regions close to surfaces of the reactant particles; these regions collectively were designated as the reaction zone. Within the reaction zone, as the amount of C−S−H increases with hydration, growing impingements between C−S−H nuclei causes deceleration of the hydration rate, all while abundant capillary pore space remains unoccupied outside of the reaction zone. The hypothesis provides novel and significant insights and, more importantly, explains the mechanisms driving the deceleration of the hydration rate beyond the main hydration peak in high w/c systems. However, the assumption of the growth rate of C−S−H being constant throughout the process of hydration, as used in the study, [34] is inconsistent with recent studies that clearly show a temporal decline of C−S−H supersaturation (i.e., driving force for the growth of C−S−H) in solution. [22,27,29,30] In addition, Masoero et al. [34] assumed the growth of C−S−H to occur at equivalent rates in all directions. This assumption has implications not just on the geometry of C−S−H nuclei but also on the overall rate of hydration. Scherer et al. [6,28] noted that at early stages of cement hydration, the growth of C−S−H occurs in a highly anisotropic manner. Specifically, the growth rate of C−S−H in the direction normal to and away from the substrate is higher than its growth rate in the direction parallel to the substrate. This theory of anisotropic growth of C−S−H gains support from recent microscopic observations of the geometry of C−S−H growth. [26–28] Assuming isotropic growth of C−S−H also results in greater impingements of its nuclei and, thus, a faster approach to the main hydration peak. [6,25] As a result of these discrepancies between experiments and assumptions made within the

model presented in ref [34], the pBNG parameters derived from the simulations are difficult to interpret. As examples, the predictions of (i) significantly higher nucleation density of C−S−H in C_3S (i.e., tricalcium silicate, the major phase in cement constituting 50−70% of its mass [3]) suspensions (i.e., w/ c = 50) as compared to that in pastes (i.e., w/c = 0.40) [34] are difficult to reconcile considering that the critical supersaturation at which nucleation of C−S−H occurs should be independent of the w/c, [5,22,35] and (ii) the smaller size of the reaction zone in suspensions as compared to that in pastes [34] is counterintuitive, considering that the capillary pore space increases with increasing w/c, thus allowing C−S−H to grow more freely. To resolve these inconsistencies and to better explain the role of w/c on the mechanisms of cement hydration, further refinement of the pBNG model is needed. Such refinements need to be based on observations from experiments reported in various recent studies. [26,27]

This study employs a combination of experiments and computer simulations to elucidate the effect of w/c on the early age hydration kinetics of cement. Isothermal microcalorimetry is used to measure the hydration rates of cementitious systems across a wide range of w/c, including both pastes and suspensions. A pBNG model, incorporating a modification of the reaction zone hypothesis and allowing anisotropic and time-dependent growth rate of the hydrate, is developed and tested against experiments. Results obtained are used to describe the mechanisms that drive the progress of nucleation and growth of the C−S−H in such systems. The outcomes provide new understanding and quantification of rate controls of cement hydration and highlight important aspects pertaining to pBNG processes that need to be considered in the development of numerical pBNG models.

2. MATERIALS AND METHODS

2.1. MATERIALS

A commercially available type I ordinary Portland cement with an estimated crystalline phase composition of 61% C_3S, 8% C_2S, 6% C_3A, 9% C_4AF, and 3.4% of gypsum ($CaSO_4 \cdot 2H_2O$) was used in this study. Further details pertaining to the chemical composition of cement — as obtained using a combination of X-ray fluorescence and quantitative X-ray diffraction (XRD) methods — are provided in the Supporting Information in the corresponding publication. The cement, as received from the supplier, was ground using a ring grinder to generate two different PSDs. In the subsequent discussions, the "as-received" and ground cements are referred to as coarse and fine cements, respectively. The PSDs of the cements, shown in Figure 1, were measured using a Beckman Coulter static light scattering (SLS) analyzer (LS13-320) using a 750 nm laser source that is incident on a dilute suspension of powder particles in isopropyl alcohol, dispersed by ultrasonication. The median particle sizes (d_{50}, μm) of the PSDs of the coarse and fine cements were determined as 15.55 and 9.23 μm, respectively. By factoring the bulk density (i.e., 3150 kg. m^{-3}, as measured using a pycnometer), the total SSA (m^2. kg^{-1}) of the coarse and fine cements were calculated from the PSDs as 196 and 441 m^2. kg^{-1}, respectively. XRD patterns were obtained for the coarse and fine cements, and based on the results, it was confirmed that there was no change in the cement's composition as a result of the grinding.

2.2. METHODS

2.2.1. Experimental Work. To study the effects of the water content, cement + water mixtures were prepared at different w/c (mass basis) ranging from 0.45 to 10. Low and high w/c cementitious mixtures are typically described as paste and suspension, respectively. However, as the limiting w/c beyond which a mixture ceases to be a paste (or becomes a suspension) is not well-known, in this paper, all mixtures are referred to as pastes. It should be noted that all pastes included in this study are water-rich, as their w/c exceeds the critical value of 0.42 (i.e., minimum w/c needed for complete hydration of cement). [36,37] The rate and extent of hydration were monitored up to 24 h after mixing using a TAM IV isothermal conduction microcalorimeter programmed to maintain the sample at a constant temperature of 20 ± 0.1 °C. Compared to conventional methods of reactivity assessment (e.g., isothermal calorimetry), microcalorimetry methods are considered more accurate as they allow quantification of the heat flow rate of the reaction at a very high resolution (10^{-7} J/s), which enables monitoring the dissolution of compounds even at high dilutions. [13,38,39] The titration cell (maximum diameter = 1.25 cm) of the microcalorimeter is fitted with an electrically driven agitator, which allows in situ mixing of hydrating pastes prepared at high w/c. However, with the exception of selected experiments (which are identified in the text), heat evolution profiles of all pastes discussed in this paper were obtained without the use of the agitator. In situ mixing was purposely avoided for two reasons: (i) to mimic practical concrete mixing protocols, which are also devoid of in situ mixing and (ii) to maintain consistent protocols across experiments, as in situ mixing cannot be applied to low w/c pastes. The cumulative and differential heat release obtained from calorimetry experiments were normalized by the enthalpy of cement hydration (as calculated from mass fractions and enthalpy of individual phases [5]), 472 J. g_{cement}^{-1}, to determine the extent of hydration [13,16] (i.e., degree of hydration, α, expressed as the fraction of cement reacted) and the rate of hydration (i.e., $d\alpha/dt$, h^{-1}) of cement, respectively, as functions of time. This method of derivation of α and $d\alpha/dt$ is based on the assumption that the measured heat release is solely on account of cement hydration. In addition to monitoring the evolution of heat linked to hydration, the evolutions of the electrical conductivity and pH of the pore solution of the pastes were measured at discrete time steps between mixing and 48 h of hydration. These measurements were carried out using a HI5522 electric conductivity and pH meter with the HI76312 and HI1131 probes, respectively. Samples used for these measurements were prepared using the same protocols as those for calorimetry experiments.

A Netzsch STA 409 PC thermogravimetric analyzer was used to identify and measure the quantities of phases present at different hydration times. Toward this, the mass loss (thermogravimetry) and the differential mass loss (DTG) traces were processed to quantify the degree of hydration and phase contents, that is, loss on ignition, evaporable and nonevaporable water, portlandite, and calcite (if any may have formed because of carbonation of calcium-rich phases). For these quantifications (i.e., α and phase contents), well established methods detailed in prior studies [40,41] were used.

2.2.2. Phase Boundary Nucleation and Growth (pBNG) Model. A modified pBNG formulation is applied to describe the effects of w/c on the hydration kinetics of cement. The cement used in our study is composed of four phases (C_3S, C_2S, C_3A, and C_4AF), all of which react with water simultaneously, though at different rates. [1] C_2S

and C_4AF have low intrinsic dissolution rates and, hence, do not release substantial amounts of heat at early ages.[1,6,14] In contrast to these phases, the reaction of C_3A with water and aqueous SO_4^{2-} ions (i.e., resulting from the dissolution of gypsum) is rapid; this causes nucleation of ettringite crystals within the first few minutes of mixing. [42,43] Nonetheless, after the initial nucleation burst, ettringite subsequently grows at a very slow (and near constant) rate for the next few hours, thus releasing little heat. [42,44] As such, in pBNG models applied to cement pastes, [6,11,12,16,25,45] including the model used herein, early age kinetics of cement hydration is assumed to be dominated by hydration of the C_3S phase. The same assumption implies that during the early stages of cement hydration, the major products in the cement paste are C−S−H and CH, both of which form in stoichiometric amounts in relation to the amount of hydrated C_3S. On the basis of these assumptions, in pBNG models, a single product of constant density (i.e., combining the bulk density of CH and C−S−H phases) is assumed to form at a given nucleation event, and its subsequent growth on solid-phase substrate boundaries (i.e., cement surfaces) is treated as the rate-controlling mechanism that drives the kinetics during the early ages of cement hydration. This assumption is referred to as the site saturation condition, implying that the growth of the product phase begins from a fixed number of nuclei that form at very early ages (i.e., at time = τ h), and no further nuclei are permitted to form after this very initial nucleation burst [46,47] (i.e., nucleation rate = 0 $\mu m^{-2} \cdot h^{-1}$). On the basis of these criteria, at any given time t (h), the volume fraction of the reactants (i.e., C_3S and water) transformed to product [X(t), unitless: volume of product divided by the total initial volume of the paste] is given by Equation 1. [13,22,25,35,48]

$$\mathrm{X(t)} = 1 - \exp\left[-2\mathrm{k_G}\cdot(\mathrm{t}-\tau).\ \left(1 - \frac{\mathrm{F_D}[\mathrm{k_S}\cdot(\mathrm{t}-\tau)]}{\mathrm{k_S}\cdot(\mathrm{t}-\tau)}\right)\right] \tag{1}$$

$$\text{where,}\qquad \mathrm{F_D(x)} = \exp(-\mathrm{x}^2)\int_0^{\mathrm{x}} \exp(\mathrm{y}^2)\,\mathrm{dy} \tag{2}$$

In Equation 1, FD is the f-Dawson function, expressed as an integral (Equation 2). The variable ks (h^{-1}) is related to the reciprocal of time required by the product nuclei to provide complete coverage of anhydrous cement particles. [6,25] The value of ks depends on the product's nucleation density ($I_{density}$, units of μm^{-2}), that is, the number of total supercritical nuclei produced per unit surface area of cement as well as on the geometry and rate of their growth (Equation 3). In the model presented in this study, the growth of the product is assumed to occur in an anisotropic fashion while varying with respect to time. $G_{out}(t)$ ($\mu m.\ h^{-1}$) is the outward growth rate of the product, representing the direction normal to and away from the substrate (i.e., surfaces of cement particles). $G_{par}(t)$ ($\mu m.\ h^{-1}$) is the growth rate in a lateral direction, that is, along the two-dimensional (2D) plane parallel to the boundary of the substrate. Along this 2D plane, the growth rate is assumed to be isotropic. The introduction of a time dependency on the product growth rate is a digression from the classical form of pBNG, which assumes the growth rate to remain constant throughout the hydration process. This is based on an implementation originally formulated by Bullard et al. [22] and subsequently adopted by Oey et al., [35] Meng et al., [13] and Lapeyre and Kumar [48] to capture the temporal variation in the growth rate of C−S−H, as its supersaturation in the solution varies nonlinearly with time. As both the outward (G_{out}) and parallel (G_{par}) growth rates vary with time, a constant 2:1 ratio for G_{out}/G_{par} is assumed, such that the anisotropy factor, that is, g (unitless) in Equation 4, is 0.25 throughout the hydration process. This relationship between G_{out} and G_{par} represents the anisotropic growth of needlelike domains of the product [6,25] and is in good agreement with recent experimental data of the geometry of C−S−H growth at early ages. [26–28,30]

$$k_s = G_{out}(t).\ (\pi.g.I_{density})^{\frac{1}{2}} \tag{3}$$

$$g = \left(\frac{G_{par}(t)}{G_{out}\ (t)}\right)^2 \tag{4}$$

In Equation 1, the variable k_G (h^{-1}) is related to the reciprocal of time required for the product to fill the capillary pore space. The value of k_G depends on the product's outward growth rate (G_{out}) as well as on the constant r_G (unitless), which represents the ratio of the growth rate into and out of the substrate in the normal direction (Equation 5). In their study, Scherer et al. [6,25] noted that at early ages of hydration, hydrates do not penetrate the cement particles, and therefore, $r_G \approx 0.50$. This is because at early ages, the ionic species, that is, $H_3SiO_4^-/H_2SiO_4^{2-}$, $CaOH^+/Ca^{2+}$, and OH^-, responsible for the precipitation of C−S−H transport predominantly from the substrate's surface toward the contiguous solution while showing little movement through the product in the reverse direction. [6] Therefore, in all simulations presented in this study, the value of r_G was assumed to be constant at 0.50. Another important parameter that dictates the value of k_G, and thus the kinetics of hydration, is the boundary area of the substrate per unit volume of the reaction vessel (a_{BV}, μm^{-1}) (Equations 5 and 6). Here, the area of the substrate is simply the initial total surface area of the cement particles. The definition of the reaction vessel, however, differs among different studies. Thomas [12] defined the reaction vessel as the space required by hydrates when the hydration of cement is complete (i.e., $\alpha = 1$), thus rendering the volume of the reaction vessel, and consequently a_{BV}, independent of the w/c ratio. As per this definition, the reaction vessel's volume is set at its minimum value, just enough to accommodate the hydrates. In several subsequent studies, [5,6,13,25,32,35] however, the reaction vessel's volume was set at its maximum allowable value, that is, equal to the volume of the paste. On the basis of this definition, a_{BV} changes in response to changes in w/c, and the implication is that the hydrates are allowed to grow throughout the capillary pore space until either it is fully occupied or the hydration of cement is complete. As different definitions of a_{BV} exist in the literature, in this study, a modified definition has been used that allows the volume of the reaction vessel to vary between the minimum and maximum allowable values (Equation 6). In Equation 6, ρ is the density (water = 1000 kg. m^{-3} and cement = 3150 kg. m^{-3}), and SSA_{cem} (m^2. kg^{-1}) is the specific surface area of cement particles. The parameter p_f (unitless) acts as a free variable used in the simulations to represent the reactive paste fraction, that is, the fraction of the paste's volume within which the formation of hydrates occurs. When $p_f = 1$, the entire volume of the paste acts as the reaction vessel, whereas for fractional values of p_f, the volume of the reaction vessel is smaller than that of the paste. In such cases (i.e., $p_f < 1$), the amount of water contained within the reaction vessel is smaller than the amount of water added to the paste, though all of the solid phases (i.e., anhydrous cement particles and hydrates) are assumed to be bounded within the reaction vessel. By accounting for the excess water (i.e., water outside of the reaction vessel), the w/c ratio of the reaction vessel (w/c_{RV}, by mass) can be calculated from Equation 7.

$$k_G = r_G . G_{out}(t) . a_{BV} \quad (5)$$

$$a_{BV} = \left[\frac{SSA_{Cem}}{\left(\frac{\frac{w}{c}}{\rho_{Water}} + \frac{1}{\rho_{cement}}\right).p_f}\right] \tag{6}$$

$$w/c\text{-}_{RV} = p_f.\frac{w}{c} - \left[\frac{\rho_{Water}}{\rho_{cement}}.(1 - p_f)\right] \tag{7}$$

The volume fraction of the product [X(t)], as calculated from Equation 1, and the degree of hydration (α, unitless) of cement are related by a constant B (unitless) [13,22,35] described in Equation 8a:

$$\alpha(t) = B.X(t) \tag{8a}$$

$$B = \left[\left(\frac{\frac{\rho_{cement}}{\rho_{products}}}{\frac{\frac{w}{c}.\rho_{cement}}{\rho_{water}} + 1}\right) + \left(\frac{c + \frac{1}{\rho_{cement}} - \frac{1}{\rho_{water}}}{\frac{1}{\rho_{products}} - \frac{1}{\rho_{water}}}\right)\right]^{-1} \tag{8b}$$

where, ρ products is the bulk density of combined hydration products (assumed to be 2070 kg. m^{-3}), [49,50] and the parameter $c = -7.04 \times 10^{-5}$ m^3. kg^{-1} represents the chemical shrinkage per kilogram of cement that is consumed over the course of its hydration. [51] On the basis of the scheme described above, measured hydration rates can be simulated using the pBNG model by varying three parameters: $G_{out}(t)$, $I_{density}$, and p_f. Of the three parameters, $I_{density}$ and p_f are constants with respect to time, whereas $G_{out}(t)$ varies with respect to time. Therefore, to obtain the optimum values (i.e., of $I_{density}$ and p_f or functional forms (i.e., of $G_{out}(t)$) of these parameters for a given system, a Nelder−Mead-based simplex algorithm [35,52,53] that uses derivative-free and nonlinear optimization principles is employed in two steps. In the first step, the value of G_{out} is kept constant throughout the 24 h of cement hydration and fixed at 0.075 μm. h^{-1} for all systems. Similar values of G_{out} have been reported in a prior study [26] based on scanning transmission electron microscopy (STEM) analyses of early age hydration of impure C3S. The simplex algorithm then iteratively varies $I_{density}$ and p_f, within predefined bounds (i.e., $0.1\ \mu m^{-2} \leq I_{density} \leq 1000\ \mu^{-2}$, and $0.0 \leq p_f \leq 1.0$), until the magnitude of the difference between the simulated and measured rates of product formation — expressed as dX/dt, or the derivative of Equation 1, for each paste is minimized. It is pointed out that within the first step, the model represents the classical pBNG formulation, [12] wherein the anisotropic growth of the product nucleating at a virtual time τ (h) is kept constant throughout the hydration process. Past studies, [13,22,35,48] however, have shown that such classical pBNG models are unable to capture the decline in the growth rate of the product as its supersaturation in the solution declines with time. Therefore, to account for the time-dependent variation in the growth rate, a second simulation step is employed. Here, at any given time t, the optimum values of $I_{density}$ and p_f yielded from the first step are used as constants, whereas G_{out} is allowed to vary iteratively within the bounds of 10^{-4} -to-102 $\mu m.\ h^{-1}$ to minimize the deviation between the simulated and measured hydration rates for each paste. When the simplex algorithm converges, the value of G_{out} is taken to be the optimum value at that time. The optimum values of G_{out} for the entire duration of cement hydration are thus determined by implementing such an optimization process over the first 24 h of hydration using a time step of 0.05 h. The time-dependent G_{out}, obtained as such, mimics the growth of the product in relation to its supersaturation in the solution, [13,22,35,48] as described in the Results and Discussion.

3. RESULTS AND DISCUSSION

To study the effect of w/c on the hydration mechanisms of cement, the kinetics of hydration of two different particle size distributions (PSDs: see Figure 1) of the same cement (i.e., of the same composition) were determined. Figure 2 shows representative heat evolution profiles of pastes prepared using the coarse cement at different w/c ratios. As can be seen, despite significant differences in water contents (i.e., 58.64 and $96.93\%_{\mathrm{vol}}$ of water in pastes prepared at w/c of 0.45 and 10, respectively), the kinetics and degree of cement hydration within the first 24 h are broadly similar across all pastes. The lack of any significant effect of w/c was also observed for pastes prepared with the fine cement (Figure 3). These results are in good agreement with those reported in prior studies. [12,16,31] Upon comparing the heat evolution profiles of pastes prepared with fine and coarse cements, faster hydration kinetics was noted for the former (Figure 3c). This enhancement in hydration of the fine cement is highlighted as the leftward shift of the heat evolution profile and a higher heat flow rate at the main hydration peak and can be attributed to the higher SSA of its particles, [5,16,54–56] which enhances the number density of topological dissolution sites as well as sites for heterogeneous nucleation of hydrates. It should be pointed out that these enhancements in hydration rates of the fine cement are smaller in relation to the augmentation in the SSA of its particles with respect to those of the coarse cement (e.g., 72% increment in the heat flow rate at the peak vis-a-vis 125% increment in SSA).` This suggests a nonlinear relationship between reactivity enhancements and surface area increments. On the basis of these results as well as those reported in prior studies, [13,16,56] it is hypothesized that improvements in reactivity are realizable only up to a threshold level of particulate fineness. Beyond this threshold, reactivity enhancements decline due to agglomeration of the finer particles, which renders a fraction of their surface area unavailable for reaction. [13,16,56] It is clarified, however, that the aforementioned loss in the surface area is not responsible for the apparent insensitivity to w/c.

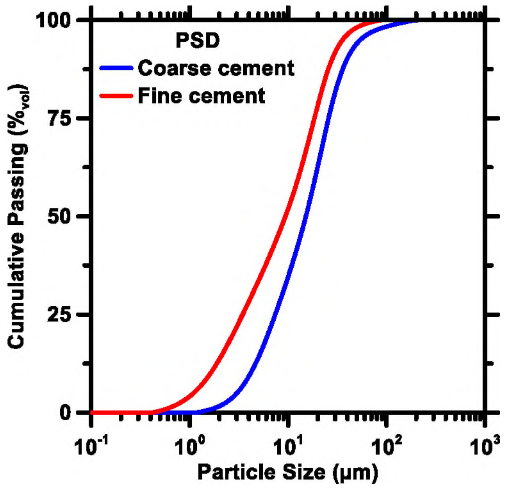

Figure 1. The PSDs of the "as-received" (coarse) and ground (fine) cement as measured using SLS methods. The largest uncertainty in the median diameter (d_{50}, μm) of the powders based on six replicate measurements, was ±6%.

Figures 2 and 3 qualitatively show the influence of w/c and cement fineness on the hydration kinetics of cement. To obtain quantitative information, portlandite contents of the pastes and the degree of hydration of cement after 24 h of hydration were determined using differential thermogravimetry (DTG) [40] and calorimetry methods (Figure 4). As can be seen, across all w/c, portlandite contents are broadly similar, provided that the fineness of the cement does not change. Pastes prepared with the finer cement have higher portlandite contents compared to their coarser cement counterparts.

This is attributed to the higher degree of hydration of the finer cement (Figure 4b). Past studies, based on microstructural investigation,[34,57,58] have shown that the precipitation of portlandite occurs homogenously in the capillary pore space. This would imply that an increment in the capillary pore volume would facilitate the formation of portlandite. However, the equivalency in portlandite contents across pastes prepared at different w/c ratios suggests that the rate controlling factor for the precipitation of portlandite is not the volume of capillary pores, but rather the rate of cement hydration, which, in turn, is driven by the nucleation and growth of C−S−H.

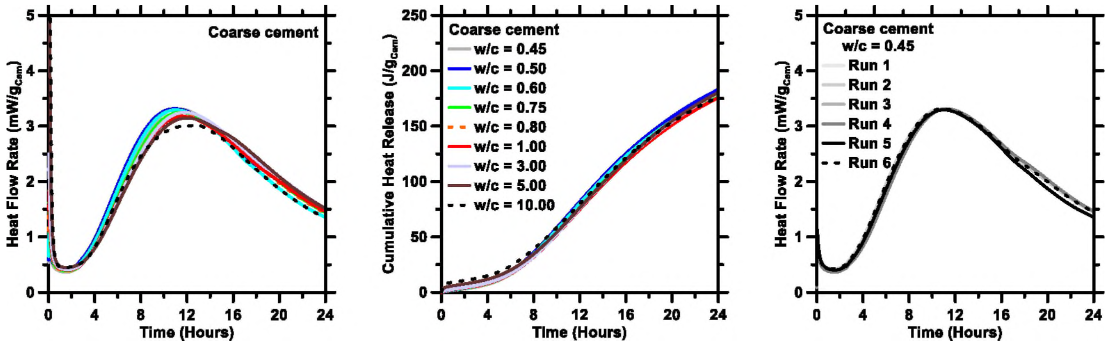

(a) (b) (c)

Figure 2. Isothermal microcalorimetry based determinations of (a) heat flow rates, and (b) cumulative heat release of pastes prepared using the coarse cement at different w/c. (c) shows the repeatability of heat flow rate determinations for a representative system. Similar analyses conducted on multiple pastes reveal that the uncertainty in the heat flow rate is within ±2%.

The heat evolution profiles (Figures 2 and 3) and the results obtained from DTG analyses (Figure 4) show that the rates of cement hydration and C−S−H precipitation are independent of the w/c and, therefore, the availability of space in the microstructural volume (i.e., capillary pore space). To quantify the evolution of the unoccupied space in the microstructure (i.e., capillary porosity) as a function of the degree of hydration of cement, the Powers model [36,37] was used. The results obtained from the Powers model (Figure 5a) clearly show that at the degree of hydration corresponding to the time of occurrence of the main hydration peak (i.e., $\alpha = 0.13$, obtained by averaging values of α determined from calorimetry profiles of pastes prepared using the coarse cement at different w/c ratios), there is plenty of space available in the microstructural volume, even in pastes prepared at a low w/c. For example, in pastes prepared at w/c of 0.45 and 10, capillary pores comprise of 52.1 and 96.3% of the paste's volume, when $\alpha = 0.13$. The decline in the hydration rate, after the main hydration peak, in spite of the abundance in space cannot be explained solely on account of impingements between C−S−H nuclei growing on cement particle surfaces. To illustrate this point, virtual microstructures of pastes generated by a three-dimensional (3D) microstructural model [5,16,33,48,59–62] are shown (Figures 5b and 5c). In these simulations, C−S−H and other hydrates (e.g., portlandite), precipitating as a result of cement hydration, are allowed to grow heterogeneously on cement particle surfaces and homogeneously in the pore space, respectively. As can be seen in Figures 5b and 5c, at the main hydration peak, although C−S−H nuclei provide partial coverage of the cement particles, impingements between C−S−H layers growing on neighboring particles are insignificant, especially in high w/c pastes. Therefore, mechanisms other than the impingements between C−S−H nuclei are responsible for deceleration of the hydration rate of cement in pastes.

To further investigate the role of w/c on cement hydration, measured hydration rates of pastes were simulated using the pBNG model. As can be seen in Figure 6, through the evaluation of optimum values of the outward growth rate of the product ($G_{out}(t)$), the product nucleation density ($I_{density}$), and the reactive fraction of the paste (p_f), the model is able to reproduce the experimental results. The variations in these simulation parameters are analyzed below to describe the alterations in the nucleation and growth process in relation to the initial process parameters, that is, w/c and cement fineness.

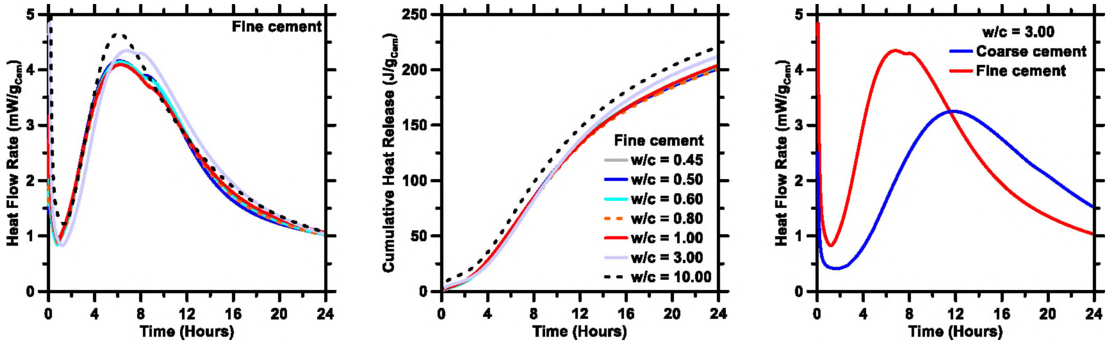

(a) (b) (c)

Figure 3. Isothermal microcalorimetry based determinations of (a) heat flow rates, and (b) cumulative heat release of pastes prepared using the fine cement at different w/c. (c) Comparison of heat flow rates of pastes prepared at equivalent w/c using cements of different fineness.

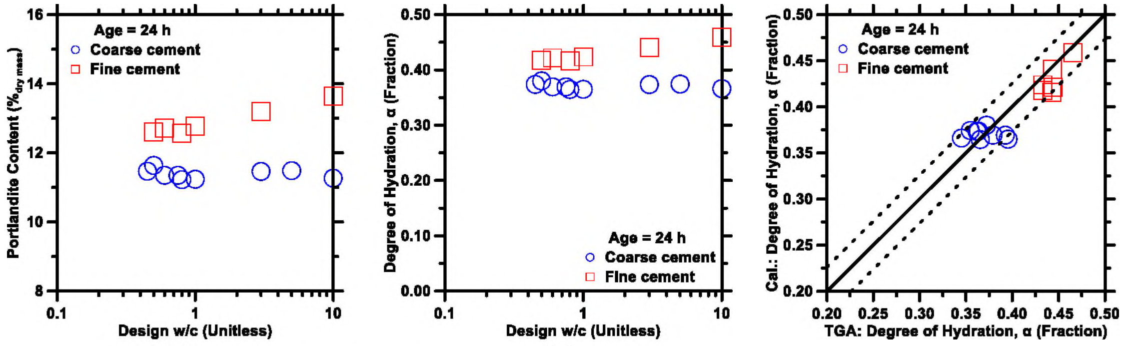

(a) (b) (c)

Figure 4. (a) Portlandite mass contents (as mass percent of the binder) and (b) degree of hydration of cement (α) after 24 h of hydration in pastes prepared at different w/c, as determined from DTG analyses. (c) Comparison between α as calculated from microcalorimetry and DTG methods. The dashed lines represent ±2.5% bounds. The highest uncertainty in phase quantifications or determination of α by DTG methods is ±2.5%.

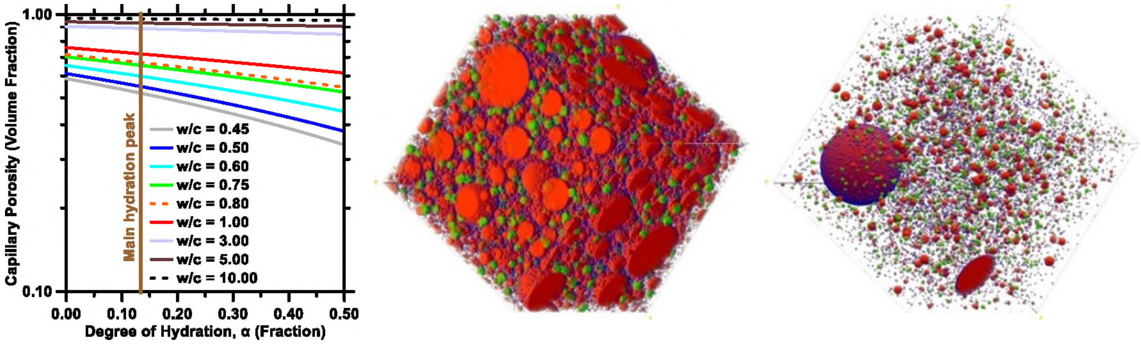

(a) (b) (c)

Figure 5. (a) Correlation between capillary porosity and degree of hydration (α) in pastes prepared at different w/c. In these calculations, α is provided as an input, and the corresponding capillary porosity is calculated based on the phase assemblages predicted by the Powers model [36,37]. The solid vertical line indicates the average value of α of all pastes, prepared using the coarse cement, at the main hydration peak. 3D virtual microstructures of cement pastes prepared using the coarse cement at (b) w/c = 0.45 and (c) w/c = 10 when $\alpha = 0.13$ (i.e., at the main hydration peak). The anhydrous cement particles (red) are packed as randomly dispersed spheres within the cubic representative elementary volume (size = 100 μm^3). As cement reacts with water, C-S-H (blue) and other hydrates (green) are allowed to grow heterogeneously on cement surfaces and homogeneously in the pore space, respectively. See Supporting Information in the corresponding publication for further details pertaining to the simulations.

As stated previously, within the pBNG framework, simulations are employed in two steps. In the first step, optimum values of $I_{density}$ and p_f are determined, and in the second step, the optimum function form of $G_{out}(t)$ is determined. On the basis of the optimizations, it was found that $I_{density}$ is 3.50 ± 0.08 μm^{-2} for all pastes, regardless of the w/c ratio and the SSA of cement. This value of $I_{density}$ is within the same order of magnitude of values reported in previous studies involving pBNG simulations of cement-based systems [6,13,16,34,35] as well as those determined from STEM analyses of early age hydration of impure C_3S. [26] Minor differences in the values of $I_{density}$ between this study and those derived from other pBNG models [6,13,34,35,59] can be attributed to multiple factors including differences in the cement composition and assumptions involving the nature of growth of the product [6] (e.g., anisotropy factor). As examples, in the simulations presented in this study, (i) changing the value of r_G from 0.5 (i.e., penetration of hydrate into the substrate grain is not permitted) to 1.0 (i.e., penetration of hydrate into the substrate is permitted) would necessitate a decrease in $I_{density}$ [6,25] from ≈3.50 to ≈1.62 μm^{-2} and (ii) increasing the anisotropy factor (g) from 0.25 to 1.0 would enhance the probability of lateral impingements between C−S−H nuclei, [6] and, thus, require a reduction in $I_{density}$ from ≈3.50 to ≈0.87 μm^{-2}. However, regardless of the choice of these parameters, measured hydration rates of all pastes presented in this study could be fitted using a unique value of $I_{density}$. This equivalency in the value of $I_{density}$ across all pastes is expected because when water is abundant, as it is during the first 24 h of hydration, the critical supersaturation at which nucleation of C−S−H occurs should be about the same and, thus, independent of the amount of water present in the system or the SSA of the cement particles. [35] It should be noted that at a high w/c, the larger dilution is expected to cause a slight delay in reaching C−S−H supersaturation. However, because of the intrinsically high dissolution rate of cement [63] and the very low solubility (i.e., Ksp) of C−S−H, [29,50] it is expected that the solution rapidly supersaturates with respect to C−S−H in all pastes regardless of the w/c, and, thus, does not cause significant alterations (e.g., lengthening of the induction period) in the early age hydration behavior. [26,45,64–69]

While the product nucleation density was found to be independent of the w/c, significant changes in the reactive paste fraction (p_f) were noted across different pastes (Figure 7a). As can be seen, p_f is unaffected by the cement's SSA, but decreases broadly in a linear manner with increasing w/c. This implies that as the water content of the paste

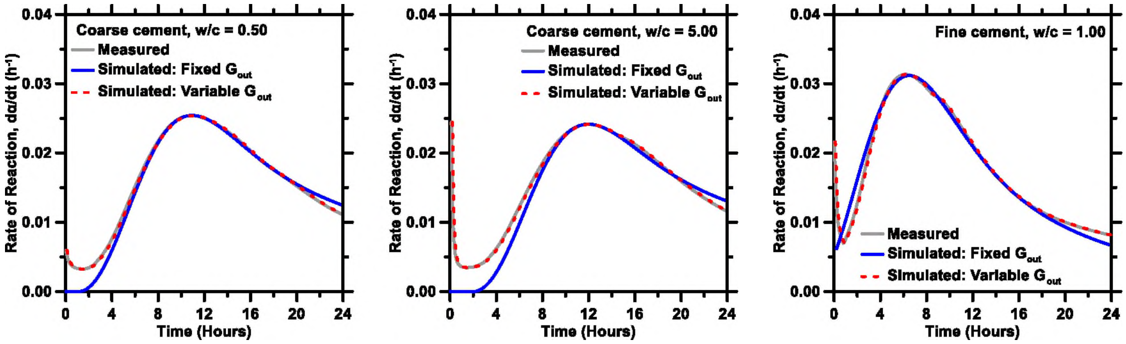

Figure 6. Representative set of simulated and measured hydration rates (dα/dt) of cement in pastes prepared at different w/c. The blue solid line represents model output at its intermediate step, wherein the outward product growth rate (G_{out}) is assumed to remain constant throughout the hydration process. The red dashed line represents the final output from the simulations, wherein G_{out} is allowed to vary with time.

increases, the formation of C−S−H is confined within smaller volume fractions of the paste. It is pointed out that if simulations are implemented by imposing a constant value of p_f (i.e., $p_f = 1$) — essentially assuming that the entire reaction vessel participates in the nucleation and growth process — the hydration rates of high w/ c pastes, as estimated from the pBNG simulations, are significantly different (i.e., broader) compared to those obtained from experiments. This is because at larger values of p_f, the enlargement of the reaction vessel ensures larger spacing between the cement particles, which results in fewer impingements between product nuclei growing on neighboring particles; this manifests as a slower approach to the main hydration peak and, more importantly, a slower decline in the hydration rate after the peak. Further details pertaining to the sensitivity of the pBNG simulations with respect to variations in p_f and the justification for varying p_f are included in the Supporting Information in corresponding publication. As described previously (pBNG Model section), the reactive fraction of the paste can be described as the reaction vessel, which consists of all of the solids (i.e., anhydrous cement particles and hydrates) but only a fraction of the capillary water. By factoring in the values of p_f (as obtained from the simulations) in Equation 7, the w/c ratio within the reaction vessel (i.e., w/c_{RV}) was determined (Figure 7b). Interestingly, regardless of the w/c ratio of the paste or the SSA of cement, in all pastes, the w/c_{RV} is broadly similar, with values ranging from 0.40 to 0.51. Strikingly, these values of w/c_{RV} are in close proximity to the critical w/c (i.e., 0.42) needed for complete hydration of cement. [36,37] This indicates that during the early stages of cement hydration, as C–S–H nucleates on cement surfaces and subsequently grows into the contiguous capillary space, its growth is confined within a region (i.e., the reaction vessel) in the vicinity of cement particles that supply the ions for C–S–H precipitation. The reaction vessel's volume is independent of the w/c and roughly equal to the critical (i.e., minimum) volume required for the occupation of the hydrates after the hydration of cement is complete (i.e., when $\alpha = 1$). Whereas the reasons for equivalency in the reaction vessel's volume across pastes prepared at different w/c ratios are not clear, it is speculated that the sedimentation of cement particles, in addition to particle-aggregation (i.e., flocculation/agglomeration caused due to interparticle forces), lead to similar particle assemblages. This definition of the reaction vessel (and, thus, of a_{BV}) is similar to that suggested by Thomas [12] and indicates that, regardless of the w/c, the calculation of a_{BV} (Equation 6) for plain pastes should be based on the volume of the hydrates at $\alpha = 1$ (as the reaction vessel's volume) rather than the total volume of the paste. The results, suggesting confined growth of C–S–H on and around the cement particles, are also in good agreement with the reaction zone hypothesis advanced by Masoero et al. [34] In spite of similarity in findings between this study and the study by Masoero et al, [34] there are differences pertaining to the origins of C–S–H's confinement, which are highlighted below.

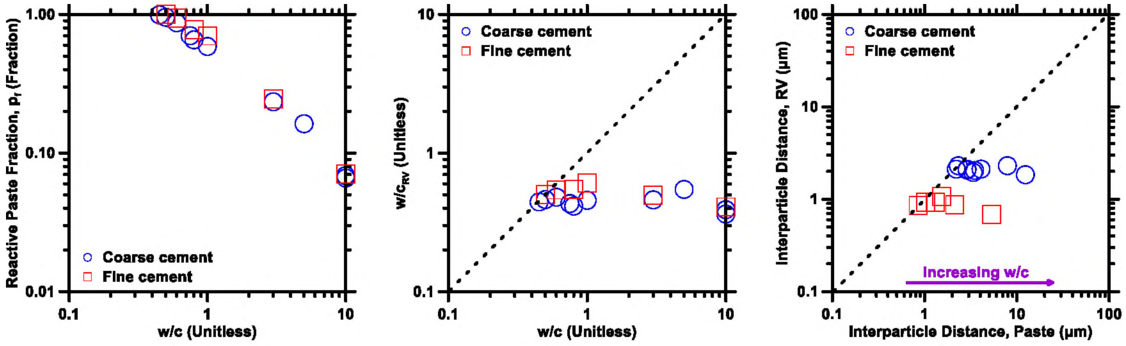

(a) (b) (c)

Figure 7. Parameters derived from the simulations: (a) reactive paste fraction (p_f) and (b) water-to-cement ratio within the reaction vessel (w/c_{-RV}) as functions of the w/c. (c) Comparison between the average spacing between cement particle surfaces within the reaction vessel (y-axis) vis-à-vis the average spacing between them when they are assumed to remain suspended (x-axis). The dashed lines represent the lines of ideality.

In the model used by Masoero et al., [34] it is assumed that the cement particles remain suspended, and the growth of C−S−H occurs in a confined region (i.e., in the semi-pore space) in proximity to the cement particles. First, in practice, because of the large density difference between cement (i.e., 3150 kg. m^{-3}) and water (i.e., 1000 kg. m^{-3}), the sedimentation of cement particles always occurs in pastes (in the absence of viscosity-modifying admixtures or when in situ mixing is not employed), as was also observed in the current experiments. Second, the assumption of particles being suspended combined with the confinement of C−S−H, as assumed in the model developed by Masoero et al., [34] significantly marginalizes the likelihood of impingement between C−S−H layers growing on different particles, especially at early ages when the degree of hydration of cement is low. This is difficult to reconcile as the setting of the paste, [70] which occurs at a low degree of hydration of cement, necessitates such early age impingements between C− S−H layers growing on adjacent cement grains. In contrast to the model presented in ref [34], the pBNG model used in this study does not incorporate any assumption regarding the occurrence, or lack thereof, of sedimentation of cement particles. However, based on the simulation results, which indicate that in high w/c pastes, the reaction vessel is consistently smaller than the paste's volume (Figure 7), it is inferred that the sedimentation of cement particles does occur. This inference gains support from experiments, in which the solids (i.e., cement particles and hydrates) were consistently found to be settled at the bottom of the reaction container after 24 h of hydration. This assemblage of cement particles within a fraction of the paste's volume causes the particles to pack more closely as compared to an equivalent system in which particles remain suspended.

To better illustrate the effects of sedimentation of cement particles on particle packing, the 3D microstructural model, described above and in ref [5,16,33,56,60–62] was used to generate virtual microstructures for two cases: one in which cement particles remain suspended and the other in which sedimentation occurs. In the former and latter cases, the water contents resemble the original w/c and the w/c_{RV} (determined from pBNG simulations), respectively. Once the sought packing is achieved, the average initial spacing between cement particle surfaces (i.e., interparticle distance) is calculated using algorithms described in ref [59]. The virtual microstructures generated from the simulations are shown in Figure 8, and the calculated interparticle distances are shown in Figure 7c. As can be seen, because of the sedimentation of cement particles in high w/c pastes, the interparticle distance within the reaction vessel is reduced to a fraction of the interparticle distance at the time of mixing (i.e., when sedimentation has not occurred). It is also noteworthy that across pastes prepared using the same PSD of cement but at different w/c ratios, the interparticle distances within the reaction vessel remain broadly the same. This is due to the equivalency in the values of w/c_{RV} (Figure 7b) and suggests that as cement particles settle, their assemblage and access to water needed for hydration remain broadly the same regardless of the original w/c. In pastes prepared with the fine cement, the interparticle distances within the reaction vessel are smaller (i.e., ≈1.0 μm) as compared to those prepared with the coarse cement (i.e., ≈2.1 μm), although the volumes of the reaction vessel are equivalent across all pastes. This is attributed to the larger number of particles (per unit mass) in the fine cement. These interparticle distances, presented in Figure 7c, are analogous to the size of the reaction zone reported by Masoero et al., [34] as in both studies, these sizes represent the linearized space within which the growth of C−S−H occurs and remains confined. In this study, the interparticle distances range between 1.0 and 2.1 μm, whereas in ref [34], the sizes of the reaction zone were estimated between ≈0.38 and ≈1.1 μm. It is reasonable to say that these differences are small and can be attributed to differences in the schemes (e.g., anisotropy in the growth of C−S−H) employed in the pBNG simulations as well as the differences in the properties (i.e., PSD and composition) of the cementing material. The assumption of particles remaining suspended, as implemented in ref [34], is also expected to alter the likelihood of impingement between C−S−H nuclei and, thus, contribute to the aforementioned differences.

On the basis of these results, it is hypothesized that the confinement of C−S−H is a manifestation of the space constraint induced by the close packing of the settled cement particles within the reaction vessel. Because of the smaller spacing between cement particles within the reaction vessel, C−S−H layers growing on adjacent cement particles are able to percolate and cause the paste to set, even when the w/c is relatively high (e.g., w/c = 0.75). The enhanced impingements between C−S−H layers as well as the impingements between C−S−H nuclei growing on the same particle contribute toward the occurrence of the main hydration peak, which occurs within 12 h of hydration and at a low degree of hydration (i.e., $\alpha \approx 0.13$) even in pastes prepared at high w/c (Figures 2 and 3). In addition to these impingements, the temporal variation in the growth rate of C−S−H (described below), as driven by its supersaturation, is expected to affect the hydration rates.

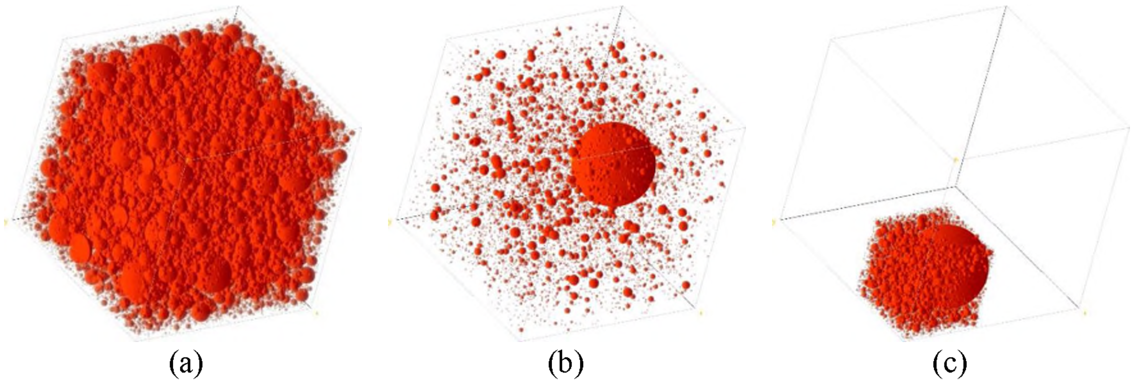

Figure 8. 3D virtual microstructures showing the packing of particles at the time of mixing (i.e., without sedimentation of particles) in pastes prepared at: (a) w/c = 0.45, and (b) w/c = 10. (c) shows the effects of sedimentation of particles in a paste prepared at w/c = 10. The smaller cubic volume schematically represents the reaction vessel, which includes all of the cement particles but only a fraction of the water. The volumetric content of water in the reaction vessel is derived from w/c$_{\text{-RV}}$, as calculated from pBNG simulations.

Figure 9a describes the influence of w/c on the product growth rate [$G_{out}(t)$]. As shown, the product grows at rates that decrease nonlinearly by about 2 orders of magnitude over the course of cement hydration in the first 24 h. This functional form of the growth rate has been reported [13,22,25] to mimic the evolving supersaturation of C−S−H in the solution, wherein high and low supersaturations imply larger and smaller driving forces for C−S−H growth, respectively. It is noted that at any given time (Figure 9a) or degree of hydration of cement (Figure 9b), G_{out} decreases with increasing w/c. This is better shown in Figure 10, which plots the growth rates of pastes, extracted at $\alpha = 10$, 20, and 30% against the w/c. The diminishment of the product growth rate with increasing w/c suggests abatement in the driving force for C−S−H growth in diluted systems. It is hypothesized that in high w/c systems, though C−S−H is confined within a smaller fraction of the paste volume (i.e., the reaction vessel), the ions [29] (i.e., $H_3SiO_4^-$ /$H_2SiO_4^{2-}$, $CaOH^+$/Ca^{2+}, and OH^-) responsible for the precipitation of C−S−H are able to transport across the entire paste's volume. As such, the supersaturation of C−S−H in the solution and, hence, the driving force for its growth are sensitive to the paste's water content and decrease with increasing w/c; this point is described in more detail through experimental results further in the text. This decrease in C−S−H supersaturation manifests as a systematic diminishment of its growth rate with increasing w/c (Figures 9 and 10). It is pointed out that, in spite of the ions being able to move throughout the paste's volume, it is expected that their abundance is relatively higher in regions in proximity to their source, that is, cement particles. This would imply higher supersaturation and, therefore, higher growth rate of C−S−H around the cement particles. While the current simulations do not consider gradients in ion concentrations, results shown in Figure 10 do support the theory. As can be seen, at equivalent w/c, growth rates at early ages (i.e., when $\alpha = 0.10$) are higher in pastes prepared with the fine cement as compared to those prepared with the coarse cement. This is hypothesized to be on account of smaller spacing between particles (Figure 7c) in pastes prepared with the fine cement, such that the overlapping (or closely packed) ion-abundant regions around the closely packed particles bolster the driving force for the growth of C− S−H. At later ages, when the supersaturation of C−S−H in the solution is low, [22] the effect of interparticle spacing on the growth rate diminishes. This is reflected in Figures 10b and 10c, which show that at higher degrees of cement hydration, growth rates are independent of the spacing between particles (or fineness of the cement).

The growth rates shown in Figure 9 qualitatively allude to the temporal evolution of the supersaturation of C−S−H in the solution. For quantitative determinations of the supersaturation, a generic relationship between the growth rate and supersaturation of C−S−H must be known. In a recent study, Scherer et al. [27] showed that the growth rate of C−S−H exhibits a cubic dependence on its supersaturation, as shown in Equation 9.

$$G_{out}(t) = G_{out-c} \cdot (\beta_{CSH}(t) - 1)^3 \quad (9)$$

where, G_{out-c} (μm. hour^{-1}) is a constant and $\beta_{CSH}(t)$ (unitless) is the time-dependent supersaturation of C−S−H in the solution. As the exact value of G_{out-c} is not known and is expected to change depending on the concentration of calcium (i.e., Ca^{2+}) in the solution, [27] a value of $G_{out-c} = 0.075$ μm. hour^{-1} is assumed in this study. This value, as described previously, is used in the first step of the pBNG simulations and is within the same order of magnitude as experimental values. [26,27,67] By plugging in the estimated value of G_{out-c} and $G_{out}(t)$ (i.e., obtained from pBNG simulations) in Equation 9, the temporal evolution of β_{CSH} in the pastes was estimated (Figure 11). Admittedly, on account of the uncertainty in the values of G_{out-c}, the values of β_{CSH} are expected to be a rough, rather than an accurate estimate. However, these estimated values are expected to capture the effects of variations in the process parameters, that is, w/c and SSA of cement, as they are all derived using the same value of G_{out-c}.

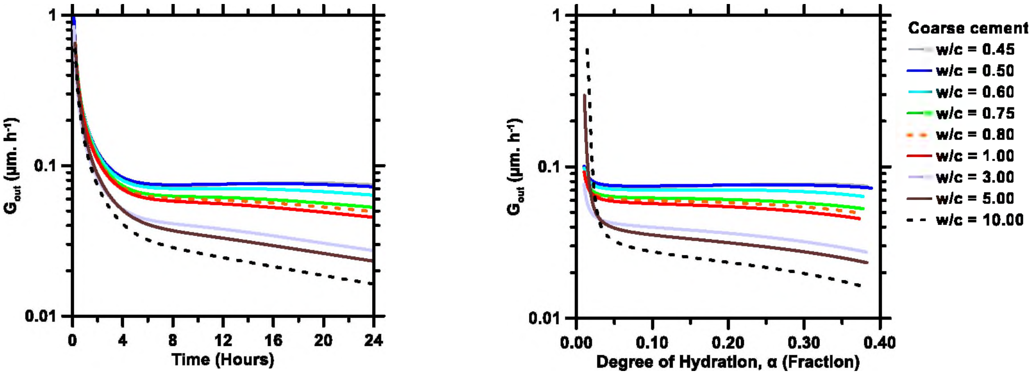

(a) (b)

Figure 9. Outward growth rate of the product (G_{out}) as function of: (a) time, and (b) degree of hydration of the coarse cement.

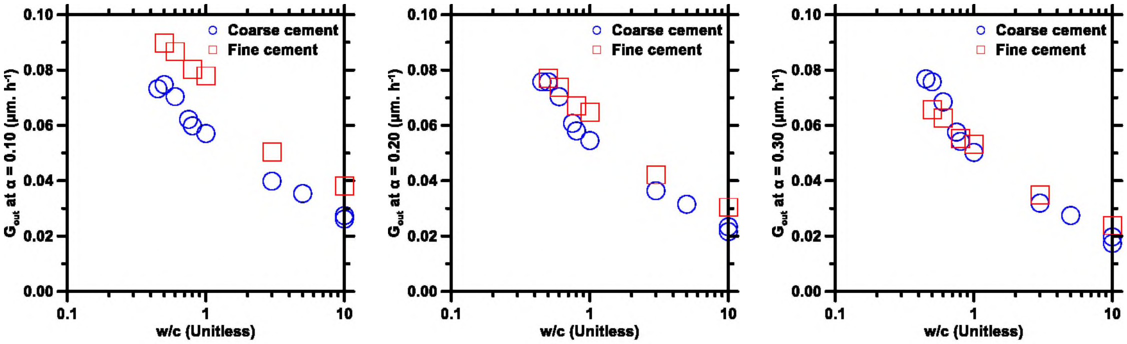

(a) (b) (c)

Figure 10. Outward growth rate of the product (G_{out}) as a function of w/c when: (a) α = 0.10, (b) α = 0.20, and (c) α = 0.30. Results for both coarse and fine cements are shown.

The temporal evolutions of β_{CSH}, shown in Figure 11, are qualitatively similar to those reported in the literature and derived from kinetic cellular automata simulations [22,27,29,30,64,71] and reflect the trends in the abundance of aqueous ionic species — the silicate species (i.e., $H_2SiO_4^{2-}$ and $H_3SiO_4^{-}$) in particular — in the solution. [64,71–74] At very early ages (i.e., around the time of mixing), when C−S−H is present in small amounts and cement continues to dissolve rapidly releasing ions at a fast rate into the solution, β_{CSH} is expectedly high. With time, the dissolution rate of cement declines, and more ions, including aqueous silicate species, are consumed as the rate of precipitation of C−S−H increases; this manifests as a steep decline in β_{CSH}. It should be noted, however, that this decline in β_{CSH} is nonmonotonic, particularly in the case of low w/c systems. Specifically, around the main hydration peak, β_{CSH} increases — albeit slightly — and then continues to decrease. These minor fluctuations in the evolution of β_{CSH} are expected to mimic the increase in the silicate concentration that occurs around the main hydration peak when there is a sharp decrease in the Ca^{2+} concentration. [22,35] At later ages (i.e., in the subsequent hours following the main hydration peak), ion concentrations in the solution stabilize, [22,45,64,72] and thus β_{CSH} also stabilizes. At any given time, pastes prepared at a lower w/c have higher β_{CSH} as compared to those prepared at a higher w/ c. This, as stated previously, is expected to be due to the larger dilution in the higher w/c pastes and is corroborated by the evolutions of the solution electrical conductivity and pH. As can be seen in Figures 12a and 12b, whereas the overall profiles of electrical conductivity and pH evolution are similar across different w/c — which is expected due to similar hydration kinetics (Figure 2 — the magnitudes of both parameters at equivalent times are lower in high w/c pastes on account of higher dilution (i.e., larger volume of solution per mole of a given ion). Lower concentration of ions in the pore solutions of high w/c pastes causes β_{CSH} to be lower compared to those prepared at low w/c. It is also interesting to note that β_{CSH} is broadly insensitive to the PSD of cement (Figures 11b and 11c). This suggests that the differences in the hydration kinetics induced by the SSA of cement (as shown in Figure 3) are unable to cast a significant impact on the composition of the solution and, therefore, the supersaturation of C−S−H.

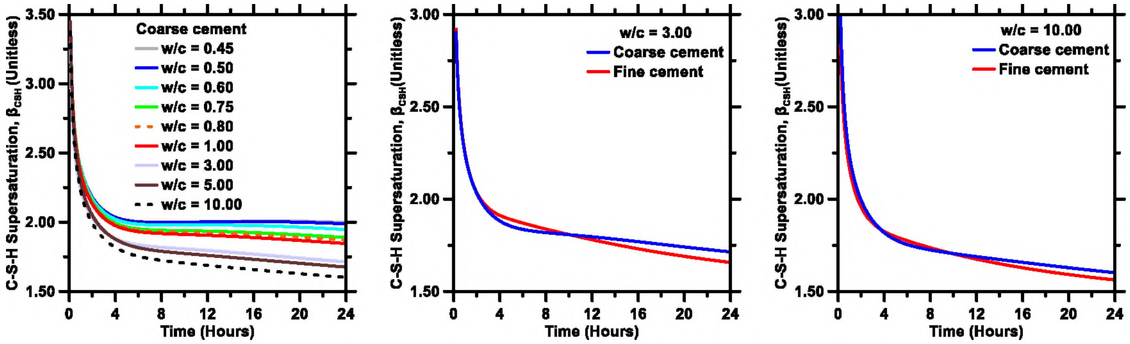

(a) (b) (c)

Figure 11. Estimated temporal evolution of the supersaturation of C-S-H (β_{CSH}) in pastes prepared using: (a) the coarse cement at different w/c, (b) the coarse and fine cements at w/c = 3, and (c) the coarse and fine cements at w/c = 10.

Overall, the results described thus far suggest that the hydration kinetics of cement is not affected by the w/c on account of the sedimentation of cement particles. As cement particles settle, they are packed more closely, which in turn creates a space constraint for the growth of C−S−H and results in its confinement. On the basis of this theory, it could be hypothesized that if the sedimentation of cement particles is prevented — or even disrupted — C−S−H would not remain confined, thus causing the hydration kinetics to change. To test this hypothesis, hydration kinetics was monitored for a paste prepared at w/c = 10, wherein the paste was continuously stirred at a low speed (i.e., 80 rpm) using an electrically-driven agitator throughout the 24 h of hydration. It is clarified that the low rotational speed of the agitator minimizes the heat released due to mixing action (i.e., These differences can be reconciled by considering the effect of stirring on the spacing between cement particles. Specifically, in the stirred pastes, sedimentation of cement particles is partially prevented, which results in larger spacing between them and, consequently, fewer impingements between C−S−H layers growing on neighboring cement particles. Because of such lack in confinement of C−S−H in the stirred pastes, the main hydration peak is delayed and the decline in the post-peak hydration rate is slower. By contrast, in the static paste, the closely packed cement particles ensure more impingements between the C−S−H layers and thus a faster approach to and departure from the main hydration peak. The results shown in Figure 12 are in good agreement with the results shown in Figure S3b (of the Supporting Information in the corresponding publication), wherein it is shown that if the reaction vessel's volume is larger (i.e., $p_f \approx 1.00$), the pBNG-simulated hydration rates of high w/c pastes have a delayed occurrence of the main hydration peak and a slower post-peak decline of the hydration rate. The results shown in Figure 12 are also in good agreement with a prior study, [31] which shows that in pastes provisioned with dispersants, the enhanced dispersion of cement particles causes cement hydration rates to change (i.e., to get progressively broader) in relation to increasing w/c.

On the basis of these results, it is hypothesized that sedimentation of cement particles is at the origin of C−S−H confinement and insensitivity of cement hydration rates to changes in w/c. It is clarified that, although this hypothesis has been construed from the hydration behavior of water-rich systems (i.e., w/c > 0.42), past studies [12,31] and additional data included in the Supporting Information of the corresponding publication show that early age hydration rates of low w/c pastes (i.e., w/c < 0.42) are also insensitive to w/c. Results obtained from pBNG simulations (not shown) indicate that even in low w/c pastes, the reaction vessel's volume is equivalent to the volume occupied by hydrates at $\alpha = 1$. Thus, it is proposed that in pBNG models, to account for C−S−H confinement, the determination of the boundary area per unit volume of the substrate (a_{BV}: Equation 6) for plain pastes should be calculated based on the volume of

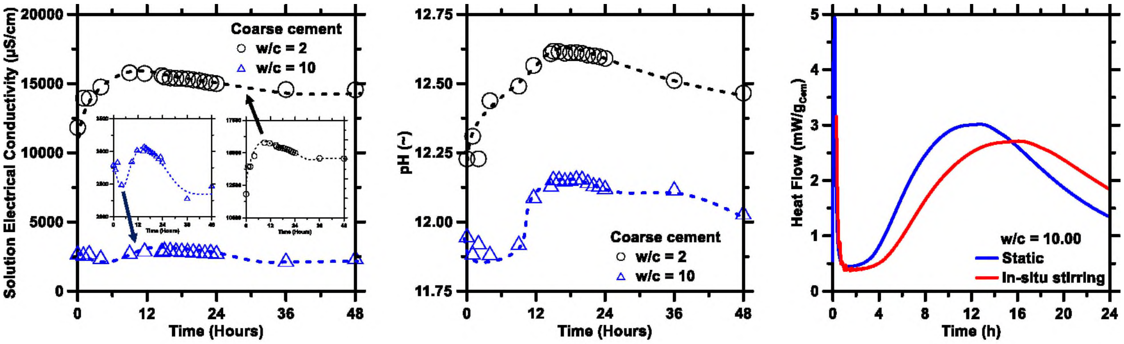

(a) (b) (c)

Figure 12. (a) Electrical conductivity and (b) pH of the pore solution of pastes prepared using the coarse cement at different w/c. Because of the large difference in magnitudes of solution's electrical conductivity, re-scaled subplots for the two curves are included within (a). (c) Heat flow rates of pastes, prepared using the coarse cement at w/c = 10, measured without (static) and with in-situ stirring.

hydrates that would form when all of the cement has reacted, rather than the total volume of the paste (including excess water) which depends on the w/c. As per this definition, in blended systems wherein cement is partially replaced by a filler, a_{BV} would be equal to the ratio of the total solid surface area at $\alpha = 0$ (i.e., combined surface areas of cement and filler) to the total volume of solids at $\alpha = 1$ (i.e., combined volumes of hydrates and filler). As pointed out by Scherer and Bellmann, [27] pBNG models should account for the highly nonlinear supersaturation-dependent variation in the growth rate of C− S−H. In this study, although the evolution of growth rate and supersaturation of C−S−H were derived indirectly from heat evolution profiles, it is possible to incorporate a supersaturation-dependent growth rate directly into pBNG models through experimental measurements of the evolving solution composition. [27] Last, it is recognized that further investigation of cement hydration kinetics in pastes, wherein sedimentation of particles is progressively mitigated (e.g., using viscosity-modifying admixtures), is required for validation and further refinement of the hypotheses presented in this study.

4. CONCLUSIONS

A series of experiments and pBNG simulations were applied to elucidate the role of w/c ratio on the hydration kinetics of cement in plain pastes. The experiments, conducted using isothermal microcalorimetry methods, show that cement hydration rates are insensitive to changes in w/c. As classical pBNG models are unable to explain such effects, a modified pBNG model is presented, in which the growth of the main hydrate, that is, C−S−H, is assumed to be anisotropic and allowed to vary in relation to the nonlinear evolution of its supersaturation in the solution.

Results obtained from the pBNG simulations show that the nucleation density of C−S−H, forming heterogeneously on cement surfaces, is unaffected by the w/c of the paste as well as the SSA of cement particulates. However, as the w/c increases, the fraction of the paste's volume that participates in the nucleation and growth process reduces. This reactive (i.e., participatory) fraction of the paste, termed as the reaction vessel in this study, was found to be equivalent (i.e., equivalent size/volume and water content) across pastes prepared at different w/c ratios and cements of different SSAs.

On the basis of these results, it is hypothesized that at early ages, the nucleation and growth of C−S−H remains confined within the reaction vessel, such that its formation is limited to ion-abundant regions in proximity to cement particles. This confinement of C−S−H is hypothesized to be a manifestation of the sedimentation of cement particles. As cement particles settle, they are packed more closely, which in turn creates a space constraint for the growth of C−S−H and results in its confinement.

Indeed, in pastes, wherein the sedimentation of cement particles is disrupted using in situ stirring, the hydration kinetics is no longer insensitive to changes in the w/c.

Results from this study also suggest that, unlike C−S−H, the ions in solution are not confined within the reaction vessel. The transport of ions throughout the volume of the paste causes the supersaturation of C−S−H, that is, the driving force for its growth, to decline with increasing w/c. This results in a systematic diminishment of C−S−H growth rate with increasing w/c.

Overall, the outcomes of this work provide novel insights into the mechanisms that cause cement hydration rates to remain insensitive to changes in the paste's water content. Whereas a simplified view is presented, the discussion highlights important aspects that need to be incorporated in pBNG models to account for C−S−H confinement as well as the sedimentation of cement particles. Investigation of the cement hydration kinetics in systems, wherein sedimentation of particles is progressively mitigated (e.g., using viscosity-modifying admixtures), is expected to aid in validation and in further refinement of the hypotheses presented in this study.

ACKNOWLEDGEMENTS

This research was conducted in the Materials Research Center (MRC) at Missouri S&T. The authors gratefully acknowledge the financial support that has made these laboratories and their operations possible. Funding for this research was provided by MRC (MRC Young Investigator Seed Funding) at Missouri S&T and University of Missouri Research Board (UMRB).

REFERENCES

[1] J.W. Bullard, H.M. Jennings, R.A. Livingston, A. Nonat, G.W. Scherer, J.S. Schweitzer, K.L. Scrivener, J.J. Thomas, Mechanisms of cement hydration, Cement and Concrete Research. 41 (2011) 1208–1223.

[2] K.L. Scrivener, P. Juilland, P.J. Monteiro, Advances in understanding hydration of Portland cement, Cement and Concrete Research. 78 (2015) 38–56.

[3] H.F. Taylor, Cement chemistry, Thomas Telford, 1997.

[4] J.J. Thomas, J.J. Biernacki, J.W. Bullard, S. Bishnoi, J.S. Dolado, G.W. Scherer, A. Luttge, Modeling and simulation of cement hydration kinetics and microstructure development, Cement and Concrete Research. 41 (2011) 1257–1278.

[5] A. Kumar, S. Bishnoi, K.L. Scrivener, Modelling early age hydration kinetics of alite, Cement and Concrete Research. 42 (2012) 903–918.

[6] G.W. Scherer, J. Zhang, J.J. Thomas, Nucleation and growth models for hydration of cement, Cement and Concrete Research. 42 (2012) 982–993.

[7] M. Avrami, Kinetics of phase change. I General theory, The Journal of Chemical Physics. 7 (1939) 1103–1112.

[8] M. Avrami, Granulation, phase change, and microstructure kinetics of phase change. III, The Journal of Chemical Physics. 9 (1941) 177–184.

[9] S. Jun, H. Zhang, J. Bechhoefer, Nucleation and growth in one dimension. I. The generalized Kolmogorov-Johnson-Mehl-Avrami model, Physical Review E. 71 (2005) 011908.

[10] J.W. Cahn, The kinetics of grain boundary nucleated reactions, Acta Metallurgica. 4 (1956) 449–459.

[11] J.J. Thomas, H.M. Jennings, J.J. Chen, Influence of nucleation seeding on the hydration mechanisms of tricalcium silicate and cement, The Journal of Physical Chemistry C. 113 (2009) 4327–4334.

[12] J.J. Thomas, A new approach to modeling the nucleation and growth kinetics of tricalcium silicate hydration, Journal of the American Ceramic Society. 90 (2007) 3282–3288.

[13] W. Meng, P. Lunkad, A. Kumar, K. Khayat, Influence of Silica Fume and Polycarboxylate Ether Dispersant on Hydration Mechanisms of Cement, The Journal of Physical Chemistry C. 120 (2016) 26814–26823.

[14] L. Nicoleau, A. Nonat, D. Perrey, The di-and tricalcium silicate dissolutions, Cement and Concrete Research. 47 (2013) 14–30.

[15] L. Nicoleau, M.A. Bertolim, Analytical model for the alite (C3S) dissolution topography, Journal of the American Ceramic Society. (2015). http://onlinelibrary.wiley.com/doi/10.1111/jace.13647/pdf (accessed February 7, 2017).

[16] T. Oey, A. Kumar, J.W. Bullard, N. Neithalath, G. Sant, The filler effect: the influence of filler content and surface area on cementitious reaction rates, Journal of the American Ceramic Society. 96 (2013) 1978–1990.

[17] E. Masoero, E. Del Gado, R.-M. Pellenq, F.-J. Ulm, S. Yip, Nanostructure and nanomechanics of cement: polydisperse colloidal packing, Physical Review Letters. 109 (2012) 155503.

[18] C.W. Price, Use of Kolmogorov-Johnson-Mehl-Avrami kinetics in recrystallization of metals and crystallization of metallic glasses, Acta Metallurgica et Materialia. 38 (1990) 727–738.

[19] A.N. Kolmogorov, On the statistical theory of the crystallization of metals, Bull. Acad. Sci. USSR, Math. Ser. 1 (1937) 355–359.

[20] V.K. Peterson, A.E. Whitten, Hydration processes in tricalcium silicate: application of the boundary nucleation model to quasielastic neutron scattering data, The Journal of Physical Chemistry C. 113 (2009) 2347–2351.

[21] V.K. Peterson, M.C.G. Juenger, Hydration of tricalcium silicate: effects of CaCl2 and sucrose on reaction kinetics and product formation, Chemistry of Materials. 18 (2006) 5798–5804.

[22] J.W. Bullard, G.W. Scherer, J.J. Thomas, Time dependent driving forces and the kinetics of tricalcium silicate hydration, Cement and Concrete Research. 74 (2015) 26–34.

[23] L. Valentini, M. Favero, M.C. Dalconi, V. Russo, G. Ferrari, G. Artioli, Kinetic Model of Calcium-Silicate Hydrate Nucleation and Growth in the Presence of PCE Superplasticizers, Crystal Growth & Design. (2016) 646–654.

[24] F. Ridi, E. Fratini, P. Luciani, F. Winnefeld, P. Baglioni, Tricalcium silicate hydration reaction in the presence of comb-shaped superplasticizers: boundary nucleation and growth model applied to polymer-modified pastes, The Journal of Physical Chemistry C. 116 (2012) 10887–10895.

[25] G.W. Scherer, Models of Confined Growth, Cement and Concrete Research. 42 (2012) 1252–1260.

[26] A. Bazzoni, S. Ma, Q. Wang, X. Shen, M. Cantoni, K.L. Scrivener, The Effect of Magnesium and Zinc Ions on the Hydration Kinetics of C3S, Journal of the American Ceramic Society. 97 (2014) 3684–3693.

[27] G.W. Scherer, F. Bellmann, Kinetic analysis of CSH growth on calcite, Cement and Concrete Research. (2016). http://www.sciencedirect.com/science/article/pii/S0008884616306457 (accessed January 30, 2017).

[28] Z. Zhang, G.W. Scherer, A. Bauer, Morphology of cementitious material during early hydration, Cement and Concrete Research. 107 (2018) 85–100. https://doi.org/10.1016/j.cemconres.2018.02.004.

[29] J.W. Bullard, G.W. Scherer, An Ideal Solid Solution Model for C–S–H, Journal of the American Ceramic Society. 99 (2016) 4137–4145.

[30] F. Bellmann, G.W. Scherer, Analysis of C-S-H growth rates in supersaturated conditions, Cement and Concrete Reseach. 103 (2018) 236–244.

[31] D.M. Kirby, J.J. Biernacki, The effect of water-to-cement ratio on the hydration kinetics of tricalcium silicate cements: Testing the two-step hydration hypothesis, Cement and Concrete Research. 42 (2012) 1147–1156.

[32] T. Oey, J. Stoian, J. Li, C. Vong, M. Balonis, A. Kumar, W. Franke, G. Sant, Comparison of Ca(NO3)2 and CaCl2 admixtures on reaction, setting, and strength evolutions in plain and blended cementing formulations, Journal of Materials in Civil Engineering. 27 (2014) 04014267.

[33] A. Kumar, G. Sant, C. Patapy, C. Gianocca, K.L. Scrivener, The influence of sodium and potassium hydroxide on alite hydration: Experiments and simulations, Cement and Concrete Research. 42 (2012) 1513–1523.

[34] E. Masoero, J.J. Thomas, H.M. Jennings, A Reaction Zone Hypothesis for the Effects of Particle Size and Water-to-Cement Ratio on the Early Hydration Kinetics of C3S, Journal of the American Ceramic Society. 97 (2014) 967–975.

[35] T. Oey, A. Kumar, G. Falzone, J. Huang, S. Kennison, M. Bauchy, N. Neithalath, J.W. Bullard, G. Sant, The Influence of Water Activity on the Hydration Rate of Tricalcium Silicate, J. Am. Ceram. Soc. 99 (2016) 2481–2492. https://doi.org/10.1111/jace.14181.

[36] T.C. Powers, Structure and physical properties of hardened Portland cement paste, Journal of the American Ceramic Society. 41 (1958) 1–6.

[37] T.C. Powers, T.L. Brownyard, Studies of the physical properties of hardened Portland cement paste, in: ACI Journal Proceedings, ACI, 1946. http://www.concrete.org/Publications/InternationalConcreteAbstractsPortal.aspx?m=details&i=15301 (accessed August 29, 2014).

[38] H. Ahmed, G. Buckton, D.A. Rawlins, The use of isothermal microcalorimetry in the study of small degrees of amorphous content of a hydrophobic powder, International Journal of Pharmaceutics. 130 (1996) 195–201.

[39] P. Darcy, G. Buckton, Quantitative assessments of powder crystallinity: Estimates of heat and mass transfer to interpret isothermal microcalorimetry data, Thermochimica Acta. 316 (1998) 29–36.

[40] J. Stoian, T. Oey, J.W. Bullard, J. Huang, A. Kumar, M. Balonis, J. Terrill, N. Neithalath, G. Sant, New insights into the prehydration of cement and its mitigation, Cement and Concrete Research. 70 (2015) 94–103.

[41] J. Zhang, G.W. Scherer, Comparison of methods for arresting hydration of cement, Cement and Concrete Research. 41 (2011) 1024–1036.

[42] A. Quennoz, K.L. Scrivener, Hydration of C3A–gypsum systems, Cement and Concrete Research. 42 (2012) 1032–1041. https://doi.org/10.1016/j.cemconres.2012.04.005.

[43] H. Minard, S. Garrault, L. Regnaud, A. Nonat, Mechanisms and parameters controlling the tricalcium aluminate reactivity in the presence of gypsum, Cement and Concrete Research. 37 (2007) 1418–1426.

[44] A. Quennoz, K.L. Scrivener, Interactions between alite and C< sub> 3</sub> A-gypsum hydrations in model cements, Cement and Concrete Research. 44 (2013) 46–54.

[45] S. Garrault, A. Nonat, Hydrated layer formation on tricalcium and dicalcium silicate surfaces: experimental study and numerical simulations, Langmuir. 17 (2001) 8131–8138.

[46] J.W. Bullard, A determination of hydration mechanisms for tricalcium silicate using a kinetic cellular automaton model, Journal of the American Ceramic Society. 91 (2008) 2088–2097.

[47] J.W. Bullard, R.J. Flatt, New insights into the effect of calcium hydroxide precipitation on the kinetics of tricalcium silicate hydration, Journal of the American Ceramic Society. 93 (2010) 1894–1903.

[48] J. Lapeyre, A. Kumar, Influence of pozzolanic additives on hydration mechanisms of tricalcium silicate, Journal of American Ceramics Society. 101 (2018) 3557–3574. https://doi.org/10.1111/jace.15518.

[49] A.J. Allen, J.J. Thomas, H.M. Jennings, Composition and density of nanoscale calcium–silicate–hydrate in cement, Nature Materials. 6 (2007) 311–316.

[50] J.J. Thomas, H.M. Jennings, A.J. Allen, Relationships between Composition and Density of Tobermorite, Jennite, and Nanoscale CaO- SiO2- H2O, The Journal of Physical Chemistry C. 114 (2010) 7594–7601.

[51] D.P. Bentz, P. Lura, J.W. Roberts, Mixture proportioning for internal curing, Concrete International. 27 (2005) 35–40.

[52] J.A. Nelder, R. Mead, A simplex method for function minimization, The Computer Journal. 7 (1965) 308–313.

[53] K.I. McKinnon, Convergence of the Nelder–Mead Simplex Method to a Nonstationary Point, SIAM Journal on Optimization. 9 (1998) 148–158.

[54] A. Kumar, T. Oey, G.P. Falla, R. Henkensiefken, N. Neithalath, G. Sant, A comparison of intergrinding and blending limestone on reaction and strength evolution in cementitious materials, Construction and Building Materials. 43 (2013) 428–435.

[55] D.P. Bentz, E.J. Garboczi, C.J. Haecker, O.M. Jensen, Effects of cement particle size distribution on performance properties of Portland cement-based materials, Cement and Concrete Research. 29 (1999) 1663–1671.

[56] A. Kumar, T. Oey, G. Falzone, J. Huang, M. Bauchy, M. Balonis, N. Neithalath, J. Bullard, G. Sant, The filler effect: The influence of filler content and type on the hydration rate of tricalcium silicate, Journal of American Ceramics Society. 100 (2017) 3316–3328.

[57] E. Gallucci, K. Scrivener, A. Groso, M. Stampanoni, G. Margaritondo, 3D experimental investigation of the microstructure of cement pastes using synchrotron X-ray microtomography (μCT), Cement and Concrete Research. 37 (2007) 360–368.

[58] H.M. Jennings, S.K. Johnson, Simulation of microstructure development during the hydration of a cement compound, Journal of the American Ceramic Society. 69 (1986) 790–795.

[59] A. Kumar, T. Oey, S. Kim, D. Thomas, S. Badran, J. Li, F. Fernandes, N. Neithalath, G. Sant, Simple methods to estimate the influence of limestone fillers on reaction and property evolution in cementitious materials, Cement and Concrete Composites. 42 (2013) 20–29.

[60] G. Puerta-Falla, A. Kumar, L. Gomez-Zamorano, M. Bauchy, N. Neithalath, G. Sant, The influence of filler type and surface area on the hydration rates of calcium aluminate cement, Construction and Building Materials. 96 (2015) 657–665.

[61] P. Juilland, A. Kumar, E. Gallucci, R.J. Flatt, K.L. Scrivener, Effect of mixing on the early hydration of alite and OPC systems, Cement and Concrete Research. 42 (2012) 1175–1188.

[62] A. Banala, A. Kumar, Numerical simulations of permeability of plain and blended cement pastes, International Journal of Advances in Engineering Sciences and Applied Mathematics. 9 (2017) 67–86. https://doi.org/10.1007/s12572-017-0184-7.

[63] A. Kumar, J. Reed, G. Sant, Vertical Scanning Interferometry: A New Method to Measure the Dissolution Dynamics of Cementitious Minerals, Journal of the American Ceramic Society. 96 (2013) 2766–2778.

[64] S. Garrault-Gauffinet, A. Nonat, Experimental investigation of calcium silicate hydrate (CSH) nucleation, Journal of Crystal Growth. 200 (1999) 565–574.

[65] S. Garrault, E. Finot, E. Lesniewska, A. Nonat, Study of CSH growth on C3S surface during its early hydration, Materials and Structures. 38 (2005) 435–442.

[66] P. Juilland, E. Gallucci, R. Flatt, K. Scrivener, Dissolution theory applied to the induction period in alite hydration, Cement and Concrete Research. 40 (2010) 831–844.

[67] A. Bazzoni, M. Cantoni, K.L. Scrivener, Impact of Annealing on the Early Hydration of Tricalcium Silicate, Journal of the American Ceramic Society. 97 (2014) 584–591.

[68] D. Damidot, A. Nonat, P. Barret, Kinetics of tricalcium silicate hydration in diluted suspensions by microcalorimetric measurements, Journal of the American Ceramic Society. 73 (1990) 3319–3322.

[69] F. Bellmann, D. Damidot, B. Möser, J. Skibsted, Improved evidence for the existence of an intermediate phase during hydration of tricalcium silicate, Cement and Concrete Research. 40 (2010) 875–884.

[70] J. Zhang, E.A. Weissinger, S. Peethamparan, G.W. Scherer, Early hydration and setting of oil well cement, Cement and Concrete Research. 40 (2010) 1023–1033.

[71] S. Garrault, T. Behr, A. Nonat, Formation of the C-S-H Layer During Early Hydration of Tricalcium Silicate Grains with Different Sizes, The Journal of Physical Chemistry B. 110 (2006) 270–275.

[72] B. Lothenbach, F. Winnefeld, Thermodynamic modelling of the hydration of Portland cement, Cement and Concrete Research. 36 (2006) 209–226.

[73] P.W. Brown, E. Franz, G. Frohnsdorff, H.F.W. Taylor, Analyses of the aqueous phase during early C< sub> 3</sub> S hydration, Cement and Concrete Research. 14 (1984) 257–262.

[74] P.W. Brown, C.L. Harner, E.J. Prosen, The effect of inorganic salts on tricalcium silicate hydration, Cement and Concrete Research. 16 (1986) 17–22.

II. INFLUENCE OF WATER ACTIVITY ON BELITE (β-C_2S) HYDRATION

Rachel Cook[1], Hongyan Ma[2], Monday Okoronkwo[3], Gaurav Sant[4], and Aditya Kumar[1]

1. Department of Materials Science and Engineering, Missouri University of Science and Technology (S&T), Rolla, MO, USA 65409.

2. Department of Civil, Architectural and Environmental Engineering, Missouri University of Science and Technology (S&T), Rolla, MO, USA 65409.

3. Department of Chemical and Biochemical Engineering, Missouri University of Science and Technology (S&T), Rolla, MO, USA 65409.

4. Department of Civil and Environmental Engineering; Department of Materials Science and Engineering; California NanoSystems Institute; and Institute for Carbon Management; University of California Los Angeles, Los Angeles, CA, USA 90095.

ABSTRACT

The hydration of the two most reactive phases of ordinary Portland cement (OPC), tricalcium silicate (C_3S) and tricalcium aluminate (C_3A) is successfully halted when the activity of water (a_H) falls below critical thresholds of 0.70 and 0.45, respectively. It's been established that the reduction in relative humidity (RH) and a_H suppresses the hydration of all anhydrous phases in OPC, including less explored phases like dicalcium silicate, that is, belite (β-C_2S). However, the degree of suppression, that is, the critical threshold, for β-C_2S, standalone has yet to be established. This study utilizes isothermal microcalorimetry and x-ray diffraction techniques to elucidate the influence of a_H on the hydration of β-C_2S suspensions via incremental replacements of water with isopropanol (IPA). Experimentally, this study shows that with increasing IPA replacements, hydration is increasingly suppressed until eventually brought to a halt at a critical threshold of approximately 27.7% IPA on a weight basis (wt.$\%_{IPA}$). From thermodynamic estimations, the exact critical a_H threshold and solubility product constant of β-C_2S (K_{C_2S}) are established as 0.913 and $10^{-12.68}$, respectively. This study provides enhanced understanding of β-C_2S reactivity and thermodynamic parameters during the hydration of β-C_2S-containing cementitious systems such as OPC-based and calcium aluminate-based systems.

Keywords: Hydration; Belite; Water Activity; Isothermal Calorimetry; X-ray Diffraction; Thermodynamics.

1. INTRODUCTION

Ordinary Portland Cement (OPC) in its anhydrous form is composed of four main phases: tricalcium silicate; dicalcium silicate; tricalcium aluminate; and tetracalciumaluminoferrite (commonly written as C_3S, C_2S, C_3A, and C_4AF, respectively, in conventional cement chemistry notation, wherein: C = CaO; S = SiO_2; A = Al_2O_3; F = Fe_2O_3; H = H_2O; etc.) — typically blended with one of the calcium sulfate hydrate states (anhydrite, hemihydrate, and/or gypsum) [1]. The complexity of the hydration reaction of OPC-based systems (i.e., pastes, mortars, concretes) can be emphasized by the fact that there are a multitude of anhydrous and hydrated phases presented within a OPC-based system at a given instance of time. As a result, a significant volume of hydration reaction (that is, the reaction that describes the chemical incorporation of water into the structure of the previously anhydrous powder) studies have focused on elucidating the hydration parameters of simple systems — such as C_3S [2–13] and C_3A/C$-phases [14–21] — due to the phases being star hydration participants at early ages in OPC-based systems.

Comparatively to the simple, anhydrous phases mentioned in the above paragraph, the hydration of C_2S standalone systems has been studied more selectively and for mainly two reasons: its comparatively smaller contribution to the overall hydration reaction, especially at early ages (i.e., approximately the initial 24 h to 36 h of the reaction) and; its inclusion in energy-friendly, alternative binders referred to as calcium aluminate (CA) [22] cements, calcium sulfoaluminate (CSA) [22–26] cements, calcium sulfoaluminate-belite (CSAB) [27,28] cements, etc. [26,29,30] in literature, wherein polymorphs of C_2S are studied in conjunction with other anhydrous phases. β-C_2S — the main form of C_2S (that is, in comparison to the α- and γ- C_2S polymorphs [1,31]) present in OPC, constitutes approximately 15% to 30 % of OPC by weight[1]. As stated previously, β-C_2S is less reactive at early ages — due to its relatively higher thermodynamic stability and densely packed structure [32,33] — compared to C_3S and C_3A/C$ phases and is credited as a contributor to the development of the hydration reaction at later ages [34–39] (that is, beyond the initial 24 h to 36 h of hydration in a given OPC-based system). With that stated the hydration reaction behavior of β-C_2S has more similarities to C_3S hydration — albeit, at physically observable slower rates (that is, a prolonged induction period, which reportedly results in the occurrence of the main hydration peak only after several days or even weeks according to the literature [34–39]) — as opposed to hydration of C_3A/C$ phases. A synopsis of β-C_2S hydration — which consists of a dissolution-precipitation process, again very similar to C_3S — is summarized in the following text.

1.1. β-C_2S HYDRATION REACTIONS

Equations 1, 2, 3, and 4 are expressed in terms of the variable x, which is used to signify the varying conditions at which the reaction can be satisfied, i.e., at equilibrium. The overall reaction of β-C_2S can be described by Equation 1, that is, Equation 1 describes the wetting of β-C_2S particulates' surfaces with the introduction of water to the system, leading to the dissociation of ions (Equation 2) — calcium (Ca^{2+}), dihydrogen orthosilicate ($H_2SiO_4^{2-}$), and hydroxyl ions (OH^-) — into the contiguous pore-solution. Once the pore-solution becomes saturated with respect to the aforesaid ions, precipitation of the hydration products — C-S-H and CH — begins to occur. Equations 3 and 4 describe the precipitation of C-S-H and CH, respectively, in context of a simplified β-C_2S system and Ca/Si stoichiometries established in literature[6] for C-S-H. These equations are based on assumptions originally made by Oey et al. [6] x is representative of the varying molar ratios of Ca/Si corresponding to known C-S-H, but also has a molar relationship to C-S-H's chemically bound water (Equation 3). This assumption's validity is unclear as C-S-H phases are known to show changes in their structure and water content with variations in a_H. It should also be briefly stated that similar stoichiometries for C-S-H can be used to thermodynamically predict both C_3S and β-C_2S hydration as they are reportedly [40,41] representative of both simple systems. A few studies — such as Brunauer et al. [40] and Goñi et al. [41] — have directly compared β-C_2S and C_3S hydration using quantitative x-ray diffraction and thermal analysis techniques, respectively, and found identical C-S-H stoichiometries presents, albeit at smaller amounts corresponding to the β-C_2S system compared to the C_3S system at a given age. It should also be stated that some researchers [42,43] believe there are differences in terms of the resulting properties of C-S-H depending on the anhydrous, simple system, that is, C_3S vs C_2S. In actuality, it is expected that a reduction in a_H would alter the thermodynamic phase relations of C-S-H phases, such that the stability of Ca/Si varies with a_H [44]. However, in regard to the current thermodynamic analysis, the stoichiometric values reported for C_3S are assumed valid for β-C_2S hydration in this study since they have been experimentally observed for both simple systems [40,41] and follow assumptions originally made by Oey et al. [6].

$$\mathrm{Ca_2SiO_4} + (2x+3)\mathrm{H_2O} \rightarrow (2-x)\mathrm{Ca(OH)_2} + \mathrm{CaO}_x \cdot \mathrm{SiO_2} \cdot \mathrm{H_2O}_{3x+1} \tag{1}$$

$$\mathrm{Ca_2SiO_4} + (2x+3)\mathrm{H_2O} \rightarrow 2\mathrm{Ca^{2+}} + \mathrm{H_2SiO_4}^{2-} + x\mathrm{OH^-} + (2x+1)\mathrm{H_2O} \tag{2}$$

$$\begin{aligned} &x\mathrm{Ca^{2+}} + \mathrm{H_2SiO_4}^{2-} + 2(x-1)\mathrm{OH^-} + (2x+1)\mathrm{H_2O} \\ &\leftrightarrow \mathrm{Ca(OH)_2} \cdot \mathrm{SiO_2} \cdot (2\mathrm{x}+1)\mathrm{H_2O} \end{aligned} \tag{3}$$

$$(2-x)\mathrm{Ca^{2+}} + 2(2-x)\mathrm{OH^-} \leftrightarrow (2-x)\mathrm{Ca(OH)_2} \tag{4}$$

1.2. PREVIOUS WATER ACTIVITY (a_H) STUDIES

As discussed above, limited work has been done to study β-C_2S hydration as a standalone system. With that stated, a thermodynamic approach was utilized in these references [6,21,45] to improve understanding of simple systems, that is, to estimate thermodynamic constants connected with the hydration of C_3S [6,45] and $C_3A/C\$$ systems [21], such as solubility and equilibrium constants of hydration products and reactants. The thermodynamic constants corresponding to the hydration reaction of OPC-based systems are known to be related to the a_H and relative humidity (RH) of the system. If the RH of the system is reduced within the microstructure, that is, internally by means of evaporation, the hydration kinetics of the system will ultimately be suppressed along with microstructural, mechanical, rheological, etc. development. Several researchers [6,45–51] have reported that below a critical value, i.e., RH = 80%, the hydration of OPC [47–51] or C_3S [6,45] — the main phases constituting OPC — is arrested. Flatt et al. [45] estimated that the chemical potential of water can be influenced and diminished via a vapor-phase route by reducing C_3S's RH internally. Conversely, Oey et al. [6] altered the chemical potential of water using a liquid-phase route by partly or completely replacing water with isopropanol (IPA) to manipulate the a_H of the system and established a critical threshold required for C_3S hydration to proceed, that is $a_H \geq 0.70$. Beyond C_3S, Lapeyre et al. [21] investigated the hydration of C_3A, due to its importance to the overall OPC hydration reaction [1,52,53] in combination with $C\$$ [1,14,54–56] and by adapting methods from Flatt et al. [45] and Oey et al. [6] was able to successfully determine the critical a_H threshold required for hydration of the $[C_3A + C\$]$ system to proceed, that is, $a_H \geq 0.45$. With that stated, a relationship has not been established between the aforementioned thermodynamic parameters and the hydration of remainder anhydrous phases in OPC-based systems, such as β-C_2S. Though there have been studies that have explored β-C_2S hydration, none have explored the effect of a_H and RH on a plain β-C_2S system.

The objective of this work is to study the effect of a_H, and therefore RH, on β-C_2S systems by systematically replacing IPA with water and observing the consequent hydration effects by determining the critical a_H at which belite hydration is arrested. More specifically, the results of this study will yield the following thermodynamic parameters: solubility product constant of β-C_2S (K_{C_2S}); and an accurate critical a_H threshold estimation. Such information would facilitate the selection of near-ideal curing conditions, giving the interested reader improved control of any β-C_2S-containing cementitious system's hydration kinetics, and therefore resulting in improved control over the development of microstructural, mechanical, rheological, etc. properties.

2. METHODS AND MATERIALS

2.1. β-C_2S SYNTHESIS AND PHYSICAL TECHNIQUES

A single, synthetic β-C_2S powder material was utilized in this study and was produced via solid-state synthesis using phase-pure precursor materials — $CaCO_3$ and SiO_2 — with a stoichiometric ratio of $CaO:SiO_2 = 2:1$. The precursor materials were then dispersed in a 1:1 ethanol-water mixture and stabilized using a dopant, that is, borax ($B_4Na_2O_7.10H_2O$) at a B/Si = 0.01 molar ratio. Stabilizing β-C_2S using boron-bearing dopants is well established in the literature [32,57,58]. However, it's known that dopants can effect β-C_2S reactivity even at low dopant levels [59], thus the employment of such a small molar ratio, which is thought to have minimal effects on β-C_2S hydration reaction rates. After drying at 150°C, the powder mixture was thermally treated at 1400°C for a 6 h duration. The material was then-air quenched, ground into powder, and characterized by x-ray diffraction (XRD; Panalytical X'Pert Pro MPD) via the instrument's continuous scanning mode. The diffractometer was operated at 45 kV and 40 mA. XRD experiments were performed using the following conditions: CuK_{α} radiation ($\lambda = 1.540598$ Å); a 2θ: 5 to 90° scanning range; and 0.026°. $step^{-1}$ at 272.34 s. $step^{-1}$. Collected patterns were analyzed using an automated Hanawalt method "Search and Match" function in the X'Pert HighScore for qualitative phase analysis. The obtained XRD pattern matches pattern peaks for larnite (i.e., the mineral form of belite: PDF no. 033-0302) and agree with diffraction patterns corresponding to synthetic belite reported in the literature [60–62].

The heat evolution relating to β-C_2S hydration in systems containing approximately 0.15 g of anhydrous β-C_2S was monitored for a minimum of 168 h, at a constant temperature of 20 ± 0.01°C, using a TAM IV isothermal microcalorimeter. Since β-C_2S is significantly less reactive compared to the hydration of simple, C_3S and C_3A systems at early ages, isothermal microcalorimetry techniques are advantageous in this study since they are able to monitor heat evolution — an indication of the hydration reaction, at a high resolution (10^{-8} J s^{-1}). To experimentally determine the critical a_H required for β-C_2S hydration arrestation, IPA was used to replace water in the liquid-portion of β-C_2S systems. A liquid-to-solid ratio of 10 was employed in this study to ensure that complete hydration of β-C_2S could be achieved, that is, the hydration reaction would not be limited by water content. Further, limited water can cause stresses within the capillary pore network of a paste system, thus suspension systems were preferred in this study. IPA was selected as an alcohol solvent because of its excellent miscibility with water, inertness, and lesser molecular size compared to water. IPA replacements were performed at a variety of replacement levels, that is from 0% to 100% on a weight basis to accurately determine the critical a_H required for β-C_2S hydration arrestation.

To support isothermal microcalorimetry findings, the diffraction patterns of select [β-C_2S + H + IPA] suspension systems, that is, systems with isopropanol replacement levels on a weight basis (wt.$\%_{IPA}$) of 0%, 10%, 20%, 25%, 40%, 80% and 100% were obtained using the aforementioned XRD technique after the initial 24 h and 168 h of hydration. Within ± 1 h of the desired examination age of the suspension system, excess liquid was removed via vacuum assisted filtration and diffraction patterns were obtained, that is, samples were immediately measured without an attempt to arrest hydration. All XRD patterns were obtained using the parameters stated above for the pristine β-C_2S powder.

2.2. A THERMODYNAMIC ANALYSIS: ESTIMATIONS OF ACTIVITIES (a_x), CRITICAL WATER ACTIVITY (a_H), AND SOLUBILITY PRODUCT CONSTANT (K_{C_2S})

2.2.1. Isopropanol (a_{IPA}) and Water Activity (a_H) Calculations. To calculate both the effective activities of IPA and water, that is, a_{IPA} (Equation 5) and a_H (Equation 6), respectively, corresponding to each [β-C_2S + H + IPA] system, the van Laar equations — which are discussed in detail here [63,64] — were utilized in this study as utilized in the referenced literature [6,21]. The mathematical relationship between a_{IPA} and a_H can be described with the following unitless variables: X_{IPA}; X_H; A; and B. That is, where: X_{IPA} is the molar fraction of IPA of a given system's liquid mixture; X_H is the molar fraction of water of a given system's liquid mixture; and A and B are unitless coefficients determined by Wilson and Simmons [63] via regression analysis of liquid-vapor equilibrium data as 1.000 and 0.483, respectively.

$$a_{IPA} = X_{IPA}\exp\left[\frac{A}{\left(1 + {}^{AX_{IPA}}/_{BX_H}\right)^2}\right] \tag{5}$$

$$a_H = X_H\exp\left[\frac{B}{\left(1 + {}^{BX_H}/_{AX_{IPA}}\right)^2}\right] \tag{6}$$

2.2.2. Solubility Product Constant (K_{C2S}) And Critical Water Activity (a_H) Calculations. A thermodynamic approach was utilized in these references [6,21,45] to estimate thermodynamic constants connected with the hydration of C_3S [6,45] and $C_3A/C\$$ systems [21], such as solubility and equilibrium constants of hydration products and pure, anhydrous phases. This approach was adapted in this study to improve understanding of hydration of β-C_2S systems. That is, this study aims to use this thermodynamic approach to estimate β-C_2S's solubility product constant (K_{C_2S}) and critical a_H below which β-C_2S hydration ceases. The following interpolation — which was adapted from Flatt et al. [45] — was utilized to estimate the molar volume of C-S-H as it varies with stoichiometry using reported C-S-H stoichiometries [65–67]. The reported molar volumes values for tobermorite, jennite, and C-S-H — where tobermorite has a Ca/Si = 0.83 [65], jennite has a Ca/Si = 1.67 [66], and C-S-H has a Ca/Si = 1.70 [67] — used to construct the interpolation (Equation 7) were 47.2 cm^3. mol^{-1}, 76.7 cm^3. mol^{-1}, and 88.5 cm^3. mol^{-1}, respectively.

$$V_{m_{C_xSH_{3x+1}}} = 15.15 + 42.16x \tag{7}$$

From Equation 7, values found for $V_{m_{C_xSH_{3x+1}}}$ can then be substituted into Equation 8, to calculate the change in the molar volume of the reactants (i.e. $\mathrm{V_{m_{C_2S}}}$ and $\mathrm{V_{m_H}}$) subtracted from the molar volume of the products (i.e. $\mathrm{V_{m_{C_xSH_{3x+1}}}}$and $\mathrm{V_{m_{CH}}}$). This expression assumes equilibrium occurs at a pressure of 1 bar and a temperature 25℃.

$$\Delta\mathrm{V_m} = \left[\mathrm{V_{m_{C_xSH_{3x+1}}}} + (2 - \mathrm{x}) \cdot \mathrm{V_{m_{CH}}}\right] - \left[\mathrm{V_{m_{C_2S}}} + (2\mathrm{x} + 3) \cdot \mathrm{V_{m_H}}\right] \tag{8}$$

The molar volumes that were calculated — in agreement with values reported in the literature [68] — for β-C_2S, H, and CH and utilized in the thermodynamic analysis performed in this study were 51.785, 18.015, and 32.915 $\mathrm{cm^3}$. $\mathrm{mol^{-1}}$, respectively. With this, the equilibrium constant corresponding to β-C_2S's hydration reaction ($\mathrm{K_{rxn}}$) could then be calculated assuming equilibrium conditions for $\mathrm{RH_K}$ and $\mathrm{a_H}$ — the ambient relative humidity of that the chemical equilibrium of water in the vapor phase with pure liquid water in a partially saturated pore and the activity of water in the pore-solution, respectively —, that is, when $\mathrm{RH_K} \leq 100\%$ and $\mathrm{a_H} \leq 1$ (Equation 9).

$$\ln(\mathrm{RH_K}) = \frac{\mathrm{V_{m\,H}}}{\Delta\mathrm{V_m}} \cdot \ln(\mathrm{K_{rxn}}) + \left[\frac{(2\mathrm{x} + 3) \cdot \mathrm{V_{m_H}}}{\Delta\mathrm{V_m} + 1}\right] \cdot \ln(\mathrm{a_H}) \tag{9}$$

Values for $\mathrm{K_{CH}}$, $\mathrm{K_{CSH_4}}$, and $\mathrm{K_{C_2SH_7}}$ have previously been reported in literature [45,69], that is, $\mathrm{K_{CH}} = 10^{-5.2}$, $\mathrm{K_{CSH_4}} = 10^{-7.52}$, and $\mathrm{K_{C_2SH_7}} = 10^{-12.96}$. C-S-H's stoichiometry varies with Ca/Si ratio, and therefore its solubility product constant varies as well. Interested readers can find more reported solubility product constants with respect to Ca/Si ratio in these references [45,70], but it should be noted that experimentally measured C-S-Hs do not strictly follow Equations 1-3, nor does this study aim to model the solubility of C-S-H based on experimental values. With a value obtained for K_{rxn} from Equation 9, K_{C_2S} was then obtained using values for $K_{C_xSH_{3x+1}}$ — corresponding to $x = 1$ and $x = 2$ — using Equation 10. The obtained values for K_{C_2S} can then be expressed as a function of a_H and related to wt.%$_{IPA}$ from the aforementioned van Laar equations (Equations 5 and 6) to calculate the critical a_H threshold.

$$K_{rxn} = \frac{K_{C_2S}}{K_{C_xSH_{3x+1}} {K_{CH}}^{2-x}} \qquad (10)$$

3. RESULTS AND DISCUSSION

Figure 1 shows the influence of the initial a_H on hydration rates of β-C_2S suspensions prepared at liquid-to-solid ratio = 10 for different levels of IPA replacement, as measured indirectly by isothermal calorimetry. Both the hydration rates and cumulative heat released corresponding to the hydration of [β-C_2S + H + IPA] systems, are substantially inhibited with increasing IPA replacements. The suppression of β-C_2S hydration is observed even when the initial water content is replaced with 2.5 wt.%$_{IPA}$ and a significant amount of water is present in the contiguous pore-solution — that is, liquid-to-solid ratio = 10. This indicates that the reactivity of β-C_2S is strongly affected by reduced a_H, more-so compared to the liquid-to-solid ratio. The effect of IPA in the contiguous pore-solution appears to diminish around 25 wt.%$_{IPA}$ especially when examining the Figure 1a insert graph, where the main hydration peak is not discernable within the initial 24 h of β-C_2S hydration. When considering the neat system, it can be

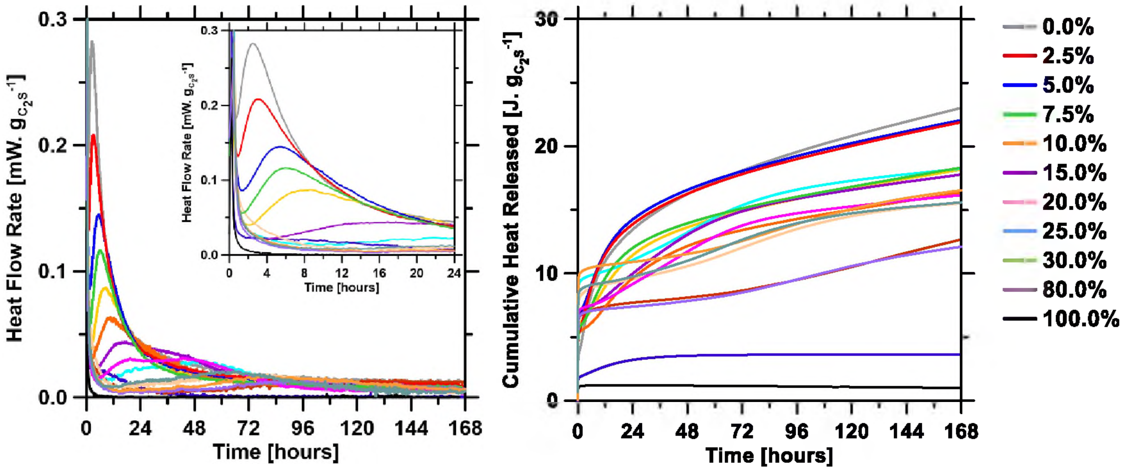

(a) (b)

Figure 1. Select isothermal microcalorimetry based determinations of the time dependent (a) heat flow rate; and (b) cumulative heat released of [β-C_2S + H + IPA] suspensions prepared at varying replacement levels (wt.%$_{IPA}$) of water, with a liquid-to-solid ratio = 10 used in this study. The inset plot represents the heat flow rate in the first 24 h of hydration. Uncertainty in heat flow rate at the observed hydration peak is ± 2%.

observed that there does not appear to be a prolonged induction period as reported in the literature [34–39], the supposed prolonged induction period that ends only after the main hydration peak is achieved. Based on heat evolution measurements corresponding to the hydration of [β-C_2S + H + IPA] systems (Figure 1), there appears to be a-type-of acceleration regime, at least for the neat system, which ends at approximately 4 h of hydration, the occurrence of which has not been reported in prior literature. This is most likely due to the employment of isothermal microcalorimetry vs, calorimetry techniques in this study. Though, the conundrum remains of a reported main hydration peak occurring after several days or weeks in literature. Based on enthalpy values — which is a reflection of the total, cumulative heat released corresponding to a reaction, thus an indication of the degree of reaction, or in this case, hydration — that can found in the literature, such as 260 kJ/kg reported here [71], it can be surmised that a second, more pronounced peak most likely does occur at a later age, but not within the initial 168 h. With that stated, it is clear that more elucidation of β-C_2S hydration is possible as modern characterization techniques and detection levels improve. Therefore, β-C_2S hydration deserves reexamination to improve holistic understanding of hydration of OPC-based systems and energy-friendly, alternative calcium aluminate-based binders such as CA, CSA, and CSAB cements.

Though a clear, well-identifiable trend was observed for isothermal microcalorimetry results (Figure 1), other characterization techniques proved to be more challenging in terms of elucidating the nuanced differences in [C_2S + H + IPA] systems with IPA replacement level and age. Figure 2 shows results from XRD analysis corresponding to the peak observed at $29.375 \pm 1.000° \, 2\theta$. With varying IPA replacement level and age, no differences were observed in diffraction patterns, with the exception of this peak — most likely due to β-C_2S's generally low reactivity (see neat system in Figure 1) and the detection limitations of the defractometer. This peak is observable in the pristine powder (i.e., anhydrous β-C_2S), and is shown to increase in raw intensity until a substantial amount of IPA, that is, 20 wt.$\%_{IPA}$, is present in the system, but then begins to decrease once 25 wt.$\%_{IPA}$ is present in the contiguous pore-solution (Figure 2a). It should be noted that to compare peak intensities in this way is more relative, that is, qualitative, and not absolute. The authors speculate that this peak's increased intensity corresponds to the formation of one of the hydrated calcium oxalate forms' — most likely similar to the formation of calcium oxalate monohydrate (i.e.., $C_2H_2CaO_5$) in these references [72,73] —, where the precipitated CH reacts with the IPA in the [H + IPA] contiguous pore-solution to form a hydrated calcium oxalate phase [73],

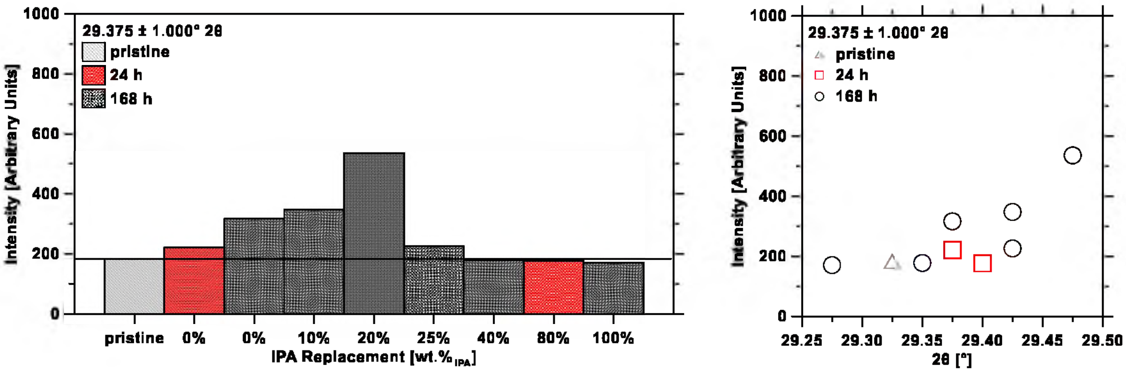

(a) (b)

Figure 2. Select XRD results of [β-C_2S + H + IPA] systems are shown as representation of the measured raw intensity of the 29.375 $\pm$ 1.000 °2θ peak by (a) IPA replacement level and (b) the occurance of the peak with respect to °2θ. The black horizontal line is the intensity of the pristine powder, (i.e., anhydrous β-C_2S), and can be used as a comparative reference against the measured intensities corresponding to the other systems. In comparison to the pristine powder, the [β-C_2S + H + IPA] system with 0% IPA by weight (wt.%$_{IPA}$) in the [H + IPA] contiguous solution after 24 h of hydration has a raw intensity increase of 20.64%, while after 168 h of hydration, the systems with 0 wt.%$_{IPA}$, 10 wt.%$_{IPA}$, 20 wt.%$_{IPA}$, and 25 wt.%$_{IPA}$ have raw intenisty increases of 72.50%, 89.50%. 192.20%, and 23.34%, respectively. $\geq$ 40 wt.%$_{IPA}$ a decrease in raw intensity is observed.

the formation of C-S-H — XRD peaks, corresponding to both ordered and disordered variants of jennite and tobermorite [74], have been reported to occur between 28.8° 2θ and 33.2° 2θ [74] —, or a combination of the two [74]. With increasing raw intensity, a rightward, ° 2θ shift can be noted in the peak of interest until 20 wt.%$_{IPA}$ (Figure 2b), then the peak begins to shift towards the left at 25 wt.%$_{IPA}$. As discussed in more detail here [74], peak shifts can indicate a change in stoichiometry, which would corroborate ideas that relate a_H to stoichiometry. It should be reiterated that the scope of this comunication and more specifically XRD experiments is not to model stoichiometry as a function of a_H, rather XRD results are soley meant to corroborate microcalorimetry findings on the critical a_H threshold. Regardless, XRD results (Figure 2) are a clear indication of the systems' reactivity — and in this case, a_H —, with a noticable decline in raw intensity from the diffraction results corresponding to the systems with > 20 wt.%$_{IPA}$ in the [H + IPA] contiguous pore-solution.

Figure 3 summarizes the results of the thermodynamic analysis conducted in this study, that is, — using CSH_4 and C_2SH_7 solubility values reported by Flatt et al. [45], and corroborated by Oey et al. [6] to elucidate "the influence of a_H on the hydration of tricalcium silicate" — Figure 3 indicates that the hydration of β-C_2S is effectively arrested when the a_H of the [H + IPA] contiguous solution is equal to 0.913 and $K_{C_2S} = 10^{-12.68}$. $K_{C_2S} = 10^{-12.68}$ was then utilized to obtain K_{rxn} at arrestation, that is, when $x = 1$ and $x = 2$, $K_{rxn} = 10^{0.21}$ and $K_{rxn} = 10^{0.29}$, respectively. When β-C_2S hydration is halted (i.e., $a_H \leq 0.913$), there are most likely one of two causations: β-C_2S is exhausted; or equilibrium has been achieved between all phases — β-C_2S, H, C_xSH_{3x+1}, and CH — in the system. Based on results obtained from physical experiments and thermodynamic calculations, it can be stated that the hydration of β-C_2S is effectively arrested at 27.7% wt.%$_{IPA}$, with the aforementioned causations being dependent on the Ca/Si of C-S-H and the initial or effective a_H of a β-C_2S system undergoing hydration.

To the best of the authors' knowledge, this is the first time values for the effective a_H and K_{C_2S} for β-C_2S hydration have been estimated. Interestingly, the reported critical a_H of 0.913 corresponding to β-C_2S hydration in this study, is greater than the critical a_H of 0.70 [6] and 0.45 [21] corresponding to C_3S and C_3A/C$ systems, respectively. This could potentially provide another explanation as to why the hydration peak observed in Figure 1b has not been observed previously, that is, $0.913 \leq a_H \leq 1.00$ is required β-

C_2S for hydration to proceed, which is a narrower range compared to the a_H conditions required for hydration to progress for C_3S and $C_3A/C\$$ systems.

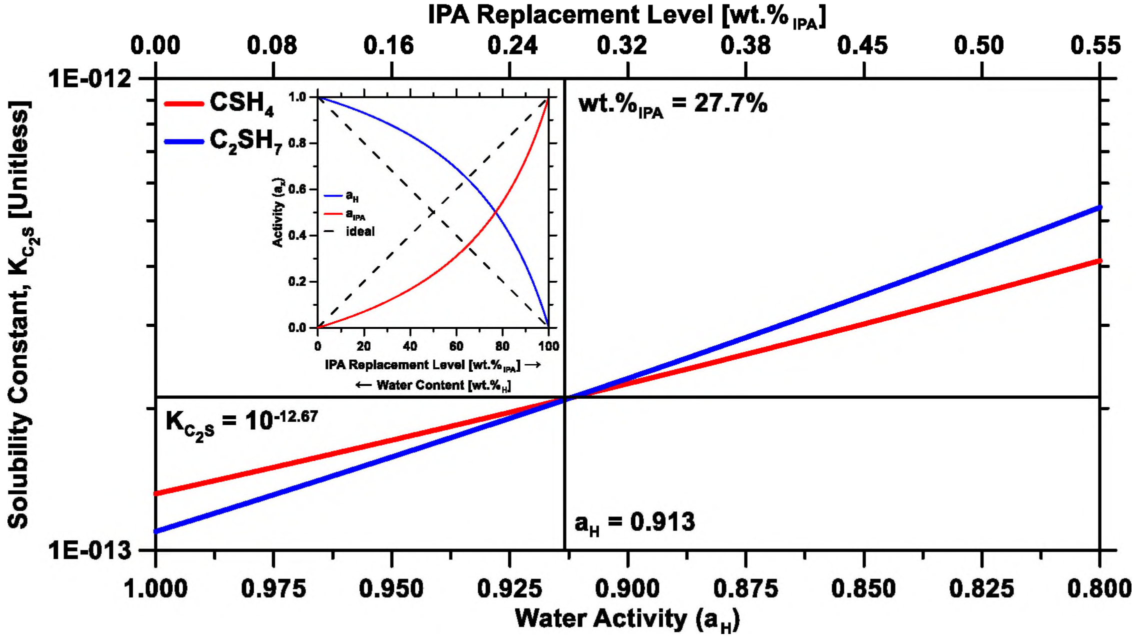

Figure 3. The solubility product constant of β-C_2S (K_{C_2S}), calculated using solubility values for CSH_4 and C_2SH_7 from literature [45,69], is shown as a function of water activity (a_H) as calculated from Equations 7 and 8, and related to IPA replacement level using the van Laar equations (Equations 5 and 6), which is graphically represented by the inset plot and included for the reader's reference. The dashed lines on the inset plot are representative of behavior for a liquid mixture, as described by Raoult's Law (i.e., a well-established thermodynamics law). The black lines are used to emphasize the point of intersection between the calculated K_{C_2S} curves, which corresponds to $a_H = 0.913$, when the wt.%$_{IPA}$ in the [H + IPA] contiguous solution is 27.7% and $K_{C_2S} = 10^{-12.68}$. All calculations are deterministic; as such, there is no associated uncertainty.

4. SUMMARY AND CONCLUSIONS

This study provides insight on the influence of water activity (a_H) on (β-C_2S) hydration via physical experiments and thermodynamic estimations for future thermo-kinetic studies as well as applied research. Suspensions' — comprised of β-C_2S powder and a liquid mixture consisting of water and isopropanol (IPA) — reaction kinetics were observed using isothermal microcalorimetry, a high-resolution technique used to measure the heat evolution of a system, and x-ray diffraction (XRD). Experimental results show that the critical a_H, required for the overall reaction to proceed, is likely related to an IPA replacement level of approximately greater than 25% on a weight basis (wt.%$_{IPA}$). From thermodynamic estimations, the critical a_H threshold and solubility product constant of β-C_2S (K_{C_2S}) are established as 0.913 and $10^{-12.68}$, respectively. Finally, the percent of IPA required to arrest β-C_2S hydration was back-estimated using the critical a_H threshold and was determined to be 27.7 wt.%$_{IPA}$, which is in excellent agreement with experimental findings. Based on this study's findings, curing conditions should be considered when working with a cementitious system containing β-C_2S hydration; conditions should be maintained so that $0.913 \leq a_H \leq 1.000$, otherwise arrestation of β-C_2S hydration will occur.

The overall result of this study is the enhancement of the current understanding of β-C_2S hydration, reactivity, and thermodynamic parameters during the hydration of cementitious systems containing β-C_2S. Based on heat evolution measurements corresponding to the hydration of [β-C_2S + H + IPA] systems, there appears to be an early peak occurring at approximately 4 h of hydration for the neat system, the occurrence of which has not been reported in prior literature to the best of the authors' knowledge. This prompts reexamination of β-C_2S hydration as modern characterization techniques improve to holistically enhance understanding of hydration of cementitious systems containing β-C_2S: OPC-based systems; and energy-friendly, alternative binders such as calcium aluminate-based systems.

ACKNOWLEDGEMENTS

Funding for this study was provided by the National Science Foundation (CMMI: 1661609 and 1932690). The authors would like to recognize the Materials Research Center at Missouri S&T Missouri S&T for providing the facilities to accomplish the work detailed in this publication.

REFERENCES

[1] H.F. Taylor, Cement chemistry, Thomas Telford, 1997.

[2] R. Cook, H. Ma, A. Kumar, Mechanism of tricalcium silicate hydration in the presence of polycarboxylate polymers, SN Appl. Sci. 1 (2019) 145. https://doi.org/10.1007/s42452-018-0153-1.

[3] R. Cook, H. Ma, A. Kumar, Influence of size-classified and slightly soluble mineral additives on hydration of tricalcium silicate, J. Am. Ceram. Soc. 103 (2019) 2764–2779. https://doi.org/10.1111/jace.16936.

[4] J. Lapeyre, H. Ma, A. Kumar, Effect of particle size distribution of metakaolin on hydration kinetics of tricalcium silicate, 102 (2019) 5976–5988. https://doi.org/10.1111/jace.16467.

[5] J. Lapeyre, A. Kumar, Influence of pozzolanic additives on hydration mechanisms of tricalcium silicate, J. Am. Ceram. Soc. 101 (2018) 3557–3574. https://doi.org/10.1111/jace.15518.

[6] T. Oey, A. Kumar, G. Falzone, J. Huang, S. Kennison, M. Bauchy, N. Neithalath, J.W. Bullard, G. Sant, The Influence of Water Activity on the Hydration Rate of Tricalcium Silicate, J. Am. Ceram. Soc. 99 (2016) 2481–2492. https://doi.org/10.1111/jace.14181.

[7] A. Kumar, S. Bishnoi, K.L. Scrivener, Modelling early age hydration kinetics of alite, Cem. Concr. Res. 42 (2012) 903–918.

[8] A. Kumar, T. Oey, G. Falzone, J. Huang, M. Bauchy, M. Balonis, N. Neithalath, J. Bullard, G. Sant, The filler effect: The influence of filler content and type on the hydration rate of tricalcium silicate, J. Am. Ceram. Soc. 100 (2017) 3316–3328.

[9] A. Bazzoni, S. Ma, Q. Wang, X. Shen, M. Cantoni, K.L. Scrivener, The Effect of Magnesium and Zinc Ions on the Hydration Kinetics of C3S, J. Am. Ceram. Soc. 97 (2014) 3684–3693.

[10] J.J. Biernacki, T. Xie, An advanced single particle model for C3S and alite hydration, J. Am. Ceram. Soc. 94 (2011) 2037–2047.

[11] S. Garrault, E. Finot, E. Lesniewska, A. Nonat, Study of CSH growth on C3S surface during its early hydration, Mater. Struct. 38 (2005) 435–442.

[12] M. Zacak, S. Garrault, J.P. Korb, A. Nonat, Effect of temperature on the development of CSH during early hydration of C3S, in: 12 Th Int. Congr. Chem. Cem., 2007: pp. W1–06. https://hal.archives-ouvertes.fr/hal-00452150/ (accessed January 31, 2017).

[13] J.W. Bullard, A determination of hydration mechanisms for tricalcium silicate using a kinetic cellular automaton model, J. Am. Ceram. Soc. 91 (2008) 2088–2097.

[14] E. Breval, C3A hydration, Cem. Concr. Res. 6 (1976) 129–137. https://doi.org/10.1016/0008-8846(76)90057-0.

[15] A. Quennoz, K.L. Scrivener, Hydration of C3A–gypsum systems, Cem. Concr. Res. 42 (2012) 1032–1041. https://doi.org/10.1016/j.cemconres.2012.04.005.

[16] A.I. Vovk, Hydration of tricalcium aluminate C3A and C3A-gypsum mixtures in the presence of surfactants: adsorption or surface phase formation?, Colloid J. 62 (2000) 24–31.

[17] A. Lagosz, J. Malolepszy, S. Garrault, Hydration of tricalcium aluminate in the presence of various amounts of calcium sulphite hemihydrate: Conductivity tests, Cem. Concr. Res. 36 (2006) 1016–1022.

[18] H. Minard, S. Garrault, A. Nonat, Understanding of Reactional Sequences and Limiting Stages during Tricalcium Aluminate Hydration with and without Gypsum., in: 12 Th Int. Congr. Chem. Cem., 2007: pp. M1–01. https://hal.archives-ouvertes.fr/hal-00452356/ (accessed August 11, 2016).

[19] H. Minard, S. Garrault, L. Regnaud, A. Nonat, Mechanisms and parameters controlling the tricalcium aluminate reactivity in the presence of gypsum, Cem. Concr. Res. 37 (2007) 1418–1426.

[20] V.T. Yilmaz, F.P. Glasser, Early hydration of tricalcium aluminate-gypsum mixtures in the presence of sulphonated melamine formaldehyde superplasticizer, Cem. Concr. Res. 21 (1991) 765–776.

[21] J. Lapeyre, H. Ma, M. Okoronkwo, G. Sant, A. Kumar, Influence of water activity on hydration of tricalcium aluminate-calcium sulfate systems, J. Am. Ceram. Soc. (2020) 1–20. https://doi.org/10.1111/jace.17046.

[22] M.C.G. Juenger, F. Winnefeld, J.L. Provis, J.H. Ideker, Advances in alternative cementitious binders, Cem. Concr. Res. 41 (2011) 1232–1243.

[23] B. Tan, M.U. Okoronkwo, A. Kumar, H. Ma, Durability of calcium sulfoaluminate cement concrete, J. Zhejiang Univ.-Sci. A. 21 (2020) 118–128. https://doi.org/10.1631/jzus.A1900588.

[24] C. Shi, A.F. Jiménez, A. Palomo, New cements for the 21st century: the pursuit of an alternative to Portland cement, Cem. Concr. Res. 41 (2011) 750–763.

[25] F. Winnefeld, B. Lothenbach, Hydration of calcium sulfoaluminate cements—experimental findings and thermodynamic modelling, Cem. Concr. Res. 40 (2010) 1239–1247.

[26] J.J. Biernacki, J.W. Bullard, G. Sant, K. Brown, F.P. Glasser, S. Jones, T. Ley, R.A. Livingston, L. Nicoleau, J. Olek, F. Sanchez, R. Shahsavari, P.E. Stutzman, K. Soblev, T. Prater, Cements in the 21st century: Challenges, perspectives, and opportunities, 100 (2017) 27.

[27] I.A. Chen, M.C.G. Juenger, Incorporation of coal combustion residuals into calcium sulfoaluminate-belite cement clinkers, Cem. Concr. Compos. 34 (2012) 893–902. https://doi.org/10.1016/j.cemconcomp.2012.04.006.

[28] K. Quillin, Performance of belite–sulfoaluminate cements, Cem. Concr. Res. 31 (2001) 1341–1349. https://doi.org/10.1016/S0008-8846(01)00543-9.

[29] C.D. Popescu, M. Muntean, J.H. Sharp, Industrial trial production of low energy belite cement, Cem. Concr. Compos. 25 (2003) 689–693. https://doi.org/10.1016/S0958-9465(02)00097-5.

[30] C. Shi, B. Qu, J.L. Provis, Recent progress in low-carbon binders, Cem. Concr. Res. 122 (2019) 227–250. https://doi.org/10.1016/j.cemconres.2019.05.009.

[31] R. Trettin, G. Oliew, C. Stadelmann, W. Wieker, Very early hydration of dicalcium silicate-polymorphs, Cem. Concr. Res. 21 (1991) 757–764. https://doi.org/10.1016/0008-8846(91)90171-D.

[32] A.M. Sharara, H. El-Didamony, E. Ebied, A. El-Aleem, Hydration characteristics of β-C2S in the presence of some pozzolanic materials, Cem. Concr. Res. 24 (1994) 966–974. https://doi.org/10.1016/0008-8846(94)90017-5.

[33] V. Kasselouri, P. Tsakiridis, C. Malami, B. Georgali, C. Alexandridou, A study on the hydration products of a non-expansive sulfoaluminate cement, Cem. Concr. Res. 25 (1995) 1726–1736. https://doi.org/10.1016/0008-8846(95)00168-9.

[34] H. El-Didamony, T.M. El-Sokkari, Kh.A. Khalil, M. Heikal, I.A. Ahmed, Hydration mechanisms of calcium sulphoaluminate C4A 3S, C4AS phase and active belite β-C2S, Ceram. - Silik. 56 (2012) 389–395.

[35] R.L. BERGER, A. BENTUR, N.B. MILESTONE, J.H. KUNG, Structural Properties of Calcium Silicate Pastes: I, Effect of the Hydrating Compound, J. Am. Ceram. Soc. 62 (1979) 358–362. https://doi.org/10.1111/j.1151-2916.1979.tb19078.x.

[36] I.M. Pritts, K.E. Daugherty, The effect of stabilizing agents on the hydration rate of β-C2S, Cem. Concr. Res. 6 (1976) 783–795. https://doi.org/10.1016/0008-8846(76)90008-9.

[37] D.L. Kantro, C.H. Weise, Hydration of various beta-dicalcium silicate preparation, J Am Ceram Soc. 62 (1979). https://doi.org/10.1111/j.1151-2916.1979.tb12746.x.

[38] K. FUJII, W. KONDO, Rate and Mechanism of Hydration of β-Dicalcium Silicate, J. Am. Ceram. Soc. 62 (1979) 161–167. https://doi.org/10.1111/j.1151-2916.1979.tb19045.x.

[39] I. Odler, J. Schüppstuhl, Combined hydration of tricalcium silicate and β-dicalcium silicate, Cem. Concr. Res. 12 (1982) 13–20. https://doi.org/10.1016/0008-8846(82)90093-X.

[40] S. Brunauer, D.L. Kantro, L.E. Copeland, The Stoichiometry of the Hydration of β-Dicalcium Silicate and Tricalcium Silicate at Room Temperature, J. Am. Chem. Soc. 80 (1958) 761–767. https://doi.org/10.1021/ja01537a001.

[41] S. Goñi, F. Puertas, M.S. Hernández, M. Palacios, A. Guerrero, J.S. Dolado, B. Zanga, F. Baroni, Quantitative study of hydration of C3S and C2S by thermal analysis, J. Therm. Anal. Calorim. 102 (2010) 965–973. https://doi.org/10.1007/s10973-010-0816-7.

[42] B. Lothenbach, A. Nonat, Calcium silicate hydrates: Solid and liquid phase composition, Cem. Concr. Res. 78, Part A (2015) 57–70. https://doi.org/10.1016/j.cemconres.2015.03.019.

[43] B. Lothenbach, D.A. Kulik, T. Matschei, M. Balonis, L. Baquerizo, B. Dilnesa, G.D. Miron, R.J. Myers, Cemdata18: A chemical thermodynamic database for hydrated Portland cements and alkali-activated materials, Cem. Concr. Res. 115 (2019) 472–506. https://doi.org/10.1016/j.cemconres.2018.04.018.

[44] E. Boehm-Courjault, J.E. Rossen, K. Scrivener, Composition and Morphology of C-S-H in C3S Pastes Hydrated by Water/Isopropanol Mixes Using Electron Microscopy, in: Proc. EMABM, Technical University, Delft, The Netherlands, 2015: p. 5.

[45] R.J. Flatt, G.W. Scherer, J.W. Bullard, Why alite stops hydrating below 80% relative humidity, Cem. Concr. Res. 41 (2011) 987–992. https://doi.org/10.1016/j.cemconres.2011.06.001.

[46] T.C. Powers, A DISCUSSION OF CEMENT HYDRATION IN RELATION TO THE CURING OF CONCRETE, in: Proc. Twenty-Seventh Annu. Meet. Highw. Res. Board Held Wash., 1948: pp. 178–188.

[47] R.G. Patel, D.C. Killoh, L.J. Parrott, W.A. Gutteridge, Influence of curing at different relative humidities upon compound reactions and porosity in Portland cement paste, Mater. Struct. 21 (1988) 192–197. https://doi.org/10.1007/BF02473055.

[48] O.M. Jensen, P.F. Hansen, E.E. Lachowski, F.P. Glasser, Clinker mineral hydration at reduced relative humidities, Cem. Concr. Res. 29 (1999) 1505–1512. https://doi.org/10.1016/S0008-8846(99)00132-5.

[49] M. Wyrzykowski, P. Lura, Effect of relative humidity decrease due to self-desiccation on the hydration kinetics of cement, Cem. Concr. Res. 85 (2016) 75–81. https://doi.org/10.1016/j.cemconres.2016.04.003.

[50] J. Stoian, T. Oey, J.W. Bullard, J. Huang, A. Kumar, M. Balonis, N. Neithalath, G.N. Sant, The Prehydration of Cement and its Mitigation, in: Delft, The Netherlands, 2015. https://tsapps.nist.gov/publication/get_pdf.cfm?pub_id=917059.

[51] J. Stoian, T. Oey, J.W. Bullard, J. Huang, A. Kumar, M. Balonis, J. Terrill, N. Neithalath, G. Sant, New insights into the prehydration of cement and its mitigation, Cem. Concr. Res. 70 (2015) 94–103.

[52] I. Jawed, J. Skalny, Surface phenomena during tricalcium silicate hydration, J. Colloid Interface Sci. 85 (1982) 235–243. https://doi.org/10.1016/0021-9797(82)90252-1.

[53] J.C. Taylor, L.P. Aldridge, Full-profile Rietveld quantitative XRD analysis of Portland cement: Standard XRD profiles for the major phase tricalcium silicate (C3S: 3CaO.SiO2), Powder Diffr. 8 (1993) 138–144. https://doi.org/10.1017/S0885715600018054.

[54] A. Quennoz, K.L. Scrivener, Hydration of C 3 A–gypsum systems, Cem. Concr. Res. 42 (2012) 1032–1041.

[55] J.W. Bullard, H.M. Jennings, R.A. Livingston, A. Nonat, G.W. Scherer, J.S. Schweitzer, K.L. Scrivener, J.J. Thomas, Mechanisms of cement hydration, Cem. Concr. Res. 41 (2011) 1208–1223.

[56] W.A. Corstanje, W.N. Stein, J.M. Stevels, Hydration reactions in pastes C3S + C3A + CaSO4 .2aq. + water at 25°C.III, Cem. Concr. Res. 4 (1974) 417–431. https://doi.org/10.1016/0008-8846(74)90107-0.

[57] I. Jelenić, A. Bezjak, M. Bujan, Hydration of B2O3-stabilized α′-and β-modifications of dicalcium silicate, Cem. Concr. Res. 8 (1978) 173–180. https://doi.org/10.1016/0008-8846(78)90006-6.

[58] A. Cuesta, E.R. Losilla, M.A.G. Aranda, J. Sanz, Á.G. [De la Torre, Reactive belite stabilization mechanisms by boron-bearing dopants, Cem. Concr. Res. 42 (2012) 598–606. https://doi.org/10.1016/j.cemconres.2012.01.006.

[59] P. Guo, B. Wang, M. Bauchy, G. Sant, Misfit Stresses Caused by Atomic Size Mismatch: The Origin of Doping-Induced Destabilization of Dicalcium Silicate, Cryst. Growth Des. 16 (2016) 3124–3132. https://doi.org/10.1021/acs.cgd.5b01740.

[60] Y. Tan, Y. Liu, Z. Zhang, M. Hofmann, L. Grover, Comparing Three Methods for the Synthesis of Pure Beta-Dicalcium Silicate, in: 2010 4th Int. Conf. Bioinforma. Biomed. Eng., 2010: pp. 1–4. https://doi.org/10.1109/ICBBE.2010.5515290.

[61] P. Koutník, Preparation of β-belite using liquid alkali silicates, Mater. Constr. 67 (2017) 140. https://doi.org/10.3989/mc.2017.10816.

[62] D. Correa, A. Almirall, R. García-Carrodeguas, L.A. dos Santos, A.H. De Aza, J. Parra, J.Á. Delgado, β-Dicalcium silicate-based cement: synthesis, characterization and in vitro bioactivity and biocompatibility studies, J. Biomed. Mater. Res. A. 102 (2014) 3693–3703. https://doi.org/10.1002/jbm.a.35041.

[63] A. Wilson, E.L. Simons, Vapor-Liquid Equilibria, Ind. Eng. Chem. 44 (1952) 2214–2219. https://doi.org/10.1021/ie50513a063.

[64] J. Mollerup, Correlation of thermodynamic properties of mixtures using a random-mixture reference state, Fluid Phase Equilibria. 15 (1983) 189–207. https://doi.org/10.1016/0378-3812(83)80152-6.

[65] R.A. of S. Institute of Experimental Mineralogy, TOBERMORITE, Crystallogr. Crystallochem. Database Miner. Their Struct. Analog. (n.d.). http://database.iem.ac.ru/mincryst/s_carta.php?TOBERMORITE+4800.

[66] R.A. of S. Institute of Experimental Mineralogy, JENNITE, Crystallogr. Crystallochem. Database Miner. Their Struct. Analog. (n.d.). http://database.iem.ac.ru/mincryst/s_carta.php?JENNITE+7193.

[67] H.M. Jennings, A model for the microstructure of calcium silicate hydrate in cement paste, Cem. Concr. Res. 30 (2000) 101–116.

[68] M. Balonis, F.P. Glasser, The density of cement phases, Cem. Concr. Res. 39 (2009) 733–739.

[69] J.W. Bullard, R.J. Flatt, New insights into the effect of calcium hydroxide precipitation on the kinetics of tricalcium silicate hydration, J. Am. Ceram. Soc. 93 (2010) 1894–1903.

[70] C.S. Walker, S. Sutou, C. Oda, M. Mihara, A. Honda, Calcium silicate hydrate (C-S-H) gel solubility data and a discrete solid phase model at 25°C based on two binary non-ideal solid solutions, Cem. Concr. Res. 79 (2016) 1–30. https://doi.org/10.1016/j.cemconres.2015.07.006.

[71] P.C. Hewlett, M. Liska, 5.4.6 Mechanisms of Cement Hydration: Experiments and Numerical Simulations, in: Leas Chem. Cem. Concr. 5th Ed., Elsevier, 2019: p. 187. https://app.knovel.com/hotlink/pdf/id:kt0122CBQ1/leas-chemistry-cement/leas-chemi-mechanisms-2.

[72] A.R. Izatulina, V.V. Gurzhiy, M.G. Krzhizhanovskaya, M.A. Kuz'mina, M. Leoni, O.V. Frank-Kamenetskaya, Hydrated Calcium Oxalates: Crystal Structures, Thermal Stability, and Phase Evolution, Cryst. Growth Des. 18 (2018) 5465–5478. https://doi.org/10.1021/acs.cgd.8b00826.

[73] A. Verganelaki, V. Kilikoglou, I. Karatasios, P. Maravelaki-Kalaitzaki, A biomimetic approach to strengthen and protect construction materials with a novel calcium-oxalate–silica nanocomposite, Constr. Build. Mater. 62 (2014) 8–17. https://doi.org/10.1016/j.conbuildmat.2014.01.079.

[74] S. Grangeon, F. Claret, Y. Linard, C. Chiaberge, X-ray diffraction: a powerful tool to probe and understand the structure of nanocrystalline calcium silicate hydrates, Acta Crystallogr. Sect. B. 69 (2013) 465–473. https://doi.org/10.1107/S2052519213021155.

III. MECHANISMS OF TRICALCIUM SILICATE HYDRATION IN THE PRESENCE OF POLYCARBOXYLATE POLYMERS

Rachel Cook[1], Hongyan Ma[2], and Aditya Kumar[1]

1. Department of Materials Science and Engineering, Missouri University of Science and Technology (S&T), B49 McNutt Hall, 1400 N. Bishop, Rolla, MO 65409, USA.

2. Department of Civil, Architectural and Environmental Engineering, Missouri University of Science and Technology (S&T), Rolla, MO 65409, USA.

ABSTRACT

The early-age hydration of cement is inhibited in the presence of comb-shaped polycarboxylate ether (PCE) polymer – a dispersant commonly added to control rheological properties of fresh cement paste. This inhibition of C_3S hydration—further the inhibition of C_3S dissolution and C-S-H nucleation and growth— has previously been attributed to PCE's ability to electrostatically adsorb onto the surface of silicate particles and the molecular structure of PCE. This study employs a series of microcalorimetry experiments and phase boundary nucleation and growth (pBNG) simulations to elucidate the effects of dosage and molecular architecture of PCE on the hydration mechanism of tricalcium silicate (Ca_3SiO_5 or C_3S in cement notation), the major phase in cement. Results show that PCE – regardless of its molecular architecture – suppresses early-age hydration of C_3S, wherein the effects of deceleration becomes increasingly more pronounced as dosage of PCE in the paste increases. Such suppression of C_3S hydration has previously been attributed to molecular architecture and adsorption of PCE molecules on silicate surfaces, which inhibit topographical sites of C_3S dissolution and C-S-H nucleation, and impede the post-nucleation growth of C-S-H. This study develops a robust correlation between molecular architecture of PCE and its ability to suppress C_3S hydration through quantitative analyses of decelerating effects induced by the three different PCEs and based on published literature. The numerical equation, describing such correlation, offers a reliable, and, more importantly, a readily quantifiable indicator of PCE's potential to suppress C_3S hydration in relation to its dosage and molecular architecture.

Keywords: C_3S; PCE; Hydration Kinetics; Nucleation and Growth; Simulation; Microcalorimetry.

1. INTRODUCTION

The reaction of cement with water, that is, hydration, involves the occurrence of two concurrent processes – dissolution of anhydrous phases present in cement, and precipitation of hydration products (subsequently referred to as hydrates) [1,2]. In a typical cement paste (i.e., [cement + water] system), the hydrate that occupies the largest volume fraction – and, thus, considered the main hydrate – is calcium-silicate-hydrate (C-S-H, wherein C = CaO, H = H_2O, and S = SiO_2 as per standard cement notation) [1,2]. C-S-H represents a highly disordered framework, comprised of tetrahedral structures of SiO_2 and layers of oxygen and calcium atoms interspersed by water[3–5] and has been characterized by various dreierkette-based models and the tobermorite-jennite structure as described in detail in a previous study [4]. The strong electrostatic bonding between the nanometer-scale components of C-S-H binds the paste cohesively, and lends the solid phase connectivity within the paste's microstructure needed for the development of mechanical properties (e.g., compressive strength) [6–9]. In cement pastes, the nucleation of C-S-H occurs in heterogeneous manner on the solid substrate boundaries, that is, cement particles' surfaces; as such, the mechanism of its precipitation is typically designated as phase boundary nucleation and growth (pBNG) [6,10–14]. As properties of cement paste are largely dictated by rate and amount of C-S-H precipitation, factors that affect C-S-H precipitation inevitably affect the development of the paste's mechanical properties. One such factor – that imparts significant effect on C-S-H's nucleation and growth – is the presence of polymer-based chemical admixtures in the paste. Polycarboxylate ether (PCE) superplasticizers are a well-known class of comb-shaped, polymer-based dispersants, typically used to control the rheological properties and fluidity of fresh cementitious systems [15,16] (e.g., high-performance concrete). A singular PCE molecule, if isolated, could be characterized as having comb-shaped architecture, consisting of an anionic backbone – usually formulated using polyacrylic acid or polymethacrylic acid – grafted with a number of hydrophilic ethylene oxide side chains [17–25]. When introduced in cement paste systems, PCE's negatively charged backbone will adsorb onto positively charged cement particles' surfaces through electrostatic interactions; meanwhile, the side-chains – which protrude into the solution, oriented away from cement particles' surfaces – induce steric hindrance between neighboring cement particles, thus alleviating the effects of particle agglomeration [17–22]. The adsorption of PCE onto cement particle surfaces, which improves rheology by mitigating particle agglomeration, also induces a side-effect – retardation of hydration kinetics of cement [17,18,26–28]. More specifically, the adsorption of PCE onto cement particles' surfaces inhibits topographical cement dissolution and C-S-H nucleation sites, thus suppressing cement's reactivity as detailed in the literature [18,19,21,27,28]. There is consensus among researchers that the molecular architecture of PCE – specifically, the number of side chains grafted onto each unit of backbone (n), the carboxylate-to-ether ratio (C/E), and the number of ethylene oxide monomers constituting the side chain (P) – significantly affects PCE's adsorption behavior, and, thus, its potential to suppress cement hydration [18–20,23,25]. Notwithstanding, the exact mechanisms of PCE-cement interactions, especially in relation to PCE's molecular architecture, are not well understood. Several prior studies have argued that the adsorption capacity of PCE is largely dependent on its side chain grafting density (i.e., inverse of C/E: carboxylate-to-ether ratio), wherein lower grafting densities (or higher C/E) entail higher residual negative charge on the backbone, and, thus, improved adsorption onto positively-charged cement particles' surfaces [18,29–31]. Other studies, however, have argued that the length of the side chain (i.e., P: number of monomers constituting each side chain) – as opposed to the side chain grafting density – has greater influence on the PCE's adsorption capacity [20,32]. The premise, here, is that shorter side chains ensure that accessibility to the negative charges on the PCE's backbone is not hindered or limited by steric hindrance (induced by its side chains); this enables better adsorption of PCE molecules onto cement particles' surfaces. In contrast to the above, some studies [18,19,33] have posited that the PCE's charge density – which acquires higher values at lower side chain grafting densities (or higher C/E) and shorter side chain lengths (P) – influences the PCE's adsorption capacity the most. More specifically, higher charge density leads to stronger, and better-distributed, electrostatic interactions between cement particles and PCE molecules, and, therefore, improved adsorption. In a recent study, Marchon et al. [25] reported that PCE's ability to suppress cement hydration cannot be quantified using a single architectural parameter; rather, a more encompassing, composite architectural parameter – that accounts for the aforementioned parameters (i.e., *C/E*, *n*, and *P*) as well as the molecular weight and dosage of PCE in the system – is required to fully describe the effects of PCE on C_3S hydration. The authors [24] showed that for a series of cement pastes, provisioned with different dosages of different PCEs, the composite architectural parameter scaled, broadly in a monotonic fashion, with respect to the deceleration of hydration kinetics. In this study, focus is given to rigorously test the ability of the composite architectural parameter to reliably quantify the deceleration caused by PCEs of different molecular architectures and consequent molecular weights.

In addition to aforementioned knowledge gaps – pertaining to correlations between PCE's molecular architecture and its ability to decelerate cement hydration kinetics – the effect of PCE on nucleation and growth of the main hydrate, i.e., C-S-H, is not well understood. C-S-H In recent studies [26,27,34], it has been suggested that in cementitious paste with PCE additions, due to blockage of nucleation sites by PCE molecules, C-S-H nucleation changes from heterogeneous (i.e., on solid surfaces) to homogeneous (i.e., in the pore space). The authors [26,27] argued that the change demands supersaturation for C-S-H precipitation to occur, which, consequently, enforces slower and prolonged dissolution of cement until massive precipitation of C-S-H can occur. However, in prior studies [19,33], it has been shown that while PCE changes the nucleation and growth processes' rate constants (e.g., rate of growth, frequency of nucleation sites), the precipitation of C-S-H occurs in a heterogeneous – not homogeneous – manner. In a more recent study, Meng et al. [28] argued that at further increased PCE dosages, the nucleation and consequent growth of C-S-H continues to occur heterogeneously, however the nucleation density and growth rate are suppressed. The authors[28] reported that the suppression is caused by the following: (i) adsorption of PCE molecules onto cement surfaces – which blocks a fraction of C-S-H nucleation sites, leading to the suppression of C-S-H's nucleation density, and (ii) adsorption of PCE molecules onto C-S-H – which partially blocks C-S-H's access to the pore solution, resulting in the inhibition of C-S-H's post-nucleation growth.

The above discussion accentuates PCE's significant influence on hydration of cementitious systems, as well as gaps in knowledge of underlying mechanisms that link PCE's molecular architecture to its ability to suppress cement hydration and nucleation and growth of C-S-H. The main reason, that would explain these knowledge gaps, is that majority of the past studies have examined the role of PCE in multi-component cementitious systems, in which it is infeasible to de-couple the effects of PCE on dissolution-precipitation hydration process of the two most reactive cement phases, that is, tricalcium silicate (C_3S) and tricalcium aluminate (C_3A, where A: Al_2O_3 as per standard cement notation). For example, in such multi-component cement systems, C_3A hydrates rapidly to form ettringite – which then serves as a favorable adsorbent for PCE molecules[20,21,35]; as PCE is drawn in substantial amounts from the solution and adsorbed onto ettringite, the influence of PCE on C_3S hydration rates is marginalized and, therefore, difficult to isolate from the overall response. Furthermore, in multi-component systems, interactions between PCE-and-C_3A and PCE-and-ettringite may affect (i.e., increase or decrease) the amount of free aluminate [$Al(OH)_4^-$] ions in the solution – which, in turn, makes it difficult to isolate and analyze the net effect of PCE (vis-à-vis that of aluminate ions) on C_3S hydration rates [23,24]. Therefore, evaluation of such behaviors should be carried out in single-compound systems, which are simpler to analyze than cement but feature the same effects. As noted previously, C_3S is the major cement phase (comprising 50-70%$_{mass}$ of cement), and, as such, mimics the overall hydration behavior of cement [1]. The hydration of C_3S produces two hydrates, that is, C-S-H and CH (portlandite), in stoichiometric quantities, and – like in cement pastes – the nucleation and growth of C-S-H is the driving mechanism in C_3S pastes. As such, C_3S is deemed a simpler single-compound alternative for cement.

In this study, a combination of experimental and simulation techniques is used to elucidate the effect of PCE on hydration of C_3S. To fully examine and describe the links between PCE's molecular architecture and its ability to suppress hydration of C_3S, PCEs with three different molecular architectures – albeit, of the same polymer family – are used. The hydration kinetics are monitored, using isothermal microcalorimetry technique, across a broad range of PCE dosages in C_3S pastes. A phase boundary nucleation and growth (pBNG) — a modified version of classical Cahn kinetics, which has only recently been applied in the literature [14,28,36] — simulation routine, with a modification involving anisotropic and saturation-dependent growth rate of hydrate, is employed to reproduce, and subsequently describe, hydration kinetics of such systems. Focus is given to consolidate results obtained from experiments and simulations, and analyze them in tandem to elucidate the mechanistic origins of PCE-induced suppression of C_3S hydration—including both early and later stages, wherein C_3S hydration is driven by dissolution and nucleation-and-growth, respectively. The mechanisms are ultimately distilled into a single numerical equation that correlates the molecular architecture and dosage of PCE with its potential to influence C_3S hydration kinetics. Such correlation is of significance for practical applications as it can be used as a robust, quantitative basis to compare and rank PCEs on the bases of their potential to suppress C_3S hydration rates, and to select optimum ones based on the type/nature of the application.

2. MATERIALS AND METHODS

2.1. MATERIALS

Triclinic C_3S (T_1-Ca_3SiO_5) was synthesized by following a high-temperature synthesis route using phase-pure precursor materials. Calcium oxide (CaO), the residual material left after calcite ($CaCO_3$) decomposition, was mixed with silica (SiO_2, α-quartz) in stoichiometric proportion ($CaO:SiO_2 = 3:1$), and pelletized at high pressure of 100 MPa. The pellets were then thermally treated in a furnace for 12 h at 1600°C in platinum receptacles, and subsequently air-quenched [37,38]. The sintered pellets were subsequently crushed with mortar and pestle, and ground in a ball mill for 24 h. The resulting powder was analyzed via X-ray diffraction (Panalytical X'Pert Pro MPD, Spectris; PDF Card #: 01-086-0402) and was determined to be C_3S powder containing $\approx$ 0.80% ± 0.20% residual CaO by mass by Rietveld analysis using RIQAS software (Materials Data, Inc.). The particle size distribution (PSD: Figure 1a) of C_3S was measured using static light scattering analyzer (Microtrac S3500) [39]; the median particle size (d_{50}, μm) of C_3S particulates was determined as 7.78 μm. By combining the

PSD of C_3S with its density (i.e., 3150 kg. m^{-3}), the specific surface area (SSA_{C3S}) of C_3S particulates was calculated as 562 m^2. kg^{-1}.

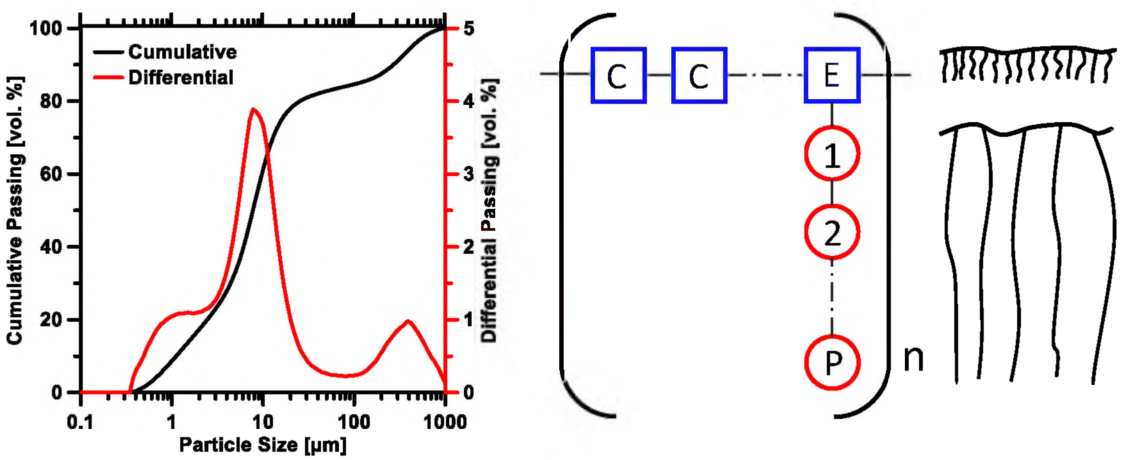

(a) (b)

Figure 1. (a) The cumulative (primary y-axis) and differential (secondary y-axis) particle size distribution (PSD) of C_3S. The largest relative uncertainty in the median diameter (d_{50}, µm) of C_3S, based on six replicate measurements, was on the order of ±6%. (b) Schematic representation of the comb-shaped architecture of PCE, wherein n is the number of repeating units, P is the side chain length, and C/E represents the carboxylate-to-ether ratio.

Three different – commercially-available – polymeric, comb-shaped, PCEs (with solid mass contents of 30%) were used in this study (Figure 1b). All three PCEs belong to the same polymer family – consisting of polymethacrylic backbone, grafted with polyethylene oxide side chains – albeit their molecular architectures are different. The different PCEs are subsequently referred to as PCE-1, PCE-2, and PCE-3. The molar mass distributions and the absolute molar masses of the PCEs were determined via size exclusion chromatography (SEC) and size exclusion multi-angle light scattering (SEC-MALS; Agilent 1260 Infinity System), respectively. Details pertaining to the PCEs' molecular architecture, as determined from SEC-MALS, high-performance liquid chromatography (HPLC) and potentiometric titration techniques [23,40], are listed in Table 1.

Table 1. Architectural parameters of the three PCEs – as determined from multi-detection size exclusion chromatography (SEC), high-performance liquid chromatography (HPLC), and potentiometric titration techniques [23,40]. Here, C/E (unitless) is the ratio of the number of carboxylate functional groups to the number of ester functional groups, P (unitless) is the number of ethylene oxide monomers per side chain, n (unitless) is the number of side chains per PCE backbone (or the number of repeating units), and M_w (g. mol^{-1}) is the calculated molecular weight. M_w is equal to [n. {P. $M_{w,SC}$ + (C/E +1). $M_{w,BB}$}] – wherein, $M_{w,SC}$ (g. mol^{-1}) and $M_{w,BB}$ (g. mol^{-1}) are the molecular weights of the side chain and backbone, respectively [23,25]. The nomenclature of the architectural parameters of PCEs was adapted from previous studies [18,23,41].

PCE #	C/E	P	N	M_w
PCE-1	1.80	23	20.05	25145.07
PCE-2	2.10	23	18.10	23166.84
PCE-3	5.20	17	9.35	11990.65

2.2. METHODS

2.2.1. Experimental Methods. Pastes were prepared by mixing deionized-water (DI-water) and C_3S at a constant liquid-to-solid mass ratio (l/s) of 0.45. To describe the role of PCE on C_3S hydration kinetics, the three different PCEs (i.e., PCE-1, PCE-2, and PCE-3, described in Table 1) were added to the pastes at dosages (C_{PCE}) of 0.000%, 0.625%, 1.250%, 1.875%, and 2.500% (by mass of C_3S). It is pointed out that these dosages signify the total (i.e., solid + liquid) mass of the PCE. Based on the liquid content of the PCE (i.e., ≈30%$_{mass}$ of all PCEs), the aforementioned dosages would amount to 0.000%, 0.188%, 0.375%, 0.563%, and 0.750% of the solid component of the

PCE per unit mass of the binder. The upper bound of dosage, that is, 2.500%, was determined by saturation point test [28,42] for PCE-1 (with respect to cement paste), and is representative of dosages used in high-performance concretes [16]. The lower dosages of PCE correspond to 25%, 50%, and 75% of the upper bound, respectively. For provision of PCE into the paste, the mixing-protocol involved mixing of DI-water and PCE for 20 seconds, followed by an additional minute of mixing with C_3S. For experiments where the upper bound of PCE dosage was employed, PCE was also deployed in delayed mode. Specifically, in delayed mode, a 5-minute period, from when the DI-water first came into contact with C_3S, was allowed to elapse before PCE was introduced to the paste. Here, prior to the addition of PCE, the paste was mixed for 1 minute, and for another 20 seconds after PCE was added – thus, following the same mixing protocol used for immediate addition of PCE.

C_3S hydration kinetics in pastes containing approximately 1 gram of anhydrous C_3S was monitored for a minimum of 72 h (144 h experiment times were required for pastes containing PCE-3), at a constant temperature of 20°C ± 0.01°C, using a TAM IV isothermal microcalorimeter. Microcalorimetry techniques are able to monitor heat evolution, resulting from a chemical reaction, at a high resolution (10^{-8} J. s^{-1}). The differential and cumulative heat evolution profiles were divided (or normalized) by the enthalpy of C_3S hydration [1,38], that is, 484 J. g_{C3S}^{-1}, to determine the rate of hydration ($d\alpha/dt$, units of h^{-1}) and the degree of hydration (α, reaction mass fraction of C_3S) of C_3S, respectively, as functions of time. The values of α and $d\alpha/dt$ calculated in such manner are premised on the assumption that the heat release, determined from microcalorimetry methods, is exclusively due to C_3S hydration. In the context of experiments conducted in this study, the aforementioned assumption is reasonable because the heat release associated with physical and chemical interactions between PCE and C_3S paste components is minuscule compared to heat released from the hydration of C_3S [28,43]. A thermogravimetric analyzer (TGA, SDT600) was used for identification and quantification of phases present in the binder after 24 h of hydration. Hydration was stopped by crushing the hydrated pastes, into small grains, immersing them in isopropanol for 24 h [44], followed by drying in the oven (T = 85°C) for an additional 24 h. The samples were then ground into fine powder. The powder samples were heated in an inert atmosphere of N_2 over a temperature range of 30 – 900°C. The cumulative and differential mass loss traces were used to quantify the amount of CH present in the system; towards this, well-established methods detailed in prior studies [44,45] were used.

2.2.2. Phase Boundary Nucleation and Growth (pBNG) Model. A modified phase boundary nucleation and growth (pBNG) model is applied to describe the influence of PCE on early-age hydration kinetics of C_3S. Akin to classical pBNG models applied to cementitious systems [6,10,11,46–49], the model used herein assumes that a single product of constant density forms heterogeneously on solid-phase substrate boundaries (i.e., C_3S particles' surfaces) at a given nucleation event (i.e., at time = τ h), and assumes that its subsequent growth drives and controls – as the rate controlling mechanism – the kinetics of C_3S hydration. This assumption – typically termed as *site saturation* – entails that after the initial burst of nucleation, no further nuclei of the product form. As per these criteria, the volume fraction of the product within the paste [$X(t)$, unitless] is given by Equation 1 [14,28,36,38,46,50].

$$X(t) = 1 - exp\left[-2k_G\cdot(t\text{-}\tau).\ \left(1\text{-}\frac{F_D[k_s\cdot(t\text{-}\tau)]}{k_s\cdot(t\text{-}\tau)}\right)\right] \tag{1}$$

$$\text{where,}\qquad F_D(x) = exp(-x^2)\int_0^x exp(y^2)\,dy \tag{2}$$

In Equation 1, F_D represents the f-Dawson function shown as the integral in Equation 2. The parameter k_s (h^{-1}) represents the inverse of time needed by the product to completely cover the surface of the anhydrous C_3S particles [10,46] (Equation 3). Its value depends on the nucleation density of the product ($I_{density}$, μm^{-2}), that is, the number of product nuclei per unit surface area of C_3S particulates, as well as the product's growth rate and geometry. In this study, it is assumed that the growth of the product occurs in an anisotropic manner, while varying with respect to time. The growth rates in the outward (i.e., normal to and away from C_3S particles' surface) and lateral (i.e., parallel to the C_3S particles' surface boundary) directions are represented as $G_{out}(t)$ and $G_{par}(t)$, respectively. Along the two-dimensional plane parallel to the C_3S surface, $G_{par}(t)$ is assumed to be isotropic [10,28,36]. It is worth noting that such temporal variation of the product growth rate is a departure from classical pBNG models – wherein, throughout the entire duration of hydration, the growth rate is assumed to remain constant. This implementation of variable product growth rate – based on the original study of Bullard et al. [50], and subsequently adopted by several researchers [14,28,36,38] – captures the sharp changes in C-S-H's growth rate as its supersaturation in the solution varies in a highly non-linear fashion with time. While G_{out} and G_{par} vary with time, a ratio of 1:0.50 for G_{out}:G_{par} is maintained; as such, the anisotropy factor [i.e., g (unitless), shown in Equation 4] of the product nuclei, remains constant at 0.25 throughout the entirety of C_3S hydration measured via microcalorimetry. This relationship between G_{out} and G_{par} causes the product to acquire needle-like geometry [10,46] – essentially mimicking needle- or fiber-like geometry of C-S-H observed experimentally at early ages [51,52].

$$k_s = G_{out}(t).\ (\pi.g.I_{density})^{\frac{1}{2}} \tag{3}$$

$$g = \left[\frac{G_{par}(t)}{G_{out}\ (t)}\right]^2 \tag{4}$$

$$k_G = r_G.G_{out}(t).a_{BV} \tag{5}$$

In Equation 1, the parameter k_G (h^{-1}) represents the inverse of time required for occupation of the capillary pore volume by the product. k_G is a function of G_{out}, and another constant r_G (unitless); here, r_G (Equation 5) represents the ratio of product growth rate into vis-à-vis out of the substrate in the direction normal to the substrate. In previous studies [10,46], focused on early age hydration of cement (and C_3S), it has been reported that hydrates do not penetrate the anhydrous particles, and, therefore, $r_G \approx 0.50$. As simulations presented in the current study pertain to early ages, the value of r_G is assumed to be constant at 0.50. The value of k_G, and thus kinetics of C_3S hydration, also depend on the boundary area of the substrate per unit volume of the paste (a_{BV}, μm^{-1}) (Equation 6). The paste's volume is simply the initial cumulative volume of the paste (i.e., volumes of C_3S and water), and the substrate's area is the initial surface area of C_3S particles that is available for nucleation of product. In Equation 6, SSA_{C3S} (units of $m^2.\ kg^{-1}$) is the specific surface area of C_3S particles, ρ_W is the density of water (i.e., 1000 kg. m^{-3}) and ρ_{C3S} is the density of C_3S (i.e., 3150 kg. m^{-3}). By combining SSA_{C3S} and $I_{density}$, the total number of supercritical product nuclei (N_{nuc}, unit of g_{C3S}^{-1}) produced per gram of C_3S can be calculated [36,47,49,53] (Equation 7).

$$a_{BV} = \left[\frac{SSA_{C_3S}}{\left\{ \frac{\frac{l}{s}}{\rho_W} + \frac{1}{\rho_{C_3S}} \right\}} \right] \tag{6}$$

$$N_{nuc} = SSA_{C3S}.\, I_{density} \tag{7}$$

The fraction of the paste' volume occupied by the product [$X(t)$], as calculated from Eq. 1, and the degree of hydration (α) of C_3S are linked by yet another constant, B (unitless) [28,38,50], as shown in Eqs. 8-9:

$$\alpha(t) = B.X(t) \tag{8}$$

$$B = \left[\left(\frac{\frac{\rho_{C_3S}}{\rho_{products}}}{\frac{\frac{l}{s} \cdot \rho_{C_3S}}{\rho_{water}} + 1} \right) \left(\frac{c + \frac{1}{\rho_{C_3S}} - \frac{1}{\rho_{water}}}{\frac{1}{\rho_{product}} - \frac{1}{\rho_{water}}} \right) \right]^{-1} \tag{9}$$

where, $\rho_{product}$ is the average wet density of hydrates (assumed to be 2070 kg. m^{-3}, based on the stoichiometric ratio of formation and individual densities of the two hydrates, C-S-H and CH) [3,54], and the parameter $c = -7.04 \times 10^{-5}$ m^3. kg^{-1} stands for the chemical shrinkage of the paste that occurs when 1 kg of C_3S is fully hydrated [38,50,55].

Based on the above equations (i.e., Equations 1-9), to numerically reproduce the experimentally-derived reaction rates, the variables that need to be ascertained are: G_{out} (t) and $I_{density}$. Of these two variables, $G_{out}(t)$ is a function of time, whereas $I_{density}$ is constant (with respect to time). For a given system, to determine the optimum functional form of G_{out} and the optimum value of $I_{density}$ and, a Nelder-Mead based simplex algorithm [38,56,57], based on non-linear optimization and derivative-free routines, is implemented in two steps. In the first step, the value of G_{out} is kept constant at 0.075 µm.

h^{-1} – a value derived from microscopy-based analyses of early age C-S-H growth in C_3S and similar systems [51,52,58]. The algorithm varies the values of $I_{density}$ within predefined bounds (i.e., 0.01-to-100 μm. h^{-1}) until the deviation between measured and simulated rates of reaction ($d\alpha/dt$) is minimalized. It is worth highlighting that up to the first simulation step, the model represents the conventional pBNG formulation [11] – wherein the anisotropic growth of product, several nuclei of which precipitate at a virtual time τ (h), is assumed to be constant. To factor in the temporal variation in product growth rate, the second and final simulation step is employed. In this step, at a given time t, the optimum value of $I_{density}$, determined from the first step, is used as constant, whereas G_{out} is iteratively varied between 10^{-5} and 10^{3} μm. h^{-1}. At convergence, that is, when the deviation between the simulated and measured reaction rates reaches its minimum (i.e., within 0.05%), the value of G_{out} yielded by the optimization process is finalized as the optimum. By implementing the optimization process over a minimum of 72 h of hydration, using a time step of 0.01 h, the optimum values of G_{out} for the entire duration of C_3S hydration are thus determined. The functional form of G_{out}, obtained from the optimization routine, mimics the product's non-monotonic and non-linear evolution of growth rate as a function of its supersaturation in the solution. In prior publications [14,28,36,38,50], which employ similar simulation scheme, it has been shown that such functional form of the product growth rate – as obtained from the simulations – reproduced the intrinsic changes in the evolution of the solution's chemistry (e.g., changes in pH, ionic strength, and water activity). Therefore, whereas this scheme of deriving the functional form of the product growth rate is indirect, the final results are still reflective of the physical processes occurring in the system [14,38,50,52,58].

3. RESULTS AND DISCUSSION

Figure 2 shows representative heat evolution profiles of C_3S pastes provisioned with PCE-1 at different dosages (i.e., 0 – 2.5%).

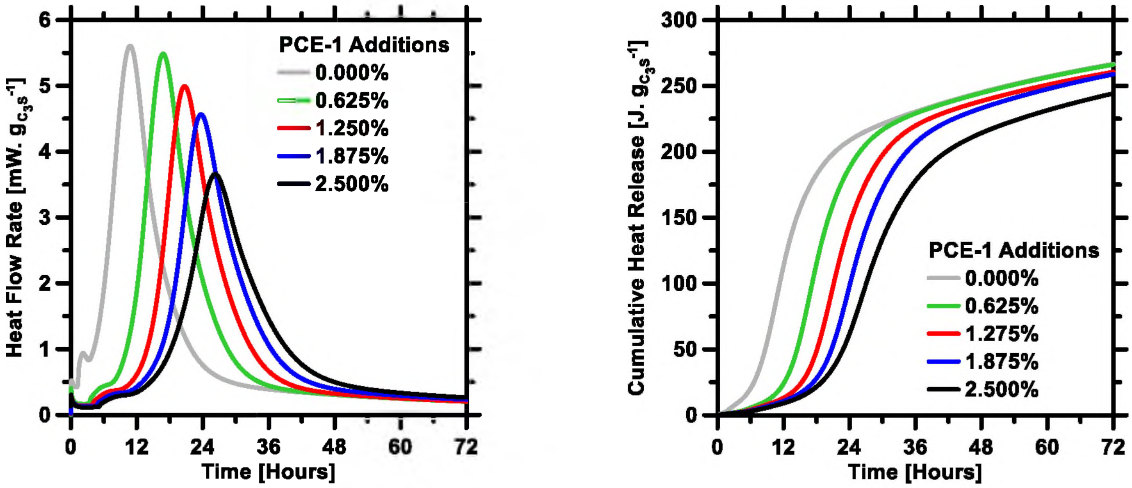

(a) (b)

Figure 2. Isothermal microcalorimetry based determinations of time-dependent (a) heat flow rate and (b) cumulative heat release of C_3S pastes provisioned with PCE-1 at different dosages (C_{PCE}). The l/s for pastes included in these figures, as well as the subsequent ones, is 0.45. The uncertainty in measured heat flow rate at the main hydration peak is ±2%.

As can be seen, PCE significantly suppresses C_3S hydration rates, as marked by various characteristic aspects of the pastes' heat evolution profiles that is, lengthening of the induction period (the period between the initial wetting peak and the onset of acceleration), rightward shift of the heat evolution curves, and reduced heat flow rates at the main hydration peak. The deceleration induced by PCE increases monotonically with its dosage, which entails good correlation between amount of PCE present in the paste and the resultant suppression of C_3S hydration rates. This correlation is indicative of inhibition of C_3S dissolution sites (thus causing prolongation of the induction period), and C-S-H nucleation sites (thus causing slower approach to the main hydration peak) – both of which most likely manifest as a result of adsorption of PCE molecules on C_3S particles' surfaces, and scale with PCE dosage [22,25–28]. It is worth pointing out that provision of PCE in the paste decelerates not only the approach to the main hydration peak but also the departure from it (i.e., lower slope of the deceleration regime, as shown in Figure 2a). Slower post-peak deceleration in [C_3S + PCE] pastes implies that, at later ages, the rate of hydration of C_3S in such pastes is relatively faster than in the control system (i.e., [C_3S + 0% PCE] paste); as such, much of the loss in early-age reactivity, that is induced by PCE, is recouped at later ages. This is better shown in Figure 2b, wherein, at later ages (i.e., ≈ 72 h), the cumulative heat release of [C_3S + PCE] pastes converge – or, appear to be on track to converge – with that of the control system.

Results shown in Figure 2, and the above discussion, describe the role of PCE dosage on C_3S hydration rates. To better understand the role of PCE's molecular architecture on C_3S hydration kinetics, heat evolution profiles of [C_3S + PCE] pastes, prepared with equivalent dosages but different types of PCE, were compared (Figure 3).

It is evident that regardless of the molecular architecture, all three PCEs suppress C_3S hydration at early ages (Figure 3a). In addition to the pre-peak deceleration (e.g., slower approach to the main hydration peak), the slower deceleration beyond the main hydration peak – resulting in convergence (or, in case of PCE-3, a trajectory that would eventually result in convergence) of cumulative heat release at later ages – is common among the three PCEs. While, qualitatively, the general nature of hydration suppression is similar amongst the three PCEs, there are substantial differences in the magnitude of such decelerations. As can be seen in Figure 3, C_3S hydration is significantly more suppressed by PCE-3 as compared to PCE-1 and PCE-2; the latter two produce similar magnitudes of suppression. Although the results shown in Figure 3 pertain to a single PCE dosage (i.e., 1.25%), the stark difference – between the magnitude of deceleration of C_3S hydration kinetics induced by PCE-3 vis-à-vis those by PCE-1 and PCE-2 – was also observed at other dosages. Since all PCEs belong to the same polymer family (i.e., same composition of backbone and side chains), it is clear that the differences (or similarities) in their potential to suppress C_3S hydration arise due to intrinsic differences (or similarities) in their molecular architecture – which, in turn, most likely dictates their adsorption capacity, and, thus, their ability to inhibit sites of C_3S dissolution and C-S-H nucleation. As PCE-3 has the highest potential to suppress C_3S hydration, it is speculated that its molecular architecture is more favorable towards adsorption on C_3S particles' surfaces. Along the same lines, as PCE-1 and PCE-2 produce equivalent deceleration at equivalent dosages, it is expected that their molecular architectures, and thus their adsorption potentials, are most likely broadly similar. Further details pertaining to the role of PCE's molecular architecture on C_3S hydration suppression are discussed later in this section.

To better contrast the suppression of C_3S hydration as prompted by the three PCEs, characteristic calorimetric parameters, that is, inverse of time corresponding to the main hydration peak (h^{-1}), heat flow rate at the main hydration peak ($mW. g_{C3S}^{-1}$), and slope of the acceleration regime ($mW. g_{C3S}^{-1}. h^{-1}$) – indicative of acceleration or retardation in hydration kinetics [28,36,47,59,60] – were extracted and plotted against the PCE dosage (Figure 4).

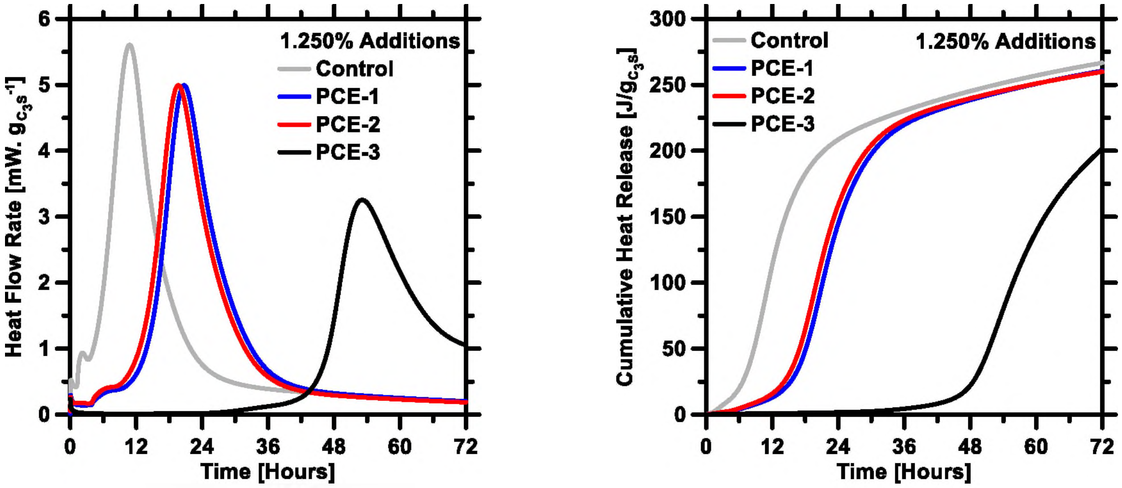

(a) (b)

Figure 3. Isothermal microcalorimetry based determinations of time-dependent (a) heat flow rate and (b) cumulative heat release of C_3S pastes provisioned with different PCEs (i.e., PCE-1, PCE-2, and PCE-3) at equivalent dosage (C_{PCE}) of 1.25%.

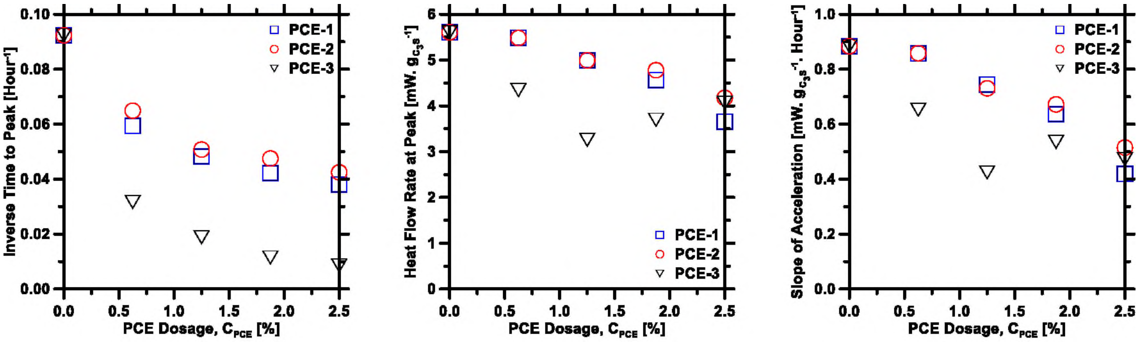

(a) (b) (c)

Figure 4. The calorimetric parameters: (a) inverse of time to the main hydration peak, (b) heat flow rate at the main hydration peak, and (c) slope of the acceleration regime, extracted from heat evolution profiles, and plotted against PCE dosage. For a given system, the uncertainty in each calorimetric parameter is ±2%.

As can be seen, with increasing PCE dosage, the induction period's length increases (Figure 2); this increases the delay in incidence of the main hydration peak (Figure 4a). This indicates that interactions between PCE and C_3S delay the hydrate nucleation event (i.e., massive precipitation of hydrates, which occurs around the time when the induction period terminates) [2,12,28,61]. These results are in good agreement with prior studies [20,25,27,28], which have reported that the adsorption of PCE molecules on C_3S particles' surfaces blocks C_3S dissolution sites, which, in turn, causes deceleration of C_3S dissolution rate and – as a consequence – prolongs the induction period. Akin to the trends in (inverse of) time of the main hydration peak, the other two calorimetric parameters – heat flow rate at the peak and slope of the acceleration regime – also decrease progressively with increasing amount of PCE in the paste (Figures 4b-4c). These results suggest that PCE not only delays the time of product nucleation but also suppresses the product's post-nucleation precipitation rate – as can also be seen in Figures 2 and 3. Past literature [27,28] suggests that such delay occurs due to interactions between PCE and C-S-H nuclei. More specifically, the adsorption of PCE molecules (i.e., those that are not adsorbed on C_3S particles' surfaces and still remain in the solution) on positively charged C-S-H nuclei most probably partially blocks their access to the contiguous solution, and, thus, diminishes their growth rate (and, hence, their precipitation rate). Furthermore, as PCE molecules remain adsorbed on C-S-H surfaces, the aforementioned inhibition of C-S-H's growth persists even at later stages of hydration. This is better revealed in Figures 2a and 3a, wherein it is shown that the post-peak deceleration of [C_3S + PCE] paste is slower than in the control paste; as such, the cumulative heat release of [C_3S + PCE] pastes progress toward convergence with control system at later ages (Figures 2b and 3b).

The equivalency in calorimetric parameters of pastes prepared with PCE-1 and PCE-2 (Figure 4) suggests that the decelerating effects of the two PCEs are broadly similar. Such similarity in decelerating effects of PCE-1 and PCE-2 is corroborated in Figure 5, which shows that in [C_3S + PCE-1] and [C_3S + PCE-2] pastes – when prepared with equivalent dosage of PCE – the degree of hydration of C_3S (α) and portlandite (CH) contents at 24 h are similar.

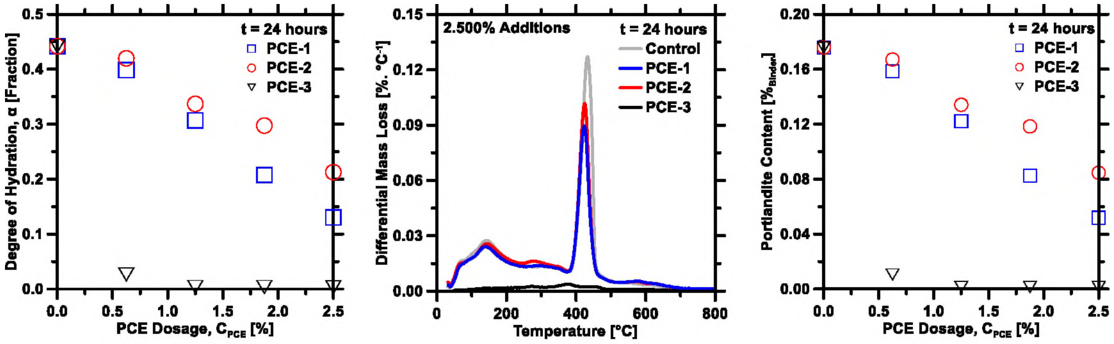

(a) (b) (c)

Figure 5. (a) Isothermal microcalorimetry based determinations of time-dependent degree of reaction (α) of C_3S, (b) DTG traces showing differential mass loss profiles, and (c) mass contents of portlandite (CH: as $\%_{mass}$ of the binder) as determined from analyses of DTG traces, in [C_3S + PCE] pastes at 24 h. The highest uncertainty in phase quantifications by DTG is ±2.5%.

These results are not surprising because PCE-1 and PCE-2 have similar, but slightly different molecular architectures – with similar values of C/E, n, P, and M_w (see Table 1) – and, thus, are expected to have similar potentials to adsorb on silicate (i.e., C_3S and C-S-H) surfaces and similar capacities to block their access to the contiguous solution. Comparisons between PCE-1/PCE-2 and PCE-3 are, however, not trivial because of significant differences in their molecular architectures (Table 1) as well as their abilities to suppress C_3S hydration (Figure 4). As can be seen in Figure 5, at a given dosage, deceleration induced by PCE-3 is considerably more severe (i.e., lower α and lower CH content at 24 h) as compared to those induced by PCE -1 and PCE-2. As the C/E of PCE-3 is significantly larger (i.e., $C/E = 5.20$) as compared to those of PCE-1 and PCE-2 (i.e., $C/E = 1.80$ and 2.10), it can be said that the lower side chain grafting density of PCE-3 permits a higher negative charge on the backbone, and, thus, improved adsorption onto positively charged silicate surfaces[18,29–31]; this manifests as greater deceleration in [C_3S + PCE-3] pastes. Furthermore, the length of the side chain (i.e., given by P) of PCE-3 is shorter (i.e., $P = 17$) than those of PCE-1 and PCE-2 (i.e., $P = 23$). As prior studies [20,32] have indicated, smaller side chains ensure that access to the negative charges on the PCE's backbone is not hindered or limited by steric hindrance (induced by the side chains); this enables better adsorption of PCE molecules onto silicate surfaces, thus resulting in superior deceleration. Lastly, on account of lower side chain grafting density, shorter side chain length, and smaller number of repeating units (i.e., n), the overall molecular weight of PCE-3 is lower (i.e., $M_w = 11990$ g. mol^{-1}) than PCE-1 and PCE-2 (i.e., $M_w = 25145$ and 23166 g. mol^{-1}). This entails that for a given (mass-based) dosage, the number of PCE-3 molecules in the paste is higher than those prepared with PCE-1 or PCE-2. On account of their larger population in the paste, PCE-3 molecules are able to adsorb more effectively on C_3S and C-S-H surfaces, and, thus, suppress C_3S hydration to a greater extent as compared to the other two PCEs.

The discussion in the above paragraph provides a basis – albeit qualitative – for explaining the links between molecular architecture of PCE and its ability to suppress C_3S hydration. However, through such qualitative basis, it is not possible to quantify the superiority of a given PCE – in terms of inducing deceleration of C_3S hydration kinetics – as compared to another PCE of a different molecular architecture. For example, while it is known that higher and lower values of C/E and P, respectively, cause superior suppression of C_3S hydration, such knowledge does not allow quantitative prediction of how much more deceleration a PCE (say, with higher C/E and lower P compared to another PCE) will induce compared to another. In a recent paper, Marchon et al. [41] suggested that the net deceleration of C_3S (or cement) hydration kinetics induced by PCE is proportional to: (i) the concentration of PCE molecules – expressed as the ratio of its dosage in paste (C_{PCE}: expressed as $\%_{mass}$) to its molecular weight (M_w) – and (ii) a function (f) of C/E, shown in Equation 10. The former proportionality (i.e., with respect to PCE concentration) is expected because larger number of PCE molecules in the paste would entail greater probability of their adsorption on silicate (i.e., C_3S and C-S-H) surfaces, and, therefore, greater deceleration. It is worth noting that PCE concentration inherently incorporates the effects of dosage and architectural parameters of PCE (i.e., n, P, C/E, and molecular weights of the side chain and backbone – as shown in Table 1 and described in [23,25]), and, therefore, serves as an encompassing parameter on its own. The latter proportionality (i.e., with respect to $f(C/E)$) captures the dependency of adsorption potential of PCE on the strength of electric field induced by its molecules on the adsorbent's surface. As described in prior publications [23,41,62], higher value of $f(C/E)$ implies greater magnitude, better exposure, and wider distribution of electric field induced by the PCE, and, therefore, better adsorption of its negatively charged backbone on the positively charged silicate surfaces. Marchon et al. [41] proposed that the overall deceleration of C_3S (or cement) hydration kinetics, as induced by a given PCE, could be quantified by consolidating the aforementioned proportionalities into a composite architectural parameter (P_{PCE}: expressed in arbitrary units), as shown in Equation 11. Marchon et al. [41] originally defined P_{PCE} by the molar mass of the repeating unit. However, Equation 11 includes the molecular weight in the expression to create a more descriptive parameter. By considering the molecular weight of (M_w) an entire PCE molecule in the expression, P_{PCE} can be applied to PCEs with varying backbone lengths. In Equation 11, the variables (i.e., C_{PCE}, C/E and M_w) are expressed in their typical units as described in the Experimental Section.

$$f(C/E) = \left(\frac{C/E}{C/E + 1}\right)^{\frac{3}{2}} \tag{10}$$

$$\text{Composite Architectural Parameter } (P_{PCE}) = \frac{c_{PCE}}{M_w} f(C/E) = \frac{c_{PCE}}{M_w} \left(\frac{C/E}{C/E + 1}\right)^{\frac{3}{2}} \tag{11}$$

To test the efficacy of Equation 11, in terms of predicting the deceleration caused by PCE, the calorimetric parameters – which capture alterations in C_3S hydration kinetics (as shown in Figure 4) – were plotted against the composite architectural parameter (P_{PCE}) of PCE. As can be seen in Figure 6, in spite of substantial differences in dosages and molecular architectures of PCEs, each calorimetric parameter – extracted from heat evolution profiles of different pastes – converges, broadly, into a unified master trend.

Admittedly, the datapoints of two of the calorimetric parameters, i.e., peak heat flow rate (Figure 6b) and slope of the acceleration regime (Figure 6c), are not as convergent as in the case of inverse of time to peak (Figure 6a). These minor deviations – from the unified master trend – can be attributed to errors associated with the experimentally-determined parameters (e.g., PCE architectural parameters such as C/E, and calorimetric parameters). In spite of the aforementioned deviations, in general, it can be said that the deceleration of C_3S hydration kinetics increases, broadly in a logarithmic manner, with respect to increasing values of the composite architectural parameter (P_{PCE}) of PCE. This correlation suggests that Equation 11 can be used as a robust, quantitative basis to compare and rank PCEs on the basis of their potential to suppress C_3S hydration rates. Equation 11 also allows prediction of additional (or reduction in) deceleration – with respect to a benchmark system – if the PCE's dosage or molecular architecture are altered. As an example, if deceleration of C_3S hydration caused by a given PCE is measured (e.g., using calorimetry), additional retardation at a higher dosage of the same PCE (or, a different PCE) can be readily predicted by plugging in the PCE dosage (or, architectural parameters) in Equation 11.

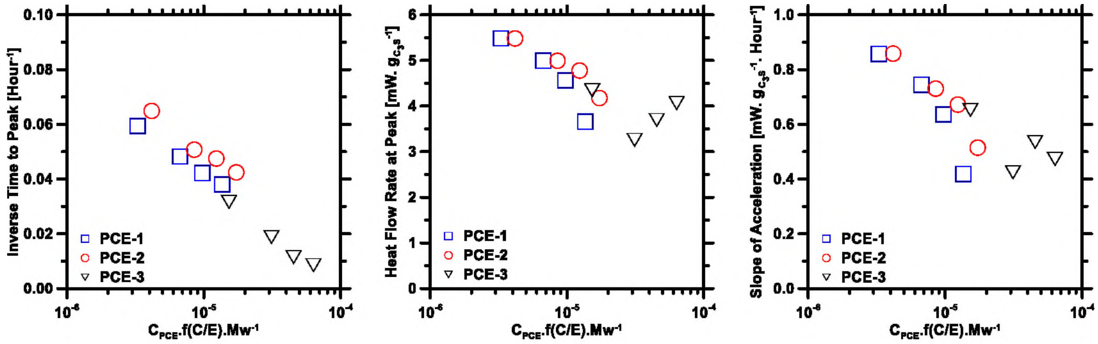

(a) (b) (c)

Figure 6. The calorimetric parameters: (a) inverse of time to the main hydration peak, (b) heat flow rate at the main hydration peak, and (c) slope of the acceleration regime extracted from the calorimetry profiles, and plotted against the composite architectural parameter of the PCE (P_{PCE}: calculated using Equation 11). The uncertainty in the value of P_{PCE} is on the order of ±15%.

The experimental results discussed thus far shed light on the effects of PCE dosage and molecular architecture on the overall hydration kinetics of C_3S. To better understand such effects, specifically in the context of alterations in nucleation and growth of the main hydrate (i.e., C-S-H), the pBNG model was applied. Figure 7 shows the simulated reaction rates of pastes compared against those obtained from experiments.

As can be seen, through optimization of the outward growth rate of the product [$G_{out}(t)$] and the product nucleation density ($I_{density}$), the experimental results are well reproduced by the model. Variations in these simulation parameters are investigated below to delineate the mechanistic origins of modifications in the nucleation and growth process in relation to PCE's molecular architecture and dosage.

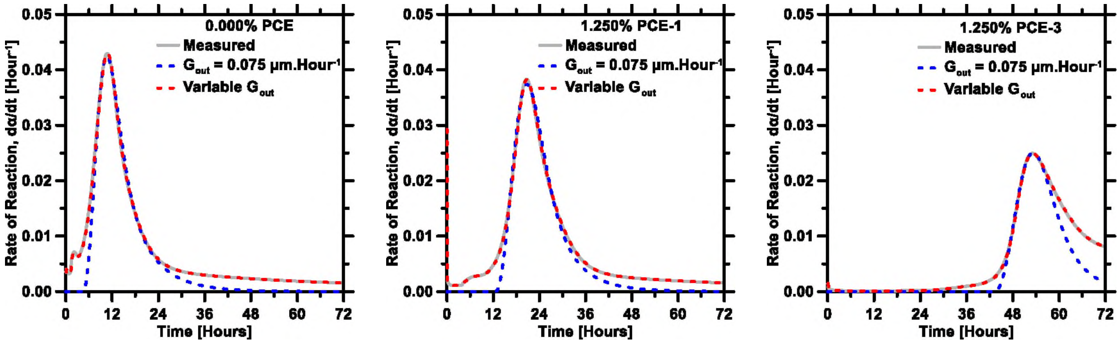

(a) (b) (c)

Figure 7. Representative set of simulated and measured reaction rates (dα/dt; primary y-axis) and degree of reaction (α; secondary y-axis) for C_3S pastes prepared with varying PCE architectures and dosages of: (a) 0.000% PCE, (b) 1.250% PCE-1, and (c) 1.250% PCE-3. Simulations are deterministic, and, therefore, there is no uncertainty associated with them.

Based on optimization of parameters by the pBNG model, it was found that PCE has profound effect on the hydrate nucleation event, which occurs at early ages, that is, in proximity to the time of termination of the induction period. As can be seen in Figure 8a, the product nucleation density decreases monotonically with increasing PCE dosage.

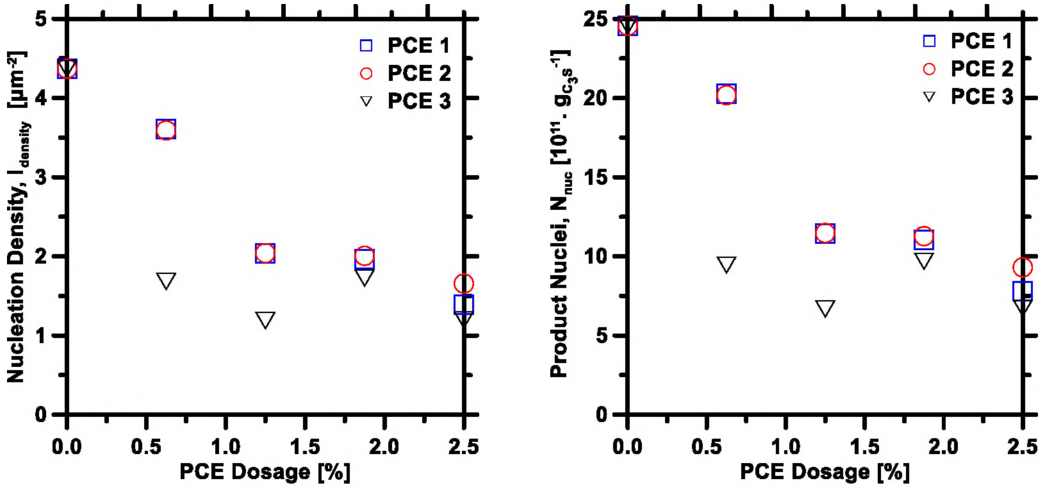

(a) (b)

Figure 8. Parameters derived from pBNG simulations: (a) nucleation density of the product ($I_{density}$), and (b) total number of super product nuclei formed per gram of C_3S (N_{nuc}: calculated from Equation 7), plotted against PCE dosage (C_{PCE}). Simulations are deterministic, and, therefore, there is no uncertainty associated with them.

This manifests as a progressive decline in the number of supercritical product nuclei (N_{nuc}: calculated from Equation 7) – forming heterogeneously on C_3S surfaces – with respect to increasing PCE dosages (Figure 8b). These results corroborate the hypotheses presented above, as well as those advanced in previous studies [27,28] – that the adsorption of PCE molecules on C_3S surfaces most likely does not only blocks C_3S dissolution sites but also inhibits topographical sites of C-S-H nucleation. As would be expected, at higher PCE dosages, larger fraction of C_3S particles' surface is blocked, and, thus, a greater number of C-S-H nucleation sites are inhibited. It is interesting to note that at any given dosage, PCE-3 results in lower product nucleation density (Figure 8a) – and, therefore, smaller number of product nuclei (Figure 8b) – as compared to the other two PCEs. These results are in very good agreement with the trends derived directly from the experiments (Figure 4), and support the above analyses suggesting that the adsorption capacity – and, therefore, the potential to suppress C-S-H nucleation (and C_3S hydration)

– of PCE-3 is superior. As stated previously, the superior deceleration induced by PCE-3 can be attributed to its intrinsic molecular architecture – more specifically, its lower side chain grafting density (i.e., higher C/E), smaller side chain length (i.e., lower P), and lower molecular weight (i.e., M_w) – which enables better adsorption of its molecules onto C_3S surfaces, and, therefore, more effective blocking of topographical C-S-H nucleation sites.

Earlier in this section, it was shown that the composite architectural parameter of PCE (P_{PCE}: calculated using Equation 11) correlated very well with the resultant deceleration of C_3S hydration (Figure 5). To further verify the applicability of the composite parameter – in terms of capturing the combined effects of PCE dosage and molecular architecture – the product nucleation density and the number of product nuclei were plotted against P_{PCE}. As can be seen in Figure 9, akin to the calorimetric parameters (Figure 5), each pBNG parameter (i.e., $I_{density}$ and N_{nuc}) converges onto a unified master trend; wherein, with increasing values of P_{PCE}, both $I_{density}$ and N_{nuc} decrease monotonically.

It is clarified that the master trends, which emerge in Figure 9, are not devoid of deviations; these deviations are, however, minor, and can be attributed to the statistical variance in the experimentally-derived parameters (e.g., C/E of PCE). Notwithstanding, these results – in conjunction with those shown in Figure 5 – provide compelling evidence that the composite architectural parameter of PCE (P_{PCE}) is a reliable, and more importantly, a readily quantifiable indicator of the PCE's potential to suppress C_3S hydration.

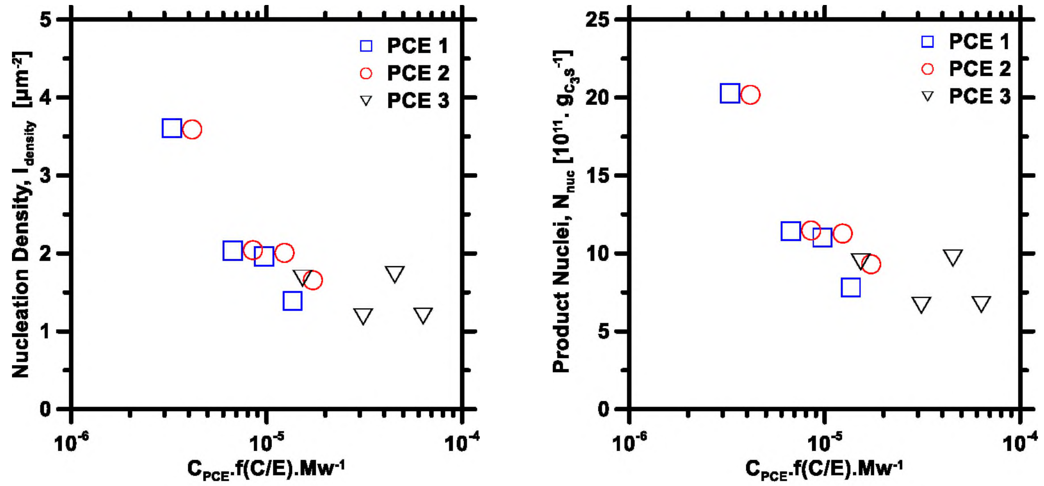

(a) (b)

Figure 9. Parameters derived from pBNG simulations: (a) nucleation density of the product ($I_{density}$), and (b) total number of super product nuclei formed per gram of C_3S (N_{nuc}), plotted against the composite architectural parameter of PCE (P_{PCE}: calculated from Equation 11).

Finally, the product's outward growth rate [G_{out} (t)], as obtained from pBNG simulations, are shown in Figure 10. As can be seen, G_{out} decreases by about three orders of magnitude – while evolving in a highly non-linear manner with respect to time – over the course of C_3S hydration within the first 72 h. Such temporal evolution of the growth rate has been reported [28,36,38,50] to mimic the time-dependent evolution of C-S-H supersaturation in the solution. It is noted that at any given time, G_{out} – particularly between ages of 1 h and 24 h – is lower at higher PCE dosages (Figure 10a). Also, at equivalent dosages, G_{out} is lower in pastes prepared with PCE-3 as compared to those prepared with PCE-1 and PCE-2. To better contrast the influence of the different PCEs, values of G_{out} were extracted at different times, i.e., at 12 h (early age), and at t = 72 h (later age), and, ultimately, plotted against the PCE dosage. As can be seen in Figure 11a, at early ages, G_{out} in [C_3S + PCE] pastes is consistently lower than in control pastes.

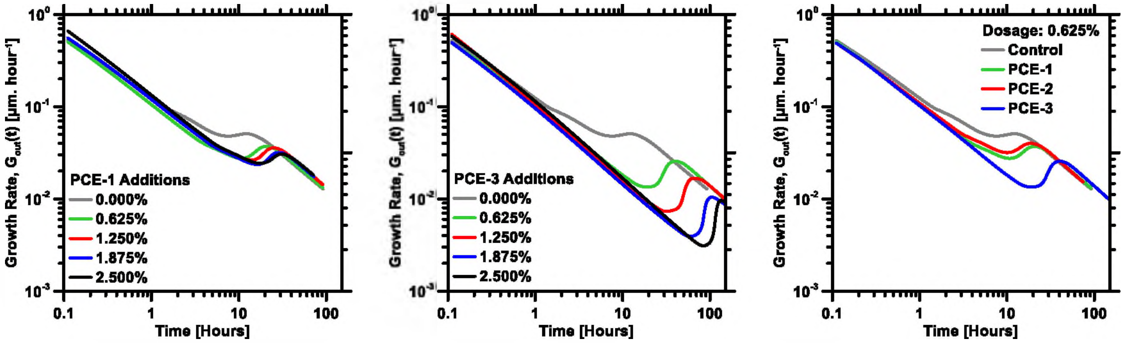

(a) (b) (c)

Figure 10. The temporal evolution of outward growth rate of the product (G_{out}), as obtained from pBNG simulations, for: (a) pastes prepared with PCE-1 at different dosages, (b) pastes prepared with PCE-3 at different dosages, and (c) pastes prepared with different PCEs at a fixed dosage of 0.625%. Simulations parameters are deterministic, and, therefore, there is no uncertainty associated with them.

This corroborates the hypothesis made earlier in this section – that the excess PCE molecules existing in the solution (that do not adsorb onto C_3S particles' surfaces) adsorb onto C-S-H nuclei, and, subsequently, block their access to the adjacent solution, thus inhibiting their growth rate [27,28]. At any given PCE dosage, lower values of G_{out} in [C_3S + PCE-3] pastes, as compared to those prepared with other two PCEs, can be attributed to higher adsorption capacity of PCE-3 (i.e., on account of its molecular architecture), as has been explained previously in this section and highlighted in Figures 4 and 8. At later ages, that is, at t = 72 h (Figure 11b), the variations in G_{out} with respect to PCE's dosage and molecular architecture are significantly less pronounced. This is attributed to depletion of C-S-H supersaturation in the solution – which, in turn, causes G_{out} to diminish [14,27,28,36] and converge to similar values, regardless of dosage or molecular architecture of the PCE in the paste.

By and large, the results described so far strongly support the theory that the hydration of C_3S is suppressed by PCE – wherein, adsorption of PCE molecules onto C_3S

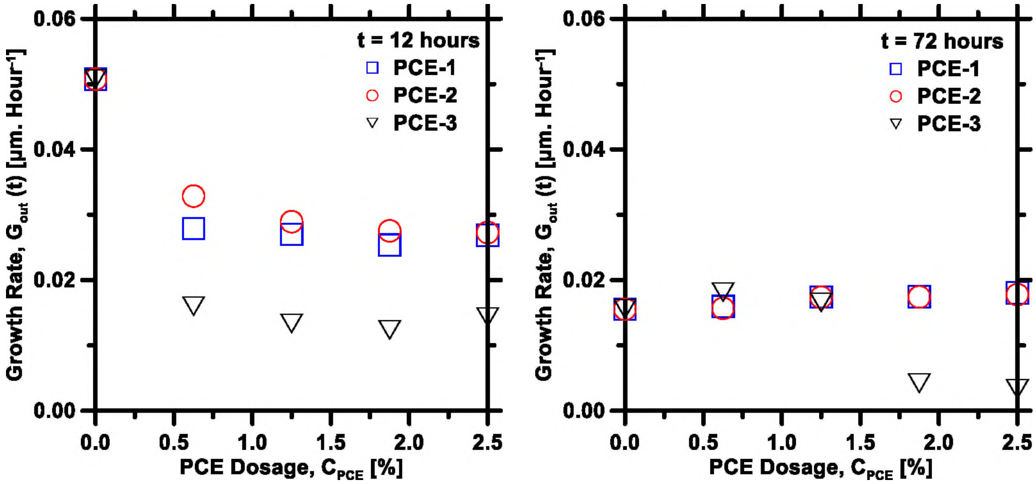

(a) (b)

Figure 11. The outward growth rate of the product, as obtained from pBNG simulations, at (a) t = 12 h, and (b) t = 72 h.

surfaces suppresses C_3S dissolution and C-S-H nucleation, and the adsorption of PCE molecules onto C-S-H surfaces suppresses the post-nucleation growth of C-S-H. Based on this theory, it is hypothesized that if the adsorption of PCE onto C_3S surfaces is reduced, the overall impact on inhibition of C_3S dissolution and C-S-H nucleation sites would consequently be reduced. To test this hypothesis, additional experiments were conducted, wherein PCE was incorporated into the paste in delayed mode (i.e., addition of PCE five mins after mixing of C_3S and DI-water). As can be seen in Figure 12, when the addition of PCE is delayed, its impact on dissolution and nucleation site inhibition are indeed marginalized (albeit, not nullified); this manifests as shorter induction period and faster incidence of the main hydration peak compared to those in pastes provisioned with PCE at the time of mixing. Notwithstanding, the adsorption of PCE molecules onto surfaces of C-S-H – that form prior to, as well as after, the addition of PCE – results in substantial inhibition of its post-nucleation growth; this manifests as slower approach to and departure from the main hydration peak. It is also worth noting that in the case of delayed addition, as PCE molecules predominantly adsorb onto C-S-H surfaces (as opposed to C_3S and C-S-H surfaces), the suppression of post-nucleation growth of C-S-H (and, therefore, C_3S hydration) is more profound compared to pastes in which PCE is added at the time of mixing (Figure 12). The results shown in Figure 12, and the mechanisms described above, are in good agreement with prior studies [27,41].

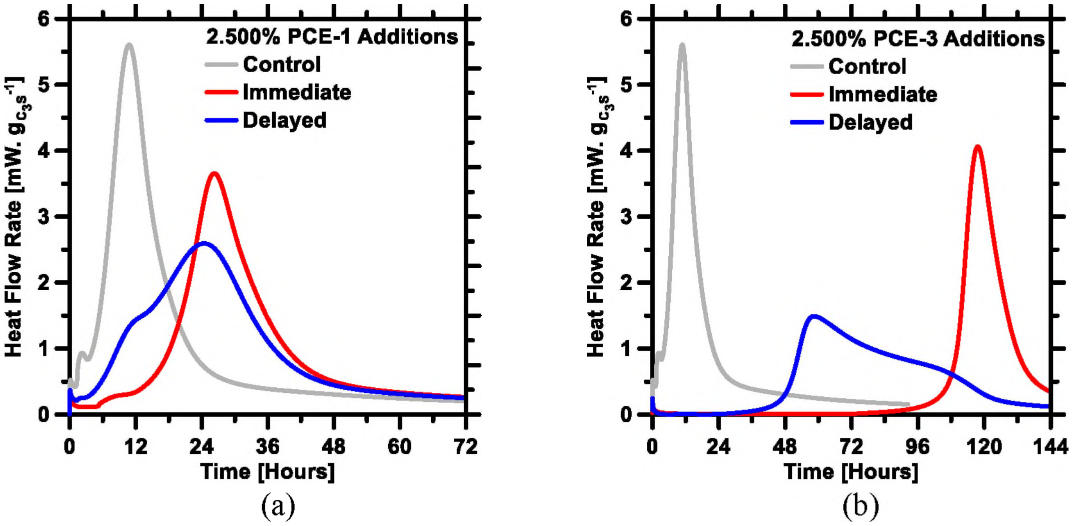

(a) (b)

Figure 12. Measured heat flow rates of [C_3S + 2.5% PCE] pastes, prepared with (a) PCE-1, and (b) PCE-3. Results corresponding to both immediate and delayed (i.e., by 5-min) addition of PCE are shown. For comparison, the control system with no PCE is also shown.

4. CONCLUSIONS

A hierarchical sequence of experiments and pBNG simulations were employed to elucidate the effects of comb-shaped polycarboxylate ether (PCE) polymer on hydration mechanisms of tricalcium silicate (C_3S). Focus was placed on description of, and contrasting, the contributions of dosage and molecular architecture of PCE on its ability to influence early hydration of C_3S.

Results clearly show that the hydration of C_3S is suppressed in the presence of PCE – wherein, the deceleration scales with PCE content in the paste. The origin of such deceleration is most likely the adsorption of PCE molecules on C_3S particles' surfaces, which inhibits topographical dissolution and C-S-H nucleation sites, and results in prolongation of the induction period. Furthermore, results strongly suggest that adsorption of PCE molecules onto surfaces of C-S-H – massive precipitation of which occurs roughly when the induction period ends – causes suppression of their growth throughout the hydration process. This results in a slower approach to, as well as departure from, the main hydration peak.

Through rigorous analyses of decelerating effects induced by three different PCEs, this study develops a robust correlation between the molecular architecture of PCE and its potential to suppress C_3S hydration. These results show that PCEs with lower side chain grafting density (i.e., higher C/E: carboxylate-to-ether ratio), smaller side chain length (i.e., smaller P: number of monomers per side chain), and lower overall molecular weight have greater potential to adsorb on silicate surfaces, and, therefore, suppress C_3S hydration. By consolidating results pertaining to the three different PCEs, the study advances a simple numerical equation – which unifies the PCE's dosage and architectural parameters into a single numerical value – to assess, in a quantitative manner, a given PCE's potential to suppress C_3S hydration.

Overall, outcomes of this study provide novel mechanistic insights into the root-cause of decelerating effects of PCE. The discussion provides an improved understanding of how the dosage and architectural parameters of PCE – which can readily be characterized using conventional experimental techniques – affect the hydration of C_3S at early ages. Such knowledge is expected to aid in uncovering the underlying mechanisms that describe the influence of PCE on the hydration of other cementitious phases (e.g., C_3A), as well as the development of fresh- (e.g., rheology) and hardened-properties (e.g., compressive strength) of cementitious systems.

ACKNOWLEDGEMENTS

Funding for this research was provided by the University of Missouri Research Board [UMRB], and the National Science Foundation [NSF, CMMI: 1661609]. Experimental and computational tasks were conducted in the Materials Research Center and Department of Materials Science and Engineering at Missouri S&T. The authors gratefully acknowledge the financial support that has made these laboratories and their operations possible.

REFERENCES

[1] H.F. Taylor, Cement chemistry, Thomas Telford, 1997.

[2] J.W. Bullard, H.M. Jennings, R.A. Livingston, A. Nonat, G.W. Scherer, J.S. Schweitzer, K.L. Scrivener, J.J. Thomas, Mechanisms of cement hydration, Cem. Concr. Res. 41 (2011) 1208–1223.

[3] A.J. Allen, J.J. Thomas, H.M. Jennings, Composition and density of nanoscale calcium–silicate–hydrate in cement, Nat. Mater. 6 (2007) 311–316.

[4] I.G. Richardson, Tobermorite/jennite-and tobermorite/calcium hydroxide-based models for the structure of CSH: applicability to hardened pastes of tricalcium silicate, β-dicalcium silicate, Portland cement, and blends of Portland cement with blast-furnace slag, metakaolin, or silica fume, Cem. Concr. Res. 34 (2004) 1733–1777

[5] L.B. Skinner, S.R. Chae, C.J. Benmore, H.R. Wenk, P.J.M. Monteiro, Nanostructure of calcium silicate hydrates in cements, Phys. Rev. Lett. 104 (2010) 195502.

[6] J.J. Thomas, H.M. Jennings, J.J. Chen, Influence of nucleation seeding on the hydration mechanisms of tricalcium silicate and cement, J. Phys. Chem. C. 113 (2009) 4327–4334.

[7] E. Masoero, E. Del Gado, R.-M. Pellenq, F.-J. Ulm, S. Yip, Nanostructure and nanomechanics of cement: polydisperse colloidal packing, Phys. Rev. Lett. 109 (2012) 155503.

[8] P. Yu, R.J. Kirkpatrick, B. Poe, P.F. McMillan, X. Cong, Structure of calcium silicate hydrate (C-S-H): Near-, Mid-, and Far-infrared spectroscopy, J. Am. Ceram. Soc. 82 (1999) 742–748.

[9] M.J. Abdolhosseini Qomi, F.-J. Ulm, R.J.-M. Pellenq, Evidence on the dual nature of aluminum in the calcium-silicate-hydrates based on atomistic simulations, J. Am. Ceram. Soc. 95 (2012) 1128–1137.

[10] G.W. Scherer, J. Zhang, J.J. Thomas, Nucleation and growth models for hydration of cement, Cem. Concr. Res. 42 (2012) 982–993.

[11] J.J. Thomas, A new approach to modeling the nucleation and growth kinetics of tricalcium silicate hydration, J. Am. Ceram. Soc. 90 (2007) 3282–3288.

[12] A. Kumar, S. Bishnoi, K.L. Scrivener, Modelling early age hydration kinetics of alite, Cem. Concr. Res. 42 (2012) 903–918.

[13] J.J. Thomas, J.J. Biernacki, J.W. Bullard, S. Bishnoi, J.S. Dolado, G.W. Scherer, A. Luttge, Modeling and simulation of cement hydration kinetics and microstructure development, Cem. Concr. Res. 41 (2011) 1257–1278.

[14] A.M. Ley-Hernandez, J. Lapeyre, R. Cook, A. Kumar, D. Feys, Elucidating the Effect of Water-To-Cement Ratio on the Hydration Mechanisms of Cement, ACS Omega. 3 (2018) 5092–5105. https://doi.org/10.1021/acsomega.8b00097.

[15] I. Mehdipour, A. Kumar, K.H. Khayat, Rheology, hydration, and strength evolution of interground limestone cement containing PCE dispersant and high volume supplementary cementitious materials, Mater. Des. 127 (2017) 54–66. https://doi.org/10.1016/j.matdes.2017.04.061.

[16] A. Arora, M. Aguayo, H. Hansen, C. Castro, E. Federspiel, B. Mobasher, N. Neithalath, Microstructural packing-and rheology-based binder selection and characterization for Ultra-high Performance Concrete (UHPC), Cem. Concr. Res. 103 (2018) 179–190.

[17] J. Cheung, A. Jeknavorian, L. Roberts, D. Silva, Impact of admixtures on the hydration kinetics of Portland cement, Cem. Concr. Res. 41 (2011) 1289–1309.

[18] F. Winnefeld, S. Becker, J. Pakusch, T. Götz, Effects of the molecular architecture of comb-shaped superplasticizers on their performance in cementitious systems, Cem. Concr. Compos. 29 (2007) 251–262.

[19] F. Ridi, E. Fratini, P. Luciani, F. Winnefeld, P. Baglioni, Tricalcium silicate hydration reaction in the presence of comb-shaped superplasticizers: boundary nucleation and growth model applied to polymer-modified pastes, J. Phys. Chem. C. 116 (2012) 10887–10895.

[20] A. Zingg, F. Winnefeld, L. Holzer, J. Pakusch, S. Becker, R. Figi, L. Gauckler, Interaction of polycarboxylate-based superplasticizers with cements containing different C 3 A amounts, Cem. Concr. Compos. 31 (2009) 153–162.

[21] A. Zingg, L. Holzer, A. Kaech, F. Winnefeld, J. Pakusch, S. Becker, L. Gauckler, The microstructure of dispersed and non-dispersed fresh cement pastes—new insight by cryo-microscopy, Cem. Concr. Res. 38 (2008) 522–529.

[22] A. Zingg, F. Winnefeld, L. Holzer, J. Pakusch, S. Becker, L. Gauckler, Adsorption of polyelectrolytes and its influence on the rheology, zeta potential, and microstructure of various cement and hydrate phases, J. Colloid Interface Sci. 323 (2008) 301–312. https://doi.org/10.1016/j.jcis.2008.04.052.

[23] G. Gelardi, N. Sanson, G. Nagy, R.J. Flatt, Characterization of comb-shaped copolymers by multidetection SEC, DLS and SANS, Polymers. 9 (2017) 61.

[24] D. Marchon, U. Sulser, A. Eberhardt, R.J. Flatt, Molecular design of comb-shaped polycarboxylate dispersants for environmentally friendly concrete, Soft Matter. 9 (2013) 10719–10728.

[25] D. Marchon, P. Juilland, E. Gallucci, L. Frunz, R.J. Flatt, Molecular and submolecular scale effects of comb-copolymers on tri-calcium silicate reactivity: Toward molecular design, J. Am. Ceram. Soc. 100 (2017) 817–841.

[26] G. Artioli, L. Valentini, M. Voltolini, M.C. Dalconi, G. Ferrari, V. Russo, Direct Imaging of Nucleation Mechanisms by Synchrotron Diffraction Micro-Tomography: Superplasticizer-Induced Change of C–S–H Nucleation in Cement, Cryst. Growth Des. 15 (2014) 20–23.

[27] L. Valentini, M. Favero, M.C. Dalconi, V. Russo, G. Ferrari, G. Artioli, Kinetic Model of Calcium-Silicate Hydrate Nucleation and Growth in the Presence of PCE Superplasticizers, Cryst. Growth Des. (2016) 646–654.

[28] W. Meng, P. Lunkad, A. Kumar, K. Khayat, Influence of Silica Fume and Polycarboxylate Ether Dispersant on Hydration Mechanisms of Cement, J. Phys. Chem. C. 120 (2016) 26814–26823.

[29] G.H. Kirby, J.A. Lewis, Comb polymer architecture effects on the rheological property evolution of concentrated cement suspensions, J. Am. Ceram. Soc. 87 (2004) 1643–1652.

[30] E. Sakai, A. Kawakami, M. Daimon, Dispersion mechanisms of comb-type superplasticizers containing grafted poly (ethylene oxide) chains, in: Macromol. Symp., Wiley Online Library, 2001: pp. 367–376.

[31] K. Yamada, T. Takahashi, S. Ogawa, S. Hanehara, Molecular structure of the polycarboxylate-type superplasticizer having tolerance to the effect of sulfate ion, Cem. Concr. Sci. Technol. 54 (2000) 79–86.

[32] J. Yoshikawa, J.A. Lewis, B.-W. Chun, Comb polymer architecture, ionic strength, and particle size effects on the BaTiO3 suspension stability, J. Am. Ceram. Soc. 92 (2009).

[33] F. Ridi, L. Dei, E. Fratini, S.-H. Chen, P. Baglioni, Hydration kinetics of tri-calcium silicate in the presence of superplasticizers, J. Phys. Chem. B. 107 (2003) 1056–1061.

[34] T. Sowoidnich, T. Rachowski, C. Rößler, A. Völkel, H.-M. Ludwig, Calcium Complexation and Cluster Formation as Principal Modes of Action of Polymers used as Superplasticizer in Cement Systems, 73 (2015) 42–50.

[35] K. Yamada, S. Ogawa, S. Hanehara, Controlling of the adsorption and dispersing force of polycarboxylate-type superplasticizer by sulfate ion concentration in aqueous phase, Cem. Concr. Res. 31 (2001) 375–383.

[36] J. Lapeyre, A. Kumar, Influence of pozzolanic additives on hydration mechanisms of tricalcium silicate, J. Am. Ceram. Soc. 101 (2018) 3557–3574. https://doi.org/10.1111/jace.15518.

[37] A. Bazzoni, M. Cantoni, K.L. Scrivener, Impact of Annealing on the Early Hydration of Tricalcium Silicate, J. Am. Ceram. Soc. 97 (2014) 584–591.

[38] T. Oey, A. Kumar, G. Falzone, J. Huang, S. Kennison, M. Bauchy, N. Neithalath, J.W. Bullard, G. Sant, The Influence of Water Activity on the Hydration Rate of Tricalcium Silicate, J. Am. Ceram. Soc. 99 (2016) 2481–2492. https://doi.org/10.1111/jace.14181.

[39] C.F. Ferraris, V.A. Hackley, A.I. Avilés, Measurement of particle size distribution in portland cement powder: Analysis of ASTM round robin studies, Cem. Concr. Aggreg. 26 (2004) 71–81.

[40] L. Ferrari, L. Bernard, F. Deschner, J. Kaufmann, F. Winnefeld, J. Plank, Characterization of Polycarboxylate-Ether Based Superplasticizer on Cement Clinker Surfaces, J. Am. Ceram. Soc. 95 (2012) 2189–2195.

[41] D. Marchon, P. Juilland, E. Gallucci, L. Frunz, R. Flatt, Molecular and submolecular scale effects of comb-copolymers on tri-calcium silicate reactivity: Toward molecular design, J. Am. Ceram. Soc. 100 (2017) 817–841. https://doi.org/10.1111/jace.14695.

[42] L. Agullo, B. Toralles-Carbonari, R. Gettu, A. Aguado, Fluidity of cement pastes with mineral admixtures and superplasticizer—a study based on the Marsh cone test, Mater. Struct. 32 (1999) 479–485.

[43] J. Plank, D. Zhimin, H. Keller, F. v Hössle, W. Seidl, Fundamental mechanisms for polycarboxylate intercalation into C 3 A hydrate phases and the role of sulfate present in cement, Cem. Concr. Res. 40 (2010) 45–57.

[44] J. Zhang, G.W. Scherer, Comparison of methods for arresting hydration of cement, Cem. Concr. Res. 41 (2011) 1024–1036.

[45] J. Stoian, T. Oey, J.W. Bullard, J. Huang, A. Kumar, M. Balonis, J. Terrill, N. Neithalath, G. Sant, New insights into the prehydration of cement and its mitigation, Cem. Concr. Res. 70 (2015) 94–103.

[46] G.W. Scherer, Models of Confined Growth, Cem. Concr. Res. 42 (2012) 1252–1260.

[47] T. Oey, A. Kumar, J.W. Bullard, N. Neithalath, G. Sant, The filler effect: the influence of filler content and surface area on cementitious reaction rates, J. Am. Ceram. Soc. 96 (2013) 1978–1990.

[48] S. Garrault, A. Nonat, Hydrated layer formation on tricalcium and dicalcium silicate surfaces: experimental study and numerical simulations, Langmuir. 17 (2001) 8131–8138.

[49] G. Puerta-Falla, A. Kumar, L. Gomez-Zamorano, M. Bauchy, N. Neithalath, G. Sant, The influence of filler type and surface area on the hydration rates of calcium aluminate cement, Constr. Build. Mater. 96 (2015) 657–665.

[50] J.W. Bullard, G.W. Scherer, J.J. Thomas, Time dependent driving forces and the kinetics of tricalcium silicate hydration, Cem. Concr. Res. 74 (2015) 26–34.

[51] A. Bazzoni, S. Ma, Q. Wang, X. Shen, M. Cantoni, K.L. Scrivener, The Effect of Magnesium and Zinc Ions on the Hydration Kinetics of C3S, J. Am. Ceram. Soc. 97 (2014) 3684–3693.

[52] G.W. Scherer, F. Bellmann, Kinetic analysis of C-S-H growth on calcite, Cem. Concr. Res. 103 (2018) 226–235. https://doi.org/10.1016/j.cemconres.2016.07.017.

[53] A. Kumar, T. Oey, S. Kim, D. Thomas, S. Badran, J. Li, F. Fernandes, N. Neithalath, G. Sant, Simple methods to estimate the influence of limestone fillers on reaction and property evolution in cementitious materials, Cem. Concr. Compos. 42 (2013) 20–29.

[54] J.J. Thomas, H.M. Jennings, A.J. Allen, Relationships between Composition and Density of Tobermorite, Jennite, and Nanoscale CaO- SiO2- H2O, J. Phys. Chem. C. 114 (2010) 7594–7601.

[55] D.P. Bentz, P. Lura, J.W. Roberts, Mixture proportioning for internal curing, Concr. Int. 27 (2005) 35–40.

[56] J.A. Nelder, R. Mead, A simplex method for function minimization, Comput. J. 7 (1965) 308–313.

[57] K.I. McKinnon, Convergence of the Nelder–Mead Simplex Method to a Nonstationary Point, SIAM J. Optim. 9 (1998) 148–158.

[58] F. Bellmann, G.W. Scherer, Analysis of C-S-H growth rates in supersaturated conditions, Cem. Concr. Res. 103 (2018) 236–244. https://doi.org/10.1016/j.cemconres.2017.05.007.

[59] E. Berodier, K. Scrivener, Understanding the Filler Effect on the Nucleation and Growth of C-S-H, J. Am. Ceram. Soc. 97 (2014) 3764–3773.

[60] D.P. Bentz, Modeling the influence of limestone filler on cement hydration using CEMHYD3D, Cem. Concr. Compos. 28 (2006) 124–129.

[61] H.M. Jennings, Refinements to colloid model of CSH in cement: CM-II, Cem. Concr. Res. 38 (2008) 275–289.

[62] I. Borukhov, Adsorption of polyelectrolytes and inter-colloidal forces, Phys. Stat. Mech. Its Appl. 249 (1998) 315–320.

IV. INFLUENCE OF SIZE-CLASSIFIED AND SLIGHTLY SOLUBLE MINERAL ADDITIVES ON HYDRATION OF TRICALCIUM SILICATE

Rachel Cook[1], Hongyan Ma[2], and Aditya Kumar[1]

1. Department of Materials Science and Engineering, Missouri University of Science and Technology (S&T), B49 McNutt Hall, 1400 N. Bishop, Rolla, MO 65409-0340, USA.

2. Department of Civil, Architectural and Environmental Engineering, Missouri University of Science and Technology (S&T), Rolla, MO 65409-0340, USA.

ABSTRACT

Early-age hydration of cement is kinetically enhanced by fillers, such as quartz and limestone. However, few studies have attempted to systematically compare the effects of different fillers on hydration rates, and none have quantified such effects using fillers with comparable, size-classified particle size distributions. This study examines the influence of size-classified fillers [i.e., limestone ($CaCO_3$), quartz (SiO_2), corundum (Al_2O_3), and rutile (TiO_2)] on early-age hydration kinetics of tricalcium silicate (C_3S) using a combination of experimental methods, while also employing a modified phase boundary and nucleation and growth model. In prior studies, wherein fillers with broad PSDs were used, it has been reported that between quartz and limestone, the latter is a superior filler due to its ability to partake in anion-exchange reactions with C-S-H. Contrary to prior investigations, this study shows that when size-classified and *area matched* fillers are used – which, essentially, eliminate degrees of freedom associated with surface area and agglomeration of filler particulates – the filler effect of quartz is found to be broadly similar to that of limestone as well as rutile. Results also show that unlike quartz, limestone, and rutile – which enhance C_3S hydration kinetics – corundum suppresses hydration of C_3S during the first several hours after mixing. Such deceleration in C_3S hydration kinetics is attributed to the dissolution and later adsorption of aluminate anions into solution and onto anhydrous particulates' surfaces, respectively, which consequently inhibit both the dissolution of C_3S and heterogeneous nucleation of C-S-H.

Keywords: Cement Hydration; Rutile; Corundum; Limestone; Calorimetry; Nucleation and Growth.

1. INTRODUCTION

As the production and use of ordinary Portland cement (OPC) continues to increase globally [1–3], pressure is mounting on the cement industry to discover alternate manufacturing processes and resources to mitigate CO_2 emission associated with OPC manufacturing [2,4–6]. A potential solution, currently being extensively explored and optimized by researchers, is partial replacement of OPC with CO_2-efficient pozzolanic mineral additives (e.g., metakaolin) and filler materials (e.g., limestone and quartz). Since OPC-based systems (i.e., pastes, mortars, and concretes) are complex, comprising of numerous anhydrous (i.e., reactants) and hydrated (i.e., reaction products) phases at any given instant of time, researchers have prioritized the examination of pure, single-phase synthetic cementitious compounds such as tricalcium silicate (written as C_3S in cement chemistry notation, where $C = CaO$; $S = SiO_2$; $A = Al_2O_3$; and $H = H_2O$) [7–16] instead of OPC. C_3S, which embodies 50-70 $\%_{mass}$ of OPC, is the phase most representative of

OPC's early-age hydration (i.e., reaction with water) and strength development [17]. Therefore, C_3S is commonly used as a model phase to examine and better understand the underlying OPC hydration mechanisms. During hydration of C_3S – a dissolution-precipitation process – portlandite (CH) and calcium silicate hydrate (C-S-H) form homogeneously in the pore-solution and heterogeneously on the anhydrous particulates' surfaces, respectively [18,19]. C-S-H formation, which commences within minutes of initial wetting of C_3S particulates and continues over several days, principally dictates the hydration kinetics of C_3S [11,18,20–22].

Typical fillers used for partial replacement of OPC are ground, mineral powders such as limestone (crystalline $CaCO_3$), quartz (crystalline SiO_2), and silica fume (amorphous SiO_2); other less commonly used fillers include polymorphs of TiO_2 (i.e., rutile and anatase) and corundum (crystalline Al_2O_3) [10,23–28]. When present in OPC or C_3S systems, fillers alter hydration rates [7,13,23,24,29] — typically by accelerating hydration of the host phase. This phenomenon, termed the filler effect, is attributed to the enhancement in total solid surface area of the system, which increases the number of nucleation sites for C-S-H to heterogeneously form upon. In early investigations of the filler effect [24,30,31], the dilution of OPC/C_3S (due to partial replacement by filler) in the system was also considered to be a factor contributing to the acceleration of hydration kinetics. However, in the past few years, several studies [13,29,32] have conclusively shown that such dilution of OPC/C_3S content is largely inconsequential to hydration kinetics, especially within the first 24 h after mixing.

It is now well established that limestone, in addition to its physical effect (i.e., providing additional surface for C-S-H nucleation) imparts chemical effects on OPC/C_3S

hydration. In OPC systems, limestone can lead to formation of carboaluminate phases (e.g., mono- and hemi-carboaluminate) – either through reactions with alumina-containing anhydrous phases (e.g., C_3A) [27,33–36], or from destabilization of the monosulfoaluminate phase [37]. In recent studies [13,29,38,39], limestone was directly compared with quartz in terms of filler performance. Oey et al. [29] concluded that, in OPC systems, limestone was the more effective filler compared to quartz due to its superior interfacial properties (i.e., surface tension and wetting angle that make limestone surface energetically favorable for heterogeneous nucleation of C-S-H), and its ability to participate in anion-exchange reactions with the C-S-H phase. The aforesaid anion-exchange reaction involves a sequence of steps [13,29]: limestone dissolves, releasing Ca^{2+} and CO_3^{2-} ions in the contiguous solution (pore-solution); the aqueous CO_3^{2-} anions progressively adsorb onto C-S-H, while OH^- anions are released from C-S-H into the pore solution; and finally, the increase in OH^- concentration in the pore-solution augments the driving force (i.e., supersaturation) for C-S-H precipitation. In a later study, Kumar et al. [13] compared the filler effects of quartz and limestone in C_3S systems, and concluded that the differences between interfacial properties of limestone and quartz have negligible, if any, effect on C_3S hydration kinetics. The authors [13] also determined that the ability of limestone to partake in anion-exchange reaction renders its filler effect superior compared to quartz. Akin to limestone, silica fume also exerts a physical, filler effect and a chemical effect that alter hydration behavior of cementitious systems. The chemical effect specifically involves the formation of additional C-S-H via the pozzolanic reaction of silica fume with CH. In recent studies [7,22,40], however, it was shown that the pozzolanic reaction of silica fume is slow – on account of its intrinsically low solubility and agglomeration of its fine particulates – and, therefore, has little effect on hydration of OPC or C_3S within the first 24 h of hydration.

Fillers such as rutile and corundum have been less widely explored compared to quartz and limestone. Rutile and anatase – naturally occurring mineral forms of TiO_2 – have both been investigated as fillers in separate studies [24,28]; rutile was investigated as a filler in OPC pastes [24], whereas the filler effect of anatase was examined in pure C_3S pastes [28]. Both studies reported systemic increase in hydration rates with increasing replacements of TiO_2. This correlation is expected because higher filler content generally entails greater enhancement in surface area (per unit mass of OPC/C_3S), and, therefore, greater increase in number of potential C-S-H nucleation sites. Notwithstanding, the filler effect of TiO_2, in any form, has yet to be compared with other fillers in pure cementitious systems. Though corundum has not been extensively studied in the literature, additions of other Al-rich compounds (e.g., metakaolin, Al_2O_3 nanoparticles, Al_2O_3-doped alite, and soluble Al salts) in pure cementitious systems have been explored [7–9,12,41–43]. Majority of these studies have reported that dissolution of the Al-based compound releases aluminate anions ($Al(OH)_4^-$) into the contacting solution, which, ultimately, results in extension of the induction period – a manifestation of suppression of early-age hydration of the cementitious material. Pustovgar et al. [8] utilized molecular dynamic simulations to show that the adsorption of aluminate anions onto C_3S's surfaces is energetically favorable due to ionic and hydrogen bonds forming between the aluminate anions and ionic species (i.e., Ca^{2+}, OH^-, and $H_2SiO_4^{2-}$/$H_3SiO_4^-$ ions) surrounding C_3S particulates. In addition to the original study [8], a pair of recent studies [7,43] have reported that such adsorption of aluminate anions results in the formation of metastable aluminosilicate complexes, which inhibit C_3S dissolution sites (e.g., kink sites found on etch pits [8,44]) as well as potential sites for C-S-H nucleation on C_3S particulates' surfaces. This results in suppression of C_3S hydration at early-ages, which, typically, manifests as prolongation of the induction period. As C_3S continues to dissolve (albeit, at a slower rate), concentrations of Ca^{2+}, $H_2SiO_4^{2-}$/$H_3SiO_4^{-}$ and OH^- species in the contacting solution increase. When the pH of the solution approaches ≈12.7 (lime saturation), the aforementioned metastable aluminosilicate complexes destabilize, causing the aluminate anions to desorb from C_3S surfaces and stabilize in solution. As the topographical coverage of aluminosilicate complexes on C_3S particulates is disrupted and the particulates' surfaces are re-exposed to the solution, hydration of C_3S is renewed, marking the end of the induction period.

The studies cited above provide significant insight into the filler effects –both physical and chemical – of various fillers on hydration behavior of cementitious systems. However, the majority of past studies have used fillers with broad PSDs (with particulate sizes varying over wide ranges) in their investigations. Such broad PSDs introduce additional degrees of freedom in the analyses – such as, disparities in surface area and (degree/extent of) agglomeration of filler particulates – thus making it difficult to isolate and quantify influences independent of individual filler (particle) size effects on C-S-H formation and hydration rates. Furthermore, from the above discussion, it is also clear that some fillers – that is, rutile and corundum – have not been studied in a comprehensive manner, and their filler effects have never been compared to those of common fillers (i.e., limestone and quartz). This study attempts to address these challenges by examining the influences of four types of size-classified fillers – limestone, quartz, corundum, and rutile – on the early-age hydration kinetics of C_3S using a combination of experimental methods (e.g., isothermal microcalorimetry and thermogravimetric analysis (TGA)) and a modified phase boundary and nucleation and growth (pBNG) model. Selected results from our previous studies on the filler effect of silica fume [7,22,40] are included to support the analyses. Size-classified fillers, with similar PSDs, were produced and used in this study to enable comparison of their intrinsic filler effects – that are independent of their PSDs, and, therefore, devoid of any complexities associated with them. Through such comparisons, this study attempts to rank the aforementioned fillers in accordance with magnitudes of their size-independent filler effects.

2. MATERIALS AND METHODS

2.1. MATERIALS AND SIZE CLASSIFICATION OF FILLERS

Synthetic triclinic C_3S (Ca_3SiO_5-T_1) was utilized in this study. Details regarding C_3S synthesis are described elsewhere [7,43]. After synthesis, the final powder was evaluated to be nearly phase pure C_3S (i.e., via Rietveld analysis of x-ray diffraction patterns) with 0.80 % ± 0.25 % of CaO.

The filler effects of four different commercially-available materials – quartz, limestone, rutile, and corundum – were examined in this study. The fillers were suspended in water, and subsequently sieved through 20 μm, 25 μm, and 32 μm sieve mesh-sizes to obtain three, distinctive PSDs, with the following particle size ranges: less than 20 μm; between 20 μm and 25 μm; and between 25 μm and 32 μm. These PSDs from hereon are referred to as *fine*, *intermediate*, and *coarse* PSDs, respectively. The PSDs were acquired from the bulk powders by employing a modified wet sieving process based on ASTM C325-07(2014) [45]. The ASTM standard dictates the use of mechanical stirring; the use of no. 100 (150 µm), no. 140 (106 µm), no. 200 (75 µm) and no. 325 (45 µm) sieve mesh-sizes; and a batch size compromising of 1L of water and 250 g of powder material. In this study, however, slight adjustments (to the standard procedures) were made to ensure repeatability and reproducibility in the final PSDs of the fillers. The amount of distilled water was constrained to approximately 200 mL (per 50 grams of filler material) and the mixture was gently hand-stirred after a two-hour soaking process before sieving using no. 635 (20 µm), no. 500 (25 µm), and no. 450 (32 µm) sized sieves.

The PSDs were verified using a static light scattering particle size analyzer (Microtrac S3500) for all materials. For such experiments, C_3S and filler powders were suspended in isopropanol and deionized water, respectively. The suspended C_3S powders were agitated with ultrasonic pulses for two minutes before three consecutive measurements, while the suspended fillers were measured immediately without any ultrasonification in order to emulate their effective PSDs upon contact with deionized water (during mixing of the pastes). PSD of the C_3S powder is shown in Figure 1a; PSDs of the filler materials as were received from suppliers – subsequently referred to as *as received* PSDs – are shown in Figure 1b. C_3S's median particle size on a volume basis (d_{v50}, µm) – extracted from static light scattering results – was determined to be 7.78 µm. Based on the C_3S's PSD, its specific surface area (SSA) was calculated to be 562 m^2. kg^{-1}; the density of C_3S [17] was assumed to be 3150 kg. m^{-3}. Details of PSDs of the *as*

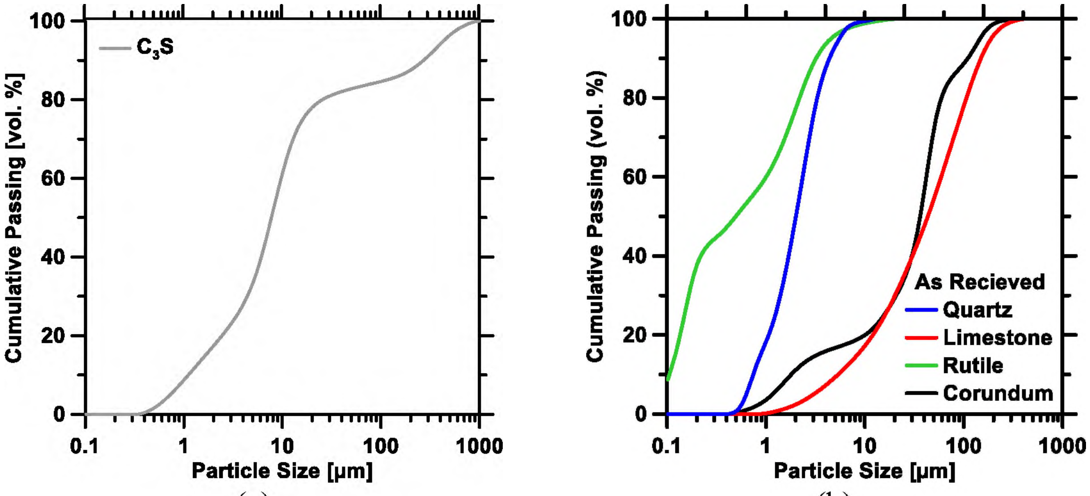

(a) (b)

Figure 1. Cumulative PSDs of (a) C_3S; and (b) *as received* fillers: quartz, limestone, rutile, and corundum. The largest relative uncertainty in median diameter (d_{v50}, µm), based on six replicate measurements of C_3S's PSD, is on the order of ± 6%.

received fillers are shown in Table 1. Here, the SSAs of the *as received* fillers were estimated using densities of 2650 kg. m^{-3}, 2710 kg. m^{-3}, 4230 kg. m^{-3}, and 3950 kg. m^{-3}, corresponding to quartz, limestone, rutile, and corundum, respectively. The PSDs of the *fine*, *intermediate*, and *coarse* size-classes are showed in Figure 2; their d_{v50}'s and SSAs are enumerated in Table 1. It is clarified that due to common difficulties associated with sieving (e.g., charging, agglomeration, etc.), the i*ntermediate* and *coarse* PSDs of fillers are somewhat broader – with wider distribution of particle sizes – than what would be expected. For example, the *intermediate* PSDs of fillers do include small fractions of particulates with sizes beyond the 20-to-25 µm range (Figure 2b). Notwithstanding, both *intermediate* and *coarse* PSDs are devoid of fine particulates (size < 0.1 µm) – which are prone to agglomerate – and feature substantially narrower spread of particle sizes compared to the *as received* ones. Because of these features, the size-classified PSDs are deemed suitable for investigation of the filler effect. Owing to the same aforementioned

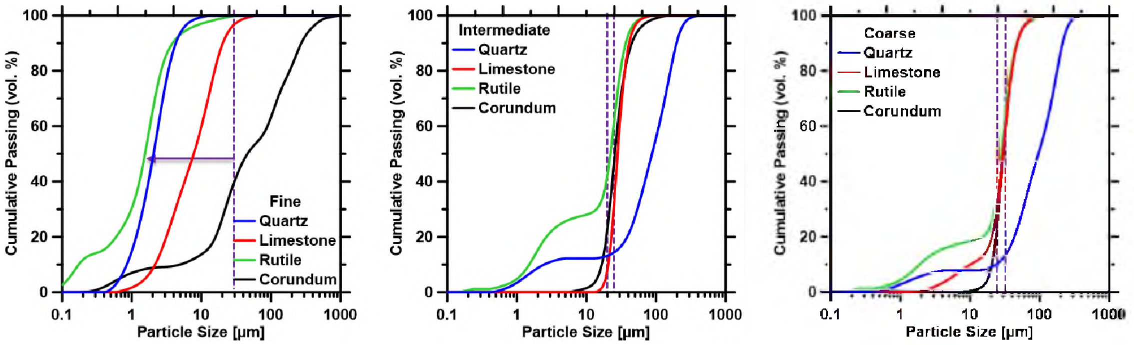

(a) (b) (c)

Figure 2. Cumulative PSDs of quartz, limestone, rutile and corundum, corresponding to: (a) *fine*; (b) *intermediate*; and (c) *coarse* size-classes. The vertical dashed lines indicate the mesh sizes of sieves that were used to generated the size-classified PSDs. The largest uncertainty in the median diameter (d_{v50}, µm) of each PSD is on the order of ± 6%.

Table 1. Median diameters (d_{v50}) and specific surface areas (SSAs) of *as received*, *fine*, *intermediate*, and *coarse* size-classes of each filler (quartz, limestone, rutile, and corundum). The three different size-classes of PSDs were obtained via sieving. However, due to common difficulties associated with sieving, such as charging, agglomeration, etc., the d_{v50}'s corresponding to the various size-classes of corundum* do not follow the same trend as: *fine* < *intermediate* < *coarse*.

Size-Classes	Filler Material	d_{v50} [µm]	SSA [m^2. kg^{-1}]
As Received	Quartz	2.01	1386
	Limestone	43.35	151
	Rutile	0.50	5275
	Corundum	36.30*	220*
Fine	Quartz	2.06	1322
	Limestone	7.78	531
	Rutile	1.55	2281
	Corundum	45.92*	277*
Intermediate	Quartz	87.44	242
	Limestone	28.07	77
	Rutile	22.09	349
	Corundum	25.59*	60*
Coarse	Quartz	95.95	178
	Limestone	29.72	65
	Rutile	28.42	278
	Corundum	30.12*	50*

issues pertaining to wet sieving, the d_{v50}'s corresponding to various size-classes of corundum do not conform to the same trend as those of other fillers. More specifically, in the case of corundum, the d_{v50} values do not increase in the same order as *fine* < *intermediate* < *coarse*. Nevertheless, this discrepancy is not expected to affect the analyses of corundum's filler effect. This – as elaborated in greater detail in the pBNG model section i.e., section 3.2. of this paper – is primarily because alterations in hydration rates of [C_3S + corundum] pastes are strongly related to corundum replacement levels, while remaining largely independent of corundum's PSD.

2.2. METHODS

2.2.1. Experimental Methods. [C_3S + filler] pastes were prepared by mixing the anhydrous powders with deionized water at fixed liquid-to-solid mass ratio of 0.60. C_3S was partially replaced by fillers (with *as received* and size-classified PSDs) at replacement levels of 15% and 30% by mass. Additional [C_3S + filler] pastes were prepared by adjusting the replacement level of C_3S by the filler (i.e., quartz, rutile, and corundum) so as to match the SSA_{total} of [C_3S + 30% limestone] pastes. This *area matching* was done for each size-class of the PSDs; the amount of powders required for *area matching* were calculated in accordance with procedures described in prior studies [13,29]. These pastes with equivalent total SSAs will be hereon referred to as *area matched*. Hydration kinetics of C_3S in the pastes (after hand-mixing for 1 minute) were observed using the TAM IV (TA Instruments) isothermal conduction microcalorimeter for 72 h at 20 °C ± 0.1 °C. Calorimetry profiles of the pastes were processed [7,16,18,32] – assuming enthalpy of hydration [11,16–18] of C_3S as 484 J. $g_{C_3S}^{-1}$ – to estimate time-dependent evolutions of degree of reaction (α) and the rate of reaction ($d\alpha/dt$; units of h^{-1}) of C_3S.

Thermogravimetric analysis (TGA) with a TA Instruments SDT-Q600 analyzer was carried out to identity and quantity hydration products in pastes at 24 h. For such investigations, hydration of the paste was arrested by submerging the crushed paste in isopropanol for 12 h. Prior to testing and following isopropanol immersion, samples were oven dried at 65 °C for 4 h. The dried powders were heated at 10 °C. min^{-1} from room temperature to 1000 °C in an Al_2O_3 crucible, with inert gas flowing over the specimen at a flow rate of 100 mL. min^{-1}.

2.2.2. Phase Boundary Nucleation and Growth (pBNG) Modeling. In addition to physical experiments, a modified phase boundary nucleation and growth (pBNG) model was employed to describe the influence of fillers on early-age hydration kinetics of C_3S in plain (pure C_3S) and binary (i.e., [C_3S + filler]) pastes. The pBNG model implemented in this study – including the foundational assumptions, simulation principles, and algorithms – are similar to those implemented in prior studies [7,11,16,22,32,43]. Therefore, to avoid replication of information, description of the model in this section is kept succinct; for further details, readers are requested to consult references [7,11,16,22,32,43].

The pBNG model uses experimentally measured hydration kinetics of C_3S or [C_3S + filler] paste (i.e., $d\alpha/dt$ as function of time) as input, and reproduces the same using a mathematical formulation of heterogeneous nucleation and growth mechanism in conjunction with an optimization algorithm. The aforesaid mechanism is premised on the assumption that hydration of C_3S in plain and binary pastes is driven by the nucleation and growth of a single hydration product (i.e., C-S-H) of constant density. This product forms under *site saturation* conditions, and then grows heterogeneously from substrate boundaries, that is, C_3S and filler surfaces, into the capillary pore space. This *site saturation* condition entails that all product nuclei form at a particular nucleation event, and that the number of nuclei remains constant throughout the hydration reaction.

The degree of hydration of C_3S as a function of time [$\alpha(t)$; Equation 1] is directly related to: a unitless constant B, which envelops characteristics of the paste as well as the chemical shrinkage that occurs during hydration; and an $X(t)$ function (unitless), which represents the volume fraction of reactant transformed into a singular product [11,15,22,46].

$$\alpha(t) = B.X(t) \tag{1}$$

The $X(t)$ function is nonlinear and non-monotonic, and is reliant on the rates at which the product completely covers the anhydrous C_3S particulates' surfaces and fully occupies the capillary pore space [21,46]. These aspects principally depend on three factors that need to be numerically defined within the pBNG model: nucleation density ($I_{density}$; units of m^{-2}); growth rate (units of $\mu m.\ h^{-1}$); and morphology of the product nuclei. During simulation of any given paste, firstly, N_{nuc} (units of kg_{C3S}^{-1}; see Equation 2) nuclei of the product (per unit mass of C_3S) are allowed to form on the substrates. Next, each product nuclei grows with lateral [i.e., $G_{par}(t)$; units of $\mu m.\ h^{-1}$] and outward [i.e., $G_{out}(t)$; units of $\mu m.\ h^{-1}$] growth rates that are different from each other and vary with time. It is clarified that while both G_{par} and G_{out} vary with time, at any given point in time, the ratio of G_{par} to G_{out} is fixed at 1:2 [21,46,47] to mimic the experimentally observed needle-like morphology of C-S-H's growth [48,49]. The lateral and outward growth rates are temporally varied to capture variations in C-S-H's growth rate in relation to its supersaturation in the solution [7,11,16].

$$N_{nuc} = SSA_{solid} I_{density} \tag{2}$$

In Equation 2, the variable SSA_{solid} (m^2. kg_{C3S}^{-1}) represents the effective (i.e., *reactive*) solid surface area of the paste at the time of product nucleation. SSA_{solid}, as shown in Equation 3, incorporates: "as measured" SSAs (m^2. kg^{-1}) of the constituent powders (i.e., C_3S and filler); the replacement level of C_3S with filler (z, $\%_{mass}$); and a free simulation variable (a_{filler}, unitless) that represents the faction of surface area of the filler that is *reactive* (i.e., not affected by agglomeration or other factors that inhibit product nucleation sites for C-S-H [7,22,43].

$$SSA_{solid} = SSA_{C_3S} + a_{filler} SSA_{filler} \frac{z}{(100 - z)} \tag{3}$$

To reproduce experimentally measured hydration kinetics of a plain or binary C_3S paste, the variables that need to be optimized are: $G_{out}(t)$; $I_{density}$; and a_{filler}. For such optimizations, a Nelder-Mead-based simplex algorithm [50] is used. In the first step, G_{out} is fixed at 0.075 μm. h^{-1} (based on values reported in references [48,49,51]), whereas $I_{density}$ and a_{filler} are allowed to vary in an iterative manner until best reproduction of the input (i.e., $d\alpha/dt$ as function of time) is achieved. The optimum values of $I_{density}$ and a_{filler}, obtained from the first step, are carried over in second step for further fine-tuning, and, more importantly, to estimate the optimal functional forms of $G_{out}(t)$. During the aforementioned optimization steps, convergence is assumed to have been achieved when: (i) the deviation between the measured and simulated reaction rates are within ±1%; and

(ii) the simulation output stays constant within $\pm 10^{-6}$ units through three, successive simulation steps.

3. RESULTS AND DISCUSSION

3.1. EXPERIMENTAL RESULTS

Figure 3 shows heat evolution profiles (i.e., heat flow rate (Figure 3a) and cumulative heat released (Figure 3b)) of [C_3S + silica fume] pastes, prepared at different replacement levels of C_3S with silica fume. These results have been adapted from the work of Lapeyre and Kumar [7]. From the results, it is evident that silica fume increasingly enhances C_3S hydration at increasing replacement levels. This enhancement is attributed to silica fume's filler effect — that is, increment in number of C-S-H nucleation sites due to the additional surface area provided by silica fume particulates. In the original study [7], the authors reported that up to 97% of silica fume's surface area (i.e., 18200 m^2 per kg of the material) is unavailable for C-S-H nucleation and growth due to the agglomeration of silica fume's fine particulates [7]. Therefore, C_3S hydration enhancements, seen in Figure 3, are caused by a small fraction (i.e., ≈ 3%) of silica fume's overall reactive area.

Figure 4 shows the heat evolution profiles of [C_3S + 30% filler] pastes, formulated using fillers of the *as received* size-class. For the purposes of benchmarking, calorimetry profiles of [C_3S + 30% silica fume] paste are also shown. In general, replacements of C_3S with fillers observably accelerate hydration rates: the main heat flow rate peak (or the main hydration peak) occurs sooner; and the slope of the acceleration

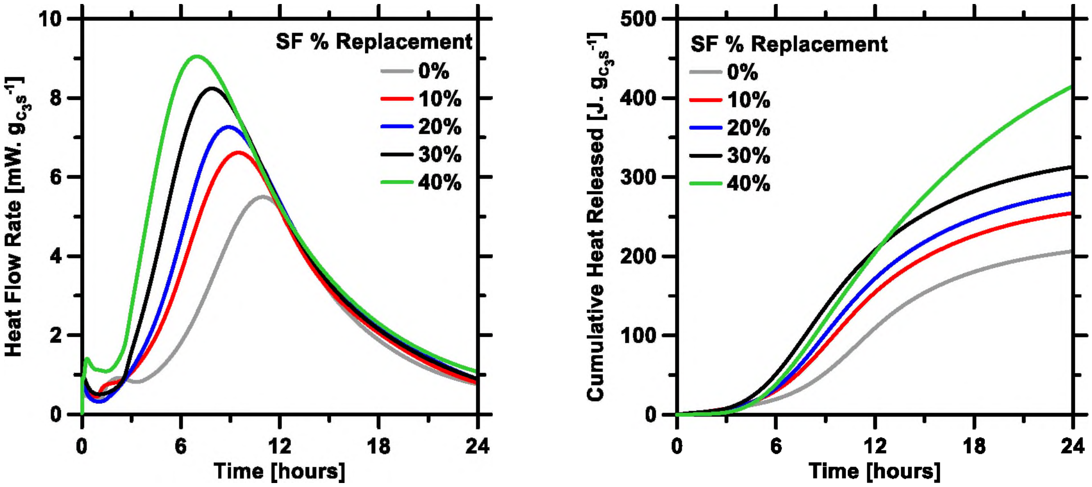

(a) (b)

Figure 3. Isothermal microcalorimetry based determinations of the time-dependent (a) heat flow rate; and (b) cumulative heat released of [C_3S + silica fume (SF)] pastes over a 24 h period [7]. Uncertainty in heat flow rate at the main hydration peak is ± 2%.

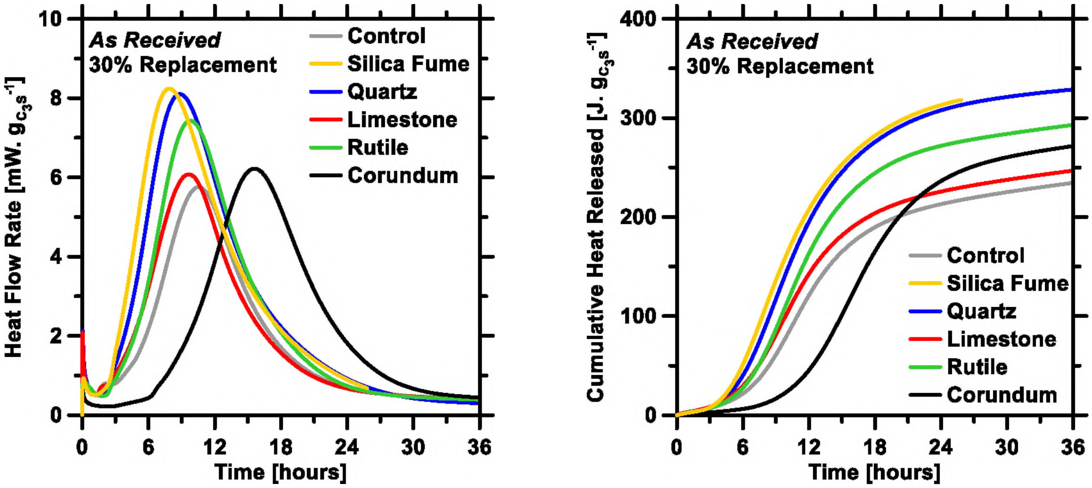

(a) (b)

Figure 4. Isothermal microcalorimetry based determinations of the time-dependent (a) heat flow rate; and (b) cumulative heat released of [C_3S + filler] pastes prepared at 30% replacement level of C_3S by *as received* PSDs of silica fume, quartz, limestone, rutile, and corundum. Uncertainty in heat flow rate at the main hydration peak is ± 2%.

regime is steeper compared to the control (i.e., plain C_3S) paste. This is, expectedly, due to increased C-S-H precipitation on the additional nucleation sites provided by the filler particulates and is in agreement with prior studies [13,28]. In terms of filler performance, silica fume and quartz appear to have similar filler effects — although it should be noted that the SSAs of the two fillers are different, and that silica fume particulates are strongly affected by agglomeration [7]. Enhancements in C_3S hydration rates were also observed for [C_3S + limestone] and [C_3S + rutile] pastes, though to a lesser degree compared to [C_3S + silica fume] and [C_3S + quartz] pastes. These differences in hydration enhancements can, once again, be attributed to differences in physical properties (e.g., SSA and propensity for agglomeration) of the fillers. In Figure 4, it is interesting to note that, hydration of [C_3S + corundum] pastes, during the first several hours after mixing, is suppressed compared to the plain and other binary pastes. This is better highlighted in Figure 4a, wherein the corundum containing paste features a protracted induction period, increased time to the main hydration peak, and lower slope of the acceleration regime. Owing to these alterations in C_3S hydration rates, the cumulative heat released of [C_3S + corundum] paste is expectedly lower compared to that of the plain paste (Figure 4b) at ages < 18 h. At ages > 18 h, however, the trend is reversed, and the cumulative heat released of the [C_3S + corundum] paste surpasses that of the plain paste. Inasmuch as cumulative heat released is a direct indicator of the degree of hydration of C_3S, it can be said that corundum results in lower degree of C_3S hydration during earlier stages of the hydration process. With time, the inhibitory effects of corundum are diminished, and, at later ages, the degree of C_3S hydration recoups and ultimately exceeds that of the plain paste. Overall, results shown in Figure 4 indicate that corundum does not strictly behave as a filler or exert the ‘filler effect’ in a conventional sense, when used to dilute C_3S pastes.

Results shown in Figure 5 support the inferences that were drawn from heat evolution profiles shown in Figure 4. As can be seen, at 24 h, the degree of hydration of C_3S (α) (Figure 5a) in all binary pastes are greater than that of the plain paste (i.e., $\alpha_{control}$ = 0.45), which is in agreement with Figure 4c. Pastes prepared using *as received* quartz and rutile feature higher values of α compared to pastes prepared using *as received* corundum and limestone. The CH contents (Figure 5b-c) of the studied pastes broadly mirror the trends in Figure 5a, that us, in all binary pastes, the CH contents are consistently above the dilution line (i.e., line representing proportional reduction in CH content in relation to the reduction in C_3S content) due to $\alpha_{control} < \alpha_{binary\ pastes}$. This shows that all fillers (including corundum) ultimately result in higher degree of C_3S hydration as compared to the plain paste < 24 hr.

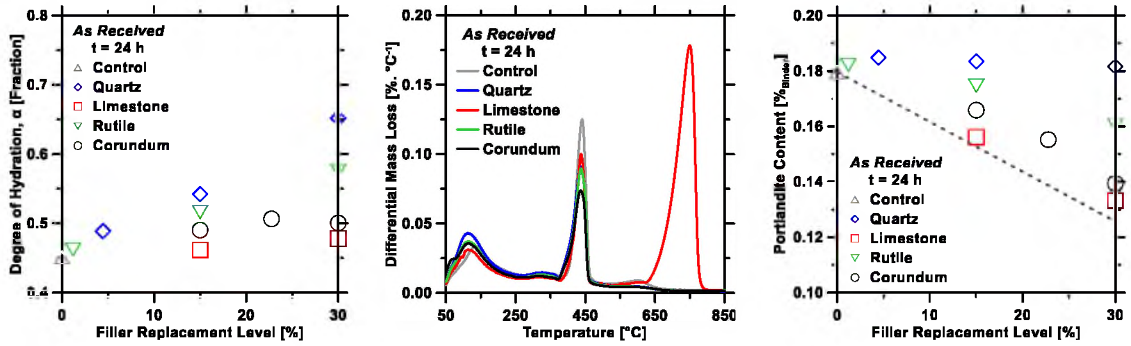

(a) (b) (c)

Figure 5. (a) Isothermal microcalorimetry based determinations of degree of reaction (α) of C_3S; (b) DTG traces showing differential mass loss profiles; and (c) mass contents of portlandite (CH: as $\%_{mass}$ of the binder) as determined from analyses of DTG traces, in [C_3S + 30% *as received* filler] pastes at 24 h. The highest uncertainty in phase quantifications by DTG is ± 2.5%.

Results shown in Figures 4-5 pertain to pastes with different values of SSA_{solid} (total initial solid surface area per unit mass of C_3S; units of m^2. kg_{C3S}^{-1}). However, for direct comparison of filler effects of different additives, it is important to examine hydration kinetics in *area matched* systems. Figure 6 shows the heat evolution profiles of [C_3S + *area matched* filler] pastes, formulated using fillers (i.e., quartz, limestone, rutile, and corundum) belonging to the *as received* size-class. Readers are reminded that, in these pastes, the replacement levels of quartz, rutile, and corundum were adjusted to match the total SSA available, that is, SSA_{solid} of [C_3S + 30% *as received* limestone] paste (i.e., 626.61 m^2. kg^{-1}). As can be seen in Figure 6a, all binary pastes, except for the one prepared using corundum, appear to have a shorter induction period, decreased time to the main hydration peak, and greater slope of the acceleration regime compared to the plain paste – although to a noticeably lesser extent, expectedly due to relatively low SSAs of the fillers (i.e., 151 m^2. kg^{-1}). These alterations in heat evolution profiles distinctly indicate enhancement of C_3S hydration and therefore, nucleation and growth of the main product, C-S-H. The [C_3S + limestone] paste appears to have a shortened induction period and a decreased time to the hydration peak compared to the plain paste and the other [C_3S + *area matched* filler] pastes, but overall the [C_3S + *area matched* filler] pastes prepared with limestone, quartz, and rutile from the *as received* size-class appears to behave broadly similar to the plain paste, and are well within the margins of experimental error (e.g., resulting from paste preparation/mixture design, and standard deviations in SSA estimations and microcalorimetry-determined heat evolution profiles). Going back to Figure 6, the one system that stands out from the rest is the [C_3S + corundum] paste. As can be seen in Figure 6a, the paste features a prolongation of the induction period and a broader hydration peak (which entails slower approach to, as well as slower departure from, the main hydration peak) compared to all other pastes. Owing to such broadening of the hydration peak, the [C_3S + *area matched* corundum] paste has noticeably lower cumulative heat at earlier ages ($t < 18$ h) and higher cumulative heat at later ages compared to the plain and other binary pastes (Figure 6b), similar to the hydration behavior observed in Figure 4 (for pastes with different values of SSA_{solid}). In both cases, corundum suppresses C_3S hydration for the first several hours after mixing. With the progression of time, corundum's inhibitory effects are, firstly, relegated, and, ultimately, reversed, thereby leading to higher degree of C_3S hydration in [C_3S + corundum] paste compared to the plain and other (i.e., limestone-, rutile-, and quartz-containing) binary pastes. This result, shown in Figure 6c, is significant as it shows that in SSA-equivalent binary pastes, corundum – despite suppressing C_3S hydration early on – ultimately (at $t > 18$ h) enhances C_3S hydration to a greater degree than limestone, quartz, and rutile.

Additional calorimetry experiments were conducted using *area matched* pastes that were prepared using *coarse* (Figure 7a) and *fine* (Figure 7b) size-classes of fillers. As can be seen, hydration kinetics of C_3S are broadly similar in binary pastes prepared using *coarse* size-class of limestone, quartz, and rutile. In the case of *fine* size-class fillers, slight differences among the pastes emerge. Pastes prepared with quartz and limestone have nearly identical heat evolution profiles, featuring slightly faster kinetics of C_3S hydration – more specifically, higher heat flow rates at their respective main hydration peaks – compared to the plain and [C_3S + rutile] pastes. Corundum – regardless of its size-class [i.e., either *coarse* (Figure 7a), or *fine* (Figure 7a)] – causes significant retardation in C_3S hydration rates at earlier ages (i.e., $t < 18$h), akin to those shown in Figure 4 and Figure 6.

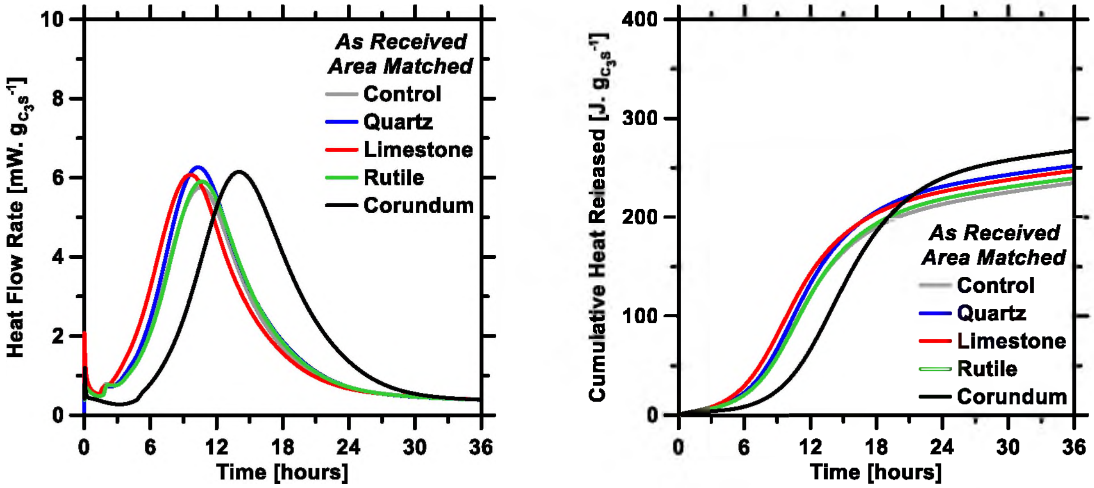

(a) (b)

Figure 6. Isothermal microcalorimetry based determinations of the time-dependent (a) heat flow rate; and (b) cumulative heat released of [C_3S + *area matched* filler] pastes prepared using *as received* PSDs of quartz, limestone, rutile, and corundum as fillers. The *area matched* pastes were prepared by 'matching' their SSA_{solid} to that of [C_3S + 30% *as received* limestone] paste (i.e., 626.61 m^2. kg^{-1}). The amount of each *as received* filler required for *area matching* was calculated in accordance with prior studies [13,29]. Uncertainty in the measured heat flow rate at the main hydration peak is ± 2%.

Based on the results presented above (Figures 4-7), it can be theorized that, in C_3S pastes: (i) the filler effects of limestone, quartz, and rutile are broadly similar; and (ii) corundum does not strictly behave as a filler – like limestone, quartz, and rutile – and causes suppression, as opposed to enhancement, of C_3S hydration kinetics during the first several hours after mixing. It is acknowledged, however, that these inferences, are qualitative as they are merely based on visual observations of heat evolution profiles of the pastes. Past studies [11,16,22,29,32,43] have shown that accurate deduction of changes (i.e., acceleration or deceleration) in C_3S (or OPC) hydration kinetics requires rigorous analyses of various characteristics of heat evolution profiles – not just the time of occurrence or intensity of the main hydration peak. Therefore, for more encompassing analyses, the calorimetry profiles of all *area matched* binary pastes were processed in two different stages. In the first stage, the profiles were processed, using a simple analytical model [13,16,22], to extract three distinct calorimetric parameters: inverse of time to the main hydration peak [h^{-1}]; heat flow rate at the main hydration peak [mW. g_{C3S}^{-1}]; and slope of the acceleration regime [mW. g_{C3S}^{-1}. h^{-1}]. Each of these parameters is an indicator of change in C_3S hydration kinetics; higher and lower values compared to the plain binary system entail relatively superior and inferior dynamics of C_3S hydration, respectively [11,13,16,22,29] . In the second stage, the pBNG modeling platform (described in section 2.2.2.) was used to reproduce the experimentally-measured heat evolution profiles of all pastes. Results obtained from the pBNG model are described later in Section 3.2..

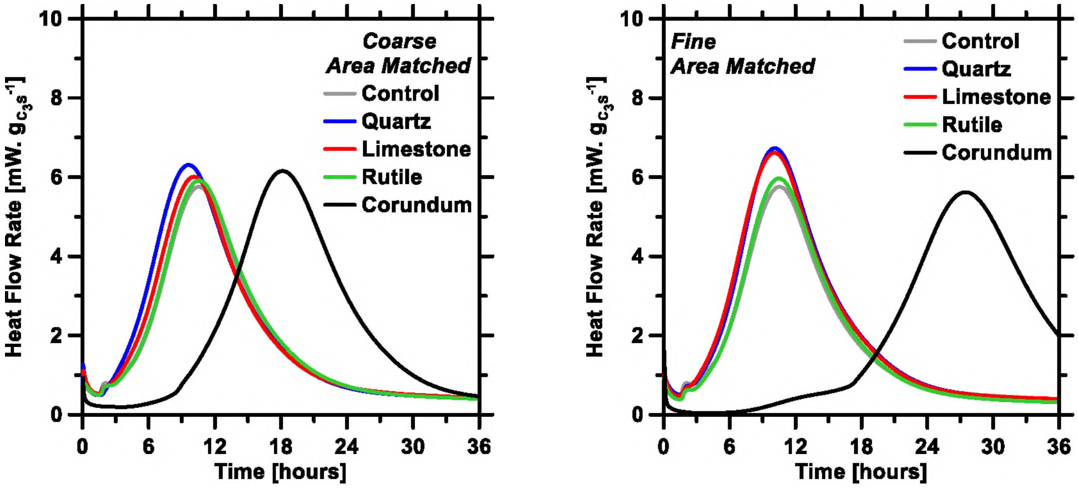

(a) (b)

Figure 7. Isothermal microcalorimetry based determinations of heat evolution profiles of [C_3S + *area matched* filler] pastes prepared using: (a) *coarse* size-class; and (b) *fine* size-class PSDs of fillers (i.e., quartz, limestone, rutile, and corundum). The *area matched* pastes were prepared by 'matching' their SSA_{solid} to that of [C_3S + 30% *coarse* limestone] and [C_3S + 30% *fine* limestone] pastes, for which the SSA_{solid} values are 789.32 m^2. kg^{-1}, and 589.84 m^2. kg^{-1}, respectively. The amount of filler required for area matching was calculated in accordance with prior studies[13,29]. The uncertainty in the measured heat flow rate at the main hydration peak is ± 2%.

Figure 8 shows the calorimetric parameters extracted from heat evolution profiles of all *area matched* binary pastes. As can be seen, all three calorimetric parameters of [C_3S + limestone], [C_3S + quartz], and [C_3S + rutile] pastes are consistently larger than those of the plain paste – thus signifying enhancement of C_3S hydration. In each size-class of the filler (i.e., *as received*, *fine*, and *coarse*), all three calorimetric parameters of binary pastes prepared using limestone, quartz, and rutile are broadly similar to each other; although, there are a few minor differences. In pastes formulated using the *coarse* and *as received* size-classes of quartz and limestone, all three calorimetric parameters (i.e., slope of the acceleration regime; peak heat flow rate; and inverse of time to the peak) are commensurable to their rutile counterpart. However, in pastes prepared using the *fine* size-class of fillers, all three calorimetric parameters of quartz- and limestone-containing pastes are different than rutile, that is, slightly – yet consistently – greater than their rutile counterpart. The exact reasons for this difference cannot be reconciled exclusively from the experimentally-measured heat evolution profiles. Nevertheless, it is hypothesized that the slightly inferior filler effect of rutile is due to agglomeration of its fine particulates, which causes reduction in its effective surface area, thereby leading to fewer nucleation sites for C-S-H as compared to quartz and limestone. The main argument – that particulates of rutile in the *fine* size-class are susceptible to the effects of agglomeration – is justified considering the presence of very fine particulates (i.e., size < 0.1 μm; see Figure 2).

Overall, on the basis of the results shown in Figure 8, it can be said that in binary pastes, at equivalent SSAs, the filler effects of limestone, quartz, and rutile are equivalent. There is, however, a caveat for the equivalence: the effects of particulate agglomeration ought to be minimal or entirely absent. The equivalence in filler effects of limestone and quartz is particularly interesting because several past studies have attempted to compare the performances of the two fillers in cementitious systems. Oey et al. [29] first concluded that, in OPC systems, limestone is a more effective filler compared to quartz. The authors attributed the superior filler effect of limestone to two of its intrinsic characteristics: (i) superior interfacial properties (i.e., low, acute contact angle with respect to C-S-H, thereby leading to more conducive wetting of C-S-H on the surface) that make it energetically more favorable for C-S-H to heterogeneously nucleate on limestone surface; (ii) ability to progressively dissolve in cementitious pore-solution environments, and engage in anion-exchange reactions with the C-S-H phase. In a separate study, Ouyang et al. [52] also reported that limestone has favorable topographical structure that facilitates heterogeneous nucleation of C-S-H on the particulates' surfaces. Ouyang et al. [52] argued that limestone surface, intrinsically, has high affinity to form strong chemical bonds with Ca^{2+} in the pore-solution, which, consequently, facilitates the adhesion of C-S-H nuclei on its surface. In contrast, quartz does not exhibit significant affinity towards the adsorption of Ca^{2+} on its surface – thus rendering its filler effect inferior compared to limestone [52]. In a more recent study, Kumar et al. [13] compared the filler effects of quartz and limestone in C_3S pastes. The authors concluded that the difference between interfacial properties of limestone and quartz (with respect to allowing the nucleation of C-S-H on their surfaces) is insignificant, and, therefore, not responsible for disparities in filler performances of the two materials. Nonetheless, the same study [13] concluded that limestone does indeed partake in anion-exchange reaction with C-S-H, which causes progressive increase in pH of the pore-solution, and, ultimately, leads to larger number of C-S-H nuclei on limestone surfaces. Quartz – unlike limestone – cannot partake in chemical reactions with C-S-H because of its very low solubility (and, therefore, very low dissolution rate). Furthermore, even when quartz does dissolve, silicate species ($H_2SiO_4^{2-}$ and $H_3SiO_4^{-}$) are released, which – unlike CO_3^{2-} anions, released from the dissolution of limestone – cannot partake in anion-exchange reactions with C-S-H (because C-S-H is already rich in silicate content). Results shown in Figure 8 – which show equivalent filler effects of limestone and quartz, across three different sets of *area matched* pastes – contradict the conclusions drawn in prior studies. More specifically, Figure 8 clearly shows that limestone's superior surface structure and its distinct ability to partake in ion-exchange reactions with C-S-H have little to no effect on the hydration of C_3S during the first 24 h. It is conceivable that the use of size-classified PSDs of fillers in this study – as opposed to the use of broad PSDs in prior studies – is at the origin of this contradiction. Such broad PSDs present surplus degrees of freedom in the analyses – such as, disparities in surface area and agglomeration of filler particulates – thus making it difficult to isolate and quantify both (particle) size-independent and size-dependent influences of the filler on C-S-H nucleation and growth. In this study, as size-classified fillers with narrow PSDs were used, it is expected that the influences of these factors were minimal, thus permitting direct comparison of the intrinsic, size-independent filler effects of the additive materials.

Looking beyond quartz, limestone, and rutile, it is important to point out that in [C_3S + corundum] pastes – regardless of the size-class of the additive – all three calorimetric parameters are consistently and substantially lower compared to other binary pastes (Figure 8). These results confirm that corundum does not strictly behave as a filler;

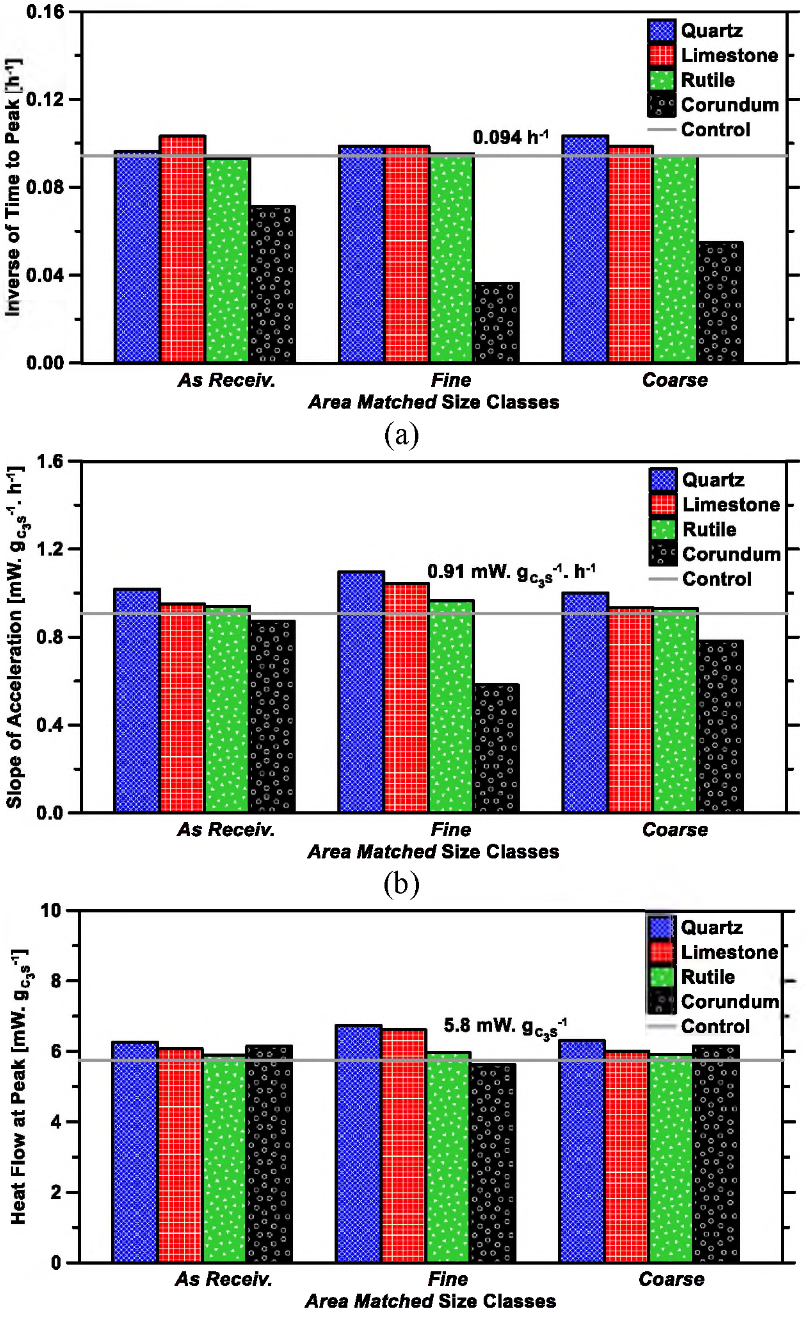

(c)

Figure 8. Calorimetric parameters: (a) inverse of time to the main hydration peak; (b) slope of the acceleration regime; and (c) heat flow at the main hydration peak, extracted from heat evolution profiles of *area matched* binary pastes. Results are grouped on the basis of size-classes of the fillers used to design the pastes. For the *as received*, *fine*, and *coarse* size-classes, the values of SSA_{solid} are 626.61 m^2. kg^{-1}, 789.32 m^2. kg^{-1}, and 589.84 m^2. kg^{-1}, respectively. The solid gray lines represent calorimetric parameters of the plain C_3S paste. For a given system, the uncertainty in each calorimetric parameter is ± 2%.

it results in suppression, rather than enhancement, of C_3S hydration at very early ages. It is worth highlighting that corundum's influence on C_3S hydration is similar to those of other aluminum-rich compounds (e.g., metakaolin, Al_2O_3 nanoparticles, and soluble Al salts). Several prior studies have shown that aluminum-rich compounds suppress C_3S hydration rates at relatively early-ages – resulting in prolonged induction period and delayed occurrence of the main hydration peak [7–9,12,41–43]. On the basis of these studies, it is hypothesized that in [C_3S + corundum] pastes, protraction of the induction period and delay in occurrence of the main hydration peak are, essentially, linked to the discharge of aluminate ($Al(OH)_4^-$) ions from the dissolution of corundum. The aluminate anions, once in the pore-solution of the pastes, are able to adsorb onto C_3S particulates and passivate the adsorbent's surfaces through the precipitation of metastable aluminosilicate complexes [7,8,43] (comprising of aluminate anions, and Ca^{2+} and OH^- ions that form an electrostatic double-layer inclosing the C_3S particulates' surfaces). Such passivation, essentially, blocks dissolution sites (e.g., kinks on etch pits of C_3S surfaces [8,44]) on C_3S particulates' surfaces, thus resulting in deceleration of C_3S's dissolution dynamics and prolongation of the induction period. Potential C-S-H nucleation sites on C_3S particulates' surfaces are also blocked because of the aforesaid surface passivation; this point is elaborated further in section 3.2. With time, as C_3S progressively (and slowly) dissolves, the pH of (or concentration of OH^- ions in) the pore-solution continues to rise. Once the pH rises to CH saturation level (i.e., $pH \approx 12.68$ [8,11,12,18]), the aluminosilicate complexes on C_3S surfaces are rendered thermodynamically unstable [8]. At (and beyond) this point, the aluminate anions detach from C_3S particulates' surfaces [8,12], and stabilize in the solution. This de-passivation of C_3S particulates' surfaces reexposes them to the contacting solution, and allows them, once again, to dissolve rapidly. Such renewed dissolution of C_3S manifests as termination of the induction period and onset of the acceleration regime. The delay in initiation of the acceleration regime of [C_3S + corundum] pastes results in delayed occurrence of the main hydration peak – as can be seen in Figure 8a.

3.2. PHASE BOUNDARY NUCLEATION AND GROWTH (PBNG) SIMULATIONS

The results presented in section 3.1. describe the influence of different types of fillers on C_3S hydration rates by experimental means. To gain further insight the pBNG model, described above in section 2.2.2., was applied. Within the model, for each paste, the reaction-rate profile (i.e., $d\alpha/dt$ as a function of time, as calculated from calorimetry profiles) was used as input. A heterogeneous nucleation and growth mechanism, coupled with an optimization scheme, was then invoked to replicate the input. Towards this, the simulation variables that needed to be varied-and-optimized are: nucleation density ($I_{density}$) of the product; reactive area fraction of the filler (a_{filler}); and product's outward growth rate [$G_{out}(t)$]. The pBNG model was applied, and was successful in reproducing the experimentally-obtained reaction-rate profiles of the plain and binary pastes (figure not shown). Optimum values of simulation parameters for the different pastes were subsequently consolidated; they are shown in Figure 9.

Figure 9a shows that the reactive area fraction (a_{filler}) is 1.00 for nearly all size-classes of limestone, quartz, and corundum (with a singular exception: *fine* size-class of quartz). This implies that in binary pastes prepared with limestone, quartz, and corundum, due to the absence of very fine particulates (size < 0.1 µm) in the PSDs (see Figure 2) of the fillers, the effects of particulate agglomeration are negligible. In contrast, for rutile, the values of a_{filler} are less than unity for the *fine* and *as received* size-classes. This shows that, due to the effects of particulate agglomeration, a fraction of surface area of rutile particulates is unable to partake in (i.e., contribute potential nucleation sites for) nucleation and growth of C-S-H. These results validate the hypothesis made above – that slightly lower values of calorimetric parameters of [C_3S + rutile] pastes, compared to those of [C_3S + limestone] and [C_3S + quartz] pastes (Figure 8), are due to the effects of agglomeration of fine rutile particulates.

Figure 9b shows the product nucleation density ($I_{density}$) in the binary pastes, as estimated from pBNG simulations. Readers are reminded that $I_{density}$ represents the total number of C-S-H nuclei, formed at the nucleation event, normalized by the total surface area of the substrates (i.e., C_3S and filler particulates). As can be seen, with the exception of corundum, $I_{density}$ remains broadly the same across all binary pastes, regardless of the size-class or replacement level of the filler. Furthermore, the magnitudes of $I_{density}$ in all [C_3S + limestone], [C_3S + quartz], and [C_3S + rutile] pastes are commensurable to that of the plain paste (i.e., 5.2 μm^{-2}). These results are consistent with the microscopy-based findings of Berodier and Scrivener [53], wherein the authors had reported that the average distribution of C-S-H nuclei on substrates of filler-containing binary pastes are analogous to those of plain pastes. Importantly, the results entail that, in terms of facilitating heterogeneous nucleation of C-S-H on their topographical sites, limestone, rutile, and quartz are generally equivalent, not just among each other but also with respect to C_3S. The equivalence between $I_{density}$ of limestone-containing and quartz-containing pastes is particularly important as it shows that limestone's superior surface structure (that favors heterogeneous nucleation of C-S-H) [29,52,53] and its ability to partake in anion-exchange reactions with C-S-H (that enhances driving force for C-S-H growth) [13,29] have little to no effect on the nucleation and growth of C-S-H within the first 24 h of hydration. In Figure 9b, it is important to note that $I_{density}$ of corundum-containing pastes, of all size-classes, are consistently lower than the plain and other binary pastes. Remarkably, such decline in $I_{density}$ was also reported in [C_3S + metakaolin] pastes. As with metakaolin-containing pastes, it is hypothesized that [C_3S + corundum] pastes have lower $I_{density}$ due to the release of aluminate anions from the dissolution of corundum. More specifically, the aluminate anions in the pore-solution of the paste progressively adsorb onto both C_3S and corundum particulates, passivating their surfaces, and therefore potential sites for C-S-H nucleation (not just C_3S dissolution sites) are blocked. Such diminution in C-S-H nucleation sites in [C_3S + corundum] pastes scales with SSA (or fineness) of corundum. For instance, corundum of the *fine* size-class, due to its higher SSA, is able to dissolve faster, and, therefore, result in greater decline in $I_{density}$ as compared to its *coarse* size-class counterpart (Figure 9b). Lastly, it should be noted that lower values of C-S-H nucleation density in [C_3S + corundum] pastes manifest as: (i) lower values of the calorimetric parameter, slope of the acceleration regime (Figure 8b); (ii) broader hydration peaks (Figure 7); and (iii) lower and higher cumulative heat released at very early and later ages, respectively (Figure 6b) in all corundum-containing pastes, compared to the plain and other binary pastes. It is posited that such similarity between experiments and simulations validates the pBNG model and its implementation.

Next, the pair of pBNG simulation parameters, a_{filler} and $I_{density}$, were combined (using Equation 3) to calculate N_{nuc}, the total number of product nuclei (per unit mass of

C_3S) that precipitated at the nucleation event in all pastes. The results are shown in Figure 9c. As can be seen, N_{nuc} of all *area matched* [C_3S + limestone], [C_3S + quartz], and [C_3S + rutile] pastes are consistently larger than N_{nuc} of the plain paste (i.e., 2.90×10^{12} g_{C3S}^{-1}). Furthermore, for any given filler (e.g., limestone), among the three size-classes, the values of N_{nuc} scale in relation to the SSA_{solid} (e.g., N_{nuc} of [C_3S + *fine* limestone] > N_{nuc} of [C_3S + *coarse* limestone]). These results confirm that enhancement of C_3S hydration – or increment in the number of C-S-H nuclei that form at the nucleation event – in the aforementioned binary pastes are due to the provision of additional C-S-H nucleation sites by the filler. As such, the intensity of the filler effect increases monotonically with increasing magnitude of the filler's effective surface area. In Figure 9c, it is important to note that in each size-class of the filler (i.e., *as received*, *fine*, and *coarse*), N_{nuc} of binary pastes prepared using limestone, quartz, and rutile are broadly similar to each other (albeit, with a few minor differences that are explained next). In pastes formulated using the *coarse* and *as received* size-classes of fillers, differences in N_{nuc} among limestone-, quartz-, and rutile-containing pastes are minor (i.e., within ± 2 units) and within the margins of experimental errors (enumerated above). However, in pastes formulated using the *fine* size-class of fillers, the differences in N_{nuc} among the three binary pastes are larger (i.e., within ± 6 units) and can be ranked as: limestone > quartz > rutile. It is hypothesized that the lower values of N_{nuc} in rutile- and quartz-containing pastes (as compared to limestone-containing pastes) are exclusively due to the effects of particulate agglomeration – which is clearly highlighted in Figure 9a (for the *fine* size-class). Furthermore, as C-S-H nucleation density in these pastes are identical (Figure 9b), it can be said that the inherent filler effects of limestone, quartz, and rutile are approximately equivalent. Simply put, at equivalent SSAs and replacement levels, limestone, quartz, and rutile are expected to produce similar enhancements in C_3S hydration (directly in relation to their SSA), provided that the effects of particulate agglomeration are entirely negated.

Going back to Figure 9c, it can be seen that owing to the reduction in $I_{density}$ (Figure 9b), the values of N_{Nuc} in [C_3S + corundum] pastes, in each size-class, are consistently lower than the plain paste (i.e., 2.90 x 10^{12} g_{C3S}^{-1}) and all other binary pastes of the same size-class. Importantly, these results confirm that suppression of early-age hydration of C_3S by corundum is directly linked with its ability to dissolve and release aluminate anions into the pore-solution of the paste. This is precisely why *fine* corundum – which is expected to dissolve faster, owing to its higher SSA compared to other PSDs (see Table 1) – results in faster release of aluminate anions, which subsequently passivate the substrates' surfaces thus blocking more potential C-S-H nucleation sites on C_3S and corundum particulates' surfaces than its *coarse* and *as received* counterparts.

It is pointed out that, in pBNG simulations, in addition to a_{filler} and $I_{density}$, $G_{out}(t)$ was also varied. The optimal function forms of $G_{out}(t)$, that were acquired for the control and [C_3S + filler] pastes, were broadly similar to each other (Figure 10), with the exception of the forms obtained for [C_3S + corundum] pastes. This suggests – as has also reported in prior studies [29,49,53] – that while fillers substantially affect the nucleation of C-S-H (at the nucleation event), their influence on the post-nucleation growth of C-S-H is predominantly driven by its supersaturation in the solution [11,15]. With that noted, the outward product growth rate of *as received* and *coarse* [C_3S + *area matched* corundum] pastes are noticeably lower compared to the control paste's growth rate for the initial 20 h or so of hydration (Figure 10a and 10b). Similarly presented in Lapeyre

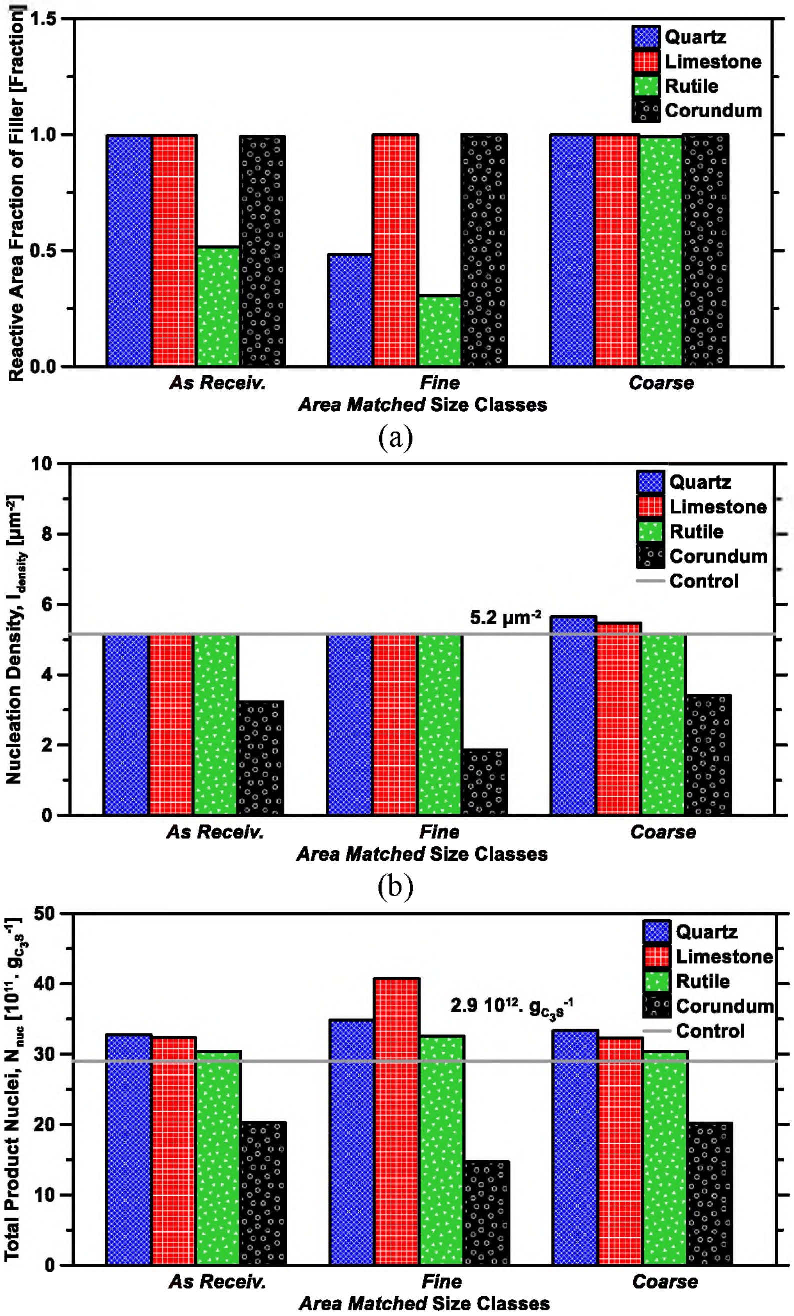

(a)

(b)

(c)

Figure 9. pBNG simulation parameters: (a) reactive area fraction of the filler (a_{filler}); (b) product nucleation density ($I_{density}$); and (c) total number of supercritical product nuclei (N_{nuc}), obtained from numerical-reproduction of experimentally-measured reaction-rate profiles of *area matched* binary pastes. Results are grouped on the basis of size-classes of fillers used to design the pastes. For the *as received*, *fine*, and *coarse* size-classes, the values of SSA_{solid} are 626.61 m^2. kg^{-1}, 789.32 m^2. kg^{-1}, and 589.84 m^2. kg^{-1}, respectively. The solid gray line represents simulation parameters of the plain C_3S paste. For a given system, the uncertainty in each calorimetric parameter is ± 2%.

and Kumar [7] and their consecutive work [43], the suppression of $G_{out}(t)$, observed in [C_3S + corundum] pastes is thought to occur due to some of the remaining aluminate anions in solution adsorbing onto C–S–H, inhibiting C-S-H growth. C-S-H growth is noticeably suppressed for an extended timeframe (i.e., 30 h) in Figure 10c, as compared to 10a and 10b, after which the effects of aluminate anions on $G_{out}(t)$ of the paste prepared with *fine* corundum is lessened. The extended suppression of $G_{out}(t)$ in Figure 10c is thought to be a result of corundum dissolving at a faster rate and/or to a greater degree due to increased SSA in the paste system compared to the *as received* and *coarse* [C_3S + *area matched* corundum] pastes, and therefore releasing a greater amount of aluminate anions in solution to inhibit both C-S-H nucleation and growth.

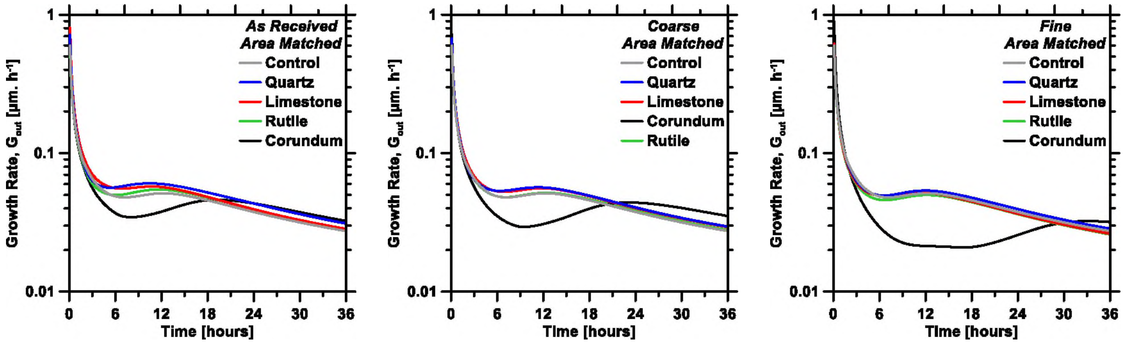

(a) (b) (c)

Figure 10. The temporal evolution of outward growth rate of the product ($G_{out}(t)$), as obtained from pBNG simulations, for: [C_3S + *area matched* filler] pastes prepared with (a) *as received*, (b) *coarse*, and (c) *fine* size-classes. For the *as received*, *coarse*, and *fine* size-classes, the values of SSA_{solid} are 626.61 $m^2. kg^{-1}$, 589.84 $m^2. kg^{-1}$, and 789.32 $m^2. kg^{-1}$, respectively.

In the above discussions, various results obtained from the pBNG simulations have been compared with experimental results (i.e., the heat evolution profiles, and the calorimetric parameters that were extracted directly from the profiles). Figure 11 directly compares the principal pBNG simulation parameter (i.e., N_{nuc}) against two calorimetric parameters (i.e., slope of the acceleration regime; and the inverse of time to the main hydration peak). As can be seen, across a wide range of pastes – formulated using different types and contents of fillers – the correlation between simulations and experiments is good. Binary pastes (compared to the plain paste), feature higher calorimetric parameter values, and, accordingly, higher values of N_{nuc}. Likewise, in all [C_3S + corundum] pastes, owing to the suppression of C_3S hydration at very early-ages (including the nucleation event), calorimetric parameters as well as N_{nuc} values are lower compared to the plain and other binary pastes. In the context of limestone, it is important to point out that the pBNG model – as presented in Section 2.2.2. – accounts for the physical manifestations of the filler effect (i.e., nucleation of C-S-H on additional limestone surfaces) but not the chemical manifestations (i.e., anion-exchange reaction between limestone and C-S-H). Therefore, on the basis of the good agreement between simulations and experiments shown in Figure 11, it can be said that the filler effect of limestone is predominantly due to its physical ability to allow heterogeneous nucleation of C-S-H – with little to no contribution from its ability to engage in anion-exchange reaction with C-S-H. Overall, Figure 11 confirms that the pBNG model is able to capture the essence of calorimetry experiments, and that N_{nuc} – a simulation parameter – is able to serve as a singular, unified measure of the filler effect of different types of fillers.

Overall, the results presented in this section show that the filler effects of limestone, quartz, and rutile – in terms of enhancing early-age hydration of C_3S – are equivalent, and solely dictated by magnitudes of additional surface area they provide for heterogeneous nucleation of C-S-H. In spite of this equivalence, minor differences in hydration kinetics of [C_3S + filler] pastes with equivalent SSAs may arise. Nonetheless, these differences can be reconciled exclusively on the bases of the effects of particulate agglomeration. [C_3S + corundum] pastes do not feature the same acceleration in C_3S hydration rates as the other [C_3S + filler] pastes do. Rather, corundum suppresses C_3S hydration rates for several hours after mixing. The influence of corundum on C_3S hydration is better shown in Figure 12, which features four different PSDs and five different replacement levels of corundum in the pastes. As can be seen, with increasing replacement levels of C_3S with corundum, the hydration peak occurs later and broader (Figure 12a). These trends, pertaining to the main hydration peak, encompass pastes with different PSDs of corundum, thus confirming the argument presented in Section 2.0 – that in [C_3S + corundum] pastes, the early-age suppression of C_3S hydration is dictated by corundum content (not its PSD or fineness of its particulates). As shown in Figure 12b, after several hours of suppressed C_3S hydration, the cumulative heat of – and, therefore, the degree of C_3S hydration in – [C_3S + corundum] pastes converge to a higher value compared to the plain paste. Pastes with low corundum content surpass the cumulative heat of plain paste earlier compared to those prepared with high corundum content. Overall, the results show that regardless of the PSD and content of corundum, the hydration-suppression effect of corundum diminishes with time, and, at later ages, the degree of C_3S hydration recoups and ultimately exceeds that of the plain paste.

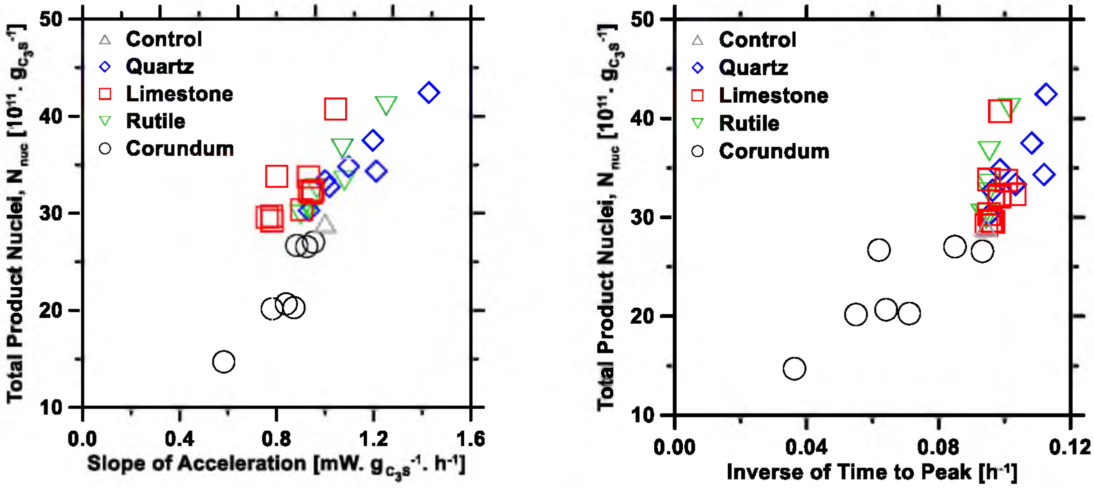

(a) (b)

Figure 11. pBNG simulation parameter (i.e., N_{nuc}: total number of supercritical nuclei of C-S-H formed per gram of C_3S) compared against experimentally-derived calorimetric parameters: (a) slope of the acceleration regime; and (b) inverse of time to the main hydration peak.

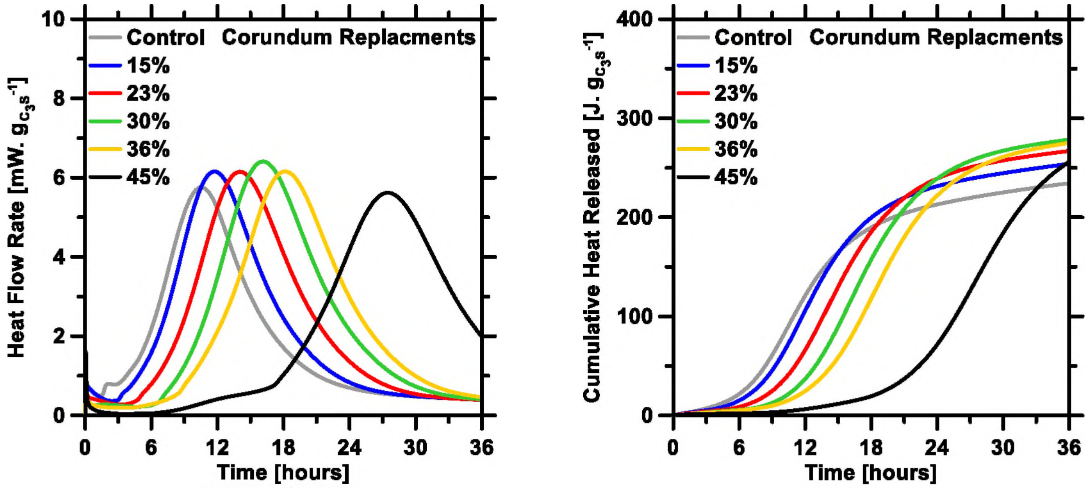

(a) (b)

Figure 12. Isothermal microcalorimetry based determinations of the time-dependent: (a) heat flow rate; and (b) cumulative heat released of plain and [C_3S + corundum] pastes prepared using different PSDs and replacement levels of corundum. The 15%, 23%, 30%, 36%, and 45% replacement levels of corundum, shown in the legends, correspond to *as received*, *as received*, *intermediate*, *coarse*, and *fine* size-classes, respectively. Uncertainty in the measured heat flow rate at the main hydration peak is ± 2%.

4. SUMMARY AND CONCLUSIONS

A series of original experiments and a modified form of the phase boundary nucleation and growth (pBNG) model were employed to better understand the effect of filler materials – including the well-explored limestone and quartzand the less-explored corundum and rutile– on early-age hydration of C_3S. Emphasis was given to use size-classified fillers, with similar PSDs, so as to enable comparison of their intrinsic, size-independent and size-dependent filler effects that are devoid of any complexities (e.g., disparities in specific surface area and particulate agglomeration). Through such comparisons, this study attempts to rank the aforementioned fillers in accordance with magnitudes of their size-independent filler effects.

The results clearly show that when size-classified PSDs are used, the filler effects of limestone, quartz, and rutile are broadly similar. For each filler, the filler effect is purely a physical mechanism, principally driven by the additional surface area provided by its particulates. As fineness or replacement level of the filler in the paste increases, hydration of C_3S is proportionally enhanced owing to the augmentation in potential sites for heterogeneous nucleation of C-S-H. In spite of the equivalence in filler effects of limestone, quartz, and rutile, minor differences in hydration kinetics of [C_3S + filler] pastes with equivalent specific surface areas may arise. These differences, however, can be attributed exclusively to agglomeration of fine particulates of the filler, which result in reduction of surface area and, therefore, decline in the number of C-S-H nucleation sites. Contrary to what has been reported in prior studies, results obtained from this study clearly show that limestone's superior surface structure (that favors heterogeneous nucleation of C-S-H) and its distinct ability to partake in anion-exchange reactions with C-S-H (that enhances driving force for C-S-H growth) have little to no effect on C_3S hydration kinetics during the first 24 h.

Experimental results – supported by pBNG simulations – also show that while corundum does influence C_3S hydration kinetics, it does not strictly function as a filler like limestone and quartz. In [C_3S + corundum] pastes, with increasing replacement levels of C_3S with corundum, the hydration of C_3S, is increasingly suppressed, resulting in protracted induction periods and delayed occurrences of the main hydration peak. Such suppression of C_3S hydration is attributed to aluminate anions ($Al(OH)_4^-$) – released from the dissolution of corundum – that adsorb onto anhydrous particulates' surfaces, and inhibit sites of C_3S dissolution and heterogeneous nucleation of C-S-H. With the progression of time, the inhibitory effects of corundum are diminished and ultimately reversed. At later ages, the degree of C_3S hydration in [C_3S + corundum] paste surpasses that of plain C_3S paste as well as those of binary pastes formulated using limestone, quartz, or rutile with equivalent SSAs. This shows that in SSA-equivalent binary pastes, corundum – despite suppressing C_3S hydration early on – ultimately enhances C_3S hydration more than limestone, quartz, and rutile.

Overall, the results and discussions presented in this study provide novel insights into the mechanistic origins of filler effect – of conventional and widely-used fillers as well as less-explored ones – in a pure-phase, cementitious systems[s].

ACKNOWLEDGEMENTS

Funding for this study was provided by the National Science Foundation (CMMI: 1661609 and CMMI: 1932690). All experiments and simulations were conducted at the Materials Research Center, Missouri S&T.

REFERENCES

[1] H.G. van Oss, USGS, Cement – Mineral Commodity Summaries., U.S. Department of the Interior, 2018.

[2] J.J. Biernacki, J.W. Bullard, G. Sant, K. Brown, F.P. Glasser, S. Jones, T. Ley, R.A. Livingston, L. Nicoleau, J. Olek, F. Sanchez, R. Shahsavari, P.E. Stutzman, K. Soblev, T. Prater, Cements in the 21st century: Challenges, perspectives, and opportunities, 100 (2017) 27.

[3] E. Gartner, T. Sui, Alternative cement clinkers, Cement and Concrete Research. 114 (2018) 27–39. https://doi.org/10.1016/j.cemconres.2017.02.002.

[4] E. Worrell, L. Price, N. Martin, C. Hendriks, L.O. Meida, Carbon dioxide emissions from the global cement industry 1, Annual Review of Energy and the Environment. 26 (2001) 303–329.

[5] E. Gartner, H. Hirao, A review of alternative approaches to the reduction of CO2 emissions associated with the manufacture of the binder phase in concrete, Cement and Concrete Research. 78, Part A (2015) 126–142. https://doi.org/10.1016/j.cemconres.2015.04.012.

[6] M. Schneider, Process technology for efficient and sustainable cement production, Cement and Concrete Research. 78, Part A (2015) 14–23. https://doi.org/10.1016/j.cemconres.2015.05.014.

[7] J. Lapeyre, A. Kumar, Influence of pozzolanic additives on hydration mechanisms of tricalcium silicate, Journal of the American Ceramic Society. 101 (2018) 3557–3574. https://doi.org/10.1111/jace.15518.

[8] E. Pustovgar, R.K. Mishra, M. Palacios, J.-B. d'Espinose de Lacaillerie, T. Matschei, A.S. Andreev, H. Heinz, R. Verel, R.J. Flatt, Influence of aluminates on the hydration kinetics of tricalcium silicate, Cement and Concrete Research. 100 (2017) 245–262. https://doi.org/10.1016/j.cemconres.2017.06.006.

[9] F. Bellmann, H.-M. Ludwig, Analysis of aluminum concentrations in the pore solution during hydration of tricalcium silicate, Cement and Concrete Research. 95 (2017) 84–94. https://doi.org/10.1016/j.cemconres.2017.02.020.

[10] J.J. Thomas, H.M. Jennings, J.J. Chen, Influence of nucleation seeding on the hydration mechanisms of tricalcium silicate and cement, Journal of Physical Chemistry C. 113 (2009) 4327–4334. https://doi.org/10.1021/jp809811w.

[11] T. Oey, A. Kumar, G. Falzone, J. Huang, S. Kennison, M. Bauchy, N. Neithalath, J.W. Bullard, G. Sant, The Influence of Water Activity on the Hydration Rate of Tricalcium Silicate, J. Am. Ceram. Soc. 99 (2016) 2481–2492. https://doi.org/10.1111/jace.14181.

[12] L. Nicoleau, E. Schreiner, A. Nonat, Ion-specific effects influencing the dissolution of tricalcium silicate, Cement and Concrete Research. 59 (2014) 118–138. https://doi.org/10.1016/j.cemconres.2014.02.006.

[13] A. Kumar, T. Oey, G. Falzone, J. Huang, M. Bauchy, M. Balonis, N. Neithalath, J. Bullard, G. Sant, The filler effect: The influence of filler content and type on the hydration rate of tricalcium silicate, Journal of American Ceramics Society. 100 (2017) 3316–3328.

[14] J.J. Thomas, A New Approach to Modeling the Nucleation and Growth Kinetics of Tricalcium Silicate Hydration, Journal of the American Ceramic Society. 90 (2007) 3282–3288. https://doi.org/10.1111/j.1551-2916.2007.01858.x.

[15] J.W. Bullard, G.W. Scherer, J.J. Thomas, Time dependent driving forces and the kinetics of tricalcium silicate hydration, Cement and Concrete Research. 74 (2015) 26–34.

[16] R. Cook, H. Ma, A. Kumar, Mechanism of tricalcium silicate hydration in the presence of polycarboxylate polymers, SN Applied Sciences. 1 (2019) 145. https://doi.org/10.1007/s42452-018-0153-1.

[17] H.F. Taylor, Cement chemistry, Thomas Telford, 1997.

[18] A. Kumar, S. Bishnoi, K.L. Scrivener, Modelling early age hydration kinetics of alite, Cement and Concrete Research. 42 (2012) 903–918. https://doi.org/10.1016/j.cemconres.2012.03.003.

[19] H.M. Jennings, S.K. Johnson, Simulation of microstructure development during the hydration of a cement compound, Journal of the American Ceramic Society. 69 (1986) 790–795.

[20] J.W. Bullard, H.M. Jennings, R.A. Livingston, A. Nonat, G.W. Scherer, J.S. Schweitzer, K.L. Scrivener, J.J. Thomas, Mechanisms of cement hydration, Cement and Concrete Research. 41 (2011) 1208–1223.

[21] G.W. Scherer, J. Zhang, J.J. Thomas, Nucleation and Growth Models for Hydration of Cement, Cement & Concrete Research. 42 (2012) 982–993.

[22] W. Meng, P. Lunkad, A. Kumar, K. Khayat, Influence of Silica Fume and Polycarboxylate Ether Dispersant on Hydration Mechanisms of Cement, The Journal of Physical Chemistry C. 120 (2016) 26814–26823.

[23] W.A. Gutteridge, J.A. Dalziel, Filler cement: the effect of the secondary component on the hydration of Portland cement: part I. A fine non-hydraulic filler, Cement and Concrete Research. 20 (1990) 778–782.

[24] W.A. Gutteridge, J.A. Dalziel, Filler cement: the effect of the secondary component on the hydration of Portland cement: part 2. fine hydraulic binders, Cement and Concrete Reseach. 20 (1990) 853–861.

[25] V. Rahhal, R. Talero, Early Hydration of Portland Cement With Crystalline Mineral Additions, Cement and Concrete Reseach. 35 (2005) 1285–1291.

[26] R.L. Sharma, S.P. Pandey, Influence of Mineral Additives on the Hydration Characteristics of Ordinary Portland Cement, Cement and Concrete Reseach. 29 (1999) 1525–1529.

[27] K. De Weerdt, M.B. Haha, G. Le Saout, K.O. Kjellsen, H. Justnes, B. Lothenbach, Hydration mechanisms of ternary Portland cements containing limestone powder and fly ash, Cement and Concrete Research. 41 (2011) 279–291.

[28] A.R. Jayapalan, B.Y. Lee, S.M. Fredrich, K.E. Kurtis, Influence of Additions of Anatase TiO2 Nanoparticles on Early-Age Properties of Cement-Based Materials, Transportation Research Record. 2141 (2010) 41–46.

[29] T. Oey, A. Kumar, J.W. Bullard, N. Neithalath, G. Sant, The filler effect: The influence of filler content and surface area on cementitious reaction rates, Journal of the American Ceramic Society. 96 (2013) 1978–1990. https://doi.org/10.1111/jace.12264.

[30] J. Baron, C. Douvre, Technical and economical aspects of the use of limestone filler additions in cement, World Cement. 18 (1987) 100–104.

[31] D.P. Bentz, Modeling the influence of limestone filler on cement hydration using CEMHYD3D, Cement and Concrete Composites. 28 (2006) 124–129.

[32] A.M. Ley-Hernandez, J. Lapeyre, R. Cook, A. Kumar, D. Feys, Elucidating the Effect of Water Content on Hydration Mechanisms of Cement, ACS Omega. 3 (2018) 5092–5105. https://doi.org/10.1021/acsomega.8b00097.

[33] M. Antoni, J. Rossen, F. Martirena, K. Scrivener, Cement substitution by a combination of metakaolin and limestone, Cement and Concrete Research. 42 (2012) 1579–1589.

[34] K. Vance, M. Aguayo, T. Oey, G. Sant, N. Neithalath, Hydration and strength development in ternary portland cement blends containing limestone and fly ash or metakaolin, Cement and Concrete Composites. 39 (2013) 93–103.

[35] A.M. Ramezanianpour, R.D. Hooten, A study on hydration, compressive strength, and porosity of Portland-limestone cement mixes containing SCMs, Cement and Concrete Composites. 51 (2014) 1–13.

[36] M. Boháč, M. Palou, R. Novotnỳ, J. Másilko, D. Všianský, T. Staněka, Investigation on early hydration of ternary Portland cement–blast–furnace slag–metakaolin blends, Construction and Building Materials. 64 (2014) 333–341.

[37] T. Matschei, B. Lothenbach, F.P. Glasser, The role of calcium carbonate in cement hydration, Cement and Concrete Research. 37 (2007) 551–558.

[38] A. Kumar, T. Oey, S. Kim, D. Thomas, S. Badran, J. Li, F. Fernandes, N. Neithalath, G. Sant, Simple methods to estimate the influence of limestone fillers on reaction and property evolution in cementitious materials, Cement and Concrete Composites. 42 (2013) 20–29.

[39] A. Kumar, T. Oey, G.P. Falla, R. Henkensiefken, N. Neithalath, G. Sant, A comparison of intergrinding and blending limestone on reaction and strength evolution in cementitious materials, Construction and Building Materials. 43 (2013) 428–435.

[40] W. Meng, A. Kumar, K. Khayat, Effect of Silica Fume and Slump-Retaining PCE on the Development of Properties of Portland Cement Paste, Cement and Concrete Composites. 99 (2019) 181–190. https://doi.org/10.1016/j.cemconcomp.2019.03.021.

[41] F. Begarin, S. Garrault, A. Nonat, L. Nicoleau, Hydration of alite containing aluminium, Advances in Applied Ceramics. 110 (2011) 127–130. https://doi.org/10.1179/1743676110Y.0000000007.

[42] G. Land, D. Stephan, Controlling cement hydration with nanoparticles, Cement and Concrete Composites. 57 (2015) 64–67. https://doi.org/10.1016/j.cemconcomp.2014.12.003.

[43] J. Lapeyre, H. Ma, A. Kumar, Influence of Particle Size Distribution of Metakaolin on Hydration Kinetics of Tricalcium Silicate, Journal of the American Ceramic Society. 102 (2019) 5976–5988. https://doi.org/10.1111/jace.16467.

[44] A.C. Lasaga, A. Luttge, Variation of crystal dissolution rate based on a dissolution stepwave model, Science. 291 (2001) 2400–2404.

[45] Standard Guide for Wet Sieve Analysis of Ceramic Whiteware Clays, 2014.

[46] G.W. Scherer, Models of Confined Growth, Cement & Concrete Research. 42 (2012) 1252–1260.

[47] S. Garrault, Study of C-S-H growth on C3S surface during its early hydration, Materials and Structures. 38 (2005) 435–442. https://doi.org/10.1617/14343.

[48] A. Bazzoni, S. Ma, Q. Wang, X. Shen, M. Cantoni, K.L. Scrivener, The Effect of Magnesium and Zinc Ions on the Hydration Kinetics of C3S, Journal of the American Ceramic Society. 97 (2014) 3684–3693.

[49] G.W. Scherer, F. Bellmann, Kinetic analysis of CSH growth on calcite, Cement and Concrete Research. (2016). http://www.sciencedirect.com/science/article/pii/S0008884616306457 (accessed January 30, 2017).

[50] J.A. Nelder, R. Mead, A Simplex Method for Function Minimization, The Computer Journal. 7 (1965) 308–313. https://doi.org/10.1093/comjnl/7.4.308.

[51] F. Bellmann, G.W. Scherer, Analysis of CSH growth rates in supersaturated conditions, Cement and Concrete Research. (2017). http://www.sciencedirect.com/science/article/pii/S0008884616301739.

[52] X. Ouyang, D.A. Koleva, G. Ye, K. van Breugel, Insights into the mechanisms of nucleation and growth of C–S–H on fillers, Mater Struct. 50 (2017) 213. https://doi.org/10.1617/s11527-017-1082-y.

[53] E. Berodier, K. Scrivener, Understanding the Filler Effect on the Nucleation and Growth of C-S-H, Journal of the American Ceramic Society. 97 (2014) 3764–3773.

V. PREDICTION OF COMPRESSIVE STRENGTH OF CONCRETE: CRITICAL COMPARISOM OF PERFORMANCE OF A HYBRID MACHINE LEARNING MODEL WITH STANDALONE MODELS

Rachel Cook[1], Jonathan Lapeyre[1], Hongyan Ma[2], and Aditya Kumar[1]

1. Department of Materials Science and Engineering, Missouri University of Science and Technology (S&T), B49 McNutt Hall, 1400 N. Bishop, Rolla, MO 65409, USA.

2. Department of Civil, Architectural and Environmental Engineering, Missouri University of Science and Technology (S&T), Rolla, MO 65409, USA.

ABSTRACT

The use of machine learning (ML) techniques to model quantitative composition-property relationships in concrete has received substantial attention in the past few years. This paper presents a novel hybrid ML model (RF-FFA) for prediction of compressive strength of concrete by combining the random forests (RF) model with the firefly algorithm (FFA). The firefly algorithm is utilized to determine optimum values of two hyper-parameters (i.e., number of trees and number of leaves per tree in the forest) of the RF model in relation to the nature and volume of the dataset. The RF-FFA model was trained to develop correlations between input variables and output of two different categories of datasets; such correlations were subsequently leveraged by the model to make predictions in previously untrained data-domains. The first category included two separate datasets featuring highly nonlinear and periodic relationship between input variables and output, as given by trigonometric functions. The second category included two real-world datasets, comprised of mixture design variables of concretes as inputs and their age-dependent compressive strengths as outputs. The prediction performance of the hybrid RF-FFA model was benchmarked against commonly used standalone ML models – support vector machine (SVM), multilayer perceptron artificial neural network (MLP-ANN), M5Prime model tree algorithm (M5P), and RF. The metrics used for evaluation of prediction accuracy included five different statistical parameters as well as a composite performance index (CPI). Results show that the hybrid RF-FFA model consistently outperforms the standalone ML models in terms of prediction accuracy – regardless of the nature and volume of datasets.

Keywords: Machine Learning; Concrete; Compressive Strength; Random Forests; Firefly Algorithm.

1. INTRODUCTION

The idea of using data-driven methods – such as supervised machine learning (ML) – for prediction and optimization of materials' performance forms the premise of the United States Materials Genome Initiative [1,2]. In pursuit of the idea, researchers from various scientific domains have compiled extensive datasets of materials, and subsequently employed ML models to better understand the underlying quantitative composition-performance correlations [3–6]. Knowledge of such correlations, for any given material, can be leveraged to mitigate the cost and time involved in an Edisonian approach – involving rigorous and iterative synthesis-testing/analyses cycles [7] – to predict a material's properties, or to design a new material that meets a desired set of performance criteria.

Concrete – the most produced-and-used material in the world – has garnered the interest of several researchers working the area of ML. The focus of various research articles [8–22] has been to employ ML models to predict concretes' properties (e.g., compressive strength and rheological parameters) using their mixture design variables (e.g., contents of cement, water, mineral additive(s), and admixture(s)) and age as inputs. Among concrete's properties, compressive strength is deemed relatively more important for quality control, and widely used as the primary specification criterion for construction of structures. Furthermore, compressive strength of concrete is very well correlated with other mechanical properties (e.g., elastic modulus, flexural strength), and, therefore, can be used to qualitatively estimate the overall mechanical stability and survivability of the structure [23,24]. Because of these reasons, most of the aforementioned studies have focused on prediction of compressive strength of concrete. The utilization of ML models – as opposed to Edisonian approaches, or simple linear regression models – is to overcome complexities pertaining to: (i) the staggeringly large compositional degrees of freedom in concrete (i.e., mixture design variables, permutations and combinations of which can vary within wide ranges and exert significant influence on properties), and (ii) the inherent nonlinear relationships between mixture design variables and properties of concrete. To be more specific on the latter point, the properties of concrete are complex – highly nonlinear, and, often, non-monotonous – functions of mixture design variables. For example, within the cement paste component of concrete, compressive strength decreases with increasing water-to-cement ratio (*w/c*, mass basis); however, this relationship exhibits non-differentiability at the critical *w/c* of 0.42, below which the paste becomes water-deficient [25,26]. This relationship between the *w/c* and compressive strength is further convoluted when a fraction of the cement is replaced with a reactive mineral additive (e.g., fly ash and blast furnace slag) [27,28]. Therefore, sophisticated approaches, such as ML, are required to reveal the hidden, and complex, semi-empirical rules that govern the correlation between mixture design and properties of concrete.

Majority of past studies, focused on prediction of compressive strength of concrete, have used nonlinear regression based ML models [i.e., ANN: artificial neural network [29] or SVM: support vector machine [30]] – presumably because of nonlinear correlations between mixture design variables and properties of concrete. Notable among these are studies conducted by [8,10–12,16,18,19,21,31,32]. The studies have shown that both ANN and SVM models, when trained using a sufficiently large dataset, can predict compressive strength of concrete with reasonable accuracy (i.e., coefficient of determination, $R^2 \geq 0.90$). However, it has been reported that ANN and SVM models are unreliable in making predictions in data-domain that features highly nonlinear, periodic functional relationship between one or more input variables and the output [33–35]. This is because both ANN and SVN models employ local search or optimization algorithms (e.g., back-propagation algorithm used in ANN), which are faced with an inherent drawback of getting trapped in local minima – especially when the functional relationship between input variables and output comprises of multiple local minima (e.g., periodic trigonometric functions) – rather than converging to the global minima. Because of this drawback, with every re-run of ANN or SVM, during the training period (i.e., when different subsets of the same dataset are used to train the models) the convergence could occur at different local minima, thus resulting in disparate prediction performances (i.e., the ability to reliably predict outputs using previously unseen input variables) during the testing [33–35]. This deficiency can be amended by using algorithms based on Genetic programing [17,31]. Alternatively, bootstrap aggregation of outputs of several models developed from various subsets of the training dataset – for example, by using bagging, voting, or stacking approaches [11,36] – can also be used. However such techniques could slow down the rate of convergence, or, in the worst case, result in overfitting [37]. This issue of ANN and SVM models, pertaining to their inferior performance on datasets featuring periodic input-output relationship, is further examined in Section 4.1.

ANN and SVM models have another drawback – the objective function produced by them are difficult to interpret, and, therefore, difficult (albeit not impossible) to employ for optimization purposes. This is because the functional relationship between input variables and output is not yielded as a transparent mathematical formula. To overcome this limitation, in some recent studies [9,11,16,17,21] "decision trees" based ML models have been employed. Decision trees are essentially rules-based models, wherein the training dataset is classified into multiple independent subsets, and subsequently processed using a collection of linear or nonlinear regression methods to develop multiple (transparent) functional relationships between input variables and output. Notable among these are application of the M5Prime [M5P: [38,39]] [9,16,40] and Random forests [RF: [41]] [21,32] models. Deepa et al. [40] and Behnood et al. [9] showed that prediction accuracy of the M5P model was superior compared to the ANN model. Similarly, as per the R^2 values reported by Young et al. [21], predictions of concrete compressive strength using the RF model were more accurate (albeit not comprehensively) compared to those using ANN and SVM models.

To the best of authors' knowledge, the prediction performances of M5P and RF models (i.e., in terms of predicting the compressive strength of concrete) have not been compared. Notwithstanding, the RF model is hypothesized to be superior compared to the M5P model; this hypothesis will be corroborated later in Section 4.. The premise of this hypothesis is that the M5P model assumes multivariate linear relationship between input variables and output in each subset of the training data [38,39]. More specifically, the training dataset is split into multiple subsets until in each subset a simple, linear input-output correlation can be established. Due to this limitation – like in the ANN and SVM models – predictions made by the M5P model in domains that feature highly nonlinear and/or periodic relationship between input variables and output are expected to be inaccurate. The RF model, on the other hand, does not suffer from this limitation because of its ability to handle continuous and discrete variables over both monotonous and non-monotonous domains [41]. Notwithstanding, in the RF model, it is important to fine-tune two hyper-parameters – that is, the number of trees in the forest and the number of leaves per tree – to ensure that input-output correlations are identified and captured, and predictions are accurate. In the absence of an optimization algorithm, the two hyper-parameters need to be adjusted through trial-and-error (e.g., by using multi-fold cross-validation [42]), which can be time-consuming and difficult. In a recent study [43], it was shown that the Firefly algorithm (FFA) – a metaheuristic optimization algorithm [44] – can be used to determine optimum values of the two aforementioned hyper-parameters in relation to the volume and nature of the training dataset. The authors showed that by combining RF with FFA, predictions (of global solar radiation) were rendered more accurate compared to those made by various standalone and ensemble ML models. In another study [45], FFA was used in conjunction with SVM to predict concretes' compressive strength. While the combined [SVM + FFA] model had better prediction performance than the standalone SVM model, it is expected that inherent limitations of SVM – as described above – could have compromised the prediction performance of the combined model. To the best of authors' knowledge, the combination of RF and FFA has never been used to process concrete datasets. Given the superior prediction performance of RF (compared to SVM as well as other ML models [21]), it is deemed important to examine if combining RF with FFA would result in further improvements in accuracy of predictions of concretes' compressive strength.

The study presents the first application of the hybrid RF-FFA model – developed by combining the RF model with FFA – to predict compressive strength of concretes in relation to their mixture design and age. The performance of the hybrid model is benchmarked against commonly used standalone ML models (i.e., SVM, multilayer perceptron ANN, M5P, and RF). Six different statistical parameters are used for comprehensive evaluation of the models' prediction performance. Firstly, highly nonlinear, non-monotonous, and periodic trigonometric functions are used to evaluate the performance of the ML models. Focus is given to determine if the hybrid model is able to reveal the complex relationship between input variables and output of the trigonometric functions, and, more importantly, reliably predict the function outputs in blank (i.e., previously untrained) data-domains. Secondly, the prediction performance of the ML models is tested using two real-world concrete datasets, comprised of concretes' mixture designs and their corresponding age-dependent compressive strengths. Based on comparisons of prediction performances – of the hybrid RF-FFA model vis-à-vis the standalone ML models – it is shown that the hybrid ML model consistently outperforms the standalone ML models.

The paper is organized as follows. Section 2. describes the five ML models implemented in this study. Section 3.0 describes the datasets used for training and testing of the ML models. A brief description of statistical parameters used for evaluation of prediction performance of the models is also included. Section 4.0 reports the results and comparison of prediction performances of various ML models. Section 5.0 presents summary of the main findings of the study.

2. MACHINE LEARNING MODELS

This section provides a brief overview of the machine learning (ML) models implemented in this study. In each of the following sub-sections (i.e., Sections 2.1 to 2.5), one or more original references are provided that describe the formulation and implementation of the ML model in more detail.

2.1. MULTILAYER PERCEPTRON ARTIFICIAL NEURAL NETWORK (MLP-ANN)

Artificial neural network (ANN) consists of several computational elements (termed as neurons) arranged in layers, resembling the network of neurons in the human brain responsible for processing information in a hierarchical fashion [29]. Multilayer perceptron artificial neural network (MLP-ANN) is a subclass of ANN with strong self-learning capabilities [46]. The hierarchical structure of MLP-ANN is comprised of: (i) one input layer – which contains a set of neurons representing the input variables (e.g., concrete mixture design variables); (ii) one or more hierarchical hidden layers – which contain computational neurons to process the information received from the previous layer so that it can be refined and passed on to the next layer; and (iii) one output layer – which contains a computation node to produce the final prediction (e.g., compressive strength of concrete). Each neuron in any given hidden layer is functionally related – as shown in Equation 1 – to all neurons in the previous layer.

$$N_j = \sum w_{ji} o_i \tag{1}$$

$$y_j = f(N_j) = \frac{1}{1 + e^{w_{ji} \cdot N_j}} \tag{2}$$

Here, N_j is the activation of the j^{th} neuron, i is the set of all neurons present in the previous layer, w_{ji} is the weight of connection between neurons j and i, and o_i is the output of the neuron. Each neuron uses activation functions (while using all neurons from the previous layer) to calculate intermediate-output values, which are subsequently passed on as input values to the next neuron layer. This process proceeds throughout the network until reaching the final neuron layer that produces the final output. In the MLP-ANN model, activation functions are represented as sigmoidal or logistic-transfer functions [46] – as shown in Equation 2, wherein $y_j = f(N_j)$ is the activation function of the j^{th} neuron. During training of the MLP-ANN model, a back-propagation algorithm [47,48] is used to minimize deviation (i.e., RMSE: root mean squared error or MAE: mean absolute error) between actual and predicted values (of the activation functions). This is accomplished by iteratively adjusting and finally determining the optimal connection weights (i.e., w_{ji}) – pertaining to each activation function – by using the gradient descent approach or the Levenberg-Marquardt algorithm [46,49].

In the MLP-ANN model used in this study, the neural network architecture comprised of 5 hidden layers, wherein each layer comprised of $(2m + 1)$ neurons [50]; m is the number of input variables of the training dataset. The choice of 5 hidden layers was made based on comparison of prediction performances of the model – whilst varying the number of hidden layers between 2-and-10 – against experimental datasets described in Section 3.1. For fine-tuning of the parameters (i.e., connection weights of each of the activation functions), the Levenberg-Marquart algorithm, as described in [49], was used because it resulted in superior prediction performance compared to the gradient descent approach.

2.2. SUPPORT VECTOR MACHINE (SVM)

Support vector machine (SVM) is a ML methodology for approximating the nonlinear relationship between input variables and output of a dataset by using an optimization approach – rather than a regression approach – to minimize a cost (i.e., ε-insensitive loss) function [51,52]. During training, the SVM, firstly, maps the input dataset from a lower dimensional to a higher dimensional feature space by using a mapping procedure. Towards this, a nonlinear kernel function (e.g., polynomial function, sigmoidal function, Gaussian radial basis kernel function, and hyperbolic tangent function [53,54]) is used to fit the input data into a higher dimensional feature space, wherein the data is distributed in a more sparse form compared to the original one. Next, the SVM attempts to determine a linear objective function $f_{SVM}(x, \omega)$ (see Equation 3) – such that its output has a maximum deviation of ε with respect to the actual (measured) value in the training dataset.

$$f_{SVM}\,(x,\omega) = \sum_{i=1}^{n} \omega_i K_i\,(x) + b \tag{3}$$

In Equation 3, K_i is the set of n nonlinear kernel (i.e., mapping) functions used for transforming the original input data (x) into higher dimensional feature space, b is a bias term, and ω represents the weight vector consisting of n choice coefficients. In order to derive the optimum objective function [$f_{SVM}(x, \omega)$] – and the associated parameters (i.e., b and ω) – the task of regression is approached as an optimization problem (Equation 4), within the constraints shown in Equation 5. The objective of the optimization effort is to determine the global minimum of Equation 4, such that for each input value (x), the output of $f_{SVM}(x, \omega)$ is within a Euclidian distance of ε from the actual value [55].

$$\text{minimize: } \frac{1}{2}\|\omega\|^2 + C\sum_{i=1}^{n} \xi_i + \xi_i^* \tag{4}$$

$$\text{subject to } \begin{cases} y_i - f_{SVM}\,(x_i,\omega) - b \le \varepsilon + \xi_i \\ f_{SVM}\,(x_i,\omega) + b - y_i \le \varepsilon + \xi_i^* \\ \xi_i \text{ and } \xi_i^* \ge 0, \text{and } i = 1, 2, 3 \ldots n \end{cases} \tag{5}$$

$$K(x,y) = e^{(-\gamma\,\|x-y\|^2)} \tag{6}$$

In Equation 4, the constant C is called the regularization term, and represents the degree of penalty of the sample with error exceeding ε (i.e., when the prediction is farther than ε from the actual value). The parameters, ξ_i and ξ_i^*, shown in Equation 5 are positive slack variables that represent the Euclidian distance of the predicted value from the corresponding boundary values of the ε-tube (i.e., a tube representing the actual training dataset, wherein each data-record is bounded by the maximum allowable error of ε). Therefore, based on the formulation described here, to derive the optimum objective function, $f_{SVM}(x, \omega)$ (and optimum values of the bias, b, and choice coefficients, ω) – that reliably links input variables with the output – the parameters that need to be optimized are ε, C, and any parameter associated with the kernel function (e.g., the parameter, γ, which is associated with the Gaussian radial basis kernel function, as shown in Equation 6 [53,54]).

In the SVM model used in this study, three different kernel functions (i.e., Gaussian radial basis kernel function, 3rd-to-5th order polynomial functions, and sigmoidal function) were used. Based on prediction performance of the model on experimental datasets (described later in Section 3.1), the Gaussian radial basis kernel function was chosen. Within the kernel function (see Equation 6), the value of γ was set at 0.10. The values of ε (representing the radius of the ε-tube) and C (the regularization term) were set at 1.5 MPa and 5.0, respectively.

2.3. M5PRIME MODEL TREE ALGORITHM (M5P)

The M5Prime model tree algorithm – often abbreviated as the M5P model – is a modification [39] of the M5Rules algorithm introduced by Quinlan [38]. The M5P model is, essentially, a decision tree model that performs logical splits in the training dataset so that the input variables can be linked with the output using multivariate linear functions. During training of the M5P model, the input space is split in several subspaces, while ensuring that data in each subspace share at least one common attribute (e.g., similar range of one or more input variables). More specifically, the splitting of data is performed in a manner that data that are alike – in terms of one or more of their attributes – are clustered and contained within the same subspace. By repeating this procedure iteratively, several subspaces, each consisting of harmonious data, are obtained. Standard deviation is typically used as the criterion for determining the specific attribute or attributes on the bases of which optimal splitting of the dataset can be achieved. Such reduction in standard deviation allows determination, and subsequent creation, of several nodes (i.e., data-clusters) on the bases of attributes. By creating such nodes, the model enables the building of an upside-down tree-like structure, wherein the root is at the top and the leaves are at the bottom. Once the tree is built, a new data-record propagates hierarchically from the root, and down through the nodes until it reaches a leaf. Each node consists of a mathematical logic, which compares the new data-record with that of the split value, and helps the data-record propagate down through the nodes until it reaches the appropriate leaf. In the M5P model, a linear regression model is used as the aforementioned mathematical logic. The regression model is developed in each of the subspaces, linking input variables and output of the data-records contained within it. To ensure that the tree-structure is optimal, a pruning technique is used to overcome the issue of over-training – that is, when the chosen attribute, for any given subspace, is not the optimal one with the maximum expectation to reduce error (i.e., standard deviation, in this study). Use of the pruning technique, however, can result in discontinuities between adjacent linear models. To mitigate this issue, a smoothing operation is employed in the final step. Such iterative pruning and smoothening operations ultimately unify all linear regression models – across all the nodes between the root and leaf of the tree – into a singular, continuous model.

The M5P model used in this study was implemented using the Waikato Environment for Knowledge Analysis (WEKA) workbench toolbox [56,57]. The only variable parameter in the M5P model is the *minimum number of splits* in the training dataset. This value was varied from 2-to-10, and the prediction performance was measured across experimental datasets (described later in Section 3.1). Based on such evaluations, the optimum value of *minimum number of splits* was selected as 4.

2.4. RANDOM FORESTS (RF)

Random forests (RF) is a modified version of the bagging (i.e., bootstrap aggregation) decision tree algorithm, which assimilates the concepts of *adaptive nearest neighbors* and *bagging* to achieve effective data-adaptive inference [41,58]. Like in conventional decision tree models, the RF model utilizes a set (albeit large) number of independent trees, and within those trees are encompassed subsets of the homogenized training data. [59]. The elementary unit of RF is a binary tree constructed using the same foundational principle as that used in the classification and regression tree (CART) model – wherein binary splits partition the tree, in recursive fashion, into "near-homogeneous" terminal nodes. When the binary split is done optimally, the propagation of data from a parent-node to its two children-nodes occurs in a way that ensures that homogeneity in the data between the children-nodes is improved compared to the parent-node. A typical RF model comprises of 100s or 1000s of trees, wherein each tree is grown using a unique bootstrap sample of the training data. Compared to the CART model, the RF model is different in the sense that trees in the latter model are grown non-deterministically using a procedure comprised of two-stage randomization. Here, the first stage of randomization involves growing the tree using a randomly chosen bootstrap sample of the original data. The second stage of randomization features at the node level – wherein, as opposed to splitting the tree node using all variables (as done in the CART model or the M5P model described in Section 2.3), a random subset of variables are selected and only those variables are used for ascertaining the best split of the node. On account of the two-stage randomization, the trees grown in the RF model are de-correlated and the ensemble has low variance. Based on this description, construction of the RF model can be summarized in the following steps:

- "n_t" bootstrap samples are drawn randomly from the original training dataset. At this point, the number of bootstrap samples (i.e., n_t) is equal to the number of trees. Based on prior studies [43,58,60], the optimum value of n_t is ≈66.66% of the overall training dataset. The remaining ≈33.33% of the dataset are labelled as "out-of-bag" (OOB) data.
- From each of the n_t bootstrap datasets, a tree is grown. Unlike conventional decision tree models (e.g., the M5P and CART models), each tree in the RF model is an unpruned regression tree, wherein at each node, rather than choosing all variables of the training dataset, a random sample of m_{try} variables is chosen. As the tree is grown, the number of leaves per tree (n_{LV}) is held constant across the entire ensemble. Based on previous studies [43,58], the optimum value of n_{LV} is between 3-and-10. In this study, the optimum value – assessed by performing predictions on different experimental datasets (described in Section 3.0) – was determined as 5.
- Next, each of the n_t trees is utilized to predict a data-point outside of the selected bootstrap space. Output of the prediction is designated as out of bag (OOB) prediction [59]. These OOB predictions, for a given input vector (x), are designated as f_{RF} (x) for each of the n_t decision trees; all OOB predictions are subsequently aggregated and

averaged to produce the overall OOB prediction $\hat{f}_{RF}^{n_t}(x)$ and OOB error rate (see Equation 7). Simply put, $\hat{f}_{RF}^{n_t}(x)$ is the arithmetic mean of the predicted values collated from all of the n_t trees. The OOB predictions – especially the OOB error rate – provide a good measure of influence of each variable on the output, which can be quantitatively estimated as variable importance (*VI*), thus eliminating the need for a test set or cross-validation [42]. *VI* of a given variable is, essentially, a measure of increment in OOB error rate when OOB prediction for a given variable is permuted while all others are left unchanged [60].

- Once the OBB predictions, OOB error rate, and *VI* are calculated, outliers in the training dataset are detected using cluster analysis (e.g., K-means cluster analysis, density model, and mean-shift clustering) [61]. In the study, the K-means cluster analysis [62] was used to determine data-records that do and do not belong in clusters. The data-records that do not belong in clusters are removed, and subsequently replaced in an iterative manner through the training process.
- Lastly, in the testing phase, new input dataset – which is not part of the training dataset – is used to perform predictions. For each input data-record, the predicted value corresponds to the average of predictions from all of the n_t trees.

$$\hat{f}_{RF}^{n_t}(x) = \frac{1}{n_t}\sum_{j=1}^{n_t} f_{RF_j}(x) \tag{7}$$

The RF model has a number of unique advantages. In the RF model, a large number of trees are grown (as opposed to other decision tree models) – on a one-node-at-a-time basis; as such, errors resulting from generalization are minimized, and, therefore, the likelihood of overfitting the training data is negligible [63]. Minimization of generalization, enabled by the large number of trees, entails that the RF model is able to proficiently deal with complex interactions and correlations among variables of the training dataset. By allowing each of n_t trees to grow to its maximum size (i.e., by allowing "deep" trees), without any pruning, and selecting only the best splits among a random subset at each node, the RF model is able to concurrently maintain diversity among trees and prediction performance. The two-stage randomization – as described earlier – diminishes correlation among unpruned trees, keeps the bias low, and reduces variance. Lastly, the RF model is easy to implement because the number of trees (n_t) and the number of leave per tree (n_{LV}) are the only two hyper-parameters that need to be optimized by the user. Both of these hyper-parameters can be optimized by cross-validation [64]. In the present study, the values of n_t and n_{LV} for the standalone RF model were set at 450 and 5, respectively. These values were determined using the cross-validation method [42], while training the model using experimental datasets described later in Section 3.1.

2.5. THE HYBRID RANDOM FORESTS – FIREFLY ALGORITHM MODEL (RF-FFA)

2.5.1. The Firefly Algorithm (FFA). The FFA – originally conceived by Yang [44] – is an optimization algorithm [65,66] based on idealized behavior of flashing characteristics of fireflies. The rules of idealized flashing characteristics are: (i) each firefly is attracted to all other fireflies; (ii) the magnitude of attractiveness between any two fireflies is proportional to the difference in brightness between them; (iii) the movement of a firefly is always towards a firefly with greater brightness; and (iv) the brightness of the firefly is determined by the landscape (i.e., the objective function, *f(x)*, that is to be optimized). The brightness, I, of a firefly at a particular location, x, can be chosen as $I(x)$ which is directly proportional to the objective function, $f(x)$. The attractiveness, β, between a pair of fireflies is a function of the distance, r_{ij}, between firefly i and firefly j. Likewise, the brightness, I_i, of firefly i varies with the distance r_i from the source in a monotonic and exponential manner (Equation 8a).

$$I_i = I_o e^{-\gamma r_i} \tag{8a}$$

$$where, \gamma = \frac{\gamma_o}{r_{max}} \tag{8b}$$

Here, I_0 is the brightness at the source (typically set at 1.0) and γ is the light absorption coefficient (representing the potential of fireflies to absorb light from the source). The value of γ can range from 0-to-10 [44]. In this study, however, γ was calculated using Equation 8b, wherein $\gamma_0 = 1.0$, and r_{max} is the maximum of distances between all pairs of fireflies [65] in the landscape. The mathematical formulation of the magnitude of attractiveness (β_{ij}) between two fireflies (i and j), in relation to the distance between them (r_{ij}), is given by Equation 9:

$$\beta_{ij} = \beta_o e^{-\gamma r_{ij}^m} \tag{9}$$

Here, β_0 is the maximum attractiveness between a pair of fireflies (i.e., at $r = 0$) and m is a positive coefficient (ranging between 2-and-4). The values of β_0 can range from 0-to-1, wherein the upper bound represents cooperative local search with the brightest firefly dictating positions of most fireflies in the swarm. As the value of β_0 digresses from 1, dominance of the brightest firefly decreases, thus rendering the local search progressively more non-cooperative. In this study, a value of 0.80 was used for β_0

and *m* was set at 2.0. The movement of a firefly *i*, as it is attracted to a brighter firefly *j*, is determined by Equation 10. Here, $x_{i,\,old}$ and x_j are locations of the fireflies *i* and *j*, respectively, and the last term is randomization with the vector of random variables (ε_i) drawn from a Gaussian distribution; $x_{i,\,new}$ is the new position of firefly *i* as its moves due to its attractiveness towards firefly *j*.

$$x_{i,new} = x_{i,old} + \beta_o e^{-\gamma r_{ij}^{m}} \left(x_j - x_i\right) + \alpha\varepsilon_i \tag{10}$$

Based on the abovementioned criteria and definitions, the FFA can be used to minimize a continuous, constrained cost function *f(x)*. Firstly, it is assumed that there exists a swarm of *m* fireflies – distributed randomly over the landscape. The fireflies are tasked to find x^*, wherein the value of the cost function $f(x^*)$ – or, in other words, the overall brightness of the landscape – is minimum. Next, the FFA is implemented in the following steps: (i) all fireflies of the swarm are allowed to move, in a sequential manner, such that each firefly moves towards another in the neighborhood on the basis of its attractiveness towards the other firefly (which is a function of difference in brightness and the distance between the two fireflies); (ii) once all fireflies have been allowed to move to their new locations, based on the new configuration of fireflies, the overall brightness of the landscape is updated, and assessed if it is lower than the original one; and (iii) steps (i) and (ii) are repeated iteratively until convergence is reached, wherein the overall brightness of the landscape reaches the global minimum (i.e., the value does not change by more than 10^{-6} units between three successive iterations).

2.5.2. The Hybrid Model (RF-FFA). In the RF model – as described in Section 2.4 – it is important to fine-tune the two hyper-parameters – that is, the number of trees in the forest (n_t) and the number of leaves per tree (n_{LV}) – to ensure that predictions are accurate. Typically, the two parameters are adjusted through trial-and-error or by cross-validation, which can be time-consuming and difficult. In a recent study [43], it was shown that the Firefly algorithm (FFA) – described in Section 2.5.1 – can be used to determine optimum values of the two aforementioned hyper-parameters in relation to the nature and volume of the dataset. The authors showed that by combining RF with FFA, predictions were rendered more accurate compared to those made by various standalone and hybrid ML models – including the RF model.

In this study, the structure of the hybrid model has been drawn from the work of Ibrahim and Khatib [43]. In Stage I, the RF model is implemented, wherein the values of n_t and n_{LV} are set at 450 and 5, respectively. In Stage II, the FFA is implemented in the following steps:

- An objective function, $f(x)$, is defined, which corresponds to the total root mean squared error (RMSE: described later in Section 3.2) of predictions of the RF model with respect to actual values of the training dataset used in Stage I.
- The FFA is implemented – by following the steps detailed in Section 2.5.1 – to optimize the values of n_t and n_{LV} such that the objective function (i.e., $f(x)$ = RMSE of the RF model) continually decreases. Towards this, at the end of every iteration of the FFA, the RF model is implemented to update predictions based on new values of the two hyper-parameters; based on the predictions, the RMSE is also updated to be used in the next iteration.
- The values of n_t and n_{LV}, at which the objective function reaches a global minimum (changes by less than 10^{-6} units between three successive iterations), are selected as the final, optimum values.

Lastly, in Stage III, the RF model is implemented to make predictions against the test dataset using the FFA-determined optimum values of the hyper-parameters.

3. DATA COLLECTION AND PERFORMANCE EVALUATION OF MACHINE LEARNING MODELS

3.1. DATA COLLECTION

Experimental datasets, consolidated from published studies [18,19,67], were used to train the ML models (described in Section 2.0), and to assess their prediction performance in previously untrained data-domains.

Table 1. A summary of statistical parameters pertaining to each of the 9 attributes (8 input and 1 output) of Dataset-1. The dataset consists of 1030 unique data-records.

Attribute	Unit	Minimum	Maximum	Mean	Standard Deviation
Cement	kg. m^{-3}	102.00	540.00	281.27	104.51
Blast Furnace Slag	kg. m^{-3}	0.0000	359.40	73.896	86.279
Fly Ash	kg. m^{-3}	0.0000	200.10	54.188	63.997
Water	kg. m^{-3}	121.80	247.00	181.57	21.354
Superplasticizer	kg. m^{-3}	0.0000	32.200	6.2050	5.9740
Coarse Aggregate	kg. m^{-3}	801.00	1145.0	972.92	77.754
Fine Aggregate	kg. m^{-3}	594.00	992.60	773.58	80.176
Age	Days	1.0000	365.00	45.662	63.170
Compressive Strength	MPa	2.3300	82.600	35.818	16.706

The first dataset – subsequently referred to as Dataset-1 – was first published by Yeh et al. [18,19], and subsequently used by several researchers [8–17,20–22,45] for training, testing, and validation of statistical and ML models. Dataset-1 consists of 1030 data-records, featuring 278 unique concrete mixture designs and their age-dependent compressive strengths. In the context of ML, in each data record, there are eight input variables – contents of cement (kg. m^{-3}), blast furnace slag (kg. m^{-3}), fly ash (kg. m^{-3}), superplasticizer (kg. m^{-3}), water (kg. m^{-3}), fine aggregate (kg. m^{-3}) and coarse aggregate (kg. m^{-3}), and age (days); and one output – compressive strength (MPa). Statistical parameters pertaining to Dataset-1 are summarized in Table 1.

The second dataset – subsequently referred to as Dataset-2 – was first published by Chopra et al. [67], and utilized in several later studies [31,32,68]. Dataset-2 consists of 76 data-records, featuring different concrete mixture designs and their compressive strengths at 28 days. In the context of ML, in each data record, there are five input variables – contents of cement (kg. m^{-3}), fly ash (kg. m^{-3}), water (kg. m^{-3}), fine aggregate (kg. m^{-3}) and coarse aggregate (kg. m^{-3}); and one output – compressive strength (MPa) at 28 days. Statistical parameters pertaining to Dataset-2 are summarized in Table 2.

Table 2. A summary of statistical parameters pertaining to each of the 6 attributes (5 input and 1 output) of Dataset-2. The dataset consists of 76 unique data-records.

Attribute	Unit	Minimum	Maximum	Mean	Standard Deviation
Cement	kg. m^{-3}	350.00	475.00	433.88	34.810
Fly ash	kg. m^{-3}	0.0000	71.250	24.030	32.641
Water	kg. m^{-3}	178.50	229.50	202.81	12.821
Coarse Aggregate	kg. m^{-3}	798.00	1253.8	1050.9	134.52
Fine Aggregate	kg. m^{-3}	175.95	641.75	524.31	69.378
28-day Compressive Strength	MPa	31.660	54.490	44.374	5.2120

3.2. EVALUATION OF PREDICTION PERFORMANCE OF ML MODELS

For training, and assessment of prediction performance of, ML models, the dataset (i.e., Dataset-1 or Dataset-2, as described in Section 3.1) was randomly partitioned into two sets: a training set and a testing set. 75% of data-records of the parent dataset were used for training of the ML models (i.e., for fine-tuning, and, ultimately, finalizing, the optimum model parameters), and the remaining 25% were used for testing (i.e., for determination of cumulative error between predicted and actual values). Such split of 75-to-25% between the training and test sets – or a ratio close to that – have been used in various past studies [10,11,21]. While the splitting was done randomly, special care was taken to guarantee that the training dataset was representative of the parent dataset. Towards this, it was ensured that the training dataset comprised of input attributes (i.e., concrete mixture design variables) with widespread values encompassing the entire range between the two extrema.

For quantitative measure of prediction performance of the ML models (against the test set), five different statistical parameters were used. The parameters, essentially, estimate the cumulative error in predictions – of compressive strength of concretes in the test dataset – with respect to the actual measurements. The statistical parameters are: Person correlation coefficient (R), coefficient of determination (R^2), mean absolute percentage error (MAPE), mean absolute error (MAE), and root mean squared error (RMSE). The mathematical formulations to estimate these errors are shown in Equations 11-15; here, y' and y are predicted and actual values, and n is the total number of data-records in the test dataset.

$$R = \frac{n \sum y.\, y' - (\sum y)(\sum y')}{\sqrt{n(\sum y^2) - (\sum y)^2}\ \sqrt{n(\sum y'^2) - (\sum y')^2}} \tag{11}$$

$$R^2 = \left[\frac{n \sum y.\, y' - (\sum y)(\sum y')}{\sqrt{n(\sum y^2) - (\sum y)^2}\ \sqrt{n(\sum y'^2) - (\sum y')^2}}\right]^2 \tag{12}$$

$$MAPE = \frac{100\%}{n}\sum_{i=1}^{i=n}\frac{|y - y'|}{y} \tag{13}$$

$$MAE = \frac{1}{n}\sum_{i=1}^{i=n}|y - y'| \tag{14}$$

$$RMSE = \sqrt{\frac{1}{n}\sum_{i=1}^{i=n}|y - y'|^2} \tag{15}$$

$$CPI = \frac{1}{N}\sum_{j=1}^{j=N}\frac{P_j - P_{min,j}}{P_{max,j} - P_{min,j}} \tag{16}$$

To obtain a comprehensive measure of prediction performance of the ML models – and to compare them – the five statistical parameters described in Equations 11-15 were unified into a composite performance index (CPI, see Equation 16) [11,69]. In Equation 16, N is the total number of performance measures (= 5, as five statistical parameters were used in this study), P_j is the value of the j^{th} statistical parameter, and $P_{j,\,min}$ and $P_{j,max}$ are the minimum (i.e., worst) and maximum (i.e., best) values of the j^{th} statistical parameter across the five values generated by the same number of ML models. Based on the formulation shown in Equation 16, the values of CPI would range from 0-to-1, wherein 0 (or the lowest value) would represent the best ML model and 1 (or the maximum value) would represent the worst ML model in terms of overall prediction performance. In this study, the different ML models were ranked – from worst to best in terms of prediction performance – on the basis of their CPI values.

4. RESULTS AND DISCUSSION

4.1. HIGHLY NONLINEAR AND PERIODIC TRIGONOMETRIC FUNCTIONS

In conventional regression-based machine learning (ML), the quality of a ML model is measured by its capability to learn from a training set, and apply the knowledge to forecast in previously unseen data-domains from the same distribution. Simply put, the prediction performance of a ML model boils down to its ability to identify trends in the dataset, and subsequently use such trends for interpolation. When trained properly (e.g., by training with adequately large dataset and by avoiding overfitting), nonlinear ML models are often able to perform interpolations with sufficient accuracy. However, it has been reported that the interpolation accuracy of many ML models (e.g., ANN and SVM) becomes unreliable in data-domains that feature complex, highly nonlinear and periodic functional relationship between one or more input variables and the output [33–35,70]. In the context of concrete, the ability to interpolate in such highly nonlinear domains could be the difference between reliable and unreliable predictions; this is because the relationships between mixture design variables and properties of concrete are also expected to be highly nonlinear and non-monotonous.

To test the ability of ML models – described in Section 2.0 – to interpolate in a highly nonlinear and periodic data-domains, datasets generated from trigonometric functions shown in Equations 17 and 18 were used. Similar functions were originally suggested by Martius and Lampert [70] to test the ability of various ML models to interpolate (and extrapolate) within periodic data-domains. In Equation 17, x is an input vector consisting of x_1, x_2, x_3, and x_4 variables, and $y_1 = F_1(x)$ is the output. For this function, $x_1 = x_2 = x_3 = 2\,x_4$. In Equation 18, x is an input vector consisting of the same x_1, x_2, x_3, and x_4 variables, and $y_2 = F_2(x)$ is the output. Here, $x_1 = x_2 = x_3 = -5x_4$. Two separate datasets were generated by varying x_1 (and, on account of the aforementioned equality, x_2, x_3, and x_4 as well) between -4.0 and 4.0, and calculating $F_1(x)$ and $F_2(x)$ as functions of all four variables. The increment in x_1 was set at 0.01; as such, each of the two datasets consisted of 800 data-records with four input variables and a single output. Next, each dataset was split randomly into a training set (75%, or 600 data-records) and a test set (25%, or 200 data-records), using the procedure described in Section 3.1. All of the five ML models implemented in this study (i.e., MLP-ANN, SVM, M5P, RF, and RF-FFA) were then trained using the training dataset; subsequently, their prediction performances were assessed using the corresponding test dataset.

$$y_1 = F_1(x) = \left[\frac{1}{3}\sin\left(\pi x_1\right)\right] + \left[x_2 \cos\left(2\pi x_1 + \frac{\pi}{4}\right)\right] + [x_3] - [x_4^2] \qquad (17)$$

$$y_2 = F_2(x) = \frac{1}{3}[(1 + x_2)(\sin(\pi x_1))] + [x_2 x_3 x_4] \qquad (18)$$

Figures 1 and 2 show predictions made by the five ML models plotted against the actual values, calculated using Equation 17 (i.e., for $F_1(x)$) and Equation 18 (i.e., for $F_2(x)$), respectively. Tables 3 and 4 summarize the statistical parameters (i.e., cumulative errors) pertaining to predictions made by the ML models, and the composite performance index (CPI, Equation 16) calculated using the five statistical parameters.

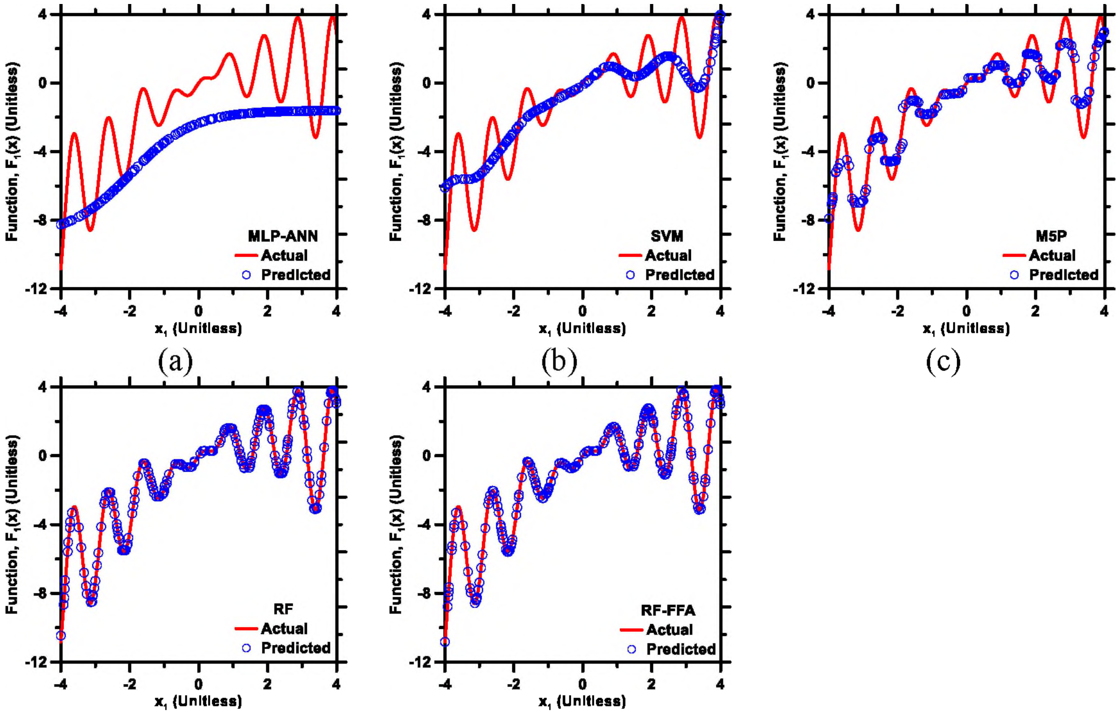

(a) (b) (c)

(d) (e)

Figure 1. Predictions made by ML models: (a) MLP-ANN; (b) SVM; (c) M5P; (d) RF; and (e) RF-FFA compared against actual values of the trigonometric function, $F_1(x)$ (Equation 17). Both the actual values and predictions are plotted against x_1, an input variable ranging from -4 to 4. Here, $x_1 = x_2 = x_3 = 2x_4$.

As can be seen in Figures 1 and 2, the MLP-ANN and SVM models are unable to capture the periodic nature of the dataset. As stated previously in Section 1.0, this is because both models employ local search or optimization algorithms, which are faced with an inherent drawback of getting trapped in local minima – especially when the functional relationship between the input variables and output comprises of multiple local minima (e.g., datasets generated using Equations 17 and 18) – rather than converging to the global minima. The poor prediction performance of MLP-ANN and SVM models is also reflected in the values of statistical parameters listed in Tables 1 and 2 (e.g., RMSE of 2.8552 and 1.5245 for MLP-ANN and SVM models, respectively, when used for prediction of $F_1(x)$; and RMSE of 1.2602 and 0.9570 for MLP-ANN and SVM models, respectively, when used for prediction of $F_2(x)$). It is indeed possible to improve prediction performance of the models by incorporating algorithms based on Genetic programing [17,31], or by using ensemble techniques (e.g., bagging, voting, or stacking approaches [11,36]). However, as stated previously in Section 1.0, such techniques could result in slower convergence and/or overfitting.

Table 3. Prediction performance of ML models, measured on the basis of the test set developed using Equation 17. Five statistical parameters (i.e., R, R2, MAE, MAPE, and RMSE) and the composite performance index (CPI) are shown.

ML Model	R	R^2	MAE	MAPE	RMSE	CPI
	Unitless	*Unitless*	*Unitless*	*Unitless*	*Unitless*	*Unitless*
MLP-ANN	0.8425	0.7098	2.4633	102.87	2.8552	1.0000
SVM	0.8707	0.7581	1.2353	51.588	1.5245	0.6334
M5P	0.9718	0.9443	0.6113	25.530	0.7891	0.2212
RF	0.9995	0.9990	0.0753	3.1436	0.0977	0.0106
RF-FFA	0.9999	0.9998	0.0354	1.4790	0.0563	0.0000

The M5P model – which attempts to split data logically and then apply lineal regression models in each data-split – performed better at predictions compared to MLP-ANN and SVM models (i.e., CPI of 0.2212 of M5P vis-à-vis 1.0000 and 0.6334 of MLP-ANN and SVM models, respectively, when used for prediction of $F_1(x)$). While the M5P model captures the periodic nature of the dataset, due to the application of linear models and limited size of the decision tree, the actual intensities of the local minima and maxima are not well captured (see Figure 1). As such, the RMSE of the model's predictions are still high, that is, 0.7891 for $F_1(x)$ and 0.1648 for $F_2(x)$.

The RF model outperformed all of the aforementioned models (i.e., MLP-ANN, SVM, and M5P) in terms of prediction accuracy. This is expected because, in the RF

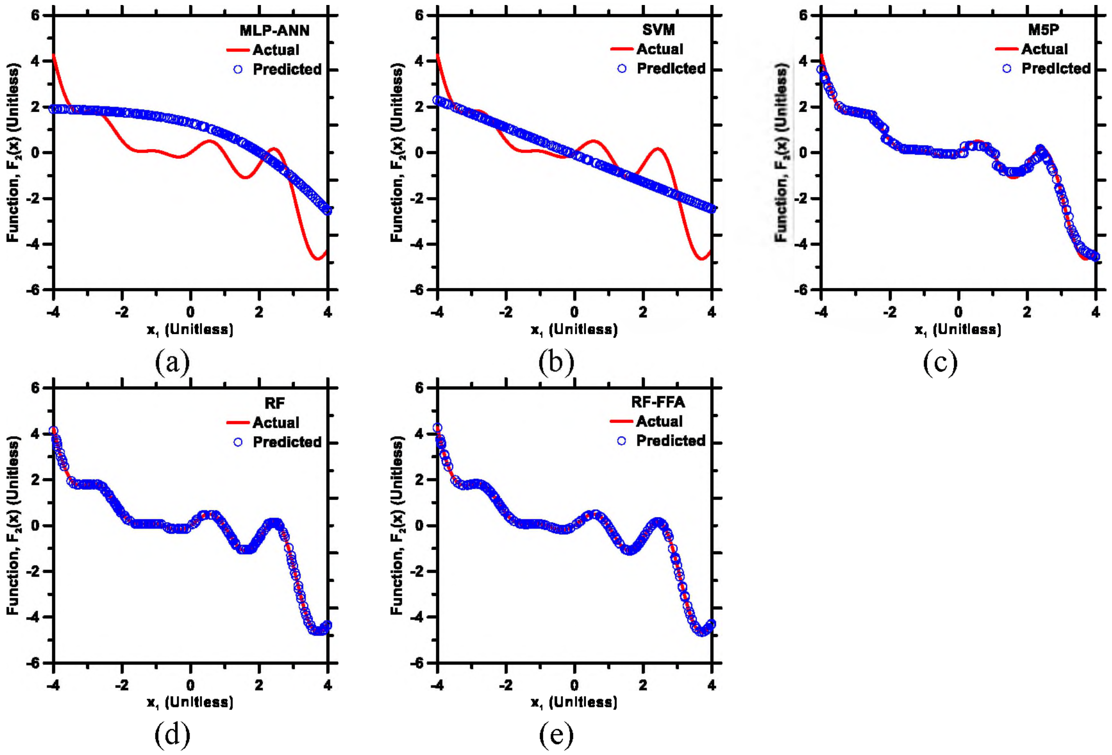

(a) (b) (c)

(d) (e)

Figure 2. Predictions made by ML models: (a) MLP-ANN; (b) SVM; (c) M5P; (d) RF; and (e) RF-FFA compared against actual values of the trigonometric function, $F_2(x)$ (Equation 18). Both the actual values and predictions are plotted against x_1, an input variable ranging from -4 to 4. Here, $x_1 = x_2 = x_3 = -5x_4$.

model, a large number of trees are grown (i.e., 450 trees, with 5 leaves per tree, as described in Section 2.4) without pruning or smoothening (as opposed to the M5P model, wherein the number of trees is restricted, and pruning and smoothening are required). On account of having large number of the trees, splits in data are more logical, and, therefore, errors resulting from generalization are minimized and overfitting of the training data is mitigated [59,63]. Furthermore, because of the two-stage randomization employed in the RF model – as described earlier and in [63] – correlation among unpruned trees is minimized (diversity among trees is high), the bias is kept low, and variance is significantly reduced. The prediction of the RF model further improved when it was combined with the firefly algorithm (FFA). As shown in Figures 1-2 and Tables 3-

4, the hybrid RF-FFA model was not only able to capture the periodic nature of the dataset but also able to reliably interpolate the local minima and maxima (and the intermedia values) across the entire -4.0-to-4.0 range of the input variable x_1. This enhancement in prediction performance of the hybrid model, with respect to the standalone RF model, can be attributed to the FFA, which is able to optimize the two hyper-parameters (i.e., number of trees and number of leaves per tree) of the RF model based on the nature and volume of the dataset. Based on overall prediction performance – as estimated using the CPI, which takes in account all of the statistical parameters (see Equation 16) – the ranking of the ML models is as follows: RF-FFA > RF > M5P > SVM > MLP-ANN.

Table 4. Prediction performance of ML models, measured on the basis of the test set developed using Equation 18. Five statistical parameters (i.e., R, R^2, MAE, MAPE, and RMSE) and the composite performance index (CPI) are shown.

ML Model	R	R^2	MAE	MAPE	RMSE	CPI
	Unitless	*Unitless*	*Unitless*	*Unitless*	*Unitless*	*Unitless*
MLP-ANN	0.8598	0.7392	1.0794	91.133	1.2602	0.9633
SVM	0.8450	0.7140	0.7201	60.797	0.9570	0.8175
M5P	0.9963	0.9926	0.1272	10.737	0.1648	0.0797
RF	0.9998	0.9996	0.0239	2.0158	0.0312	0.0104
RF-FFA	1.0000	1.0000	0.0063	0.5359	0.0107	0.0000

4.2. COMPRESSIVE STRENGTH OF CONCRETE: DATASET-1

Based on results shown in Section 4.1, it was established that the hybrid RF-FFA model outperformed the standalone MLP-ANN, SVM, M5P, and RF models in terms of prediction accuracy. The standalone RF model came as a close second. Notwithstanding, these results pertain to user-created trigonometric functions, wherein the relationship between input variables and output could be far more complex than real-world datasets. Therefore, to get a better understanding of prediction performance of the ML models, a real-world dataset of concrete – that is, Dataset-1, described in Section 3.1 – was used. Each data-record in the dataset consists of eight input variables – representing contents of cementitious materials and admixture, and age – and one output (i.e., compressive strength). Predictions of compressive strength of concretes from the test set of Dataset-1, as produced by the ML models, are shown in Figure 3; statistical errors pertaining to predictions are summarized in Table 5.

As shown in Figure 3 and Table 5, all ML models presented in this study were able to predict the age-dependent compressive strength of concrete with reasonable accuracy. This is evidenced by the relatively low and high values of RMSE (ranging between 4.0098-and-6.3300 MPa) and R^2 (ranging between 0.8664-and-0.9448), respectively, of predictions made by the ML models. It must be pointed out that the differences in statistical parameters among the different ML models are not as significant as in the case of Section 4.1, wherein datasets developed from periodic trigonometric functions (Equations 17 and 18) were used. This is hypothesized to be on account of the relatively simpler input-output relationship in the concrete dataset compared to the ones dictated by trigonometric functions. Several other studies – that have used the same dataset (i.e., published originally in [18,19]) and applied different ML models for predictions – have reported RMSE and/or R^2 values similar to those shown in Table 5. Selected examples of prediction performance of various ML models (on Dataset-1) reported in literature are provided below; a comprehensive review, with additional examples, can be found in another study [16].

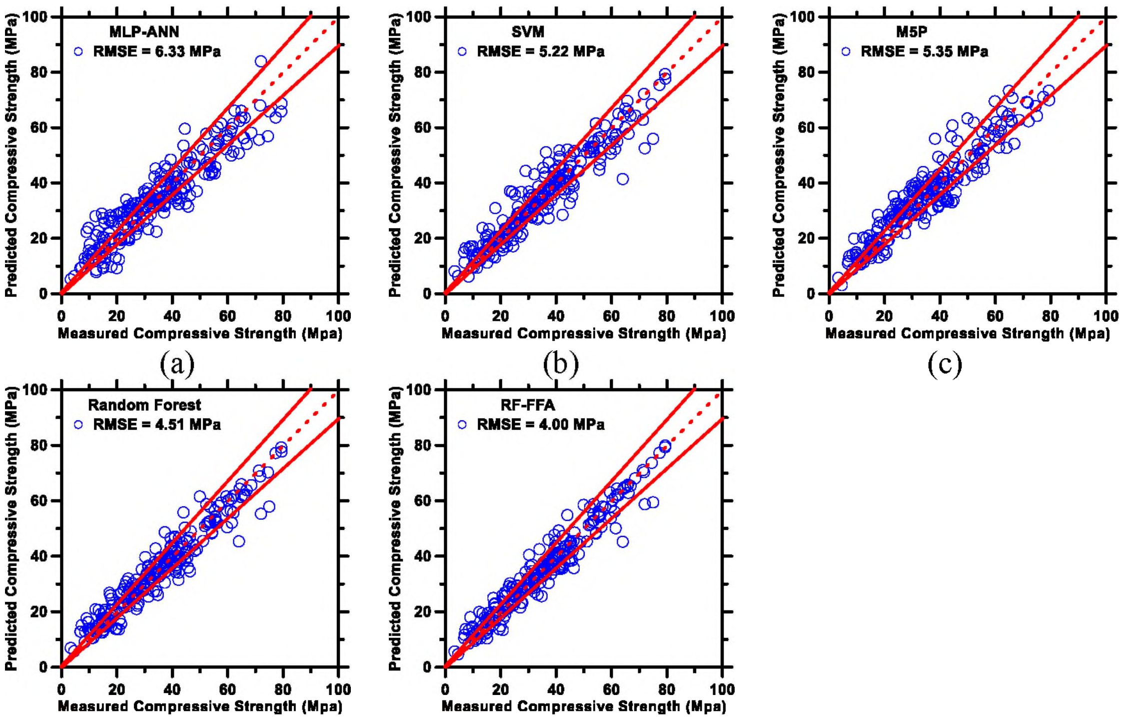

(a) (b) (c)

(d) (e)

Figure 3. Predictions made by ML models: (a) MLP-ANN; (b) SVM; (c) M5P; (d) RF; and (e) RF-FFA compared against actual compressive strength of concretes (drawn from Dataset-1). The dashed line represents the line of ideality and the solid lines represent a ±10% bound.

In the study conducted by Young et al. [21], linear regression, ANN, RF, boosted tree, and SVM models were used, and the RMSE of predictions made by the models ranged between 4.4-and-5.0 MPa. In another study conducted by Veloso de Melo and Banzhf [17], Kaizen Programming with Simulated Annealing was used, and the RMSE was ≈6.8 MPa. In the study of Chou et al. [11], several standalone and ensemble ML models were implemented to forecast compressive strengths of concretes listed Dataset-1. Among the standalone models, the RMSE was between 5.59-and-10.11 MPa; and, among the ensemble models, the RMSE was between 5.51-and-38.41 MPa. In the study of Behnood et al. [9], the M5P model was used, and the RMSE of predictions was reported as 6.178 MPa – a value close to the one obtained by the M5P model used in this study (see Table 5). Lastly, in a study conducted by Chou and Pham [45], the SVM algorithm was combined with FFA, and applied to predict compressive strength of concretes from Dataset-1. Based on the reported results, the hybrid [SVM + FFA] model outperformed other standalone (e.g., SVM) and ensemble models (e.g., ANN + SVM), and yielded predictions with RMSE of 5.631 MPa.

Table 5. Prediction performance of ML models, measured on the basis of the test set of Dataset-1. Five statistical parameters (i.e., R, R^2, MAE, MAPE, and RMSE) and the composite performance index (CPI) are shown.

ML Model	R	R^2	MAE	MAPE	RMSE	CPI
	Unitless	*Unitless*	*MPa*	*%*	*MPa*	*Unitless*
MLP-ANN	0.9308	0.8664	5.0421	36.143	6.3300	1.0000
SVM	0.9525	0.9073	3.5756	25.624	5.2234	0.4385
M5P	0.9502	0.9029	4.2369	30.367	5.3518	0.5884
RF	0.9654	0.9320	3.2674	23.443	4.5103	0.1999
RF-FFA	0.9720	0.9448	2.7301	19.571	4.0098	0.0000

Going back to Table 5, it is clear from all of the five statistical parameters that the RF and the hybrid RF-FFA models have superior prediction performance compared to MLP, SVM, and M5P models. Based on the values of CPI – the unified measure of prediction performance – the ML models can be ranked as RF-FFA > RF > SVM > M5P > MLP-ANN. This order is similar to the one that emerged in Section 4.1, wherein periodic trigonometric functions were used to generate datasets. Here again, the superiority of the RF model – compared to MLP-ANN, SVM, and M5P models – is attributed to the large number of unpruned trees that are grown (i.e., 450 trees, with 5 leaves per tree, as described in Section 2.4). Such depth in the model's structure allows more logical splits in the data, which, in turn, results in development of logical input-output correlations, and mitigates overfitting and generalization errors. Even further enhancement in prediction performance was achieved when the RF model was combined with FFA. This enhancement is attributed to the FFA's ability to optimize the number of trees and leaves per tree of the RF model – based on intrinsic characteristics of the dataset, and all without any user intervention.

On a closing note of this section, it is pointed out that the RMSE of predictions produced by the RF-FFA model are lower (i.e., RMSE = 4.0098 MPa) than the values reported in all other studies found in the authors' literature review [8–18,20–22,45]. Admittedly, the RMSE value alone cannot be used to assert that the RF-FFA model is superior compared to others. This is mainly because such comparison of prediction performance of ML models, developed and implemented by different users (in spite of utilization of the same database), is complex on account of differences in: (i) description of cumulative statistical error (e.g., in some papers, R^2 – rather than RMSE – was used to assess accuracy); (ii) splitting of parent dataset into training and test sets (e.g., in some papers, the parent dataset was split as per 80-and-20% or 66.66-and-33.33% between the training and test sets – as opposed to 75-and-25%, as used in this study); (iii) total number of data-records used for training and testing of the ML models (e.g., in some papers, all 1030 data-records of Dataset-1 were used, whereas in some only a fraction of them were used); and (iv) methodology used for optimization of model parameters (e.g., some papers used the cross-validation method to optimize model parameters using the training dataset, whereas, in this study, the FFA was used to optimize hyper-parameters of the RF model). Notwithstanding, the low RMSE (i.e., 4.0098 MPa) – combined with low values of MAE and MAPE and high values of R and R^2 (see Table 5) – produced by the hybrid RF-FFA model certainly suggest that the model is a promising tool for prompt, reliable, and accurate predictions of age-dependent compressive strength of concretes using their mixture design variables as inputs.

4.3. COMPRESSIVE STRENGTH OF CONCRETE: DATASET-2

In Section 4.2, it was shown that the proposed hybrid RF-FFA model produced predictions of concrete compressive strength with RMSE of 4.0098 MPa — suggesting a reasonably high degree of accuracy, especially in comparison to predictions produced by ML models reported in literature as well as other ML models presented in this study (i.e., MLP-ANN, SVM, M5P, and RF). The dataset used in Section 4.2 comprised of 1030 data-records, providing the RF-FFA model adequate number of data-records (i.e., 0.75 x 1030 = 772) for developing logical input-output correlations and, thus, making accurate predictions. It is, however, important to examine if the RF-FFA model is able to retain its superior prediction performance when a much smaller dataset is used for training (and testing). Such examination is deemed necessary because generating large datasets of concrete performance is very time-consuming; thus, it is important to evaluate whether or not the proposed RF-FFA model is applicable to smaller concrete datasets that are more abundant and easily-found in literature. Towards this, the prediction performance of the RF-FFA model was evaluated using Dataset-2 (described in Section 3.1) and benchmarked against the performance of other ML models. Readers are reminded that Dataset-2 consists of 76 data-records, featuring different concrete mixture designs and their compressive strengths at 28 days. The mixture design variables were used as inputs;

the 28-day compressive strength was used as an output. Predictions of compressive strength of concretes from the test set of Dataset-2, as produced by the ML models, are shown in Figure 4; statistical errors pertaining to the predictions are summarized in Table 6.

Akin to the results shown in Section 4.2, all five ML models were able to predict the age-dependent compressive strength of concretes from Dataset-2 with reasonable accuracy. The RMSE of predictions made by the ML models range from 0.9213-to-2.6754 MPa, attesting to the high degree of accuracy of predictions. These RMSE values are lower than those reported in some prior studies [31,67], albeit similar to those reported in a recent study [32] – wherein ANN, RF, and decision tree models were used for making predictions. Upon comparing the overall prediction performances, based on the values of CPI (Table 6), the following order emerges: RF-FFA = FA > SVM > MLP-ANN > M5P. This order, once again, suggests that prediction performance of the RF-FFA model is superior compared to other ML models presented in this study. Although the aforementioned order is broadly similar to the one obtained from predictions of strength of concretes from Dataset-1 (Section 4.2), there are a few small differences. Firstly, in Dataset-2, the prediction performance of the M5P model is the worst; this was not the case when Dataset-1 was used. It is expected that the deterioration in performance of the M5P model is due to the much smaller volume of Dataset-2 (i.e., 76 data-records as opposed to 1030 of Dataset-1) – thus resulting in inferior quality of splits in the training dataset, and, consequently, poor input-output linear correlations within each split. The poor prediction performance of the M5P model indicates – as was also suggested in a prior study [32] – that, when the dataset volume is small, decision tree models with

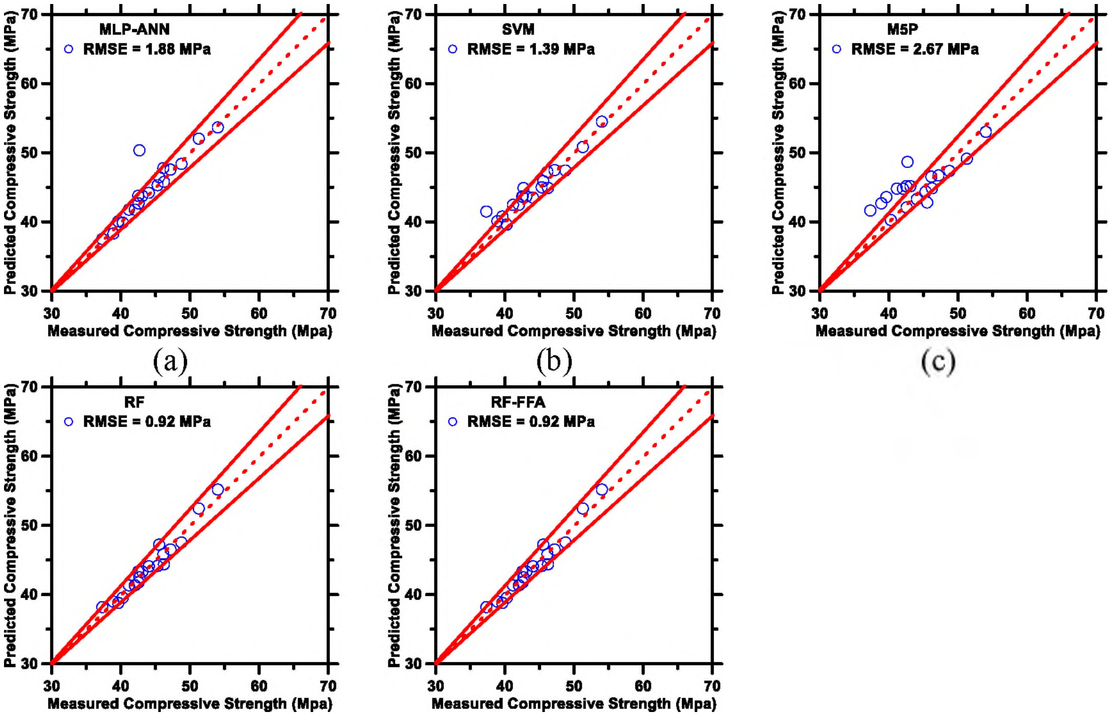

(a) (b) (c)

(d) (e)

Figure 4. Predictions made by ML models: (a) MLP-ANN; (b) SVM; (c) M5P; (d) RF; and (e) RF-FFA compared against actual compressive strength of concretes (drawn from Dataset-2). The dashed line represents the line of ideality and the solid lines represent a ±10% bound.

limited number of trees: (i) cannot ensure homogeneity in data clustered in each node, (ii) cannot maintain diversity among the different nodes, and, therefore, (iii) are unable to make predictions in an accurate manner. Secondly, it is also interesting to note in Table 6 that both the RF and RF-FFA models have similar prediction performances. The implication of this equivalency is that when the dataset is small, the application of FFA – for optimization of the two hyper-parameters (i.e., number of trees and number of leaves per tree in the forest) of the RF model – is redundant and does not necessarily elicit any substantial improvement in prediction performance. However, when the dataset is large – for example, Dataset-1 – the application of FFA is beneficial in that it produces substantial improvement in prediction performance of the RF model by optimizing its two hyper-parameters in relation to the nature and volume of the dataset (see Table 5).

Table 6. Prediction performance of ML models, measured on the basis of the test set of Dataset-2. Five statistical parameters (i.e., R, R^2, MAE, MAPE, and RMSE) and the composite performance index (CPI) are shown.

ML Model	R	R^2	MAE	MAPE	RMSE	CPI
	Unitless	*Unitless*	*MPa*	*%*	*MPa*	*Unitless*
MLP-ANN	0.9201	0.8464	0.9163	27.352	1.8783	0.2857
SVM	0.9565	0.9149	1.0635	31.744	1.3841	0.1876
M5P	0.8003	0.6400	2.1480	64.127	2.6754	1.0000
RF	0.9778	0.9561	0.7718	23.041	0.92313	0.0000
RF-FFA	0.9778	0.9561	0.7718	23.041	0.92313	0.0000

5. CONCLUSIONS

This study developed and presented a novel hybrid machine learning (ML) model (RF-FFA) for prediction of compressive strength of concrete, in relation to its mixture design and age, by combining the random forests (RF) model with the firefly algorithm (FFA). The firefly algorithm – a metaheuristic optimization technique – was used to optimize the two hyper-parameters of the RF model (i.e., the number of trees and the number of leaves per tree in the forest) in relation to the volume and nature of the dataset, and without any user intervention.

The RF-FFA model was trained to develop correlations between input variables and output of two different categories of datasets; such correlations were subsequently leveraged by the model to make predictions. The first category included two separate datasets featuring highly nonlinear and periodic relationship between input variables and output as given by trigonometric functions. The second category included two real-world datasets, comprised of mixture design variables and age of concretes as inputs and their compressive strengths as outputs. The performance of the hybrid RF-FFA model was benchmarked against commonly used standalone ML models – support vector machine (SVM), multilayer perceptron artificial neural network (MLP-ANN), M5Prime model tree algorithm (M5P), and RF. The metrics used for evaluation of prediction accuracy of the ML models included five different statistical measures (i.e., R, R^2, MAE, RMSE, and MAPE) as well as a composite performance index (CPI).

The prediction performances of MLP-ANN and SVM models were reasonable for concrete datasets; however, their inability to identify and converge to global minima rendered their prediction performances poor when datasets generated from trigonometric functions were used. The prediction performance of the M5P model, in general, was commensurable to, or slightly superior compared to, those of MLP-ANN and SVM models. However, on account of limited size (or depth) of the decision tree and utilization of multivariate linear regression models, prediction performance of the M5P model was consistently inferior compared to those of RF and RF-FFA models. The superiority of the RF model was attributed to the large number of unpruned trees, which, in turn, results in development of logical input-output correlations, and mitigates overfitting and generalization errors. Even further enhancement in prediction performance was achieved when the RF model was combined with FFA (i.e., RF-FFA model). This enhancement in prediction performance was attributed to the FFA's ability to optimize the number of trees and leaves per tree of the RF model based on the volume and nature of the dataset.

The high degree of prediction accuracy (i.e., RMSE of ≈4.0 and ≈0.92 MPa for the large and small datasets, respectively) produced by the hybrid RF-FFA model suggests that the model is a promising tool for prompt and reliable prediction of composition-dependent properties of concrete. It is expected that utilization of higher quality of database – wherein influential physical (e.g., particle size distribution) and chemical (e.g., composition) attributes of concrete components (e.g., cement and fly ash) and curing conditions (e.g., temperature and relative humidity of curing) are also described – will lead to even superior prediction performance.

ACKNOWLEDGEMENTS

Funding for this research was provided by the National Science Foundation [NSF, CMMI: 1661609]. Computational tasks were conducted in the Materials Research Center and Department of Materials Science and Engineering at Missouri S&T. The authors gratefully acknowledge the financial support that has made these laboratories and their operations possible.

REFERENCES

[1] A. Jain, S.P. Ong, G. Hautier, W. Chen, W.D. Richards, S. Dacek, S. Cholia, D. Gunter, D. Skinner, G. Ceder, Commentary: The Materials Project: A materials genome approach to accelerating materials innovation, Apl Materials. 1 (2013) 011002.

[2] J. Warren, Materials Genome Initiative, in: AIP Conference Proceedings, American Institute of Physics, Ste. 1 NO 1 Melville NY 11747-4502 United States, 2012.

[3] J. Carrasquilla, R.G. Melko, Machine learning phases of matter, Nature Physics. 13 (2017) 431.

[4] G. Pilania, C. Wang, X. Jiang, S. Rajasekaran, R. Ramprasad, Accelerating materials property predictions using machine learning, Scientific Reports. 3 (2013) 2810.

[5] L. Ward, A. Agrawal, A. Choudhary, C. Wolverton, A general-purpose machine learning framework for predicting properties of inorganic materials, Npj Computational Materials. 2 (2016) 16028.

[6] L. Zdeborová, Machine learning: New tool in the box, Nature Physics. 13 (2017) 420.

[7] Y. Liu, T. Zhao, W. Ju, S. Shi, Materials discovery and design using machine learning, Journal of Materiomics. 3 (2017) 159–177. https://doi.org/10.1016/j.jmat.2017.08.002.

[8] K.O. Akande, T.O. Owolabi, S. Twaha, S.O. Olatunji, Performance comparison of SVM and ANN in predicting compressive strength of concrete, IOSR Journal of Computer Engineering. 16 (2014) 88–94.

[9] A. Behnood, V. Behnood, M.M. Gharehveran, K.E. Alyamac, Prediction of the compressive strength of normal and high-performance concretes using M5P model tree algorithm, Construction and Building Materials. 142 (2017) 199–207.

[10] J.-S. Chou, C.-K. Chiu, M. Farfoura, I. Al-Taharwa, Optimizing the prediction accuracy of concrete compressive strength based on a comparison of data-mining techniques, Journal of Computing in Civil Engineering. 25 (2010) 242–253.

[11] J.-S. Chou, C.-F. Tsai, A.-D. Pham, Y.-H. Lu, Machine learning in concrete strength simulations: Multi-nation data analytics, Construction and Building Materials. 73 (2014) 771–780. https://doi.org/10.1016/j.conbuildmat.2014.09.054.

[12] Z.-H. Duan, S.-C. Kou, C.-S. Poon, Prediction of compressive strength of recycled aggregate concrete using artificial neural networks, Construction and Building Materials. 40 (2013) 1200–1206.

[13] R. Gupta, M.A. Kewalramani, A. Goel, Prediction of concrete strength using neural-expert system, Journal of Materials in Civil Engineering. 18 (2006) 462–466.

[14] J. Kasperkiewicz, J. Racz, A. Dubrawski, HPC strength prediction using artificial neural network, Journal of Computing in Civil Engineering. 9 (1995) 279–284.

[15] N.K. Nagwani, S.V. Deo, Estimating the concrete compressive strength using hard clustering and fuzzy clustering based regression techniques, The Scientific World Journal. 2014 (2014).

[16] B.A. Omran, Q. Chen, R. Jin, Comparison of data mining techniques for predicting compressive strength of environmentally friendly concrete, Journal of Computing in Civil Engineering. 30 (2016) 04016029.

[17] V. Veloso de Melo, W. Banzhaf, Improving the prediction of material properties of concrete using Kaizen Programming with Simulated Annealing, Neurocomputing. 246 (2017) 25–44. https://doi.org/10.1016/j.neucom.2016.12.077.

[18] I.-C. Yeh, Modeling of strength of high-performance concrete using artificial neural networks, Cement and Concrete Research. 28 (1998) 1797–1808.

[19] I.-C. Yeh, Modeling concrete strength with augment-neuron networks, Journal of Materials in Civil Engineering. 10 (1998) 263–268.

[20] I.-C. Yeh, L.-C. Lien, Knowledge discovery of concrete material using genetic operation trees, Expert Systems with Applications. 36 (2009) 5807–5812.

[21] B.A. Young, A. Hall, L. Pilon, P. Gupta, G. Sant, Can the compressive strength of concrete be estimated from knowledge of the mixture proportions?: New insights from statistical analysis and machine learning methods, Cement and Concrete Research. 115 (2019) 379–388.

[22] M.F. Zarandi, I.B. Türksen, J. Sobhani, A.A. Ramezanianpour, Fuzzy polynomial neural networks for approximation of the compressive strength of concrete, Applied Soft Computing. 8 (2008) 488–498.

[23] D.G. Manning, B.B. Hope, The effect of porosity on the compressive strength and elastic modulus of polymer impregnated concrete, Cement and Concrete Research. 1 (1971) 631–644.

[24] F.A. Oluokun, E.G. Burdette, J.H. Deatherage, Elastic modulus, Poisson's ratio, and compressive strength relationships at early ages, Materials Journal. 88 (1991) 3–10.

[25] H.M. Jennings, A. Kumar, G. Sant, Quantitative discrimination of the nano-pore-structure of cement paste during drying: New insights from water sorption isotherms, Cement and Concrete Research. 76 (2015) 27–36.

[26] T.C. Powers, T.L. Brownyard, Studies of the physical properties of hardened Portland cement paste, in: ACI Journal Proceedings, ACI, 1946. http://www.concrete.org/Publications/InternationalConcreteAbstractsPortal.aspx?m=details&i=15301 (accessed August 29, 2014).

[27] G. Li, X. Zhao, Properties of concrete incorporating fly ash and ground granulated blast-furnace slag, Cement and Concrete Composites. 25 (2003) 293–299.

[28] C.S. Poon, L. Lam, Y.L. Wong, A study on high strength concrete prepared with large volumes of low calcium fly ash, Cement and Concrete Research. 30 (2000) 447–455.

[29] R.J. Schalkoff, Artificial neural networks, McGraw-Hill New York, 1997.

[30] M.A. Hearst, S.T. Dumais, E. Osuna, J. Platt, B. Scholkopf, Support vector machines, IEEE Intelligent Systems and Their Applications. 13 (1998) 18–28.

[31] P. Chopra, R.K. Sharma, M. Kumar, Prediction of compressive strength of concrete using artificial neural network and genetic programming, Advances in Materials Science and Engineering. 2016 (2016) http://dx.doi.org/10.1155/2016/7648467.

[32] P. Chopra, R.K. Sharma, M. Kumar, T. Chopra, Comparison of Machine Learning Techniques for the Prediction of Compressive Strength of Concrete, Advances in Civil Engineering. 2018 (2018) https://doi.org/10.1155/2018/5481705. https://doi.org/10.1155/2018/5481705.

[33] P. Cunningham, J. Carney, S. Jacob, Stability problems with artificial neural networks and the ensemble solution, Artificial Intelligence in Medicine. 20 (2000) 217–225.

[34] X. Yao, Evolving artificial neural networks, Proceedings of the IEEE. 87 (1999) 1423–1447.

[35] G. Zhang, B.E. Patuwo, M.Y. Hu, Forecasting with artificial neural networks:: The state of the art, International Journal of Forecasting. 14 (1998) 35–62.

[36] R. Polikar, Ensemble based systems in decision making, IEEE Circuits and Systems Magazine. 6 (2006) 21–45.

[37] T.G. Dietterich, Ensemble methods in machine learning, in: International Workshop on Multiple Classifier Systems, Springer, 2000: pp. 1–15.

[38] J.R. Quinlan, Learning with Continuous Classes, in: Proceedings of the Australian Joint Conference on Artificial Intelligence, World Scientific, Singapore, 1992: pp. 343–348. https://researchcommons.waikato.ac.nz/handle/10289/1183 (accessed December 5, 2018).

[39] Y. Wang, I.H. Witten, Induction of model trees for predicting continuous classes, in: Proceedings of European Conference on Machine Learning, University of Economics, Faculty of Informatics and Statistics, Prague, 1997. https://researchcommons.waikato.ac.nz/handle/10289/1183 (accessed December 5, 2018).

[40] C. Deepa, K. SathiyaKumari, V.P. Sudha, Prediction of the compressive strength of high performance concrete mix using tree based modeling, International Journal of Computer Applications. 6 (2010) 18–24.

[41] L. Breiman, Random forests, Machine Learning. 45 (2001) 5–32.

[42] C. Schaffer, Selecting a classification method by cross-validation, Machine Learning. 13 (1993) 135–143.

[43] I.A. Ibrahim, T. Khatib, A novel hybrid model for hourly global solar radiation prediction using random forests technique and firefly algorithm, Energy Conversion and Management. 138 (2017) 413–425.

[44] X.-S. Yang, Firefly Algorithms for Multimodal Optimization, in: O. Watanabe, T. Zeugmann (Eds.), Stochastic Algorithms: Foundations and Applications, Springer Berlin Heidelberg, 2009: pp. 169–178.

[45] J.-S. Chou, A.-D. Pham, Smart artificial firefly colony algorithm-based support vector regression for enhanced forecasting in civil engineering, Computer-Aided Civil and Infrastructure Engineering. 30 (2015) 715–732.

[46] M.W. Gardner, S.R. Dorling, Artificial neural networks (the multilayer perceptron)—a review of applications in the atmospheric sciences, Atmospheric Environment. 32 (1998) 2627–2636. https://doi.org/10.1016/S1352-2310(97)00447-0.

[47] T. Mueller, A.G. Kusne, R. Ramprasad, Machine learning in materials science: Recent progress and emerging applications, Reviews in Computational Chemistry. 29 (2016) 186–273.

[48] A.T.C. Goh, Back-propagation neural networks for modeling complex systems, Artificial Intelligence in Engineering. 9 (1995) 143–151. https://doi.org/10.1016/0954-1810(94)00011-S.

[49] J.J. Moré, The Levenberg-Marquardt algorithm: implementation and theory, in: Numerical Analysis, Springer, 1978: pp. 105–116.

[50] T. Hegazy, P. Fazio, O. Moselhi, Developing practical neural network applications using back-propagation, Computer-Aided Civil and Infrastructure Engineering. 9 (1994) 145–159.

[51] A.J. Smola, B. Schölkopf, A tutorial on support vector regression, Statistics and Computing. 14 (2004) 199–222.

[52] Vapnik, Vladimir, The Nature of Statistical Learning Theory, 2nd ed., Springer-Verlag, New York, 2000.

[53] P. Garg, J. Verma, In silico prediction of blood brain barrier permeability: an artificial neural network model, Journal of Chemical Information and Modeling. 46 (2006) 289–297.

[54] S.M. Clarke, J.H. Griebsch, T.W. Simpson, Analysis of Support Vector Regression for Approximation of Complex Engineering Analyses, J. Mech. Des. 127 (2004) 1077–1087. https://doi.org/10.1115/1.1897403.

[55] S.F. Fang, M.P. Wang, W.H. Qi, F. Zheng, Hybrid genetic algorithms and support vector regression in forecasting atmospheric corrosion of metallic materials, Computational Materials Science. 44 (2008) 647–655. https://doi.org/10.1016/j.commatsci.2008.05.010.

[56] E. Frank, M. Hall, L. Trigg, G. Holmes, I.H. Witten, Data mining in bioinformatics using Weka, Bioinformatics. 20 (2004) 2479–2481.

[57] G. Holmes, A. Donkin, I.H. Witten, Weka: A machine learning workbench, in: Intelligent Information Systems, 1994. Proceedings of the 1994 Second Australian and New Zealand Conference On, IEEE, 1994: pp. 357–361.

[58] X. Chen, H. Ishwaran, Random forests for genomic data analysis, Genomics. 99 (2012) 323–329.

[59] L. Breiman, Bagging predictors, Machine Learning. 24 (1996) 123–140. https://doi.org/10.1007/BF00058655.

[60] V. Svetnik, A. Liaw, C. Tong, J.C. Culberson, R.P. Sheridan, B.P. Feuston, Random forest: a classification and regression tool for compound classification and QSAR modeling, Journal of Chemical Information and Computer Sciences. 43 (2003) 1947–1958.

[61] M. Sarstedt, E. Mooi, Cluster analysis, in: A Concise Guide to Market Research, Springer, 2014: pp. 273–324.

[62] J.A. Hartigan, M.A. Wong, Algorithm AS 136: A k-means clustering algorithm, Journal of the Royal Statistical Society. Series C (Applied Statistics). 28 (1979) 100–108.

[63] Gãš. Biau, L. Devroye, Gãą. Lugosi, Consistency of random forests and other averaging classifiers, Journal of Machine Learning Research. 9 (2008) 2015–2033.

[64] G. James, D. Witten, T. Hastie, R. Tibshirani, eds., An introduction to statistical learning: with applications in R, Springer, New York, 2013.

[65] S. Lukasik, S. Żak, Firefly algorithm for continuous constrained optimization tasks, in: International Conference on Computational Collective Intelligence, Springer, 2009: pp. 97–106.

[66] X.-S. Yang, X. He, Firefly algorithm: Recent Advances and Applications, Internation Journal of Swarm Intelligence. 1 (2013) 36–50.

[67] P. Chopra, R.K. Sharma, M. Kumar, Predicting compressive strength of concrete for varying workability using regression models, International Journal of Engineering & Applied Sciences. 6 (2014) 10–22.

[68] P. Chopra, R.K. Sharma, M. Kumar, Artificial neural networks for the prediction of compressive strength of concrete, International Journal of Applied Sciences & Engineering. 13 (2015) 187–204.

[69] V. Chandwani, V. Agrawal, R. Nagar, Modeling slump of ready mix concrete using genetic algorithms assisted training of Artificial Neural Networks, Expert Systems with Applications. 42 (2015) 885–893.

[70] G. Martius, C.H. Lampert, Extrapolation and learning equations, ArXiv Preprint ArXiv:1610.02995. (2016).

VI. PREDICTION OF FLOTATION EFFICIENCY OF METAL SULFIDES USING AN ORIGINAL HYBRID MACHINE LEARNING MODEL

Rachel Cook[1], Keitumetse Cathrine Monyake[2], Muhammad Badar Hayat[2], Aditya Kumar[1], and Lana Alagha[2]

1. Missouri University of Science and Technology, Department of Materials Science and Engineering,1400 N Bishop Ave, Rolla Mo, 65409, USA.

2. Missouri University of Science and Technology, Department of Mining and Nuclear Engineering,1400 N Bishop Ave, Rolla Mo, 65409, USA.

ABSTRACT

Froth flotation process is extensively used for selective separation of base metal sulfides from uneconomic mineral resources. Reliable prediction of process outcomes (metal recovery and grade) is vital to ensure peak performance. This work employs an innovative hybrid machine learning (ML) model - constructed by combining the random forest model and the firefly algorithm – to predict froth flotation efficiency of galena and chalcopyrite in relation to various experimental process parameters. The hybrid model's prediction performance was rigorously evaluated, and compared against four different standalone ML models. The outcomes of this study illustrate that the hybrid ML model has the prediction ability to process outcomes with high-fidelity, while consistently outperforming the standalone ML models.

Keywords: Froth Flotation; Complex Sulfide Ore; Machine Learning; Random Forests; Firefly Algorithm.

1. INTRODUCTION

1.1. BACKGROUND

Froth flotation process is the most widely used practice to concentrate sulfide minerals – the main economic sources of world supplies of base metals. The flotation efficiency of metal sulfides is influenced by several key process variables [e.g., water chemistry, reagents chemistry, feed characteristics, cell type, and aeration rate] [1–3]. Although each of these parameters influences the flotation process outcomes (metal recovery and grade) independently, their interdependence makes the process control very difficult. Therefore, there is an urgent need to develop and employ adaptive intelligent control tools that take into account the diversity of these variables and their mutual interaction to ensure process stability and desired outcomes.

Several studies have employed conventional modeling tools (e.g., semi-empirical mathematical functions and unconstrained/unsupervised statistical approaches) in attempts to predict flotation outcomes in relation to experimental process parameters that can be readily measured [2,4–6]**.** Such modeling tools, however, are often based on semi-empirical laws, that are unable to explicitly account for the underlying mechanisms that drive the froth flotation process. Thus, the models suffer from a number of limitations, including lack of applicability in complex systems (or systems that are different from the ones used for the model's calibration), requirement of extensive model validation, and poor prediction capabilities [5,7]. Furthermore, the prediction performance of conventional modeling tools is further aggravated due to the intrinsically nonlinear cause-effect relations in such systems, wherein a large number of influential variables exist and interact thereby causing large degrees of freedom and complex input-output correlations.

Because of the highlighted limitations of more conventional modeling tools, as mentioned in the above paragraph, a focus has been placed on supervised and unsupervised utilizations of machine learning (ML) models for optimization and prediction of flotation processes [8–19]. ML models – if properly trained using high-quality datasets – have ample allure due to their ability to elucidate relationships from inherently non-linear relationships between inputs (i.e., experimental process parameters) and outputs (e.g., grade and concentration of metals) of the system, but are also able to perform predictions in previously untrained data-domains. If the prediction performance is excellent, a well-trained ML model can potentially be used to perform optimizations as well. ML Process optimization can be performed by generating a database with satisfactory number of experiments followed by modeling the physical correlation between process parameters and the process performance criteria (outputs). Optimal process parameters can be determined thereafter using the created process model which in this case will lead to peak process performance [20,21]. For Example, Al-Thyabat used artificial neural networks (ANNs) to optimize the flotation performance of a Jordanian siliceous phosphate ore by studying the effect of feed mean size, collector dosage, and impeller speed on the flotation process efficiency in terms of concentrate's grade and recovery [22]. The results indicated that optimum flotation conditions were 321.28µm, 0.7354 kg/t and 1225.25 rpm of feed mean size, collector dosage and impeller speed, respectively. In larger scale flotation operations, intelligent models can be created using a plant datasets and these models can be implemented in real-time using microcontrollers, dedicated to monitoring and controlling the input conditions, which ensures that the metallurgical performance of the plant is never hampered. However, when applying these models for process optimization, it should be kept in mind that these models are limited to the particular type of ore being tested. In case of any significant change in terms of ore complexity, mineral associations and/or ore variability, the AI models would have to be re-trained [9].

Several ML models, in particular artificial neural networks (ANNs), have been recently used to predict metallurgical performance of flotation process in various applications. Multi-layered ANN and random forests models were used to predict the concentrate grade in platinum flotation by analyzing the froth textural features extracted from the froth images [2]. The accuracy of predictions produced by the random forest model (measured in terms of R^2, the coefficient of determination) was 75.5%, whereas the R^2 value of the ANN model was 0.82 for the same datasets. Labidi [15] used ANN with two hidden layers each comprising of 100 neurons to study the effect of three process variables on the flotation kinetics during paper de-inking, and compared the results with experimental data collected at laboratory level. Authors concluded that the ANN model was able to reproduce the influences of all significant operation variables with satisfactory accuracy (R^2 ranging from 0.95-0.98) [15]. A cascade-forward NN with the back-propagation (BP) algorithm was applied to predict the impact of five operational parameters on the flotation performance and the recoveries of coal and ash in the presence of $Al(OH)_3$-PAM polymer which served as ash depressants [18,23]. Simulation results obtained by ANN model were in good agreement with experimental results obtained using a batch flotation process (R^2 values were 0.997 and 0.991 for ash and coal recoveries, respectively) [14]. Ali et al. used five different machine learning models: ANN, random forest, adaptive neuro-fuzzy inference system (ANFIS), Mamdani fuzzy logic (MFL), and hybrid neural fuzzy inference system (HyFIS) to predict the froth ash content and the combustible recovery of fine high-ash coal [9,18]. Authors indicated that the performance difference among all models was marginal with the highest R^2 value of 0.92 obtained for MFL model. Mohanty developed an ANN based model for controlling the froth layer depth in a laboratory scale coal flotation column by manipulating tailing flowrate [17]. The model was found to perform well, with an average absolute error of 0.054%, 0.048% and 0.051% for the training, validation and test datasets, respectively. Çilek used back-propagation ANN to predict the flotation performance of copper ore in locked cycle tests [11]. The developed ANN model was used to simulate various circuits' types with a reasonable error (~ 4%). Multi-layered ANN and multivariate non-linear regression (MNLR) have been applied to predict the grade and the recovery of copper (Cu) and molybdenum (Mo) in a pilot plant flotation column [10,19]. The R^2 values obtained for Cu grade, Cu recovery, Mo grade, and Mo recovery were 0.92, 0.92, 0.92, and 0.89, respectively. The model was also tested at industrial flotation plant using 92 different datasets collected at different operational conditions and showed good accuracy for the prediction of Cu and Mo recoveries and grades with R^2 values ranging from 0.92-0.94 [10]. ANN and adaptive neuro fuzzy interference system (ANFIS) have been used to predict the flotation performance of copper sulfide in batch process where five metallurgical parameters were tested as inputs. The models showed much better prediction performances compared to those obtained from unsupervised statistical approaches [12]. The unsupervised statistical approaches were based on semi-empirical laws which are data intensive and restrained in scope [24,25].

Based on the above description of ML models developed for froth flotation applications, it is clear that majority of the past studies have employed nonlinear regression based ML models – particularly ANN [26] and ANN-based models – to predict various outcomes of laboratory- and commercial-scale froth flotation processes. Despite the fact that the ANN-based models generally outperform statistical approaches, it should, however, be stated that ANN models often tend to make inaccurate predictions for input-outputs with highly nonlinear and/or highly non-monotonic functional relationships [27–30] – as would be the case with froth flotation of polymetallic sulfides. Cook et al. [30] recently showed that the hybridization of random forests (RF) with the firefly algorithm (FFA) consistently produces more accurate predictions than several commonly used ML models (including ANN) – especially when the dataset consists of highly nonlinear and non-monotonic data-domains. The authors attributed the hybrid model's (i.e., RF-FFA's) superior prediction performance to its main component, that is, the random forest model, which has the distinctive capability to process variables throughout both monotonic and non-monotonic data-domains [31]. On the basis of our literature review, it is apparent that such hybridization of the firefly algorithm with random forest has never been used to process froth flotation datasets. Given the model's superior prediction performance, as reported in the prior study [30], it is deemed important to examine if the hybrid RF-FFA model would be able to produce high-fidelity predictions of froth flotation efficiency in polymetallic sulfide systems.

In this study, the aforementioned hybrid RF-FFA model – developed by assimilating the random forest model and the firefly algorithm – is used to predict froth flotation efficiency of galena and chalcopyrite (i.e., grade and recovery of Pb and Cu) in relation to a number of influential experimental process parameters: collector's dosage (sodium isopropyl xanthate, $C_4H_7NaOS_2$); frother's dosage (4-methyl-2-pentanol or MIBC, $C_6H_{14}O$); pyrite depressant's dosage (sodium cyanide, NaCN); sphalerite depressant's dosage (zinc sulfate, $ZnSO_4$); impeller speed; air flow-rate; flotation time; and pulp's pH. The ML models utilized in this study (e.g., the hybrid and standalone models) are ranked by means of five statistical parameters and ultimately by the composite performance index (CPI) — a unified, quantitative summary of the five statistical parameters. The overall outcome of the work demonstrations the hybrid model's superior performance compared to all standalone models included in this study.

1.2. MACHINE LEARNING MODELS

Section 1.2.1., below, five standalone ML models — including the firefly algorithm (FFA; a component of the hybrid ML model) — are briefly presented, while additional specifics concerning the ML models, such as principal algorithms, can be viewed in Supporting Information (sections S.1.0 – S.5.0) in the corresponding publication. The hybrid ML model is described in section 1.2.2.

1.2.1. Standalone ML Models. The five standalone models are as follows: Multilayer perceptron artificial neural network; support vector machine; The M5Prime model tree algorithm; random forests; and the firefly algorithm.

- Artificial neural network (ANN) contains numerous neurons, that is, computational elements, organized in hierarchical layers, resembling the network of inter-connected neurons within the human brain [26]. Each neuron is responsible for processing and simplifying information received from the preceding neuron layer of neurons and communicating the processed information to the next layer of neurons [26]. Multilayer perceptron artificial neural network — a subclass of ANN — has robust self-learning capabilities due to the model's structure containing multiple neuron layers. [32].
- Support vector machine (SVM) utilizes an optimization scheme to curtail an objective cost function, that is, a ε-insensitive loss function [33], which is comprised of nonlinear kernel function sets (which are able to transform the input data from lower- to higher-dimensional feature space, a procedure commonly referred to as mapping). Support vector machines can approximate correlations between the inputs and output — related in an inherent, nonlinear fashion — of a given dataset.
- The M5Prime model tree algorithm is a modified form of the decision-tree model that employs a set of logical rules (e.g., binary yes/no criteria, and if/else statements) to split the training dataset into multiple sets. The model, subsequently, uses multivariate linear functions to develop links between input variables and output(s) in each of the split data-domains [34].
- Random forests is an adapted decision tree algorithm that utilizes bootstrap aggregation, which unifies both *bagging* and *adaptive nearest neighbors* to elucidate relationships between inputs and outputs in a dataset. Random forest

employs two-stage randomization to grow a large number of un-pruned, uncorrelated “deep” trees (unlike the M5Prime model tree algorithm, which does require pruning) [35,36].

- First developed by Yang [37], the firefly algorithm is a metaheuristic “swarm optimization” algorithm [38,39], inspired by the *theoretically perfect* behavior of flashing characteristics of a collection of lightning bugs or fireflies. This study employs the firefly algorithm to finetune, and ultimately optimize, the hyper-parameters of the hybrid RF-FFA model, as described in section 1.2.2.

All ML models briefly detailed in this this section are comprised of hyper-parameters that require supervision for enhanced prediction performance. For instance, multilayer perceptron artificial neural network’s and support vector machines’ require supervision for the selection of optimal functions. For the selection of optimal functions and hyper-parameters in this work, a 10-fold cross-validation (CV) method [40–42] was implemented as the chief technique to asses prediction performance; the 10-fold CV method is described in more detail in the following reference [30].

1.2.2. The Hybrid Random Forests — Firefly Algorithm (RF-FFA) Model. As described in Section S.4.0 of Supporting Information in the corresponding publication, the standalone RF model consists of two hyperparameters: number of leaves per tree (n_{LV}) and number of trees in the forest (n_t). Optimizing the two hyper-parameters is of great significance in the RF model as it dictates its prediction performance In recent publications [30,43], the firefly algorithm was used to compute optimum values of n_t and n_{LV}, all based on the dataset’s volume and nature, and without any user-intervention. In both studies, the authors demonstrated that predictions of the hybrid RF-FFA model were more accurate compared to predictions produced by several standalone ML models (including random forest) as well as various ensemble ML models (e.g., voting, grading, and stacking based unions of multiple ML models). The authors also argued that this method – of combining the random forest model with the firefly algorithm – is not only easier but also more time-efficient in comparison to the standalone random forest model, wherein the two hyper-parameters need to be varied-and-optimized by the user through time-consuming methods such as cross-validation or trial-and-error based approaches.

In the current study, the hybrid RF-FFA model consists of three stages of data processing. The random forest model is used in stage I, wherein the values of n_t and n_{LV} are set at 450 and 5, respectively; this is followed by the use of the firefly algorithm in stage II, as described in steps below:

- An objective function, F, — a numerical value equivalent to the total root mean squared error of random forest model's predictions —, as estimated at the end of stage I, is defined.
- The firefly algorithm is implemented (see Supporting Information in the corresponding publication for more details) to vary-and-optimize n_t and n_{LV} values so that the objective function, F, continually decreases. Here, after termination of every iteration of the firefly algorithm, the random forest model is employed to update predictions (i.e., outputs) on the bases of the latest values of n_t and n_{LV}, that is, the two hyper-parameters. After predictions are updated, the RMSE is evaluated again and updated for the next iteration.
- The objective function, F, is assumed to reach its global minimum when its value deviates by fewer than 10^{-6} units between 3 consecutive iterations. When the criterion

is satisfied, the corresponding n_t and n_{LV} values are determined to be the final, optimum values.

Lastly, in stage III, predictions are made alongside new test dataset(s) by incorporating the optimum firefly algorithm -found n_t and n_{LV} values in the random forest portion of the hybrid model.

2. MATERIALS AND PHYSICAL EXPERIMENTS

2.1. MATERIALS

Sulfide ore samples of Mississippi valley type (MVT) were obtained from a mine located in North America. The sulfide ore samples were comprised of galena (PbS), sphalerite (ZnS), pyrite (FeS_2), chalcopyrite ($CuFeS_2$), and dolomite ($CaMg(CO_3)_2$). Silicate minerals such as quartz, muscovite, and K-Feldspar were also present in trace amounts. Hydrochloric acid and sodium hydroxide were used to adjust the pH of the flotation pulp. Sodium isopropyl xanthate ($C_4H_7NaOS_2$), sodium cyanide (NaCN) and zinc sulfate ($ZnSO_4$) were purchased from Fisher Scientific, USA. 4-Methyl-2-pentanol ($C_6H_{14}O$, MIBC) was obtained from ACROS, USA Inc. All flotation experiments were performed using tap water.

Due to the high degree of interlocking and fine dissemination of base metal sulfides with other minerals [44], the enrichment process requires excessive crushing and grinding to liberate the valuable sulfide grains. Sulfide ore samples were crushed in two stages. In the first stage, a laboratory-scale jaw crusher was used to crush the large samples of ore. In the second stage, a cone crusher was used as a secondary crusher to further reduce the ore size. Homogenized samples from the crushed ore were stored in airtight bags at -10^{o}C to avoid oxidation. Prior to flotation tests, samples were dry ground for approximately 20 minutes in a batch rod mill.

2.2. CHARACTERIZATION OF FLOTATION FEED

In order to determine the particle size distribution of the flotation feed, screens of 74, 62, 53, 44, and 37 μm were used. The sieving process was performed as per the protocols defined by the American Society for Testing and Materials (ASTM). The composite particle size distribution as determined by sieve analysis is provided in the supporting information (Figure S.1) in the corresponding publication. The 80% passing size (P_{80}) of the flotation feed was ≈60 μm.

The mineralogical composition of the flotation feed was determined by Mineral Liberation Analysis (MLA). The flotation feed contained high amounts of metal sulfides: galena, sphalerite, pyrite, and chalcopyrite. The feed was also found to contain dolomite as a major gangue mineral (> 70 % of the feed). Other gangue minerals such as quartz, muscovite, and K-Feldspar were present in trace amounts. Figure 1a shows an image of mineral association in the flotation feed obtained from MLA analysis. The presentations of the mineralogical composition in different size fractions of the flotation feed is shown in Figure 1b and Table S.1 (see Supporting Information in the corresponding publication).

The total concentration of lead (Pb), copper (Cu), zinc (Zn), and iron (Fe) metals contained in galena, chalcopyrite, sphalerite, and pyrite, respectively, was determined using Inductively Coupled Plasma Optical Emission Spectrometer ICP-OES (Thermo

Fisher ICP/OES iCAP6000 series) after a complete sample dissolution by mixed acid digestion (HCl and HNO_3). Results of elemental analysis yielded feed to contain 5 wt% Pb, 4.3 wt% Zn, 0.88 wt% Cu and 2.33 wt% Fe.

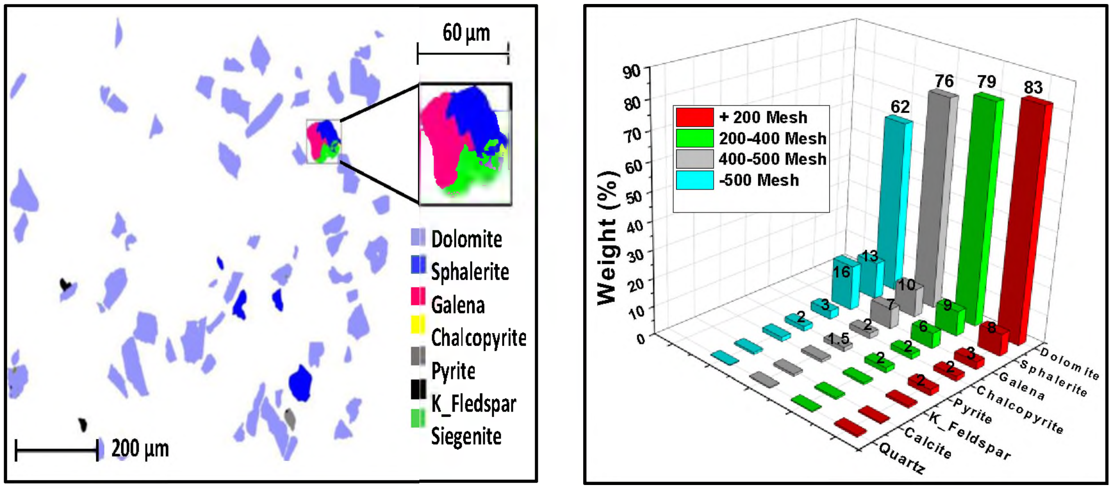

(a) (b)

Figure 1. (a) MLA image showing mineral association in the flotation feed and (b) Mineralogical composition of sulfides-containing flotation feed in different size fractions.

2.3. BATCH FLOTATION EXPERIMENTS

A total of 66 sets of experiments were designed using Box-Behnken design (BBD). This method is a class of second order rotatable design based on three level incomplete factorial design. More details about the design can be found in [7]. This method was chosen because it is known to be the most efficient design as it avoids combinations where factors are at the highest or lowest levels concurrently [45]. This specific design is advantageous as it does not require a large set of experiments hence saving time and also has the capability of revealing the optimum conditions of the factors being studied [46].

To simulate industrial procedures of froth flotation process of MVT sulfide ores, galena and chalcopyrite were allowed to float together as a "bulk" concentrate, while other sulfide minerals were depressed. The depressants used include sodium cyanide (NaCN) and zinc sulfate ($ZnSO_4$) which were used to depress the flotation of pyrite and sphalerite, respectively (as per industrial application).

All flotation tests were conducted in a Denver flotation cell with an impeller diameter of 3.88 in, and a 1-L flotation tank. In all the experiments, solids concentration was kept at 45 wt% in tap water. Other parameters such as collector's dosage, depressants' dosages, frother's dosage, impeller's speed, flotation time, pulp's pH, and air flowrate were varied. The experimental datasets collected are shown in Table S.2 (see Supporting Information in the corresponding publication). The depressants were added first followed by the collector (sodium isopropyl xanthate) then the frother (MIBC) which was added lastly . Reagents were given a 2-3-minute conditioning time. After the assigned flotation time was reached, the concentrate (froth) and tailing products were collected, dried, weighed and assayed for lead (Pb) and copper (Cu) metals. Metal recoveries were calculated using dry weights of concentrate and tailing products using Equation 1, where *C* and *T* are dry weights of the concentrate and tailing products, respectively; *c* and *t* are wt% of metals in concentrates and tailings, respectively. The values of *c* and *t* were determined using ICP-OES.

$$Recovery\ (R) = \frac{\mathrm{Cc}}{Cc + Tt} * 100 \tag{1}$$

3. DATABASE DEVELOPMENT AND EVALUATION OF ML MODEL PREDICTION PERFORMANCE

3.1. DATABASE DEVELOPMENT

Data generated from laboratory tests (described in section 2.3) were compiled into a database and used for training the ML models (described in section 1.2. and in Supporting Information in the corresponding publication) and testing their prediction performance. The database consists of 66 distinct data-records, featuring eight process parameters of froth flotation experiments and their respective efficiencies (i.e., grades and recovery of Pb and Cu). In each data-record of the database, there are: (i) 8 input variables – dosages of sodium isopropyl xanthate (g. ton^{-1}), MIBC (g. ton^{-1}), NaCN (g. ton^{-1}) and $ZnSO_4$ (g. ton^{-1}); air flow-rate (L. min^{-1}); impeller speed (rpm); pH (Unitless); and flotation time (min); and (ii) 4 outputs – Pb-grade (wt%); Pb-recovery (%); Cu-grade

Table 1. Statistical parameters relevant to the 12 attributes (8 inputs and 4 outputs) of the database. The database comprises of 66 data-records, each of which are distinct from the rest.

Attribute	Minimum	Maximum	Mean	Standard Deviation
Sodium IPX [g. ton^{-1}]	100.00	450.00	285.61	114.36
MIBC [g. ton^{-1}]	50.000	350.00	190.91	98.022
NaCN [g. ton^{-1}]	5.0000	100.00	52.500	28.863
$ZnSO_4$ [g. ton^{-1}]	200.00	700.00	465.152	163.37
Air Flow-Rate [L. min^{-1}]	3.0000	9.0000	6.0000	1.8230
Impeller Speed [RPM]	800.00	1800.0	1300.0	303.82
pH [unitless]	6.0000	12.000	8.062	0.6090
Flotation Time [sec]	2.0000	8.0000	5.0000	1.8230
Pb-Grade [wt%]	13.020	56.480	25.885	8.1560
Pb-Recovery [%]	19.260	98.940	59.251	19.613
Cu-Grade [wt %]	0.0400	8.3400	2.7820	1.2590

(wt%); and Cu-recovery (%). Statistical parameters relevant to the data-records are enumerated in Table 1. During training and testing of the ML models, it was assumed that that all four outputs are independent of each other, albeit each of the outputs are expected to be correlated with – and influenced by – all input variables. Therefore, for each of the 4 outputs, the ML models were trained (using all 8 input variables) and tested separately.

3.2. EVALUATION OF ML MODELS PREDICTION PERFORMANCE

The experimental database (described in Section 3.1.) was randomly allocated into two datasets, that is, 75% of data-records of the parent database was allocated to the training set, wherein functions and hyper-parameters were optimized, while the remaining 25% of the data-records were employed for testing prediction performance. The 75%-to-25% data partition of the parent database has been used in past studies [30,40,47,48] for training and testing of the ML models. Data partitioning was done randomly, but such that care was taken to ensure that the training dataset was representative of the parent database.

Five distinct statistical parameters were obtained through appraisals of the models' predictions against actual values to quantitatively assess ML model performance. The following are the five parameters: coefficient of determination (R^2); Person correlation coefficient (R); mean absolute percentage error (MAPE); mean absolute error (MAE)); and root mean squared error (RMSE). The calculation details for the five parameters are described in this reference [30]. The resulting values of the five statistical parameters, were amalgamated into a sixth parameter, that is, the composite performance index (CPI)

[30,40,49]. The purpose of the CPI parameter is to obtain a singular, unified value to assess and then rank (from best to worst) each ML model's performance.

4. RESULTS AND DISCUSSION

4.1. BULK FLOTATION OF GALENA AND CHALCOPYRITE

In industrial operations, two flotation practices have been adopted to separate base metal sulfides: sequential (or selective) flotation and bulk flotation. In sequential flotation, each sulfide mineral is floated separately whereas in the bulk flotation, galena (PbS) and chalcopyrite ($CuFeS_2$) are floated together in the first stage followed by several cleaning stages to separate galena from chalcopyrite. Since bulk flotation is the most widely used practice for the enrichment of Mississippi valley type (MVT) sulfides (used in this work), bulk flotation procedures were followed in this study to float galena and chalcopyrite together while depressing sulfide minerals including sphalerite (ZnS) and pyrite (FeS_2). As stated in section 2.3., a total 66 sets of experiments were designed using the Box-Behnken design (BBD) method. In these tests, different combinations of collector's (sodium isopropyl xanthate) dosage, frother's (MIBC) dosage, pyrite's depressant (NaCN) dosage, sphalerite's depressant ($ZnSO_4$) dosage, air flowrate, impeller's speed, flotation time, and pulp's pH were tested as input variables. Flotation process efficiency in terms of metal recoveries and concentrate grades (wt% of metal in concentrate) of lead (Pb) and copper (Cu) were used as response variables (outputs). As indicated from the grade and recovery results shown in Table S.2, it is hard to predict the flotation behavior of chalcopyrite and galena when diverse and interdependent variables are involved. The flotation efficiency here is a complex and nonlinear function of these variables. For example, when process variables (e.g., pH of the flotation pulp and pyrite's depressant dosage) change, the flotation recoveries and concentrate grades of Pb and Cu fluctuate with no regular pattern (Figure 2a and 2b). As depicted in Figure 2a, Pb recovery decreased from ~ 58% to 42% when the pulp's pH increased from 6 to 8. At pH 10, Pb recovery increased to 50% and with further increase in pulp's pH to 12, Pb recovery sharply increased to 89%. Similar behavior was observed for Cu where the recovery increased from 38% to 60% by increasing the pH from 6 to 8. A sharp drop in Cu recovery to 20% occurred at pH 10 then the recovery increased to 40% at pH 12. When metal recoveries were plotted as a function of pyrite depressant's dosage, unusual trends in flotation behavior were also obvious for both Cu and Pb as illustrated in Figure 2b [7].

Response surface methodology (RSM), a statistical modeling technique, was used to model the bulk flotation process of galena and chalcopyrite in real metal sulfide system (shown in Figure 2) of MVT type [7]. In that study, 62 sets of experiments were conducted where seven control process parameters were varied excluding the pulp's pH which was fixed at 8. Details about this study and the modeling methodology used – in terms of experimental design and variable levels, analysis of variance (ANOVA) and quadratics equations developed for response variables (i.e. Pb, Cu, Zn, and Fe recoveries and grades) – can be found elsewhere [7]. Results of the SRM work showed a poor agreement ($R^2 = 85\%$) between the predicted values obtained from the derived equations and the actual values obtained from flotation experiments. Same datasets described above were processed using standalone machine learning (ML) models: artificial neural networks (ANN), adaptive neuro-fuzzy inference system (ANFIS), Mamdani fuzzy logic (MFL) and a hybrid neural fuzzy inference system (HyFIS). The ML models produced reasonably accurate predictions, wherein R^2 ranged between 87-and-91% [7].

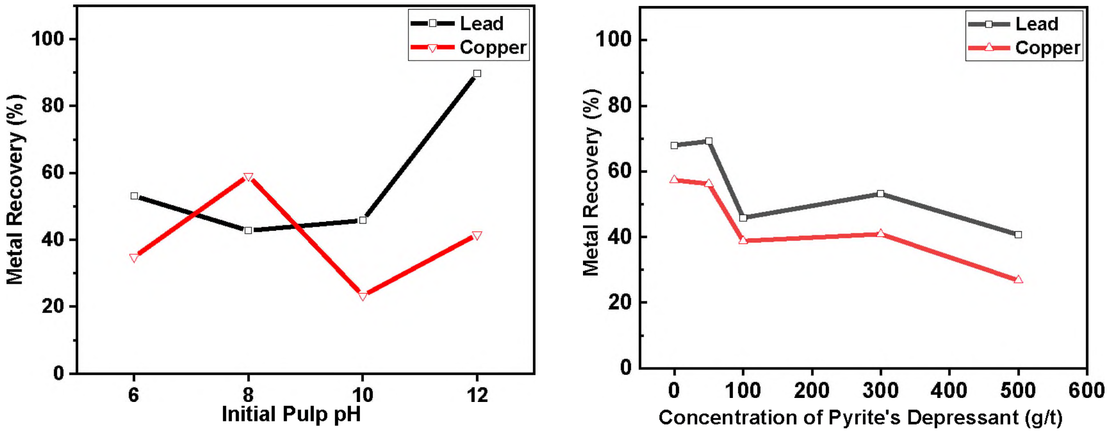

(a) (b)

Figure 2. Influence of process variables on the flotation behavior of galena and chalcopyrite from a complex sulfide ore of MVT (a)* effect of pulp's pH and (b)† Effect of pyrite's depressant dosage. (Here, zinc sulfate (zinc depressant) = 700 g/t; sodium isopropyl xanthate (collector) = 450g/t; 4-Methyl-2-pentanol (frother) = 50 g/t, using 45% solids, flotation time = 5 minutes; air flow-rate = 6 l/min; and impeller speed = 1300rpm. *pyrite's depressant dosage = 50 g/t; †pH = 8.). g/t = grams of reagent per ton of ore.

Motivated by the significant economic importance of modeling the flotation process of sulfide ores and the poor prediction capabilities of the classical and intelligent models developed for the same type of ore (MVT), experimental datasets obtained for the bulk flotation process of MVT sulfides (Table S.2) were further processed using ML models described in section 1.2.. The results and comparison of prediction performances of various ML models used in this study are discussed in Section 4.2.

4.2. PREDICTIONS: MACHINE LEARNING MODELS

As stated previously, during training and testing of the ML models, it was assumed that that all four outputs are independent of each other; notwithstanding, it is acknowledged that each output is correlated with – and influenced by – all input variables. Therefore, for each of the 4 outputs, the ML models were trained separately (using all 8 input variables) and then tested separately.

The predictions of Pb-grade, Pb-recovery, Cu-grade, and Cu-recovery (from the test set of the parent database, described in section 3.1), as yielded by the ML models, are demonstrated in Figures 3, 4, 5, and 6, respectively. Statistical errors pertaining to predictions of Pb-grade, Pb-recovery, Cu-grade, and Cu-recovery are summarized in Tables 2, 3, 4, and 5, respectively.

As can be seen in Figures 3-6, the multilayer perceptron artificial neural network and support vector machine models are unable to capture the intrinsic correlations – at any rate, not in a reliable manner – between the input variables and outputs of the experimentally-obtained database. This is primarily because – as also stated previously in section 1.2. – both multilayer perceptron artificial neural network and support vector machine models service local search-and-optimization techniques throughout training. This causes convergence to occur sooner and leads to consistent detection of min-/max-imums in the database, however bears a distinguishing drawback of convergence to occur at locally as opposed to globally.

This shortcoming is often negligible – that is, there is minimal consequence on the predictability of the models – for datasets with linear and/or monotonic functional relationships between inputs and output variables. Conversely, the input-output

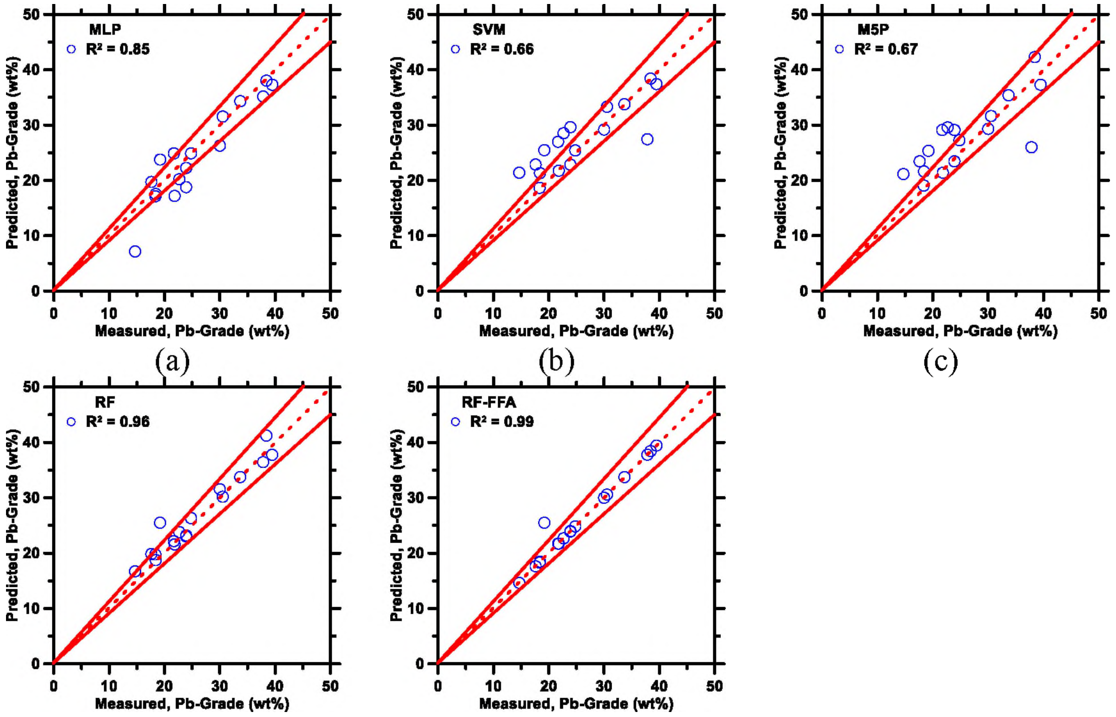

(a) (b) (c)

(d) (e)

Figure 3. Predictions made by ML models: (a) multilayer perceptron artificial neural network (MLP-ANN); (b) support vector machine (SVM); (c) M5Prime model tree algorithm (M5P); (d) random forest (RF); and (e) RF-FFA compared against measured values of Pb-grade (drawn from the dataset described in Section 2.1.). The dashed line represents the line of ideality and the solid lines represent a ±10% bound.

relationships corresponding to froth flotation dataset(s) are anticipated to be extremely nonlinear, thus rendering the predictions of multilayer perceptron artificial neural network and SVM models inaccurate – as reflected in the values of various performance measures in Tables 2-4 (e.g., R^2 of 0.8453, 0.8545, 0.7632, and 0.8032 for the multilayer perceptron artificial neural network model, when used for predictions of Pb-grade, Pb-recovery, Cu-grade, and Cu-recovery, respectively; and R^2 of 0.6603, 0.5574, 0.0488, 0.3869 for the support vector machine model, when used for predictions of Pb-grade, Pb-recovery, Cu-grade, and Cu-recovery, respectively). It is worth mentioning, here, that prediction performances of multilayer perceptron artificial neural network and support vector machine models can be improved by combining them with Genetic programing algorithms [50–52].

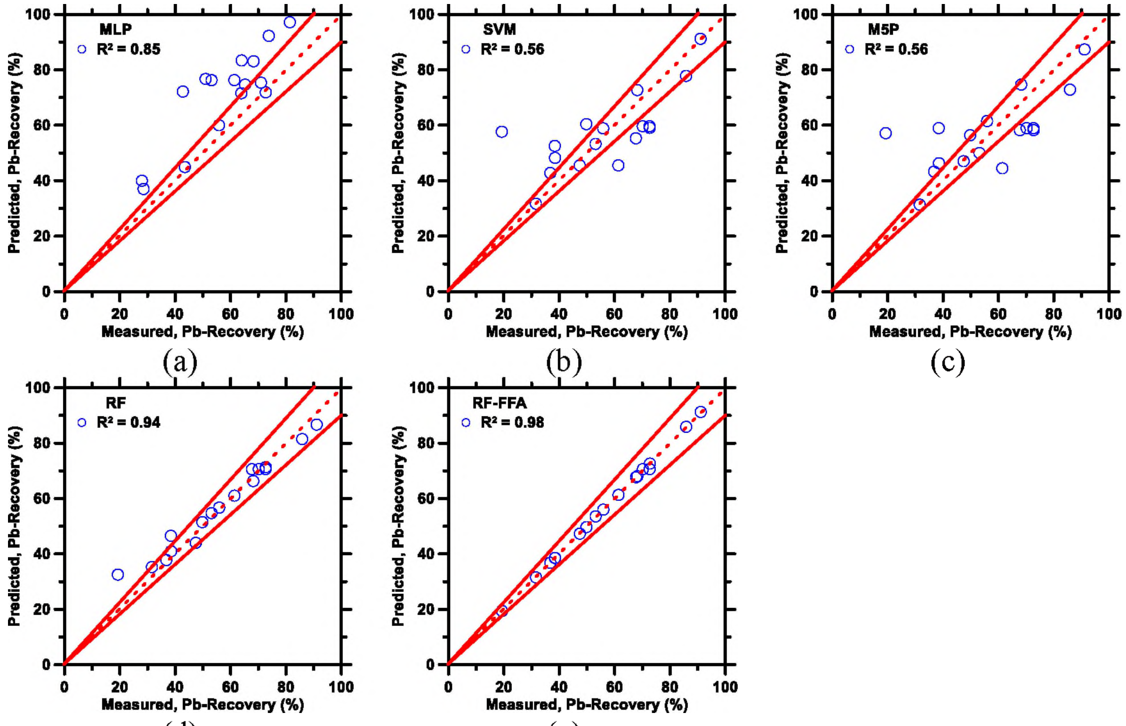

(a) (b) (c)

(d) (e)

Figure 4. Predictions made by ML models: (a) multilayer perceptron artificial neural network (MLP-ANN); (b) support vector machine (SVM); (c) M5Prime model tree algorithm (M5P); (d) random forest (RF); and (e) RF-FFA compared against actual values of Pb-recovery (drawn from the dataset described in Section 2.1.). The dashed line represents the line of ideality and the solid lines represent a ±10% bound.

Improvements can be also effectuated by employing bagging, or voting, or grading, or stacking approaches [25,36] – approaches that are typically used in development of ensemble ML models – to metaheuristically reduce the models' prediction errors thereby improving their prediction performances. However, such techniques are prone to slowing down the rate of convergence, and, in the worst case, risking the chances of overfitting (which results in poor prediction performance when new testing datasets are used).

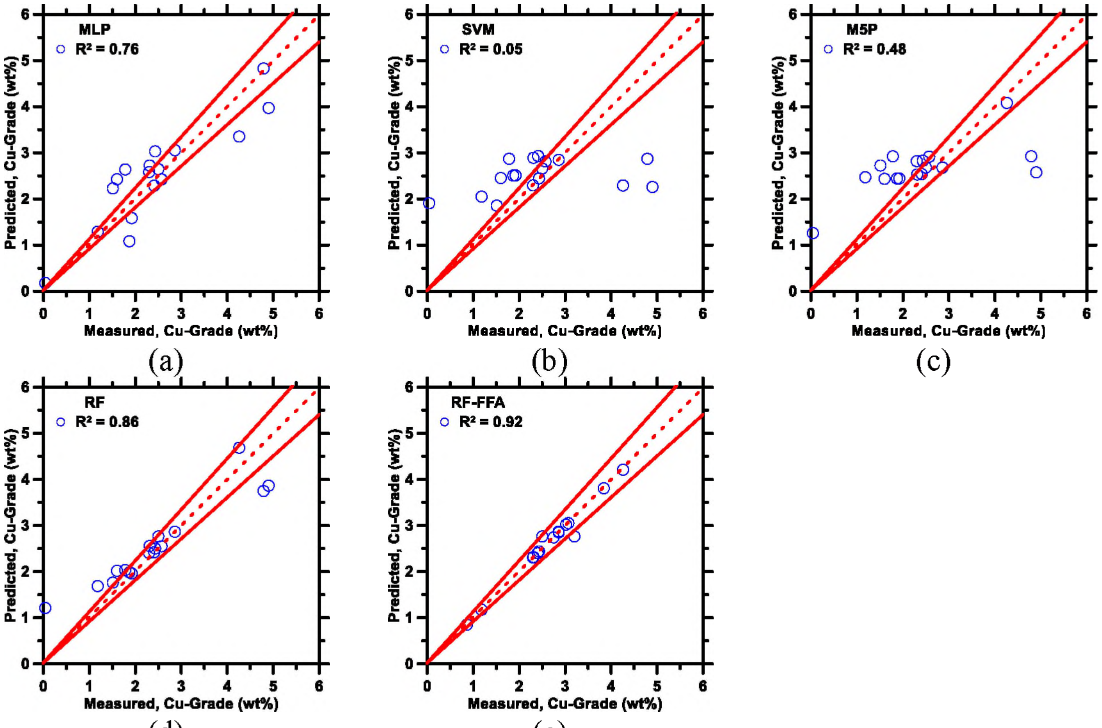

(a) (b) (c)

(d) (e)

Figure 5. Predictions made by ML models: (a) multilayer perceptron artificial neural network (MLP-ANN); (b) support vector machine (SVM); (c) M5Prime model tree algorithm (M5P); (d) random forest (RF); and (e) RF-FFA compared against actual values of Cu-grade (drawn from the dataset described in Section 3.1.). The dashed line represents the line of ideality and the solid lines represent a ±10% bound.

Table 2. Statistical parameters pertaining ML models' predictions of Pb-grade.

ML Model	R	R^2	MAE	MAPE	RMSE	CPI
	Unitless	*Unitless*	*wt%*	*%*	*wt%*	*Unitless*
MLP-ANN	0.9194	0.8453	2.6419	40.7171	3.5942	0.6022
SVM	0.8126	0.6603	3.3245	51.2372	4.7205	0.9786
M5P	0.8186	0.6701	3.4959	53.8791	4.6490	0.9836
RF	0.9797	0.9598	1.4045	21.6457	1.9109	0.2219
RF-FFA	0.9932	0.9864	0.2860	4.4085	0.9434	0.0000

The prediction performance of the M5Prime model tree algorithm was, in general, inferior compared to multilayer perceptron artificial neural network and support vector machine models (see Figures 3-6, and Tables 2-4). In the specific case of Cu-grade (Figure 5, and Table 4), predictions made by the M5Prime model tree algorithm intermediated (in terms of values of CPI: the composite performance index) between the multilayer perceptron artificial neural network and support vector machine models. However, in all other cases, the M5Prime model tree algorithm's prediction performance was the worst among all ML models that were employed in this study. The origin of such poor prediction performance of the M5Prime model tree algorithm is expected to be the small volume of the dataset (i.e., consisting of only 66 data-records, out of which only 50 used for training), which, presumably, caused the splits in the training dataset to be of poor quality. Owing to poor splitting of the database, it is expected that the multivariate linear functions were unable to accurately capture the input-output correlations within each split. These results, therefore, indicate – as was also suggested in a prior study [54] – that decision tree models with limited number of trees are not ideal for predictions when the dataset volume is small.

Table 3. Statistical parameters pertaining ML models' predictions of Pb-recovery.

ML Model	R *Unitless*	R^2 *Unitless*	MAE *wt%*	MAPE %	RMSE *wt%*	CPI *Unitless*
MLP-ANN	0.9244	0.8545	11.7649	70.5681	13.7802	0.7112
SVM	0.7466	0.5574	9.7193	58.2985	12.9810	0.9099
M5P	0.7470	0.5580	10.2023	61.1955	12.9400	0.9263
RF	0.9704	0.9417	4.2258	25.3474	5.5749	0.2022
RF-FFA	0.9883	0.9767	0.8980	5.3863	2.9738	0.0000

Based on the values for the statistical parameters (Tables 2-4), it's apparent that random forest has superior prediction performance compared to the remaining standalone ML models employed in this study. This expected outcome is consistent with prior studies which have observed that prediction performance of random forest model is better than several standalone and ensemble ML models [30,48]. The superior predictability of the random forest model is credited to its configuration and two-step randomization (see Supporting Information for more details in the corresponding publication) of unpruned "deep" trees that allow data in the training set to be split in a logical manner. This results in a diminution of parallels unpruned trees correlation, a lessening of generalization errors, and the mitigation of training data overfitting. As shown in Figures 3-6 and Tables 2-4, when assimilated with the firefly algorithm, the prediction performance of the random forest model is augmented. The hybrid RF-FFA ML model consistently elucidated the functional input-output relationship by leveraging the learned associations to unfailingly interpolate for the testing dataset. This is better reflected in the R^2 values of predictions made by the RF-FFA model: 0.9864, 0.9767, 0.9216, and 0.9817, when used for predictions of Pb-grade, Pb-recovery, Cu-grade, and Cu-recovery, respectively. The enhanced performance of RF-FFA model, that is, the random forest model predictability is improved by the joining with the firefly algorithm, resulting in the hybrid model varying and optimizing iteratively the number of trees and leaves per tree repeatedly until the deviation amid actual and predicted values reach an ultimate minimum. From Tables 2-4 it can be observed that the prediction performance of the RF-FFA model is slightly superior to random forest. This implies that training and testing datasets with limited data-records do not particularly benefit by the incorporation of the firefly algorithm to create the hybrid model. On the other hand, it was shown previously [30] that when the volume of the parent database is increased (e.g., the database (with > 1000 data-records), the incorporation of the firefly algorithm is unambiguously beneficial, leading to enhancements in the random forest model's prediction ability.

Table 4. Statistical parameters pertaining ML models' predictions of Cu-grade.

ML Model	R	R^2	MAE	MAPE	RMSE	CPI
	Unitless	*Unitless*	*wt%*	*%*	*wt%*	*Unitless*
MLP-ANN	0.8736	0.7632	0.4581	52.6710	0.6078	0.3348
SVM	0.2209	0.0488	0.7712	88.6630	1.2308	1.0000
M5P	0.6897	0.4757	0.6954	79.9480	0.9700	0.6717
RF	0.9255	0.8566	0.3424	39.3664	0.5379	0.2157
RF-FFA	0.9600	0.9216	0.0881	10.1290	0.3507	0.0000

Table 5. Statistical parameters pertaining ML models' predictions of Cu-recovery.

ML Model	R	R^2	MAE	MAPE	RMSE	CPI
	Unitless	*Unitless*	*%*	*%*	*%*	*Unitless*
MLP-ANN	0.8962	0.8032	5.0081	45.4201	6.3726	0.4562
SVM	0.6220	0.3869	7.6230	69.1361	10.6281	0.9850
M5P	0.6245	0.3900	7.8962	71.6100	10.5406	0.9956
RF	0.9572	0.9162	4.1174	37.3427	5.4325	0.3149
RF-FFA	0.9908	0.9817	0.6015	5.4555	1.8279	0.0000

As a final point, it is established that the hybrid model's prediction errors — quantified by the statistical parameters such as R^2 and RMSE — were dependably and considerably negligible compared to those conveyed in the literature that places emphases on prediction of outcomes of froth flotation processes [7,9–12,15,17,19,22,55]. It is recognized that RMSE and R^2 alone are not convincing proof that — compared to

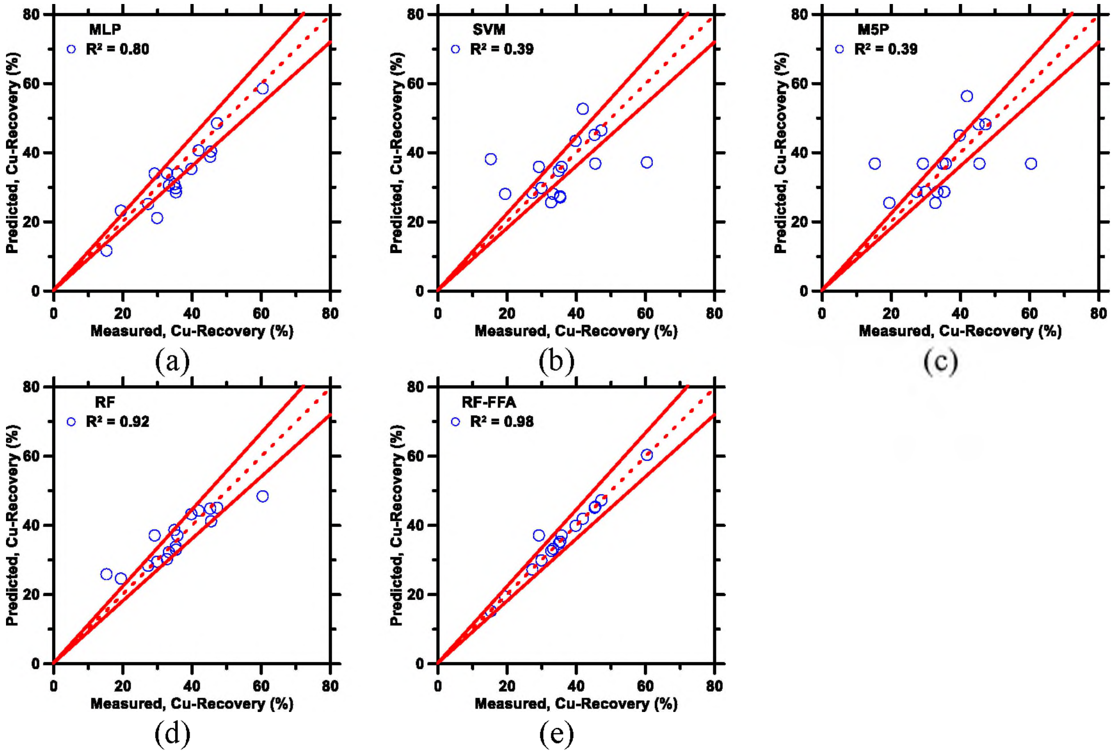

(a) (b) (c)

(d) (e)

Figure 6. Predictions made by ML models: (a) multilayer perceptron artificial neural network (MLP-ANN); (b) support vector machine (SVM); (c) M5Prime model tree algorithm (M5P); (d) random forest (RF); and (e) RF-FFA compared against actual values of Cu-recovery (drawn from the dataset described in Section 3.1). The dashed line represents the line of ideality and the solid lines represent a ±10% bound.

other ML models — the combination of random forest and the firefly algorithm will reliably yield more accurate predictions (of flotation efficiency or other flotation outcomes). The comprehensive prediction ability of a given ML model is influenced by numerous aspects, and, as a result, it is challenging to assess (or rank) dissimilar, supervised ML models. These aspects include: (*1*) nature, size, and splitting of the parent database; (*2*) pre-processing (or lack thereof) of the parent database, as well as the training and testing sets; (*3*) type and number of statistical parameters used for evaluation of prediction performance; and (*4*) methods used to optimize the ML models' hyper-parameters. To accentuate the significance of point *1*, additional computations were

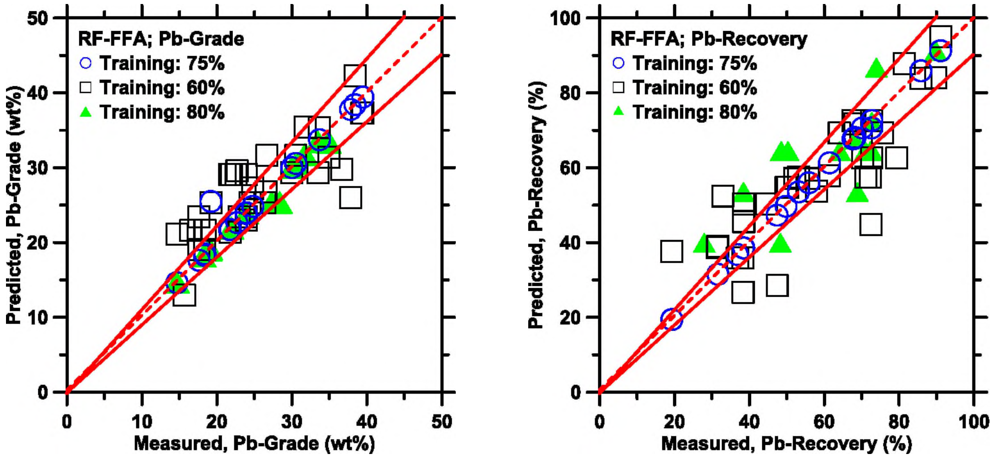

(a) (b)

Figure 7. Predictions of: (a) Pb-grade; and (b) Pb-recovery produced by the RF-FFA model using training sets consisting of 75%, or 60% or 40%, or 80% of total data-records. The dashed line represents the line of ideality and the solid lines represent a ±10% bound.

Table 6. Statistical parameters pertaining RF-FFA model's predictions of Pb-grade in relation to the percentage of data-records used in the training set.

Training set volume	R	R^2	MAE	MAPE	RMSE
	Unitless	*Unitless*	*wt%*	*%*	*wt%*
75% of data-records	0.9932	0.9864	0.2860	4.4085	0.9434
60% of data-records	0.8186	0.6701	3.4959	53.879	4.6491
80% of data-records	0.9913	0.9827	0.2622	4.3496	0.9412

implemented using the best performing ML model, that is, RF-FFA model. In these computations, in addition to the 75%-to-25% split in the parent database for training and testing of the RF-FFA model, splits of 60%-to-40% and 80%-to-20% (for training and testing, respectively) were used. Predictions of Pb-grade and Pb-recovery produced by the model – in relation to the volumes of the training (and, thus, the testing) sets – are shown in Figure 7; the corresponding predictions errors are enumerated in Tables 6 and 7.

As can be seen, the splitting of the parent database into training and testing sets – which inevitably dictates the rigor of training received by the ML model – imparted significant influence on the RF-FFA model's prediction performance. When the model was trained using only 60% of the parent database, owing to its inadequate training, the predictions errors were invariably large (i.e., R and R^2 were low, whereas MAE, MAPE, and RMSE were high). Conversely, when the model was trained using 80% of the parent database – whilst using only the remaining 20% for testing – the prediction performance was erratic (e.g., good for Pb-grade predictions but poor for Pb-recovery predictions, as shown in Figure 7). Such strong dependency of RF-FFA model's prediction performance on the volume of the training set is ostensibly because the parent database's volume is small (i.e., only 66 data-records). It is expected that when a high-volume parent database is used, the model's prediction performance would exhibit less sensitivity to minor changes in the training set's volume.

Table 7. Statistical parameters pertaining RF-FFA model's predictions of Pb-recovery in relation to the percentage of data-records used in the training set.

Training set volume	R	R^2	MAE	MAPE	RMSE
	Unitless	*Unitless*	*%*	*%*	*%*
75% of data-records	0.9883	0.9767	0.8980	5.3863	2.9738
60% of data-records	0.8718	0.7600	7.2919	43.7381	9.5571
80% of data-records	0.7994	0.6391	9.1778	55.054	11.694

With that stated, low values of RMSE, MAE, and MAPE and high values of R and R^2 (see Table 5), strongly suggest that the RF-FFA model is a dependable prediction model for froth flotation efficiency, particularly for polymetallic sulfide systems, using experimental process parameters as inputs. With the hybrid model's exceptional prediction ability, it can be speculated that increased enhancements (e.g., the utilization of a bigger dataset for training), the model has the latent requirements to determine ideal experimental process parameters that lead to preferred flotation efficiencies — the reverse of the prediction procedure presented in this work.

5. CONCLUSIONS

The RF-FFA ML hybrid model is presented in this paper. The model — developed by uniting the random forests model with the firefly algorithm – is used to predict froth flotation efficiency of galena and chalcopyrite in relation to various experimental process parameters. the firefly algorithm was used to metaheuristically vary-and-optimize the random forest models' hyper-parameters (i.e., the number of trees, and the number of leaves per tree in the forest) so as to reduce deviations between random forest model's predictions and actual observations.

Training of the hybrid RF-FFA was completed by means of 66 unique data-records (i.e., via 75% of the parent database). Individual data-records were presented with 8 different froth flotation (i.e., experimental process) parameters as inputs; outputs included outcomes of the froth flotation process (i.e., grades and recoveries of Pb and Cu). After the hybrid model was trained, the input-output relationships learned were leveraged to perform predictions corresponding to the remaining 25% of the parent database. The ability of the hybrid model to make accurate predictions was analyzed against 4 standalone ML models, that is, multilayer perceptron artificial neural network, M5P, support vector machine, and random forest, by means of 5 statistical parameters, which were ultimately united into a singular parameter, the composite performance index (CPI).

Multilayer perceptron artificial neural network and support vector machine models had reasonable prediction performance compared to the M5Prime model tree algorithm. Nevertheless, as a result of multilayer perceptron artificial neural network and support vector machine models' incapable of convergence at a global minimum, their prediction performances were inferior juxtaposed to the random forest and RF-FFA standalone models. Random forest's excellent prediction performance is credited to the organization of the model, which is comprised of a sizeable number of un-pruned "deep" trees. The prediction ability of the random forest model was additionally strengthened when joined with the firefly algorithm to form the hybrid model. This augmentation was attributed to the firefly algorithm ability to repeatedly vary random forest's number of trees and leaves per tree (i.e., hyper-parameters) and optimize them until the deviation between actual and predicted values were minimized to the global minimum.

The high accuracy of predictions made by the hybrid model is an indicator that the model has potential as a tool for optimization of froth flotation processes at plant scale. In this study, a database of reasonably small volume (i.e., <100 data-records) was used for training of the model. While, in general, expansion of the volume of the database and increasing its diversity boosts ML models' prediction performances (thereby making the models more apposite for optimizations), it remains an interesting open question if the RF-FFA model's prediction performance would still be outperform other ML standalone models if the parent database were to be expanded and further diversified. As more data pertaining to froth-flotation processes are generated – and, thereafter, consolidated and processed under the framework of ML (including the RF-FFA model used in this study) – it is conceivable that the aforesaid query can be categorically resolved.

ACKNOWLEDGEMENTS

Funding for computational component of this study was provided by the National Science Foundation [NSF, CMMI: 1661609; and NSF, CMMI: 1932690]. Computational tasks were conducted in the Materials Research Center and Department of Materials Science and Engineering at Missouri S&T. The authors gratefully acknowledge the financial support that has made these laboratories and their operations possible.

REFERENCES

[1] G. Berglund, Pulp chemistry in sulphide mineral flotation, International Journal of Mineral Processing. 33 (1991) 21–31. https://doi.org/10.1016/0301-7516(91)90040-P.

[2] D. Hodouin, Methods for automatic control, observation, and optimization in mineral processing plants, Journal of Process Control. 21 (2011) 211–225. https://doi.org/10.1016/j.jprocont.2010.10.016.

[3] K.H. Rao, I.V. Chernyshova, Challenges in Sulphide Mineral Processing, The Open Mineral Processing Journal. 4 (2011) 7–13. https://doi.org/10.2174/1874841401104010007.

[4] C. Aldrich, C. Marais, B.J. Shean, J.J. Cilliers, Online monitoring and control of froth flotation systems with machine vision: A review, International Journal of Mineral Processing. 96 (2010) 1–13. https://doi.org/10.1016/j.minpro.2010.04.005.

[5] I. Jovanović, I. Miljanović, Contemporary advanced control techniques for flotation plants with mechanical flotation cells – A review, Minerals Engineering. 70 (2015) 228–249. https://doi.org/10.1016/j.mineng.2014.09.022.

[6] P. Zhang, Advanced Industrial Control Technology, Elsevier Inc, Oxford, English, 2010.

[7] M.B. Hayat, Mitigation of Environmental Hazards of Sulfide Mineral Flotation with an Insight into Froth Stability and Flotation Performance, ProQuest Dissertations and Theses. (2018) 252.

[8] L. Alagha, S. Wang, Z. Xu, J. Masliyah, Adsorption Kinetics of a Novel Organic–Inorganic Hybrid Polymer on Silica and Alumina Studied by Quartz Crystal Microbalance, J. Phys. Chem. C. 115 (2011) 15390–15402. https://doi.org/10.1021/jp202563q.

[9] D. Ali, M.B. Hayat, L. Alagha, O.K. Molatlhegi, An evaluation of machine learning and artificial intelligence models for predicting the flotation behavior of fine high-ash coal, Advanced Powder Technology. 29 (2018) 3493–3506. https://doi.org/10.1016/j.apt.2018.09.032.

[10] E. Allahkarami, O.S. Nuri, A. Abdollahzadeh, B. Rezai, M. Chegini, Estimation of Copper and Molybdenum Grades and Recoveries in the Industrial Flotation Plant Using the Artificial Neural Network, International Journal of Nonferrous Metallurgy. 05 (2016) 23–32. https://doi.org/10.4236/ijnm.2016.53004.

[11] E.C. Çilek, Application of neural networks to predict locked cycle flotation test results, Minerals Engineering. 15 (2002) 1095–1104. https://doi.org/10.1016/S0892-6875(02)00259-5.

[12] A. Jahedsaravani, M.H. Marhaban, M. Massinaei, Application of statistical and intelligent techniques for modeling of metallurgical performance of a batch flotation process, Chemical Engineering Communications. 203 (2016) 151–160. https://doi.org/10.1080/00986445.2014.973944.

[13] E. Jorjani, S.C. Chelgani, S. Mesroghli, Prediction of microbial desulfurization of coal using artificial neural networks, Minerals Engineering. 20 (2007) 1285–1292. https://doi.org/10.1016/j.mineng.2007.07.003.

[14] M. Khodakarami, O. Molatlhegi, L. Alagha, Evaluation of Ash and Coal Response to Hybrid Polymeric Nanoparticles in Flotation Process: Data Analysis Using Self-Learning Neural Network, International Journal of Coal Preparation and Utilization. 39 (2019) 199–218. https://doi.org/10.1080/19392699.2017.1308927.

[15] J. Labidi, M.À. Pèlach, X. Turon, P. Mutjé, Predicting flotation efficiency using neural networks, Chemical Engineering and Processing: Process Intensification. 46 (2007) 314–322. https://doi.org/10.1016/j.cep.2006.06.011.

[16] C. Marais, Estimation of concentrate grade in platinum flotation based on froth image analysis, (2010).

[17] S. Mohanty, Artificial neural network based system identification and model predictive control of a flotation column, Journal of Process Control. 19 (2009) 991–999. https://doi.org/10.1016/j.jprocont.2009.01.001.

[18] O. Molatlhegi, L. Alagha, Ash Depression in Fine Coal Flotation Using a Novel Polymer Aid, International Journal of Clean Coal and Energy. 5 (2016) 65–85. https://doi.org/10.4236/ijcce.2016.54006.

[19] F. Nakhaei, M.R. Mosavi, A. Sam, Y. Vaghei, Recovery and grade accurate prediction of pilot plant flotation column concentrate: Neural network and statistical techniques, International Journal of Mineral Processing. 110–111 (2012) 140–154. https://doi.org/10.1016/j.minpro.2012.03.003.

[20] J. Schmidt, M.R.G. Marques, S. Botti, M.A.L. Marques, Recent advances and applications of machine learning in solid-state materials science, Npj Computational Materials. 5 (2019) 83. https://doi.org/10.1038/s41524-019-0221-0.

[21] D. Weichert, P. Link, A. Stoll, S. Rüping, S. Ihlenfeldt, S. Wrobel, A review of machine learning for the optimization of production processes, The International Journal of Advanced Manufacturing Technology. 104 (2019) 1889–1902. https://doi.org/10.1007/s00170-019-03988-5.

[22] S. AL-THYABAT, On the optimization of froth flotation by the use of an artificial neural network, Journal of China University of Mining and Technology. 18 (2008) 418–426. https://doi.org/10.1016/S1006-1266(08)60087-5.

[23] L. Alagha, L. Guo, M. Ghuzi, O. Molatlhegi, Z. Xu, Adsorption of hybrid polyacrylamides on anisotropic kaolinite surfaces: Effect of polymer characteristics and solution properties, Colloids and Surfaces A: Physicochemical and Engineering Aspects. 498 (2016) 285–296. https://doi.org/10.1016/j.colsurfa.2016.03.031.

[24] P.J. Grylls, F. Shankar, L. Zanisi, M. Bernardi, A statistical semi-empirical model: satellite galaxies in groups and clusters, Monthly Notices of the Royal Astronomical Society. 483 (2018) 2506–2523. https://doi.org/10.1093/mnras/sty3281.

[25] J. Holloway, K. Mengersen, Statistical Machine Learning Methods and Remote Sensing for Sustainable Development Goals: A Review, Remote Sensing. 10 (2018). https://doi.org/10.3390/rs10091365.

[26] R.J. Schalkoff, Artificial neural networks, McGraw-Hill New York, 1997.

[27] P. Cunningham, J. Carney, S. Jacob, Stability problems with artificial neural networks and the ensemble solution, Artificial Intelligence in Medicine. 20 (2000) 217–225.

[28] X. Yao, Evolving artificial neural networks, Proceedings of the IEEE. 87 (1999) 1423–1447.

[29] G. Zhang, B.E. Patuwo, M.Y. Hu, Forecasting with artificial neural networks:: The state of the art, International Journal of Forecasting. 14 (1998) 35–62.

[30] R. Cook, J. Lapeyre, H. Ma, A. Kumar, Prediction of Compressive Strength of Concrete: A Critical Comparison of Performance of a Hybrid Machine Learning Model with Standalone Models, ASCE Journal of Materials in Civil Engineering. 31 (2019) 04019255. https://doi.org/10.1061/(ASCE)MT.1943-5533.0002902.

[31] L. Breiman, Random forests, Machine Learning. 45 (2001) 5–32.

[32] M.W. Gardner, S.R. Dorling, Artificial neural networks (the multilayer perceptron)—a review of applications in the atmospheric sciences, Atmospheric Environment. 32 (1998) 2627–2636. https://doi.org/10.1016/S1352-2310(97)00447-0.

[33] C.-C. Chia, I. Rubinfeld, B.M. Scirica, S. McMillan, H.S. Gurm, Z. Syed, Looking Beyond Historical Patient Outcomes to Improve Clinical Models, Science Translational Medicine. 4 (2012) 131ra49–131ra49. https://doi.org/10.1126/scitranslmed.3003561.

[34] Y. Wang, I.H. Witten, Induction of model trees for predicting continuous classes, in: Proceedings of European Conference on Machine Learning, University of Economics, Faculty of Informatics and Statistics, Prague, 1997. https://researchcommons.waikato.ac.nz/handle/10289/1183 (accessed December 5, 2018).

[35] C. Strobl, A.-L. Boulesteix, A. Zeileis, T. Hothorn, Bias in random forest variable importance measures: Illustrations, sources and a solution, BMC Bioinformatics. 8 (2007) 25. https://doi.org/10.1186/1471-2105-8-25.

[36] K.J. Archer, R.V. Kimes, Empirical characterization of random forest variable importance measures, Computational Statistics & Data Analysis. 52 (2008) 2249–2260. https://doi.org/10.1016/j.csda.2007.08.015.

[37] X.-S. Yang, Firefly Algorithms for Multimodal Optimization, in: O. Watanabe, T. Zeugmann (Eds.), Stochastic Algorithms: Foundations and Applications, Springer Berlin Heidelberg, 2009: pp. 169–178.

[38] S. Lukasik, S. Żak, Firefly algorithm for continuous constrained optimization tasks, in: International Conference on Computational Collective Intelligence, Springer, 2009: pp. 97–106.

[39] X.-S. Yang, X. He, Firefly algorithm: Recent Advances and Applications, Internation Journal of Swarm Intelligence. 1 (2013) 36–50.

[40] J.-S. Chou, C.-F. Tsai, A.-D. Pham, Y.-H. Lu, Machine learning in concrete strength simulations: Multi-nation data analytics, Construction and Building Materials. 73 (2014) 771–780. https://doi.org/10.1016/j.conbuildmat.2014.09.054.

[41] T.G. Dietterich, Ensemble methods in machine learning, in: International Workshop on Multiple Classifier Systems, Springer, 2000: pp. 1–15.

[42] C. Schaffer, Selecting a classification method by cross-validation, Machine Learning. 13 (1993) 135–143.

[43] I.A. Ibrahim, T. Khatib, A novel hybrid model for hourly global solar radiation prediction using random forests technique and firefly algorithm, Energy Conversion and Management. 138 (2017) 413–425.

[44] S.R. Rao, Surface Chemistry of Froth Flotation, 2nd ed., Plenum Publishers, New York, NY, 2004.

[45] M.M. Ba-Abbad, P.V. Chai, M.S. Takriff, A. Benamor, A.W. Mohammad, Optimization of nickel oxide nanoparticle synthesis through the sol–gel method using Box–Behnken design, Materials & Design. 86 (2015) 948–956. https://doi.org/10.1016/j.matdes.2015.07.176.

[46] S.L.C. Ferreira, R.E. Bruns, H.S. Ferreira, G.D. Matos, J.M. David, G.C. Brandão, E.G.P. da Silva, L.A. Portugal, P.S. dos Reis, A.S. Souza, W.N.L. dos Santos, Box-Behnken design: An alternative for the optimization of analytical methods, Analytica Chimica Acta. 597 (2007) 179–186. https://doi.org/10.1016/j.aca.2007.07.011.

[47] J.-S. Chou, C.-K. Chiu, M. Farfoura, I. Al-Taharwa, Optimizing the prediction accuracy of concrete compressive strength based on a comparison of data-mining techniques, Journal of Computing in Civil Engineering. 25 (2010) 242–253.

[48] B.A. Young, A. Hall, L. Pilon, P. Gupta, G. Sant, Can the compressive strength of concrete be estimated from knowledge of the mixture proportions?: New insights from statistical analysis and machine learning methods, Cement and Concrete Research. 115 (2019) 379–388.

[49] V. Chandwani, V. Agrawal, R. Nagar, Modeling slump of ready mix concrete using genetic algorithms assisted training of Artificial Neural Networks, Expert Systems with Applications. 42 (2015) 885–893.

[50] P. Chopra, R.K. Sharma, M. Kumar, Prediction of compressive strength of concrete using artificial neural network and genetic programming, Advances in Materials Science and Engineering. 2016 (2016) http://dx.doi.org/10.1155/2016/7648467.

[51] V. Veloso de Melo, W. Banzhaf, Improving the prediction of material properties of concrete using Kaizen Programming with Simulated Annealing, Neurocomputing. 246 (2017) 25–44. https://doi.org/10.1016/j.neucom.2016.12.077.

[52] V. Chandwani, V. Agrawal, R. Nagar, Modeling slump of ready mix concrete using genetic algorithms assisted training of Artificial Neural Networks, Expert Systems with Applications. 42 (2015) 885–893.

[53] R. Polikar, Ensemble based systems in decision making, IEEE Circuits and Systems Magazine. 6 (2006) 21–45.

[54] P. Chopra, R.K. Sharma, M. Kumar, T. Chopra, Comparison of Machine Learning Techniques for the Prediction of Compressive Strength of Concrete, Advances in Civil Engineering. 2018 (2018) https://doi.org/10.1155/2018/5481705. https://doi.org/10.1155/2018/5481705.

[55] E. Jorjani, H. Asadollahi Poorali, A. Sam, S. Chehreh Chelgani, S. Mesroghli, M.R. Shayestehfar, Prediction of coal response to froth flotation based on coal analysis using regression and artificial neural network, Minerals Engineering. 22 (2009) 970–976. https://doi.org/10.1016/j.mineng.2009.03.003.

VII. MACHINE LEARNING FOR HIGH-FIDELITY PREDICTION OF CEMENT HYDRATION KINETICS IN BLENDED SYSTEMS

Rachel Cook[1], Taihao Han[1], Alaina Childers[1], Cambria Ryckman[1], Kamal Khayat[2], Hongyan Ma[2], Jie Huang[3], and Aditya Kumar[1]

1. Department of Materials Science and Engineering, Missouri University of Science and Technology, Rolla, MO, USA 65409

2. Department of Civil, Architectural, and Environmental Engineering, Missouri University of Science and Technology, Rolla, MO, USA 65409

3. Assistant Professor, Department of Electrical and Computer Engineering, Missouri University of Science and Technology, Rolla, MO, USA 65409

ABSTRACT

The production of ordinary Portland cement (OPC), the most broadly utilized man-made material, has been scrutinized due to its contributions to global anthropogenic CO_2 emissions. Thus — as a method to mitigate CO_2 emissions — mineral additives have been promulgated in literature as partial replacements for OPC. However, it has been well established that mineral replacements of differing types and physical properties can have varying effects on cement hydration kinetics. Therefore — in regards to more complex systems — it is infeasible for semi-empirical kinetic models to reveal the underlying nonlinear composition-property (i.e., reactivity) relationships. In the past decade or so, machine learning (ML) has arisen as a promising, holistic approach to reveal such composition-property correlations in composite materials, even without an across-the-board comprehension of the underlying kinetic mechanisms. This paper describes the use of a random forests (RF) model to enable high-fidelity predictions of time-dependent hydration kinetics of OPC-based systems — more specifically [OPC + mineral additives] systems — using the system's physiochemical attributes as inputs. Results show that the RF model — once meticulously trained and thoroughly validated — can also be used to formulate mixture designs that satisfy target (user-imposed) kinetics-related criteria.

Keywords: Machine Learning; Random Forests; Portland Cement; Hydration; Mineral Additives.

1. INTRODUCTION

Compared to other construction materials (e.g., wood; steel; masonry; etc.), concrete has the highest annual production [1], with 4.1 billion tons produced in the United States in 2019 [2]. Concrete is especially vital to emerging nations, as it is an economically viable material and its precursors plentiful enough to satisfy the demand for decent low-cost housing and infrastructure [1]. Thus, the complete eradication of concrete and cementitious materials in pursuit of a greener material is most likely an impossibility in the near future. With that stated, research that can provide improved understanding — or even further, predict the behavior and composition-property linkages — of OPC-based (i.e., pastes; mortars; and concretes) systems, can improve the efficiency of the implementation of said materials in practice. As a standalone product, the production of OPC is responsible for 9% of CO_2 emissions globally [3–5]. As the overall demand for OPC continues to increase [6–8], there is rising pressure to discover alternate practices and resources to reduce CO_2 emissions resulting from OPC production [3,4,7,9]. Currently being extensively explored and optimized by researchers is partial replacement of OPC with CO_2-efficient mineral additives such as pozzolanic and filler materials. Examples of said additives, in the form of ground powder, are limestone (crystalline $CaCO_3$), quartz (crystalline SiO_2), and silica fume (amorphous SiO_2); other less commonly used additives include polymorphs of TiO_2 (i.e., rutile and anatase), metakaolin (dominantly amorphous $Al_2Si_2O_7$), and corundum (crystalline Al_2O_3) [10–17]. When present in OPC-based systems, filler materials are known to alter hydration rates [10,11,18–20] — typically by accelerating the hydration (i.e., the reaction with water) of the host phase by providing additional surface sites for calcium silicate hydrate (C-S-H) — universally considered to be the “glue” of OPC-based systems and the most important hydrate phase — to heterogeneously nucleate and grow upon. The acceleration of hydration rates as a result of inclusion of fillers in OPC-based systems is commonly referred to as the *filler effect* [19–21]. To follow that point, when present in OPC-based systems, pozzolanic materials are known to contribute to a pozzolanic reaction, which ultimately yields an increased percentage of C-S-H present in the system — an effect known to increase with time [18,22]. However, materials such as silica fume and metakaolin have an additional layer of complexity. These materials have been established to contribute to the hydration of OPC-systems as pozzolanic and filler materials simultaneously, with the contributions to each effect varying with time [18,22].

The hydration of the abovementioned systems is often fitted to physical results to predict the hydration behavior and microstructural development of cement systems with respect to time. A technique that is often at the forefront of cement hydration studies is isothermal calorimetry, which measures the heat absorbed or emitted, that is, endo-/exothermic processes, for a given system. The measured heat is often represented in the literature in terms of heat flow rate and the overall heat produced at a fixed temperature with respect to time: the heat flow rate is indicative of reaction rates, while the cumulative heat released can be used to extract thermodynamic information (e.g., degree of hydration of cement) at a desired time in the hydration process. The heat flow emitted over the course of the entire hydration reaction, with respect to each unique cementitious system, can serve as a characteristic heat-evolution "fingerprint," yielding information regarding underlying kinetic mechanisms. Early hydration of cement is often described in four periods that correspond to observable regime changes in heat flow rate as a function of time. The four stages of early hydration are often referred to in the literature as: the (I) *initial period*; (II) *induction period*; (III) *acceleration period*; and (IV) *deceleration period*. This reference [23] is provided for more information on the early stages of hydration.

As stated above, these kinetic phenomena are commonly observed via unique heat evolution signatures with time, which are used to demonstrate hydration degree and microstructural development of cement systems, typically by numerical kinetic models described in the literature [24–27]. Arguably the most prominent, prolifically-cited numerical kinetic works developed in the past century, relatively around the same time, has been by William A. Johnson and Robert F. Mehl [28], Melvin Avrami [29–31], and Andrey N. Kolmogorov [32], whose collective work is commonly denoted as JMAK kinetics. JMAK kinetics assume that nucleation occurs in a random, homogeneous fashion over the total untransformed material of the given system, where the growth rate is an independent factor and assumed to occur isotropically. Several studies [33–40] have applied JMAK kinetics to cement hydration, with relatively poor fits. For some time, it's been known that such assumptions do not fit with what has been experimentally observed in terms of cement microstructure development after mixing. That is, it is well established that one of the more important hydration products of OPC systems, C-S-H, grows heterogeneously in a needle-like fashion (sometimes also referred to as fibrillar [41], sheet-like [42], or globular [43] in the literature) on cement surfaces at early ages, eventually leading to setting and the consequent development of mechanical properties. Thomas [44] pointed out that experimental observations contradict assumptions set by the JMAK equations and consequently chose to frame cement hydration in the context of John W. Cahn's original work [45]. Cahn's boundary nucleation and growth model — similar to the JMAK equations — is based on a few assumptions; Cahn's work assumes that nuclei form on planar boundaries that are randomly oriented and distributed within the system, a constant nucleation rate per unit area of the unreacted surface, and a constant, isotropic growth rate.

The work discussed in the previous paragraph has served as a springboard for several numerical studies [16,18,19,21,22,24,44,46–57], whose collective work has sought to comprehensively explain the rate-limiting steps driving the early stages of hydration — corresponding to nucleation and growth — and eventually leading to the slowing or decelerating of hydration reaction rates. Though the referenced works [16,18,19,21,22,24,44,46–57] serve as examples of important milestones in understanding underlying hydration mechanisms of OPC-based systems, there are still points of contention within the literature, in regards to the aforementioned slowing of hydration rates that occurs 10 hours or so after mixing for a plain OPC-based system, with a specific example being diffusion-limited [16,50–53] vs. dissolution-limited [54,58,59] kinetics. In addition, the process of elucidating hydration mechanisms to then predict hydration behavior based on said mechanisms is an approach that has and still requires numerous studies with varying physical and numerical approaches.

There are numerical methods, currently existing, that can predict properties, based on physical data, however these methods do not consider reaction kinetics, but instead take an engineering approach by utilizing artificial intelligence, machine learning (ML) techniques. Previous studies [60–69] have proposed that improving understanding of the relationship between hydration kinetics and consequent mechanical properties [60–62,64,65,70–81] of OPC-based systems can be assisted by a ML approach, based on the large-scale analysis of experimental data. Bangaru et al. [69] applied random forests (RF), Naïve Bayes, Logistic, K-Nearest Neighbors, and support vector machine (SVM) models to predict the degree of hydration based on the microstructural development of concrete systems. Conversely, Cruz et al. [68] predicted the microstructural development of cement systems using the degree of hydration as an input via an artificial neural network (ANN) model. Based on the results of the mentioned studies [68,69], ML can serve as a promising platform to predict the heat evolution of the hydration reaction, which can be directly linked to the kinetics of the overall reaction. By utilizing ML platforms, complexities pertaining to large compositional degrees of freedom — that is, mixture design variables, permutations of which can vary significantly and exert substantial influence on properties — and consequent, nonlinear relationships between design variables and properties of OPC-based systems can be overcome. For example, the inclusion of ground limestone in OPC-based systems, depending on the replacement level, can lead to formation of additional, carboaluminate phases in OPC-based systems via reactions with alumina-containing anhydrous phases (e.g., C_3A) [14,82–85], or from destabilization of the monosulfoaluminate phase [86]. The dissolution of metakaolin is known to release aluminate [$Al(OH)_4^-$] anions, ultimately suppressing the nucleation and growth of C-S-H [18]. Further, mineral additives, as stated previously, can function as pozzolanic or filler materials or both to varying degrees at different ages, complicating the hydration reaction. Their performances have been linked to the available specific surface area (SSA; $cm^2 . g^{-1}$) and other parameters related to physiochemical effects, such as agglomeration [18,22], which can effectively alter the total SSA contributing to the hydration reaction. Therefore, sophisticated approaches, such as ML, are required to reveal the hidden, and complex, semi-empirical rules that govern the correlation between mixture design and properties of OPC-based systems.

In this study, the RF model — a modification of the classification-and-regression decision trees (CART) ML models — is used to perform novel predictions of the time-dependent, kinetically-related heat-evolution behavior with variations correlated with different mineral additive types, such as: quartz; limestone; metakaolin; and silica fume and physiochemical attributes such as SSA. The prediction results show that the RF model can predict and optimize the relatively continuous (i.e., short time steps) and long time period (i.e., 24 hours) heat-evolution-determined kinetic profiles corresponding to plain and [OPC + mineral additive] systems as well as predict profiles for new systems when properly and rigorously trained, a feat that is currently impossible with current numerical kinetic models. The database constructed from heat evolution experimental data includes 1-additive and 2-additive systems. In order to evaluate the performance of the ML model, five different statistical parameters are used to compare the predicted cumulative heat and heat flow rate against measured data. The correlations between the inputs and outputs developed by the RF model utilized in this study can be used to optimize the mixture design based on desired hydration kinetics.

2. MATERIALS AND METHODS

A database was generated for numerous cement mixtures containing varying replacements of four commonly utilized mineral additives (i.e., quartz; limestone; metakaolin; and silica fume) in order to demonstrate the predictability of heat evolution data, relating to hydration kinetics of OPC systems, with time. The database was designed so the following parameters, known to affect the rate and degree of hydration, could be utilized as inputs: cement and mineral additive content; additive type(s); surface area(s) corresponding to cement content; and time, that is, the age of the hydrated cement.

2.1. MATERIALS

The materials utilized in this study are: Type I/II OPC (Lafarge-Holcim); quartz (MIN-U-SIL from U.S. Silica and locally sourced masonry sand); limestone (construction grade from Mississippi Lime); metakaolin (MetaMax from Imerys); and silica fume (Masterlife SF 100 from BASF). To generate a quality database with a high variance in particle size distributions (PSDs) and PSD types (e.g., bimodal, etc.), various PSDs were obtained using a few methods: randomly separating PSDs to create new ones via sieving; systematically utilizing a rule of mixtures; or a combination of the two. The obtained PSDs were then quantified via static light scattering and were implemented into mixture designs that were ultimately monitored via isothermal calorimetry to extract heat evolution data. The details of physical particle size and isothermal calorimetry measurements are further elaborated upon in the following paragraphs.

The PSDs were verified using a static light scattering particle size analyzer (Microtrac S3500) for all materials with the exception of silica fume, which was measured externally using dynamic light scattering (Zetasizer Nano). For such experiments, OPC and mineral additives were suspended in isopropanol and water, respectively. All the suspended powders were measured immediately without ultrasonification in order to emulate their effective PSDs upon contact with deionized water for mixes created and tested for isothermal calorimetry experiments. The PSD of the OPC powder is shown in Figure 1a; OPC's median particle size on a volume basis (d_{v50}, μm) — extracted from static light scattering results — was determined to be 14.63 μm. Based on OPC's measured PSD, its specific surface area (SSA) — a common indicator of the fineness of a material — was calculated to be 1726.55 $cm^2. g^{-1}$ using an assumed density of 3.15 $cm^2. g^{-1}$. In the same manner, the SSAs of the various quartz; limestone; and metakaolin PSDs were estimated using densities of 2.65 $cm^2. g^{-1}$; 2.71 $cm^2. g^{-1}$; 0.89 $cm^2. g^{-1}$, corresponding to quartz; limestone; and metakaolin; respectively. The PSDs of the three limestone distributions are shown in Figure 1b. It can be seen that the d_{v50} of the material does not necessarily increase with decreasing SSA, that is, fineness, as a result of the differential passing [vol. %] of Limestone-2's PSD not being perfectly unimodal. The inclusion of such non-unimodal PSDs has been included in both training and testing to demonstrate the predictability of systems containing materials that are perhaps nonideal in nature. The details for the type I/II OPC (whose PSD is depicted in Figure 1a) used for all calorimetry experiments is listed in Table 1. The d_{v50}s and SSAs corresponding to the mixed materials used for training and validation of the machine learning (ML) algorithms are shown in Table 1, while the details of the PSDs that were used for testing of the ML algorithms are shown in Table 2.

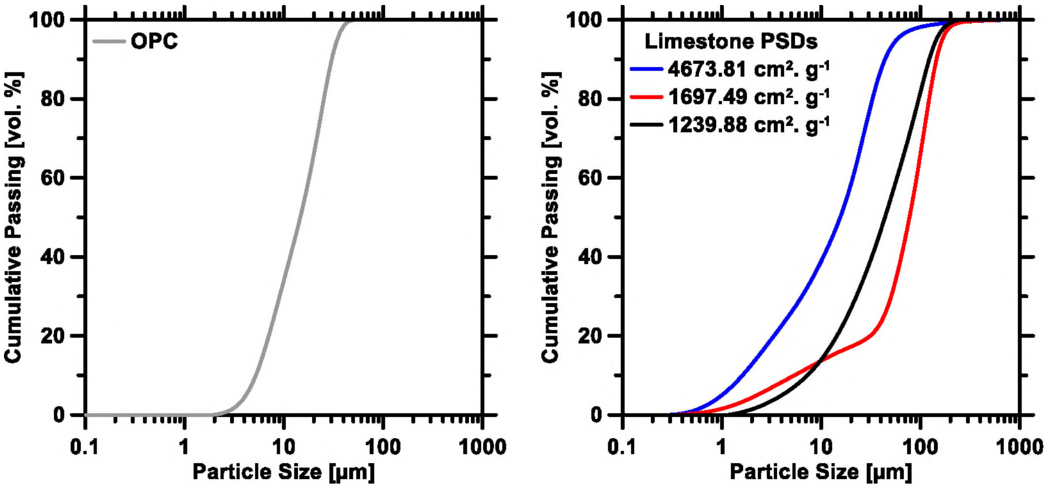

(a) (b)

Figure 1. The cumulative particle size distributions (PSDs) of (a) ordinary Portland cement (OPC); and (b) varying distributions of limestone, that is, Limestone-1; Limestone-2; and Limestone-3 which correspondingly have SSAs of 4673.81 cm^2. g^{-1}; 1697.49 cm^2. g^{-1}; and 1239.88 cm^2. g^{-1}, respectively. It can be seen that the d_{v50} of the limestone PSDs depicted do not appear to increase with decreasing SSA. Such non-unimodal PSDs have been included in the database to demonstrate the predictability of systems containing materials that are perhaps non-ideal in nature. The largest relative uncertainty in the median diameter (d_{v50}, μm), based on six replicate measurements, is on the order of ± 6%.

Table 1. The median diameters (d_{v50}) and specific surface areas (SSAs) detailing particle size distributions (PSDs) corresponding to the type I/II ordinary Portland cement (OPC); quartz limestone; metakaolin; and silica fume* that were utilized in training and later testing of the ML algorithms. The details corresponding to silica fume's particle size distribution were measured via dynamic light scattering and supplied by BASF.

Material-#	d_{v50} [μm]	SSA [cm^2. g^{-1}]
OPC	14.63	1726.55
Quartz-1	1.431	17677.21
Quartz-2	1.412	19131.56
Quartz-3	1.238	20528.18
Quartz-4	270.4	1347.17
Quartz-5	255.2	2949.89
Quartz-6	257.4	2607.13
Quartz-7	259.9	3437.85
Quartz-8	261.6	4196.163
Quartz-9	236.8	5712.76
Quartz-10	7.47	8247.762
Limestone-1	43.88	1239.88
Limestone-2	77.52	1697.49
Limestone-3	15.55	4673.81
Metakaolin-1	3.99	21678.61
Silica Fume-1*	0.1	198000

The SSA of OPC and Metakaolin-1 were also measured according to the Brunauer-Emmet-Teller theory, that is, multi-point BET (Quantachrome Nova E2000) using N_2. Before the powders were measured, the powders underwent a degassing procedure in-which they were placed under vacuum condition for 2 hours at 200°C. From six BET measurements, a SSA of 14573.33 ± 964.05 cm^2. g^{-1} was obtained for OPC and 112812.50 ± 20424.22 cm^2. g^{-1} for Metakaolin-1 from three measurements. Comparing the SSA values obtained from the two techniques, the values obtained using the BET are approximately 5.2-to-8.5 times greater than the values calculated from static light scattering results due to spherical particle shape and no internal porosity assumptions of the former [87,88]. This is corroborated by studies conducted at the National Institute of Standards and Technology by Bullard and Garboczi [87] and Garboczi and Bullard [88].

Table 2. Median diameters (d_{v50}) and specific surface areas (SSAs) of quartz; limestone; and metakaolin. The PSDs in this table have been assigned slightly different distinguishers from the PSDs presented previously, that is, "Material-R#". These distinguishers are meant to reflect that these PSDs were created in a "random" manner, respectively, as opposed to systematic manner.

		d_{v50} [μm]	SSA [cm^2. g^{-1}]
Limestone	Limestone-R1	25.73	2108.06
	Limestone-R2	42.29	1577.13
	Limestone-R3	69.27	1054.10
	Limestone-R4	22.13	2459.70
	Limestone-R5	23.36	2283.35
	Limestone-R6	33.21	1755.08
Quartz	Quartz-R1	2.52	11319.10
	Quartz-R2	2.21	12616.911
	Quartz-R3	1.87	14970.08
	Quartz-R4	1.80	15502.17
	Quartz-R5	2.02	13138.68
	Quartz-R6	2.18	12128.87
	Quartz-R7	2.30	11355.59
Metakaolin	Metakaolin-R1	10.34	11472.54
	Metakaolin-R2	7.57	16970.63
	Metakaolin-R3	5.28	18828.47
	Metakaolin-R4	4.25	21804.95
	Metakaolin-R5	4.47	21180.53
	Metakaolin-R6	6.02	17616.63
	Metakaolin-R7	4.14	22136.98

2.2. METHODS

2.2.1. Experimental Methods. The hydration rates of type I/II OPC at varying replacement levels of mineral additives were monitored using the I-Cal 8000 isothermal calorimetry for the initial 24 hours of hydration at 20°C. For all systems, [OPC + mineral additives] powders were mixed for 30 seconds before deionized water was added using a liquid-to-solid ratio of 0.45. The consequent paste was then hand-mixed for 1 min before insertion into the calorimeter.

In total, isothermal calorimetry was conducted on 352 systems (326 systems were utilized as the training dataset, while 26 random systems as the testing dataset for ML predictions), most of which were conducted in a systematic fashion for the training of ML models as opposed to randomly for testing of ML models. Two different types of cement systems were systematically monitored: systems containing 1 mineral additive (1-additive); and systems containing 2 mineral additives (2-additive). For 1-additive systems, replacements of OPC with metakaolin, quartz, silica fume, and limestone were implemented in 2.5% replacement increments: pastes containing Metakaolin-1, Quartz-1, and Limestone-1 employed replacement levels up to 60%; while pastes containing Silica Fume-1, Quartz-2, Quartz-3, Limestone-2, and Limestone-3 employed replacement levels up to 30%. For 2-additive systems, replacements of OPC with mineral additives were implemented slightly differently. Herein, replacements of Metakaolin-1, Quartz-1, Silica Fume-1, and Limestone-1 were implemented in 5.0% replacement increments: pastes containing Metakaolin-1, Quartz-1, and Limestone-1 employed total replacement levels up to 15.0%, 30.0%, 45.0% and 60.0%; while pastes containing Silica Fume-1 employed total replacement levels up to 15.0% and 30.0%. In addition to experiments conducted in a systematic fashion, 26 experiments were conducted randomly for testing of ML models. These random experiments encompass both 1-additive and 2-additive systems with randomly determined replacement levels, utilizing PSDs from both Table 1 and Table 2.

2.2.2. Database Collection and Assessment of Prediction Accuracy of ML Model. The cumulative heat and heat flow rate corresponding to the hydration of [OPC +

mineral additive] paste systems collected from isothermal calorimetry, described in section 2.0, were consolidated into the training database (Table 3) and the testing database (Table 4). The training database was used for training the ML model, and subsequently the testing database was used for evaluating its prediction performance (i.e., ability to predict hydration heat flow rate and cumulative heat that were precluded from the training database). The training database comprised of 7800 unique data-records from 326 systems, wherein the time-dependent cumulative heat and heat flow rate of each mixture design at every hour from 0 to 24 hours are outputs. The training database included 8 inputs related to physicochemical properties of the system: mineral additive type (e.g., 0 = OPC; 1 = Quartz; 2 = Limestone; 3 = Metakaolin; 4 = Silica Fume; 5 = Quartz + Limestone; 6 = Quartz + Metakaolin; 7 = Quartz + Silica Fume; 8 = Limestone + Metakaolin; 9 = Limestone + Silica Fume; 10 = Metakaolin + Silica Fume); mineral additive type (Unitless); normalized OPC content (Unitless); normalized additive-1 content (Unitless); normalized additive-2 content (Unitless); SSA of OPC ($cm^2. g^{-1}$); SSA of additive-1 ($cm^2. g^{-1}$); SSA of additive-2 ($cm^2. g^{-1}$); and time (hour). For both 1-additive and 2-additive systems, the mineral additive replacement level varied as described in section 2.0. Statistical parameters pertaining to the training database are shown in Table 3. The testing database consisted of 312 unique data-records from 26 systems and the same 8 inputs and 2 outputs as the training database. The time-dependent cumulative heat and heat flow rate of each system were predicted every two hours from 0 to 24 hours. The mineral additive replacement levels for both 1-additive and 2-additive system in the testing database were randomly selected. Statistical parameters pertaining to the testing database are shown in Table 4.

In this study, 5 unique statistical parameters — Person correlation coefficient (R); mean absolute percentage error (MAPE); coefficient of determination (R^2); root mean squared error (RMSE); and mean absolute error (MAE) — were to quantitatively and rigorously assess the prediction performance of a ML model (RF) against the testing databases. Mathematical formulations for each of these parameters can be found elsewhere [60,89].

Table 3. Summary of four statistical parameters related to each of the 10 attributes (8 inputs and 2 outputs) of the training database. The database consists of 7800 unique data-records.

Attribute	Unit	Minimum	Maximum	Mean	Standard Deviation
Mineral Additive Type	Unitless	0.0000	10.000		
Normalized OPC Content	Unitless	0.2650	0.6902	0.4670	0.1333
Normalized Additive-1 Content	Unitless	0.0000	0.4136	0.1694	0.1105
Normalized Additive-2 Content	Unitless	0.0000	0.3787	0.0507	0.0856
Cement SSA	$cm^2. g^{-1}$	1726.5	1726.5	1726.5	0.0000
Additive-1 SSA	$cm^2. g^{-1}$	0.0000	198000	22659	43392
Additive-2 SSA	$cm^2. g^{-1}$	0.0000	198000	34359	71681
Time	Hour	1.0000	24.000	12.500	6.9222
Cumulative Heat	$J. g_{opc}^{-1}$	4.1620	312.53	141.75	83.571
Heat Flow	$mW. g_{opc}^{-1}$	0.4117	6.0298	2.7629	1.2437

Table 4. Summary of four statistical parameters related to each of the 10 attributes (8 inputs and 2 outputs) of the testing database. The database consists of 312 unique data-records.

Attribute	Unit	Minimum	Maximum	Mean	Standard Deviation
Additive Type	Unitless	0.0000	10.000		
Normalized Cement Content	Unitless	0.2827	0.6132	0.4169	0.1186
Normalized Additive-1 Content	Unitless	0.0690	0.3714	0.1961	0.0908
Normalized Additive-2 Content	Unitless	0.0000	0.3171	0.0758	0.0955
Cement SSA	$cm^2. g^{-1}$	1726.5	1726.5	1726.5	0.0000
Additive-1 SSA	$cm^2. g^{-1}$	1054.1	198000	32552	60228
Additive-2 SSA	$cm^2. g^{-1}$	0.0000	198000	49603	81587
Time	Hour	2.0000	24.000	13.000	6.9041
Cumulative Heat	$J. g_{opc}^{-1}$	16.407	301.20	161.21	84.608
Heat Flow	$mW. g_{opc}^{-1}$	0.5321	7.2012	2.8690	1.2483

3. RESULTS

3.1. EXPERIMENTAL ISOTHERMAL CALORIMETRY OF [OPC + MINERAL ADDITIVE] SYSTEMS

Isothermal calorimetry was used to measure the hydration rates of OPC that was partially replaced by four mineral additive types (e.g. quartz, limestone, metakaolin, and silica fume), in 1-additive (Figure 2) and 2-additive designs (Figure 3). Figures 2 and 3 show representative heat evolution profiles of OPC paste systems prepared by substituting OPC with different mineral additives at various replacement levels. In Figure

2, all additive replacements appear to significantly enhance OPC hydration rates, by means of a leftward shift of the main hydration peak — indicated by a shortened induction period — and higher heat flow rate peak. The acceleration of hydration rates increases with increasing additive replacement level (Figure 2a) due to the filler effect [19–21]— a phenomenon which intensifies as the total solid surface area of the system increases.

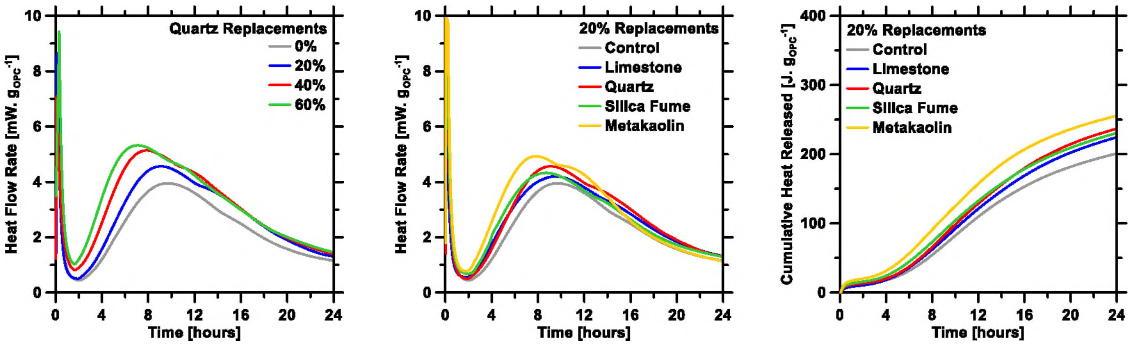

(a) (b) (c)

Figure 2. Isothermal calorimetry determinations of time-dependent (a) heat flow rate of [OPC + quartz] systems at replacement levels varying from 0 wt.% to 60 wt.%, and (b) heat flow rate and (c) cumulative heat release of [OPC + 1-additive] systems at identical 20 wt.% replacements of limestone; quartz; silica fume; and metakaolin. All calorimetry measurements were recorded over the initial 24 hours of hydration. Uncertainty in heat flow rate at the main hydration peak is ± 2%.

Figures 2b and 2c compare the heat evolution profiles of OPC replaced by the four mineral additives, with 1-additive included in each system, at the identical replacement level of 20 wt. %. Each system exhibits accelerated hydration rates compared to the neat system, largely due to the *filler effect* [18–22]. However, the varying degrees of acceleration (Figure 2b) and cumulative heat released at 24 hours (Figure 2c) are a result of the varying chemical and physical effects consequent of the inclusion of each mineral additive, as discussed in section 1.0. These systems (shown in Figure 2) are fairly simple and have been predicted using traditional thermo-kinetic models [18,19,21,22,57].

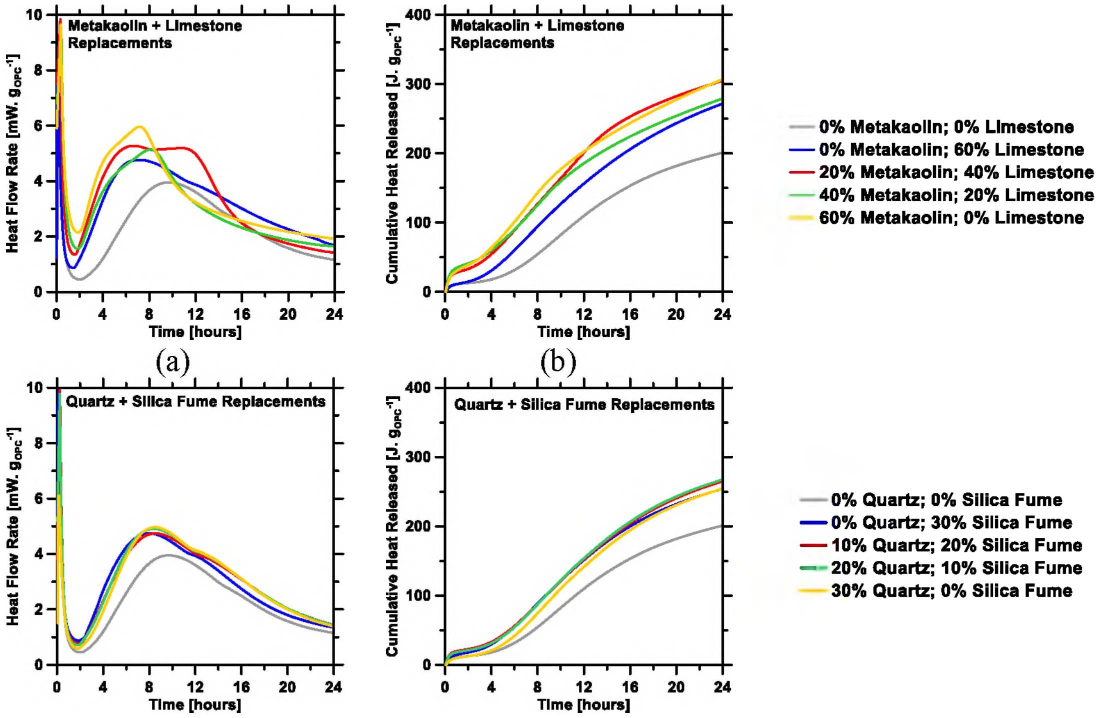

(a) (b)

(c) (d)

Figure 3. Isothermal calorimetry determinations of time-dependent 2-additive systems, that is, (a) heat flow rate and (b) cumulative heat released of [OPC + metakaolin + limestone] systems as replacement levels ranging from 0% to 60% with respect to each additive in the system; and (c) heat flow rate and (d) cumulative heat released of [OPC + quartz + silica fume] systems as replacement levels ranging from 0% to 30% with respect to each additive in the system. All calorimetry measurements were recorded over the initial 24 hours of hydration. Uncertainty in heat flow rate at the main hydration peak is ± 2%.

However, for only slightly more-complex OPC systems, such as those represented by the heat evolution profiles shown in Figure 3, which show OPC systems prepared by replacing OPC with 2-additives at different replacement levels, the hydration process of each system is much more difficult to predict by traditional means due to increased compositional degrees of freedom. [OPC + metakaolin + limestone] systems (Figures 3a and 3b), although showing accelerated heat flow rates and greater cumulative heat released at 24 hours compared to the neat system, exhibit no clear trends in terms of the occurrence of main hydration peak and the cumulative heat released at 24 hours with increasing replacement levels. With the many behaviors metakaolin is known to exhibit in a simple system [18,57], it is difficult to determine which mechanism dominates its contributions to the acceleration of OPC hydration. Adding another layer of complexity is the incorporation of limestone, which, can form carboaluminate phases in the presence of aluminate phases [14,82–86]. Heat evolution profiles corresponding to [OPC + quartz + silica fume] systems, (Figures 3c and 3d) also exhibit no clear trends with increasing replacement level, with the exception of accelerated heat flow rates and greater cumulative heat released at 24 hours compared to the neat system. However, it can be speculated that the *filler effect* is the dominating effect in [OPC + quartz + silica fume] systems. Even so, it is truly unknown if the accelerated rates resulting from the incorporation of quartz and silica fume in this study are equivalent or not. The contributions of additive chemistry and/or physical effects such as effective SSA can potentially vary with both the individual replacement level and total replacement level. Such complexity, nonetheless, is expected because each input variable — pertaining to either the additive chemistry, mixture design, or SSA — consistently casts unique and significant impact on the OPC hydration; when more than one input variable are concomitantly adjusted — especially hydration mechanism — the cumulative impact on properties is even more complex. Precisely because of such complexities, derivation of empirical, concurrent physical and chemical property relationships in OPC hydration is not feasible using simple statistical and analytical kinetic models; more sophisticated models such as machine learning are needed for such tasks.

3.2. HEAT EVOLUTION PREDICTION OF [OPC + MINERAL ADDITIVE] SYSTEMS

As described in section 4.0, the RF model was trained using the training database; thereafter, the prediction performance of the trained ML model was evaluated against the testing database. To maximize the RF model's prediction performance, it is important to ascertain that: inputs-output correlations are properly established; outliers are accounted for; and variance and bias among trees (i.e., CARTs) of the model are kept as low as possible. To accomplish these objectives, the two hyper-parameters of the RF model (i.e., number of trees in the forest; and number of leaves per tree) were rigorously optimized based on the nature and volume of the database. In this study, for such optimizations, the grid-search method [90,91] was used. This method involves autonomous, iterative variations in the hyper-parameters — while concurrently employing the 10-fold CV method [92] — to determine optimal values of hyper-parameters that result in a minimum deviation between RF model predictions and measured values. The aforesaid deviation between predictions and observations is quantified using all five statistical parameters listed in section 4.0 (i.e., R; R^2; MAE; MAPE; and RMSE). Simply put, hyper-parameters are determined to be optimal when R and R^2 are at (or close to) their global maximum, while MAE, MAPE, and RMSE are at (or close to) their global minimum.

The representative results of the RF model, which were obtained from the grid-search method, are shown in Figure 4. The statistical parameters that were used to measure the deviation between predictions and measured values of cumulative heat flow and heat flow rate (averaged over the 24-hours period) are MAPE and R^2. On the basis of MAPE and R^2, the optimal prediction performance of the RF model for the cumulative heat prediction occurred for common values of the two hyper-parameters: that is, *number of trees in the forest* = 800; and *number of splits in each tree* = 5. Moreover, the RF model structured using 800 trees and 5 splits produced accurate prediction of the heat flow rate as well. Therefore, 800 trees and 5 splits were selected as optimal hyper-parameters for further predictions in this study. When the *number of splits* was less than 5, logical splits in the databases were numerically inadequate and too simplistic to fully encompass the complex, underlying correlations between inputs and output. When the *number of splits* was larger than 5, the complex structure of the trees (CARTs) heightened the likelihood of bias, which in turn resulted in overfitting. Likewise, when the *number of trees* was less than 800, the RF model did not have enough independent bootstraps to produce accurate predictions (for new OPC systems in the testing dataset). However, when excessive trees (i.e., >800) were used, while the computational complexity of the model indubitably increased, the prediction performance did not improve (akin to *law of diminishing returns* [93,94]). This is hypothesized to be caused by increased redundancy among the trees. More specifically, it is expected that — in the forest with >800 trees, all of which were meant to be distinct — several trees (that were forced to be grown from similar bootstraps) ended up having similar structures, and, therefore, produced similar predictions; thereby, resulting in little to no improvement in the RF model's overall prediction accuracy.

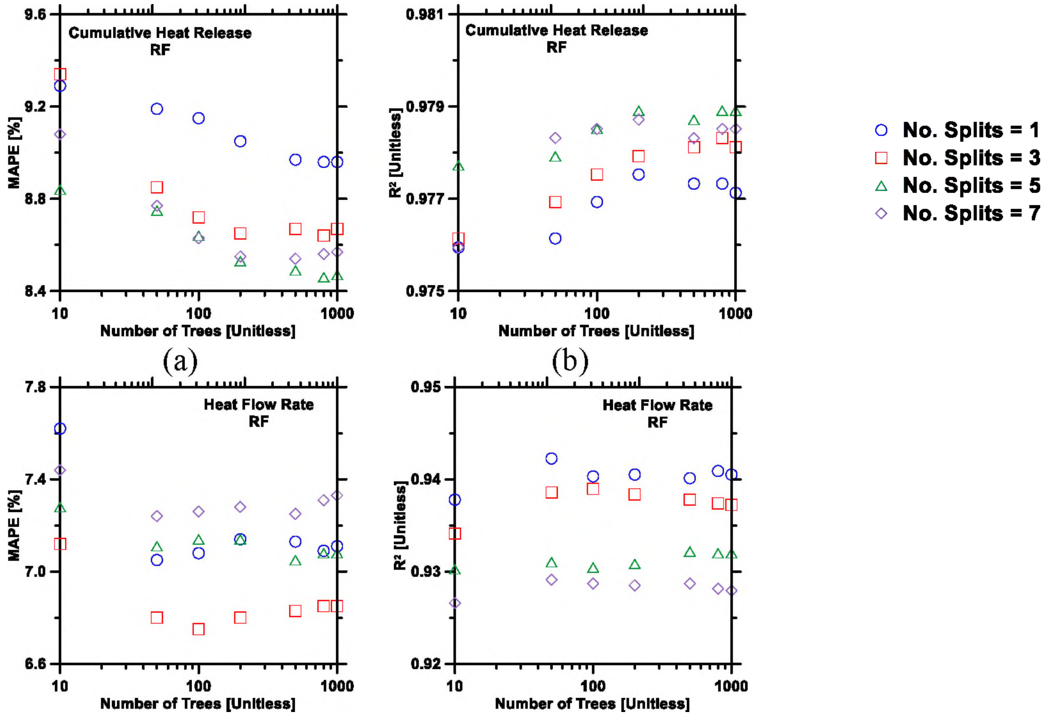

(a) (b)

(c) (d)

Figure 4. Grid-search method used to optimize hyper-parameters (*number of trees in the forest*; and *number of splits in each tree*) of the RF model to improve its prediction performance against: (a) cumulative heat flow, as evaluated by MAPE; (b) cumulative heat flow, as evaluated by R^2; (c) heat flow rate, as evaluated by MAPE; and (d) heat flow rate, as evaluated by R^2.

Prediction performance using heat evolution data, related to the kinetics of the hydration reaction corresponding to [OPC + mineral additive] systems, are compared — in the form of the five statistical parameters — against extracted physical values in Figures 5-7 for every two hours. The statistical parameters (averaged over the 24-hours period of hydration) corresponding to the testing set are itemized in Table 5. Figure 7 shows representative predicted results against the measured values; for reference, the entire cumulative heat and heat flow rate spectrum of representative systems from calorimetry experiments are included to exhibit a visual comparison between predicted values and measured values.

Table 5. Prediction performance of ML models, measured on the basis of the cumulative heat release and heat flow rate of cement pastes in the testing database. Five statistical parameters (i.e., *R*, *R*^{2}, *MAE*, *MAPE*, and *RMSE*) – averaged over the period of 24 hours – and the composite performance index (CPI) are shown.

	ML Model	R	R^2	MAE	MAPE	RMSE
Heat Flow Rate	RF	*Unitless*	*Unitless*	mW. g_{opc}^{-1}	%	mW. g_{opc}^{-1}
		0.965	0.932	0.197	7.078	0.331
Cumulative Heat Release		*Unitless*	*Unitless*	J. g_{opc}^{-1}	%	J. g_{opc}^{-1}
		0.989	0.979	10.417	8.460	14.398

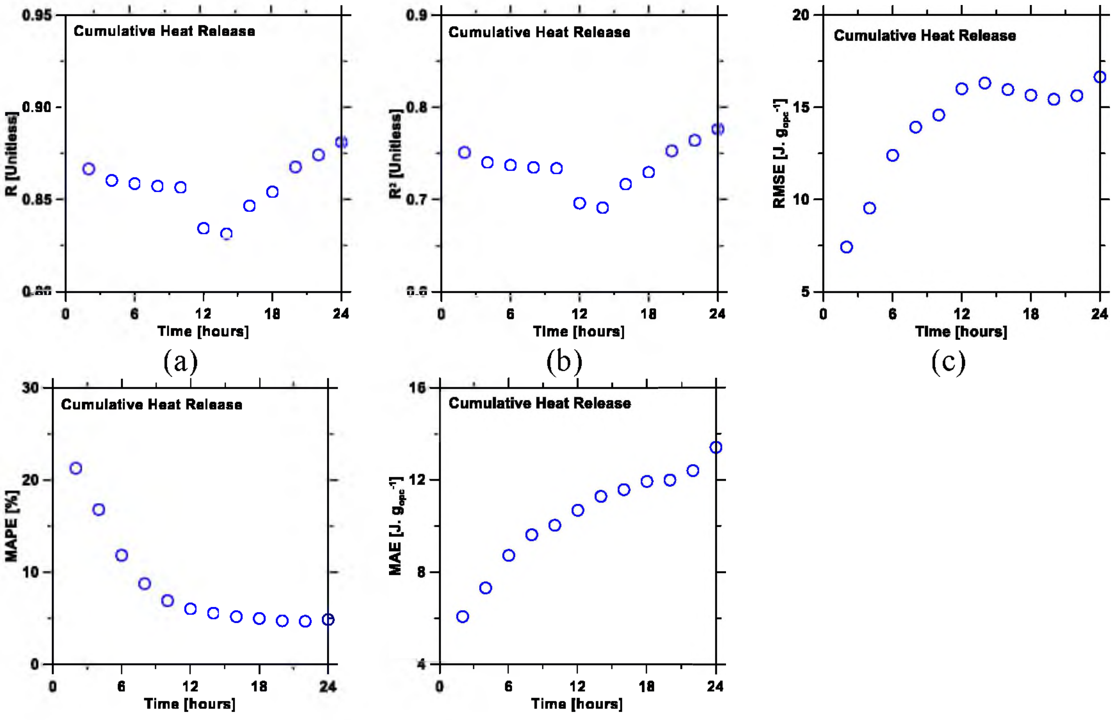

(a) (b) (c)

(d) (e)

Figure 5. Statistical parameters describing errors in prediction of cumulative heat release of pastes over a 24-hour period in the testing database: (a) Person correlation coefficient (R); (b) coefficient of determination (R^2); (c) root mean squared error (RMSE); (d) mean absolute percentage error (MAPE); and (e) mean absolute error (MAE) as functions of time.

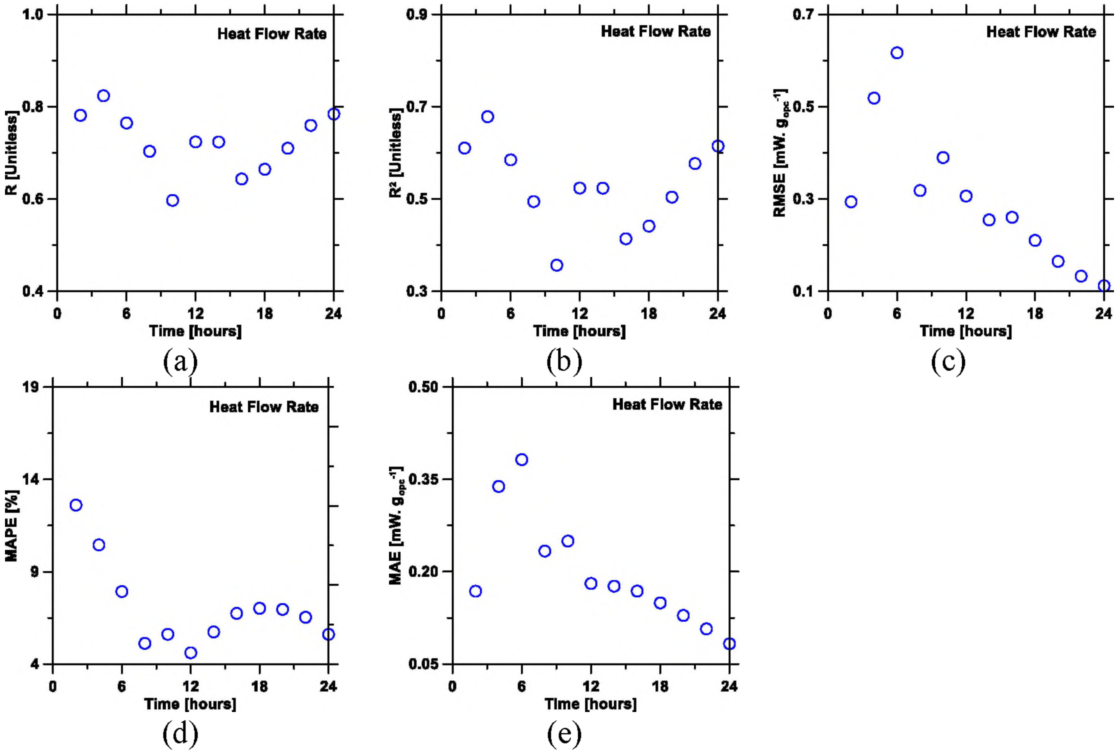

(a) (b) (c)

(d) (e)

Figure 6. Statistical parameters describing errors in prediction of heat flow rate of pastes over a 24-hour period in the testing database: (a) Person correlation coefficient (R); (b) coefficient of determination (R^2); (c) root mean squared error (RMSE); (d) mean absolute percentage error (MAPE); and (e) mean absolute error (MAE) as functions of time.

As can be seen in Table 5, predictions of heat flow rate and cumulative heat, as produced by the RF model, are accurate. The prediction of heat flow rate had a Pearson correlation coefficient (*R*) value of 0.965 and a root mean squared error (*RMSE*) value of 0.331 mW. g_{opc}^{-1}, while the prediction of the cumulative heat had a Pearson correlation coefficient (*R*) value of 0.983 and a root mean squared error (*RMSE*) value of 11.669 J. g_{opc}^{-1}. In Figures 5 and 6, it is worth pointing out that the prediction for early-age hydration reaction behavior reveals lower accuracy than the prediction for later hours because of significant variations among pastes. For example, the hydration reaction needs to experience three stages — the *initial period*, *induction period*, and *acceleration period*

— within the first 2-to-4 hours, and each stage exhibits a unique "footprint" (e.g., distinct kinetic behaviors) corresponding to different mechanisms. However, hydration undergoes only two stages (i.e., the *acceleration period* and *deceleration period*) for the latter twenty hours, during which the kinetic behavior is occurring at a significantly slower rate. As seen in Figure 7 (g-h), the prediction of the paste containing metakaolin replacement presented relatively lower accuracy compared to other [OPC + mineral additive] systems without metakaolin. The most plausible reason is that the volume of the training database used is not large enough, despite containing more than 300 unique compositions (i.e., OPC systems). The inclusion of more data-records into the database will enhance its volume and diversity, which will, in turn, further reduce the model's prediction errors, especially errors for the metakaolin system, thereby making the model more amenable for optimization-based tasks.

The high-fidelity prediction of cumulative heat and heat flow rate from the RF model is expected because several past studies have already reported that the RF model produces superior predictions of materials' properties [60–62,80,89,95,96]. This disparity in the RF model's prediction performance vis-à-vis other ML models can be traced back to the former model's structure, which gives it several advantages [93,97,98]. In the RF model, a large number of trees (i.e., number of CARTs >>100) are grown, one-by-one in a recursive manner by using randomly-selected bootstraps of identical volume; as such, generalization errors (likelihood of overfitting) are minimized [99]. As each tree is permitted to grow — and not pruned or smoothened at all — until it reaches it maximum size, the RF model is proficient at developing rational *input-output* correlations, while ensuring that seemingly anomalous data-records (i.e., outliers with respect to already established trends) are not ignored or removed during any stage of the training process.

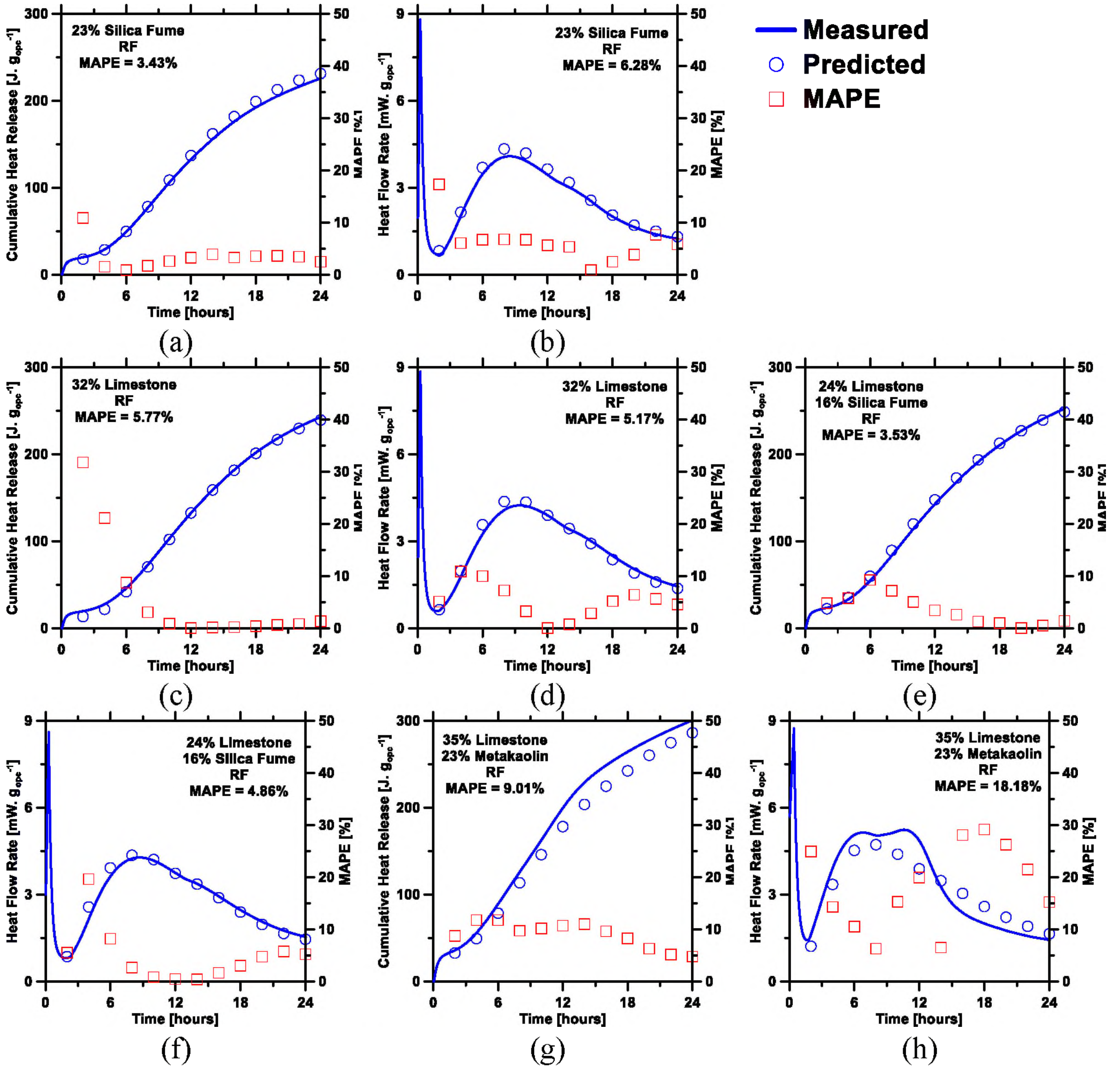

(a) (b)

(c) (d) (e)

(f) (g) (h)

Figure 7. The RF model's predictions of: (a) cumulative heat and (b) heat flow rate of [OPC + silica fume]; (c) cumulative heat and (d) heat flow rate of [OPC + limestone]; (e) cumulative heat and (f) heat flow rate of [OPC + silica fume + limestone]; and (g) cumulative heat and (h) heat flow rate of [OPC + metakaolin + limestone] compared against experimental measurements. Mean absolute error (MAE) of each prediction is shown in the figure. The overall mean absolute errors (MAE) of the predictions are shown in the legends.

Furthermore, the RF model employs two-stage randomization, which goes a long way in ensuring that each of the *deep, unpruned* trees, is distinct in its structure and does not exhibit any dependency to the rest of the trees in the forest. Such independency among the trees is crucial because it ensures that predictions produced by the trees are truly independent of each other; which in turn, results in low variance in the final predictions (i.e., average of predictions from all trees). Lastly, the RF model is easy to implement because the *number of trees in the forest* and *number of splits in each tree* are the only two hyper-parameters that are required as inputs from the user. Adjusting these parameters through trial-and-error is generally cumbersome and time-consuming, and could compromise prediction performance [100]. Therefore, in this study, we used the grid-search method along with the 10-fold CV method (see Figures 4) for such adjustments.

3.3. OPTIMIZATION OF [OPC + MINERAL ADDITIVE] MIXTURE DESIGN

The results and discussion shown in the above section have proven that the RF model — and further ML in general — can be utilized to predict the time-dependent heat flow rate and cumulative heat corresponding to the hydration reaction of [OPC + mineral additive] systems — in relation to additive replacement level and particle size distribution — in a high-fidelity manner. The authors, therefore, posit that this ability of the RF model — to understand hidden correlations between physiochemical attributes of the paste and hydration behavior of cement in such pastes — can be leveraged to develop optimal mixture design of [OPC + mineral additive] systems that exhibit target (user-imposed) hydration behavior. To verify this, an optimization scheme was designed to accept three target calorimetric features – the heat flow rate corresponding to the main hydration peak; time corresponding to the occurrence of the main hydration peak; and the slope of heat flow curve during the acceleration period – as inputs, along with selected mixture design inputs. Then, the Bayesian optimization approach [101,102] was employed, wherein the RF model was invoked to leverage its knowledge of composition-reactivity correlations (obtained during its training and validation) to reveal the optimal mineral additive type, additive SSA, and additive replacement level, which in combination would yield a calorimetry profile featuring the target (user-imposed) calorimetric features (i.e., slope of acceleration; time of main hydration peak; and heat flow rate at the main hydration peak). To the best of authors' knowledge, no kinetic models reported in previous studies are capable of producing such reverse predictions of the mixture design (i.e., mineral additive type, SSA, and replacement level) using heat evolution signatures as inputs.

During the optimization process, four variables were used as the primary inputs: the heat flow rate corresponding to the main hydration peak ($J.\ g_{opc}^{-1}$); time corresponding to the occurrence of the main hydration peak (hour); slope of the acceleration period ($J.\ g_{opc}^{-1}.\ hour^{-1}$); and normalized water mass (unitless). The optimization process — altogether, comprised of three steps — was utilized to determine physicochemical information corresponding to the relevant mineral additive, which were subsequently used to achieve the targeted heat flow rate signature corresponding to 1-additve systems. (I) Initially, the RF model was used to predict the mineral additive type (unitless) present in each cement system using the aforementioned four inputs. (II) The output mineral additive type was then utilized as an additional, secondary input (i.e., in additional to the primary inputs) to consecutively predict the mineral additive's SSA (cm^2. g^{-1}). (III) In the final step, both the mineral additive type and the SSA of the mineral additive, predicted in steps (I) and (II), respectively, were utilized as additional, secondary inputs adjunct to the primary inputs to predict the replacement level of the relevant mineral additive. The training dataset consisted of 208 1-additive systems; while the target calorimetric parameters were extracted from six 1-additve systems (see Figure 8) that were randomly selected from the testing dataset used in section 5.2. Results obtained from the optimizations, corresponding to the 1-additive systems, are shown in Table 6. Here, the optimal values of mineral additive type, additive replacement level, and additive's SSA – as produced by the RF model – are compared against actual values.

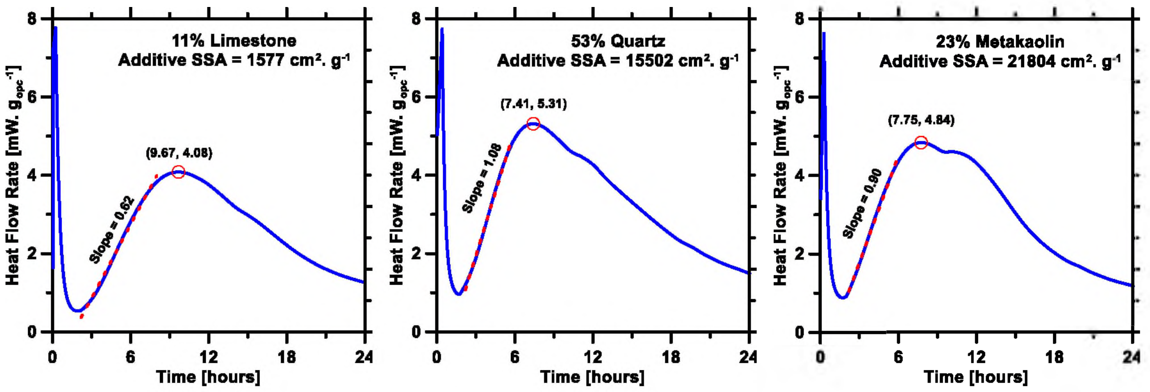

(a) (b) (c)

Figure 8. Isothermal calorimetry profiles of (a) [OPC + limestone]; (b) [OPC + quartz]; and (c) [OPC + metakaolin]. These, and heat evolution profiles of three other 1-additive systems, were randomly selected from the testing database. From these profiles, heat flow rate and time of the main hydration peak (marked by red circle), and slope of the acceleration period (marked by red dashed line) were extracted; and subsequently used as inputs (target calorimetric parameters) for mixture design optimization.

As can be seen in Table 6, the optimization of mineral additive type was successful, and the predictions of additive SSA and replacement level are reasonably

Table 6. Optimization results of six 1-additive systems compared against actual values of additive type, additive replacement level, and additive SSA.

	11% Limestone			53% Quartz			23% Metakaolin		
	Actual	Predicted	Error (%)	Actual	Predicted	Error (%)	Actual	Predicted	Error (%)
Additive Type	2	2	0	1	1	0	3	3	0
Additive Replacement Level (%)	11	7.9	27.90	53	48.9	7.64	23	24.6	7.17
Additive SSA ($cm^2. g^{-1}$)	1577	1676	6.30	15502	16744	8.01	21804.95	21608	0.90
	18% Silica Fume			23% Silica Fume			13% Quartz		
	Actual	Predicted	Error (%)	Actual	Predicted	Error (%)	Actual	Predicted	Error (%)
Additive Type	4	4	0	4	4	0	1	1	0
Additive Replacement Level (%)	18	21.7	21.03	23	28.3	23.30	13	12.0	7.51
Additive SSA ($cm^2. g^{-1}$)	198000	198000	0	198000	198000	0	14970	14442	3.53

accurate. Overall, these results are expected. This is because various combinations of thereby leading to potential error (i.e., deviation between predicted and actual additive replacement level or SSA). For example, high peak heat flow rate could be obtained by using a coarse mineral additive at high replacement level, or a fine mineral additive at low replacement level. The presence of different mineral additives in each OPC system contributes to the uniqueness of the respective heat flow signatures, consequent of the hydration reaction. Thus, additive type is highly predictable when ML techniques are properly utilized.

A limitation of the optimization scheme described above is insufficient data-records (i.e., 208 unique compositions), and limited variations in the inputs, leading to error in predictions of replacement level and SSA of the additive. A larger and more diverse database will enable the ability to optimize mixture design in high-fidelity manner. With that stated, there is potentially room for improvement within the optimization process in future studies; however, the novel work within this publication is the first step to optimize cementitious mixture designs that are likely to exhibit target/desired heat evolution signatures.

4. CONCLUSIONS AND FUTURE WORK

In the past decade or so, machine learning (ML) has arisen as a promising, holistic approach to reveal such composition-property correlations in composite materials. This study describes the use of a random forests (RF) model to enable high-fidelity predictions of time-dependent hydration kinetics of blended ordinary Portland cement (OPC) systems

— more specifically [OPC + mineral additives] systems — using the system's mix design features and physiochemical attributes as inputs. As a method to limit OPC's contributions to global anthropogenic CO_2 emissions, mineral additives have been endorsed by literature as partial replacements for OPC. However, it has been well established that mineral replacements of differing types and physical properties can have varying effects on the hydration kinetics of OPC-based systems. Therefore — in regards to more complex systems — it is infeasible for semi-empirical kinetic models to reveal the underlying nonlinear composition-property (i.e., reactivity) relationships.

To elucidate the aforementioned underlying nonlinear composition-property (i.e., reactivity) relationships, an original application of the random forests (RF) ML model was utilized to predict the time-dependent hydration behavior (i.e., heat flow rate; and cumulative heat release) of ordinary Portland cement (OPC) based plain and blended systems. The prediction results have proven that the RF model has the ability to predict and optimize the relatively continuous (i.e., short time steps) and long time period (i.e., 24 hours) heat-evolution-determined kinetic profiles corresponding to plain and blended OPC systems. Further, these novel ML results demonstrate for the first time that rapid and reliable predictions — once the model is properly and rigorously trained, are possible for new OPC-based systems without further experimentation — of time-dependent hydration behavior of plain and blended OPC systems are indeed feasible, a feat that is currently impossible with current numerical kinetic models. To the best of the authors' knowledge, this is the first study that employs ML to predict time-dependent kinetic behavior of cement hydration that features multiple mineral additives and focuses on mixture design parameters and physiochemical attributes.

The results from this study can be expanded to formulate mixture designs that satisfy target (user-imposed) kinetic criteria, even without a comprehensive understanding of the underlying kinetic mechanisms. For example, if the current training database is extended to include additional [OPC + mineral additives] permutations, the heat-evolution profiles corresponding to the hydration of more complex blended systems could be potentially predicted with reasonable accuracy. Such examples include, a system with numerous mineral additives, such as a [OPC + limestone + quartz + metakaolin + silica fume] system or even a system containing other commonly used additives such as fly ashes and/or geopolymers if said additives are included in additional permutations. In terms of optimization, a database with additional data-entries could also be utilized to predict in a high-fidelity approach the exact ideal amount and additive type for a [OPC + mineral additive(s)] system with a desired time-dependent heat-evolution profile and strength threshold. There are additionally a plethora of potential opportunities for improvement within the prediction and optimization processes in future studies; however, the novel work within this publication represents an important initial design optimization milestone for cementitious mixture designs that successfully demonstrates the feasible for a given ML model to elucidate underlying nonlinear time-dependent composition-property (i.e., reactivity) relationships.

ACKNOWLEDGEMENTS

The authors acknowledge financial support for this research provided by the UM system; the Federal Highway Administration (Award no: 693JJ31950021); the Leonard

Wood Institute (LWI) and the National Science Foundation (NSF-CMMI: 1661609 and 1932690). The authors would like to gratefully thank Theodore Lewis and Missouri S&T for providing the assistance and facilities, respectively, to accomplish both the experimental and computational work portions of the research detailed in this communication.

REFERENCES

[1] K.L. Scrivener, Straight talk with Karen Scrivener on cements, CO2 and sustainable development, American Ceramic Society Bulletin. 91 (2012) 47–50.

[2] K.C. Curry, Mineral Commodity Summaries 2020, U.S. Department of the Interior, Reston, Virginia, 2020.

[3] E. Gartner, H. Hirao, A review of alternative approaches to the reduction of CO2 emissions associated with the manufacture of the binder phase in concrete, Cement and Concrete Research. 78, Part A (2015) 126–142. https://doi.org/10.1016/j.cemconres.2015.04.012.

[4] M. Schneider, Process technology for efficient and sustainable cement production, Cement and Concrete Research. 78, Part A (2015) 14–23. https://doi.org/10.1016/j.cemconres.2015.05.014.

[5] H.-M. Ludwig, W. Zhang, Research review of cement clinker chemistry, Cement and Concrete Research. 78, Part A (2015) 24–37. https://doi.org/10.1016/j.cemconres.2015.05.018.

[6] H.G. van Oss, USGS, Cement – Mineral Commodity Summaries., U.S. Department of the Interior, 2018.

[7] J.J. Biernacki, J.W. Bullard, G. Sant, K. Brown, F.P. Glasser, S. Jones, T. Ley, R.A. Livingston, L. Nicoleau, J. Olek, F. Sanchez, R. Shahsavari, P.E. Stutzman, K. Soblev, T. Prater, Cements in the 21st century: Challenges, perspectives, and opportunities, 100 (2017) 27.

[8] E. Gartner, T. Sui, Alternative cement clinkers, Cement and Concrete Research. 114 (2018) 27–39. https://doi.org/10.1016/j.cemconres.2017.02.002.

[9] E. Worrell, L. Price, N. Martin, C. Hendriks, L.O. Meida, Carbon dioxide emissions from the global cement industry 1, Annual Review of Energy and the Environment. 26 (2001) 303–329.

[10] W.A. Gutteridge, J.A. Dalziel, Filler cement: the effect of the secondary component on the hydration of Portland cement: part I. A fine non-hydraulic filler, Cement and Concrete Research. 20 (1990) 778–782.

[11] W.A. Gutteridge, J.A. Dalziel, Filler cement: the effect of the secondary component on the hydration of Portland cement: part 2. fine hydraulic binders, Cement and Concrete Reseach. 20 (1990) 853–861.

[12] V. Rahhal, R. Talero, Early Hydration of Portland Cement With Crystalline Mineral Additions, Cement and Concrete Reseach. 35 (2005) 1285–1291.

[13] R.L. Sharma, S.P. Pandey, Influence of Mineral Additives on the Hydration Characteristics of Ordinary Portland Cement, Cement and Concrete Reseach. 29 (1999) 1525–1529.

[14] K. De Weerdt, M.B. Haha, G. Le Saout, K.O. Kjellsen, H. Justnes, B. Lothenbach, Hydration mechanisms of ternary Portland cements containing limestone powder and fly ash, Cement and Concrete Research. 41 (2011) 279–291.

[15] A.R. Jayapalan, B.Y. Lee, S.M. Fredrich, K.E. Kurtis, Influence of Additions of Anatase TiO2 Nanoparticles on Early-Age Properties of Cement-Based Materials, Transportation Research Record. 2141 (2010) 41–46.

[16] J.J. Thomas, H.M. Jennings, J.J. Chen, Influence of nucleation seeding on the hydration mechanisms of tricalcium silicate and cement, Journal of Physical Chemistry C. 113 (2009) 4327–4334. https://doi.org/10.1021/jp809811w.

[17] M. Bellotto, A. Gualtieri, G. Artioli, S.M. Clark, Kinetic Study of the Kaolinite-Mullite Reaction Sequence. Part I: Kaolinite Dehydroxylation, Physics and Chemistry of Minerals. 22 (1995) 207–217. https://doi.org/10.1007/BF00202253.

[18] J. Lapeyre, A. Kumar, Influence of pozzolanic additives on hydration mechanisms of tricalcium silicate, Journal of the American Ceramic Society. 101 (2018) 3557–3574. https://doi.org/10.1111/jace.15518.

[19] A. Kumar, T. Oey, G. Falzone, J. Huang, M. Bauchy, M. Balonis, N. Neithalath, J. Bullard, G. Sant, The filler effect: The influence of filler content and type on the hydration rate of tricalcium silicate, Journal of American Ceramics Society. 100 (2017) 3316–3328.

[20] T. Oey, A. Kumar, J.W. Bullard, N. Neithalath, G. Sant, The filler effect: the influence of filler content and surface area on cementitious reaction rates, Journal of the American Ceramic Society. 96 (2013) 1978–1990.

[21] R. Cook, H. Ma, A. Kumar, Influence of size-classified and slightly soluble mineral additives on hydration of tricalcium silicate, Journal of the American Ceramic Society. 103 (2019) 2764–2779. https://doi.org/10.1111/jace.16936.

[22] W. Meng, P. Lunkad, A. Kumar, K. Khayat, Influence of Silica Fume and Polycarboxylate Ether Dispersant on Hydration Mechanisms of Cement, The Journal of Physical Chemistry C. 120 (2016) 26814–26823.

[23] J.W. Bullard, H.M. Jennings, R.A. Livingston, A. Nonat, G.W. Scherer, J.S. Schweitzer, K.L. Scrivener, J.J. Thomas, Mechanisms of cement hydration, Cement and Concrete Research. 41 (2011) 1208–1223.

[24] A.M. Ley-Hernandez, J. Lapeyre, R. Cook, A. Kumar, D. Feys, Elucidating the Effect of Water Content on Hydration Mechanisms of Cement, ACS Omega. 3 (2018) 5092–5105. https://doi.org/10.1021/acsomega.8b00097.

[25] A. Ouzia, K. Scrivener, The needle model: A new model for the main hydration peak of alite, Cement and Concrete Reseach. 115 (2019) 339–360.

[26] K.L. Scrivener, P. Juilland, P.J. Monteiro, Advances in understanding hydration of Portland cement, Cement and Concrete Research. 78 (2015) 38–56.

[27] J.J. Thomas, J.J. Biernacki, J.W. Bullard, S. Bishnoi, J.S. Dolado, G.W. Scherer, A. Luttge, Modeling and simulation of cement hydration kinetics and microstructure development, Cement and Concrete Research. 41 (2011) 1257–1278.

[28] W.A. Johnson, R.F. Mehl, Reaction Kinetics in Processes of Nucleation and Growth, Transactions of the American Institute of Mining. 195 (1939) 416–442.

[29] M. Avrami, Kinetics of phase change. I General theory, The Journal of Chemical Physics. 7 (1939) 1103–1112.

[30] M. Avrami, Kinetics of Phase Change. II Transformation-Time Relations for Random Distribution of Nuclei, The Journal of Chemical Physics. 8 (1940) 212–224.

[31] M. Avrami, Granulation, phase change, and microstructure kinetics of phase change. III, The Journal of Chemical Physics. 9 (1941) 177–184.

[32] A.N. Kolmogorov, On the statistical theory of the crystallization of metals, Bull. Acad. Sci. USSR, Math. Ser. 1 (1937) 355–359.

[33] A.J. Allen, J.C. McLaughlin, D.A. Neumann, R.A. Livingston, In situ quasi-elastic scattering characterization of particle size effects on the hydration of tricalcium silicate, (2004).

[34] P.W. Brown, J. Pommersheim, G. Frohnsdorff, A Kinetic Model for the Hydration of Tricalcium Silicate, Cement and Concrete Reseach. 15 (1985) 35–41.

[35] A. Damasceni, L. Dei, E. Fratini, F. Ridi, S.-H. Chen, P. Baglioni, A Novel Approach Based on Differential Scanning Calorimetry Applied to the Study of Tricalcium Silicate Hydration Kinetics, The Journal of Physical Chemistry B. 106 (2002) 11572–11578. https://doi.org/10.1021/jp020211l.

[36] S.A. FitzGerald, D.A. Neumann, J.J. Rush, D.P. Bentz, R.A. Livingston, In situ quasi-elastic neutron scattering study of the hydration of tricalcium silicate, Chemistry of Materials. 10 (1998) 397–402.

[37] S.A. Grant, G.E. Boitnott, C.J. Korhonen, R.S. Sletten, Effect of temperature on hydration kinetics and polymerization of tricalcium silicate in stirred suspensions of CaO-saturated solutions, 36 (2006) 672–677. https://doi.org/10.1016/j.cemconres.2005.10.001.

[38] N. Tenoutasse, A. De Donder, The kinetics and mechanism of hydration of tricalcium silicate, Silicates Ind. 35 (1970) 301–307.

[39] J.J. Thomas, H.M. Jennings, Effects of D2O and mixing on the early hydration kinetics of tricalcium silicate, Chemistry of Materials. 11 (1999) 1907–1914.

[40] D.R. Vollet, A.F. Craievich, Effects of temperature and of the addition of accelerating and retarding agents on the kinetics of hydration of tricalcium silicate, The Journal of Physical Chemistry B. 104 (2000) 12143–12148.

[41] I.G. Richardson, Tobermorite/jennite- and tobermorite/calcium hydroxide-based models for the structure of C-S-H: applicability to hardened pastes of tricalcium silicate, β-dicalcium silicate, Portland cement, and blends of Portland cement with blast-furnace slag, metakaolin, or silica fume, Cement and Concrete Research. 34 (2004) 1733–1777. https://doi.org/10.1016/j.cemconres.2004.05.034.

[42] A. Nonat, The structure and stoichiometry of C-S-H, Cement and Concrete Research. 34 (2004) 1521–1528. https://doi.org/10.1016/j.cemconres.2004.04.035.

[43] A.J. Allen, R.C. Oberthur, D. Peasrson, P. Schofield, C.R. Wilding, Development of the fine porosity and gel structure of hydrating cement systems, Philosophical Magazine B. 56 (1987) 263–288. https://doi.org/10.1080/13642818708221317.

[44] J.J. Thomas, A new approach to modeling the nucleation and growth kinetics of tricalcium silicate hydration, Journal of the American Ceramic Society. 90 (2007) 3282–3288.

[45] J.W. Cahn, The kinetics of grain boundary nucleated reactions, Acta Metallurgica. 4 (1956) 449–459.

[46] J.W. Bullard, A determination of hydration mechanisms for tricalcium silicate using a kinetic cellular automaton model, Journal of the American Ceramic Society. 91 (2008) 2088–2097.

[47] J.W. Bullard, A three-dimensional microstructural model of reactions and transport in aqueous mineral systems, Modelling and Simulation in Materials Science and Engineering. 15 (2007) 711.

[48] F. Ridi, E. Fratini, P. Luciani, F. Winnefeld, P. Baglioni, Tricalcium silicate hydration reaction in the presence of comb-shaped superplasticizers: boundary nucleation and growth model applied to polymer-modified pastes, The Journal of Physical Chemistry C. 116 (2012) 10887–10895.

[49] L. Valentini, M. Favero, M.C. Dalconi, V. Russo, G. Ferrari, G. Artioli, Kinetic Model of Calcium-Silicate Hydrate Nucleation and Growth in the Presence of PCE Superplasticizers, Crystal Growth & Design. (2016) 646–654.

[50] A. Kumar, S. Bishnoi, K.L. Scrivener, Modelling early age hydration kinetics of alite, Cement and Concrete Research. 42 (2012) 903–918.

[51] V.K. Peterson, M.C.G. Juenger, Hydration of tricalcium silicate: effects of CaCl2 and sucrose on reaction kinetics and product formation, Chemistry of Materials. 18 (2006) 5798–5804.

[52] V.K. Peterson, A.E. Whitten, Hydration processes in tricalcium silicate: application of the boundary nucleation model to quasielastic neutron scattering data, The Journal of Physical Chemistry C. 113 (2009) 2347–2351.

[53] G.W. Scherer, J. Zhang, J.J. Thomas, Nucleation and growth models for hydration of cement, Cement and Concrete Research. 42 (2012) 982–993.

[54] S. Garrault, T. Behr, A. Nonat, Formation of the C-S-H Layer During Early Hydration of Tricalcium Silicate Grains with Different Sizes, The Journal of Physical Chemistry B. 110 (2006) 270–275.

[55] E. Masoero, J.J. Thomas, H.M. Jennings, A Reaction Zone Hypothesis for the Effects of Particle Size and Water-to-Cement Ratio on the Early Hydration Kinetics of C3S, Journal of the American Ceramic Society. 97 (2014) 967–975.

[56] R. Cook, H. Ma, A. Kumar, Mechanism of tricalcium silicate hydration in the presence of polycarboxylate polymers, SN Applied Sciences. 1 (2019) 145. https://doi.org/10.1007/s42452-018-0153-1.

[57] J. Lapeyre, H. Ma, A. Kumar, Effect of particle size distribution of metakaolin on hydration kinetics of tricalcium silicate, 102 (2019) 5976–5988. https://doi.org/10.1111/jace.16467.

[58] C. Naber, F. Bellmann, T. Sowoidnich, F. Goetz-Neunhoeffer, J. Neubauer, Alite dissolution and C-S-H precipitation rates during hydration, Cement and Concrete Reseach. 115 (2019) 283–293. https://doi.org/10.1016/j.cemconres.2018.09.001.

[59] L. Nicoleau, A. Nonat, A new view on the kinetics of tricalcium silicate hydration, Cement and Concrete Reseach. 86 (2016) 1–11. https://doi.org/10.1016/j.cemconres.2016.04.009.

[60] R. Cook, J. Lapeyre, H. Ma, A. Kumar, Prediction of Compressive Strength of Concrete: A Critical Comparison of Performance of a Hybrid Machine Learning Model with Standalone Models, ASCE Journal of Materials in Civil Engineering. 31 (2019) 04019255. https://doi.org/10.1061/(ASCE)MT.1943-5533.0002902.

[61] T. Han, A. Siddique, K. Khayat, J. Huang, A. Kumar, An ensemble machine learning approach for prediction and optimization of modulus of elasticity of recycled aggregate concrete, Construction and Building Materials. 244 (2020) 118271. https://doi.org/10.1016/j.conbuildmat.2020.118271.

[62] J.-S. Chou, C.-F. Tsai, A.-D. Pham, Y.-H. Lu, Machine learning in concrete strength simulations: Multi-nation data analytics, Construction and Building Materials. 73 (2014) 771–780. https://doi.org/10.1016/j.conbuildmat.2014.09.054.

[63] A. Behnood, V. Behnood, M.M. Gharehveran, K.E. Alyamac, Prediction of the compressive strength of normal and high-performance concretes using M5P model tree algorithm, Construction and Building Materials. 142 (2017) 199–207. https://doi.org/10.1016/j.conbuildmat.2017.03.061.

[64] J.-S. Chou, C.-K. Chiu, M. Farfoura, I. Al-Taharwa, Optimizing the prediction accuracy of concrete compressive strength based on a comparison of data-mining techniques, Journal of Computing in Civil Engineering. 25 (2010) 242–253.

[65] B.A. Omran, Q. Chen, R. Jin, Comparison of data mining techniques for predicting compressive strength of environmentally friendly concrete, Journal of Computing in Civil Engineering. 30 (2016) 04016029.

[66] I.-C. Yeh, Modeling of strength of high-performance concrete using artificial neural networks, Cement and Concrete Research. 28 (1998) 1797–1808.

[67] Z.H. Duan, S.C. Kou, C.S. Poon, Using artificial neural networks for predicting the elastic modulus of recycled aggregate concrete, Construction and Building Materials. 44 (2013) 524–532. https://doi.org/10.1016/j.conbuildmat.2013.02.064.

[68] D. Cruz, D.A. Talbert, W. Eberle, J. Biernacki, A Neural Network Approach for Predicting Microstructure Development in Cement, in: 2016. https://www.semanticscholar.org/paper/A-Neural-Network-Approach-for-Predicting-in-Cement-Cruz-Talbert/0306a66e8574e39cf4700f83d0c6ef0606b4540f (accessed April 7, 2020).

[69] S.S. Bangaru, C. Wang, M. Hassan, H.W. Jeon, T. Ayiluri, Estimation of the degree of hydration of concrete through automated machine learning based microstructure analysis – A study on effect of image magnification, Advanced Engineering Informatics. 42 (2019) 100975. https://doi.org/10.1016/j.aei.2019.100975.

[70] K.O. Akande, T.O. Owolabi, S. Twaha, S.O. Olatunji, Performance comparison of SVM and ANN in predicting compressive strength of concrete, IOSR Journal of Computer Engineering. 16 (2014) 88–94.

[71] A. Behnood, V. Behnood, M.M. Gharehveran, K.E. Alyamac, Prediction of the compressive strength of normal and high-performance concretes using M5P model tree algorithm, Construction and Building Materials. 142 (2017) 199–207.

[72] Z.-H. Duan, S.-C. Kou, C.-S. Poon, Prediction of compressive strength of recycled aggregate concrete using artificial neural networks, Construction and Building Materials. 40 (2013) 1200–1206.

[73] R. Gupta, M.A. Kewalramani, A. Goel, Prediction of concrete strength using neural-expert system, Journal of Materials in Civil Engineering. 18 (2006) 462–466.

[74] J. Kasperkiewicz, J. Racz, A. Dubrawski, HPC strength prediction using artificial neural network, Journal of Computing in Civil Engineering. 9 (1995) 279–284.

[75] N.K. Nagwani, S.V. Deo, Estimating the concrete compressive strength using hard clustering and fuzzy clustering based regression techniques, The Scientific World Journal. 2014 (2014).

[76] V. Veloso de Melo, W. Banzhaf, Improving the prediction of material properties of concrete using Kaizen Programming with Simulated Annealing, Neurocomputing. 246 (2017) 25–44. https://doi.org/10.1016/j.neucom.2016.12.077.

[77] I.-C. Yeh, Modeling of strength of high-performance concrete using artificial neural networks, Cement and Concrete Research. 28 (1998) 1797–1808.

[78] I.-C. Yeh, Modeling concrete strength with augment-neuron networks, Journal of Materials in Civil Engineering. 10 (1998) 263–268.

[79] I.-C. Yeh, L.-C. Lien, Knowledge discovery of concrete material using genetic operation trees, Expert Systems with Applications. 36 (2009) 5807–5812.

[80] B.A. Young, A. Hall, L. Pilon, P. Gupta, G. Sant, Can the compressive strength of concrete be estimated from knowledge of the mixture proportions?: New insights from statistical analysis and machine learning methods, Cement and Concrete Research. 115 (2019) 379–388.

[81] M.F. Zarandi, I.B. Türksen, J. Sobhani, A.A. Ramezanianpour, Fuzzy polynomial neural networks for approximation of the compressive strength of concrete, Applied Soft Computing. 8 (2008) 488–498.

[82] M. Antoni, J. Rossen, F. Martirena, K. Scrivener, Cement substitution by a combination of metakaolin and limestone, Cement and Concrete Research. 42 (2012) 1579–1589.

[83] K. Vance, M. Aguayo, T. Oey, G. Sant, N. Neithalath, Hydration and strength development in ternary portland cement blends containing limestone and fly ash or metakaolin, Cement and Concrete Composites. 39 (2013) 93–103.

[84] A.M. Ramezanianpour, R.D. Hooten, A study on hydration, compressive strength, and porosity of Portland-limestone cement mixes containing SCMs, Cement and Concrete Composites. 51 (2014) 1–13.

[85] M. Boháč, M. Palou, R. Novotnỳ, J. Másilko, D. Všianský, T. Staněka, Investigation on early hydration of ternary Portland cement–blast–furnace slag–metakaolin blends, Construction and Building Materials. 64 (2014) 333–341.

[86] T. Matschei, B. Lothenbach, F.P. Glasser, The role of calcium carbonate in cement hydration, Cement and Concrete Research. 37 (2007) 551–558.

[87] J.W. Bullard, E.J. Garboczi, A model investigation of the influence of particle shape on portland cement hydration, Cement and Concrete Research. 36 (2006) 1007–1015. https://doi.org/10.1016/j.cemconres.2006.01.003.

[88] E.J. Garboczi, J.W. Bullard, Shape analysis of a reference cement, Cement and Concrete Research. 34 (2004) 1933–1937.

[89] T. Han, N. Stone-Weiss, J. Huang, A. Goel, A. Kumar, Machine learning as a tool to design glasses with controlled dissolution for application in healthcare industry, Acta Biomaterialia. 107 (2020) 286–298. https://doi.org/10.1016/j.actbio.2020.02.037.

[90] J. Bergstra, Y. Bengio, Random Search for Hyper-Parameter Optimization, Journal of Machine Learning Research. 13 (2012) 281–305.

[91] T. Eitrich, B. Lang, Efficient optimization of support vector machine learning parameters for unbalanced datasets, Journal of Computational and Applied Mathematics. 196 (2006) 425–436. https://doi.org/10.1016/j.cam.2005.09.009.

[92] C. Schaffer, Selecting a classification method by cross-validation, Machine Learning. 13 (1993) 135–143. https://doi.org/10.1007/BF00993106.

[93] L. Breiman, Random forests, Machine Learning. 45 (2001) 5–32.

[94] M.R. Segal, Machine Learning Benchmarks and Random Forest Regression, (2004). https://escholarship.org/uc/item/35x3v9t4 (accessed April 18, 2020).

[95] R. Cook, C.M. Keitumetse, M.B. Hayat, A. Kumar, L. Alagha, Prediction of Flotation Performance of Sulfide Minerals Using an Original Hybrid Machine Learning Model, Engineering Reports. Article in Press (2020) 1–33. https://doi.org/10.1002/eng2.12167.

[96] N.M. Anoop Krishnan, S. Mangalathu, M.M. Smedskjaer, A. Tandia, H. Burton, M. Bauchy, Predicting the dissolution kinetics of silicate glasses using machine learning, Journal of Non-Crystalline Solids. 487 (2018) 37–45. https://doi.org/10.1016/j.jnoncrysol.2018.02.023.

[97] X. Chen, H. Ishwaran, Random forests for genomic data analysis, Genomics. 99 (2012) 323–329.

[98] V. Svetnik, A. Liaw, C. Tong, J.C. Culberson, R.P. Sheridan, B.P. Feuston, Random forest: a classification and regression tool for compound classification and QSAR modeling, Journal of Chemical Information and Computer Sciences. 43 (2003) 1947–1958.

[99] Gãš. Biau, L. Devroye, Gãą. Lugosi, Consistency of random forests and other averaging classifiers, Journal of Machine Learning Research. 9 (2008) 20152033.

[100] C. Schaffer, Selecting a classification method by cross-validation, Machine Learning. 13 (1993) 135–143.

[101] M. Pelikan, Hierarchical Bayesian Optimization Algorithm, in: M. Pelikan (Ed.), Hierarchical Bayesian Optimization Algorithm: Toward a New Generation of Evolutionary Algorithms, Springer Berlin Heidelberg, Berlin, Heidelberg, 2005: pp. 105–129. https://doi.org/10.1007/978-3-540-32373-0_6.

[102] K. Swersky, J. Snoek, R.P. Adams, Multi-Task Bayesian Optimization, in: C.J.C. Burges, L. Bottou, M. Welling, Z. Ghahramani, K.Q. Weinberger (Eds.), Advances in Neural Information Processing Systems 26, Curran Associates, Inc., 2013: pp. 2004–2012. http://papers.nips.cc/paper/5086-multi-task-bayesian-optimization.pdf (accessed June 19, 2018).

SECTION

2. CONCLUSIONS AND RECOMMENDATIONS FOR FUTURE WORK

2.1. SUMMARY AND CONCLUSIONS OF DISSERATION WORK

The work presented within this dissertation helps further understanding of multi-phase OPC-based systems and its pure phase derivatives. The overall impact of this work is improved understanding and explanations of how various process parameters effect OPC-based and other relevant cementitious systems. That is, from this work, the understanding of cement hydration kinetics in the presence of varying process parameters is improved through physical experiments and further computational techniques, such as: numerical kinetic-based modelling; and artificial intelligence techniques like machine learning (ML) models.

To improve current understanding within the literature, the effect of water was effectively explored with two very different approaches: firstly, it was explored in ordinary Portland cement (OPC) paste systems by studying the effect of sedimentation in systems with varying with water-to-cement ratio and; secondly, it was explored by studying the effect of the thermodynamic activity of the water present in the considered paste system — that is, water activity (a_H) — an important thermodynamic parameter – on the progression of the belite (β-C_2S) hydration reaction. Overall, Paper I provide a novel insights into the mechanisms that cause cement hydration rates to remain insensitive to changes in the paste's water content and highlights important aspects that need to be incorporated in phase boundary nucleation and growth (pBNG) models to account for C−S−H confinement as well as the sedimentation of cement particles. Paper II on the other hand, enhances current thermodynamic understanding of all cementitious systems containing β-C_2S, including OPC-based systems and calcium aluminate-based systems, by providing thermodynamic constant values for the critical a_H threshold and solubility product constant of β-C_2S (K_{C_2S}) for the first time. This brings novel insight to curing conditions necessary for hydration of β-C_2S to proceed and also invites further investigations regarding β-C_2S hydration as instrumental techniques improve over-time.

Additionally, Paper III and IV separately explore the effects of two varied process parameters on tricalcium silicate (C_3S) hydration, that is, the work explores the effect of a common superplasticizer, polycarboxylate ether (PCE), and various filler mineral additives on C_3S hydration. The outcomes of the [C_3S + PCE] study provide mechanistic insights linking the decelerating effects of PCE to the overall dosage and molecular architecture through a novel composite parameter, observed via experimental means and corroborated with pBNG model results. Such knowledge is expected to aid in uncovering the underlying mechanisms that describe the influence of PCE on the hydration of other cementitious phases as well as other fresh properties. The outcomes presented in the [C_3S + mineral additive] study provide novel insights into the mechanistic origins of the *filler effect* by exploring and directly comparing the fillers materials — limestone, quartz, rutile, and corundum – to one another under approximately equivalent conditions. Through physical (i.e., isothermal calorimetry) and computational (i.e., pBNG model) means, it was concluded that limestone, quartz, and rutile perform roughly equivalent as filler materials. This is contrary to what has been reported in prior studies, which have reported that limestone is able to enhance hydration better than quartz due to limestone's excellent surface properties (i.e., relatively lower wetting angle) and ability to participate in anion-exchange reactions. However, corundum did not appear to conventionally exhibit the *filler effect*. As the replacement level of corundum was increased, C_3S hydration was increasingly decelerated. After the initial 36 hours of hydration, the decelerating effects of corundum were ultimately ebbed and annulled.

Papers V and VI present a novel hybrid machine learning (ML) model, that is the Random Forests – Firefly Algorithm (RF-FFA) model, and its ability to predict the designated output from two different types of data; that is, in Paper V, the mix design of concrete systems were used to predict compressive strength, while in Paper VI, the various procedural parameters corresponding to froth flotation process of galena and chalcopyrite were used to predict the metallurgical efficiency of the overall flotation procedure. The hybrid model's performance was compared against five standalone ML models and were evaluated using five statistical parameters (i.e., R, R^2, MAE, RMSE, and MAPE) and the composite performance index (CPI). In both Papers V and VI, the prediction performance of the Random Forests (RF) ML model and the RF-FFA model was superior compared to the other standalone models. The overall outcome of these studies demonstrate the potential of ML models as a promising tool to reveal underlying nonlinear input-output relationships.

Lastly, Paper VII built upon the work of Papers IV, V, and VI, that is, Paper VII presented a database constructed at Missouri University of Science and Technology comprising of isothermal calorimetry results. More specifically, the database is comprised of the heat flow rate and the cumulative heat released during the initial 24 hours of hydration for [OPC + mineral additive] paste systems corresponding to over 300 compositional unique systems. The outcomes of this study have demonstrated that the RF model can successful predict and optimize the relatively continuous (i.e., short time steps) and long time period (i.e., 24 hours) heat-evolution-determined kinetic profiles corresponding to plain and blended OPC systems. Further, these novel ML results demonstrate for the first time that rapid and reliable predictions for profiles corresponding to compositions without a corresponding data entry when properly and rigorously trained, a feat that is currently impossible with current numerical kinetic models.

2.2. RECOMMENDATIONS FOR FUTURE WORK

The work presented in this dissertation is focused on varying well-established process parameters corresponding to OPC-based systems to better understand, or further, predict early age hydration kinetics. The outcomes of this dissertation made great strides forward in fulfillment of that object. With that stated, the thermodynamic estimations utilized to determine the critical water activity (a_H) necessary for the belite (β-C_2S) hydration reaction progress can be reutilized for tetracalcium aluminoferrite (C_4AF), the last phase in OPC for this thermodynamic approach to be applied to. Conducting an additional study on tetacalcium aluminoferrite (C_4AF) will give a complete, holistic picture of the effect of a_H on each anhydrous phase present in OPC. Beyond OPC, there are other cementitious systems that are of interest. Phases present within sustainable binders such as calcium aluminate-based cements also warrant study for improved understanding and implementation efficiency.

In the context of the [PCE + C_3S] study — on the condition that there is/are readily, easily characterizable PCE(s), synthesized in sufficient amounts —, it could be potentially worthwhile to conduct an extended study exploring the hydration kinetics and rheological properties of [PCE + C_3S], [PCE + C_3A/C\$], and [PCE + C_3S + C_3A/C\$] paste systems. Such experiments would not have to be limited to PCE, that is, the study could extend to other super-plasticizing admixtures as well. The outcome of such a study or studies could potentially provide further insight as to how to overcome incompatibility issues that is not always but is commonly involving C_3A/C\$ phases and superplasticizers. Such knowledge has the potential to improve mixture design efficiency for high-performance concretes.

In terms of potential future work for prediction of properties corresponding to OPC-based systems via ML models, the possibilities are near endless. Obvious possibilities include expanding the existing isothermal calorimetry database by incorporating systems corresponding to a multitude of other cement types that can be utilized for construction applications. Progressively the paste systems can become more and more complex, via: the additional of three or more filler materials, non-filler mineral additives such as fly ash or slag; the incorporation of a superplasticizer admixture; etc. However, future work could potentially extend beyond the constructed of the isothermal calorimetry database and expand towards the building of a new database. Potential database ideas include, but are not limited to the construction of a database that includes rheological and heat-evolution data for each composition, scanning electron microscopy micrographs of OPC-based systems at varying ages, micro-computed x-ray tomography radiographs of OPC-based systems at varying ages, etc.

APPENDIX A.

CURRICULUM VITAE

Rachel E. Cook

611 West 8th Street, Rolla, MO 65401 • (330) 620-2726 • recwx7@umsystem.edu

Education

Missouri University of Science and Technology Aug. 2016 – Sept. 2020

Ph.D. Ceramic Engineering, 3.5 GPA

Advisor: Aditya Kumar

Co-Advisor: Hongyan Ma

Dissertation title: Studying the Effects of Various Process Parameters on Early age Hydration of Single- and Multi-phase Cementitious Systems (successfully defended Sept. 16, 2020)

Alfred University Aug. 2012 – May 2016

B.S. Ceramic Engineering

Research Experiences

Graduate Research Assistant, Rolla, MO Aug. 2016 – Sept. 2020

- Created experimental database and manually selected attributes for machine learning-based predictions of rheological properties and hydration kinetics of ordinary Portland cement-based systems.
- Mentored undergraduate students on data collection for machine learning platforms.
- Studied the effects of polycarboxylate-type dispersants and various size-classified fillers on early hydration of tricalcium silicate via a kinetic-based numerical model and experimental means.
- Studied the influence of water activity on the hydration of belite via thermodynamic estimations and experimental means.

Undergraduate Research Assistant, Alfred, NY Spring 2015 & 2016

Sol-gel processing, studies of SiO_2, ZrO_2, and Ta_2O_5 coatings.

Skills and Proficiencies

isothermal, adiabatic, and differential scanning calorimetry; thermogravimetric analysis; rheometry; scanning electron microscopy; X-ray diffraction; Raman spectroscopy; B.E.T.; scatter/dynamic light scattering particle size analysis; powder processing and material synthesis; modulus of rupture; modulus of elasticity; compression strength; MATLAB; SolidWorks.

Industry Experiences

Ceramic Engineering Intern, Dal-Tile, Gettysburg, May 2015 – Aug. 2015

- Conducted tests for absorption, color, shrinkage, and strength to maintain product tolerances. Eliminated Pyrotrol — a filler material — from the mix design, saving the company ~$56,000 annually and gaining 14000 cu. ft. of storage.

MFG Intern, Swagelok, Solon, OH June 2014 – Aug. 2014

- Designed "jaws" to accommodate Okuma machines, the implementation of which saved the company ~$10,000 annually.

Publications

Cook R, Han T, Childers A, Ryckman C, Khayat K, Ma H, Huang J, Kumar A. Machine Learning for High-Fidelity Prediction of Cement Hydration Kinetics in Blended Systems. *Submitted for Publication.*

Kittikunakorn N, Paul S, Koleng III JJ, Liu T, **Cook R**, Sun CC, Kumar A, Zhang. Is the Melt Granulation Behavior Same Between Leistritz Nano-16 and Micro-18 Extruders? *Submitted for Publication*.

Cook R, Ma H, Okoronkwo M, Sant G, Kumar A Influence of Water Activity on Belite (β-C_2S) Hydration. *Submitted for Publication.*

Cook R, Monyake KC, Hayat MB, Kumar A, Alagha L (2020) Prediction of Flotation Efficiency of Metal Sulfides Using an Original Hybrid Machine Learning Model. Engineering Reports 2(6):e12167. https://doi.org/10.1002/eng2.12167

Cook R, Lapeyre J, Ma H, Kumar A (2019) Prediction of Compressive Strength of Concrete: Critical Comparison of Performance of a Hybrid Machine Learning Model with Standalone Models. Journal of Materials in Civil Engineering 31:1–15. https://doi.org/10.1061/(ASCE)MT.1943-5533.0002902

Cook R, Ma H, Kumar A (2019) Influence of Size-classified and Slightly Soluble Mineral Additives on Hydration of Tricalcium Silicate. Journal of the American Ceramic Society 103:2764–2779. https://doi.org/10.1111/jace.16936

Cook R, Ma H, Kumar A (2019) Mechanism of Tricalcium Silicate Hydration in the Presence of Polycarboxylate Polymers. SN Applied Sciences 1:145. https://doi.org/10.1007/s42452-018-0153-1

Ley-Hernandez AM, Lapeyre J, **Cook R**, Kumar A, Feys D (2018) Elucidating the Effect of Water Content on Hydration Mechanisms of Cement. ACS Omega 3:5092–5105. https://doi.org/10.1021/acsomega.8b00097

Predicting the Effect of Admixtures on Hydration and Rheology of Early-age Portland Cement Systems Using Machine Learning Models. *In Progress.*

Composition-based Predictions of Early-age Hydration for Pastes Containing Fly Ash and Portland Cement Using Machine Learning Models. *In Progress.*

Presentations

Cook R (2019) The Effects of Various Size Classified Fillers on Tricalcium Silicate Hydration. *Contributed Talk.*

Cook R (2019) Ensemble and Hybrid Machine Learning Models for High-Fidelity Prediction and Optimization of Properties of Cementitious Systems. *Contributed Talk.*

Cook R (2019) The Effects of Various Filler Types and Size Classification on Early Hydration of C_3S. *Poster.*

Cook R (2018) Influence of Comb-Shaped Polymers on Hydration Mechanisms of Tricalcium Silicate. *Contributed Talk.*

Cook R (2017) The Effects of Immediate and Delayed Additions of PCEs on Early

Teaching Experiences

Graduate Teaching Assistant (TA), Rolla, MO

Ceramic Materials Laboratory I — Characterization of Materials (Cementitious Ceramics; CER ENG 2315) Aug. 2018 – Dec. 2018

- Led and instructed students during weekly laboratory times on topic relating and pertaining to cementitious ceramics, that is, calcium aluminate cements, used for refractory applications.
- Tested and developed laboratory exercises pertaining to mixture design variables, adiabatic calorimetry, modulus of rupture, and modulus of elasticity.
- Wrote laboratory procedures and handouts; wrote and graded weekly homework.

Ceramic Materials Laboratory I — Characterization of Materials (CER ENG 2315) (CER ENG 2315) Aug. 2017 – Dec. 2017

- Led and instructed students during weekly laboratory times on topics relating and pertaining to traditional porcelain and stoneware materials.
- Graded: weekly homeworks; student presentations; student laboratory notebooks and reports.

Memberships & Extracurricular Activities

American Ceramic Society (ACerS)	2018 – present
Keramos (National Professional Ceramic	2013 – present
ASM Materials Camp at Missouri University of	July 2017 & 2019

- Hosted a small group's project for camp attendees involving cement and the effects of various colorants on the resulting products' durability.

APPENDIX B.

REUSE PERMISSIONS

The following are the reuse permissions as they relate to the published works within this dissertation:

Paper I has been published in *ACS Omega* in May, 2018. It is included in this dissertation with permission from the American Chemical Society (ACS), and requires ACS's permission for any additional use. This material may be downloaded for personal use only. This material may be found at: https://pubs.acs.org/doi/10.1021/acsomega.8b00097.

Paper III has been published in *SN Applied Sciences* in January, 2019. It is included in this dissertation with permission from Springer Nature and requires the publisher's permission for any additional use. This material may be downloaded for personal use only. This material may be found at: https://doi.org/10.1007/s42452-018-0153-1.

Paper IV has been published in the *Journal of the American Ceramic Society* in November, 2019 by. It is included in this dissertation with permission from the John Wiley & Sons, Inc and requires the publisher's permission for any additional use. This material may be downloaded for personal use only. This material may be found at: https://doi.org/10.1111/jace.16936.

Paper V, found on pages 176-222 has been published in the *Journal of Materials in Civil Engineering* in November, 2019. This material may be downloaded for personal use only. Any other use requires prior permission of the American Society of Civil Engineers (ASCE). It is included in this dissertation with permission from ASCE. This material may be found at: https://doi.org/10.1061/(ASCE)MT.1943-5533.0002902.

Paper VI, found on pages 223-260 has been published in *Engineering Reports* in June, 2020. This paper was published as an open access article distributed under the terms of the Creative Commons CC BY license, which permits unrestricted use, distribution, and reproduction in any medium, provided the original work is properly cited. The original work may be found at: https://doi.org/10.1002/eng2.12167.

BIBLIOGRAPHY

[1] K.L. Scrivener, Straight talk with Karen Scrivener on cements, CO2 and sustainable development, American Ceramic Society Bulletin. 91 (2012) 47–50.

[2] K.C. Curry, Mineral Commodity Summaries 2020, U.S. Department of the Interior, Reston, Virginia, 2020.

[3] R. Cook, T. Han, A. Childers, C. Ryckman, K. Khayat, H. Ma, J. Huang, A. Kumar, Machine Learning for High-Fidelity Prediction of Cement Hydration Kinetics in Blended Systems, Submitted for Publication. (2020).

[4] R. Cook, H. Ma, A. Kumar, Influence of size-classified and slightly soluble mineral additives on hydration of tricalcium silicate, Journal of the American Ceramic Society. 103 (2019) 2764–2779. https://doi.org/10.1111/jace.16936.

[5] P.-C. Aïtcin, Binders for Durable and Sustainable Concrete, Taylor & Francis, 2008.

[6] H.F. Taylor, Cement chemistry, Thomas Telford, 1997.

[7] A. Kumar, S. Bishnoi, K.L. Scrivener, Modelling early age hydration kinetics of alite, Cement and Concrete Research. 42 (2012) 903–918. https://doi.org/10.1016/j.cemconres.2012.03.003.

[8] J.W. Bullard, H.M. Jennings, R.A. Livingston, A. Nonat, G.W. Scherer, J.S. Schweitzer, K.L. Scrivener, J.J. Thomas, Mechanisms of cement hydration, Cement and Concrete Research. 41 (2011) 1208–1223.

[9] G.W. Scherer, J. Zhang, J.J. Thomas, Nucleation and Growth Models for Hydration of Cement, Cement & Concrete Research. 42 (2012) 982–993.

[10] P.K. Mehta, P.J. Monteiro, Concrete-Microstructure, Properties and Materials. 2006, Utilization of Palm Oil Fuel Ash in Concrete: A Review. (1976).

[11] H.M. Jennings, A. Kumar, G. Sant, Quantitative discrimination of the nano-pore-structure of cement paste during drying: New insights from water sorption isotherms, Cement and Concrete Research. 76 (2015) 27–36.

[12] T.C. Powers, T.L. Brownyard, Studies of the physical properties of hardened Portland cement paste, in: ACI Journal Proceedings, ACI, 1946. http://www.concrete.org/Publications/InternationalConcreteAbstractsPortal.aspx?m=details&i=15301 (accessed August 29, 2014).

[13] R. Flatt, Understanding the Rheology of Concrete: Chapter 7 - Superplasticizers and the rheology of concrete, Woodhead Publishing Limited, 144-208, 2012.

[14] P.-C. Aïtcin, Cements of yesterday and today: concrete of tomorrow, Cement and Concrete Research. 30 (2000) 1349–1359.

[15] D.M. Kirby, J.J. Biernacki, The effect of water-to-cement ratio on the hydration kinetics of tricalcium silicate cements: Testing the two-step hydration hypothesis, Cement and Concrete Research. 42 (2012) 1147–1156.

[16] J.J. Thomas, A new approach to modeling the nucleation and growth kinetics of tricalcium silicate hydration, Journal of the American Ceramic Society. 90 (2007) 3282–3288.

[17] T. Oey, A. Kumar, J.W. Bullard, N. Neithalath, G. Sant, The filler effect: the influence of filler content and surface area on cementitious reaction rates, Journal of the American Ceramic Society. 96 (2013) 1978–1990.

[18] D.P. Bentz, M.A. Peltz, J. Winpigler, Early-age properties of cement-based materials. II: influence of water-to-cement ratio, Journal of Materials in Civil Engineering. 21 (2009) 512–517.

[19] R.J. Flatt, G.W. Scherer, J.W. Bullard, Why alite stops hydrating below 80% relative humidity, Cement and Concrete Research. 41 (2011) 987–992. https://doi.org/10.1016/j.cemconres.2011.06.001.

[20] T. Oey, A. Kumar, G. Falzone, J. Huang, S. Kennison, M. Bauchy, N. Neithalath, J.W. Bullard, G. Sant, The Influence of Water Activity on the Hydration Rate of Tricalcium Silicate, J. Am. Ceram. Soc. 99 (2016) 2481–2492. https://doi.org/10.1111/jace.14181.

[21] J. Lapeyre, H. Ma, M. Okoronkwo, G. Sant, A. Kumar, Influence of water activity on hydration of tricalcium aluminate-calcium sulfate systems, Journal of the American Ceramic Society. (2020) 1–20. https://doi.org/10.1111/jace.17046.

[22] O.M. Jensen, P.F. Hansen, Water-entrained cement-based materials: I. Principles and theoretical background, Cement and Concrete Research. 31 (2001) 647–654.

[23] K.A. Snyder, D.P. Bentz, Suspended hydration and loss of freezable water in cement pastes exposed to 90% relative humidity, Cement and Concrete Research. 34 (2004) 2045–2056. https://doi.org/10.1016/j.cemconres.2004.03.007.

[24] J. Zhang, G.W. Scherer, Comparison of methods for arresting hydration of cement, Cement and Concrete Research. 41 (2011) 1024–1036.

[25] I. Mehdipour, A. Kumar, K. Kamal H., Rheology, hydration, and strength evolution of interground limestone cement containing PCE dispersant and high volume supplementary cementitious materials, Materials & Design. 127 (2017) 54–66.

[26] A. Arora, M. Aguayo, H. Hansen, C. Castro, E. Federspiel, B. Mobasher, N. Neithalath, Microstructural packing- and rheology-based binder selection and characterization for Ultra-high Performance Concrete (UHPC), Cement and Concrete Research. 103 (2018) 179–190. https://doi.org/10.1016/j.cemconres.2017.10.013.

[27] M. Palacios, Y.F. Houst, P. Bowen, F. Puertas, Adsorption of superplasticizer admixtures on alkali-activated slag pastes, Cement and Concrete Research. 39 (2009) 670–677.

[28] M. Palacios, F. Puertas, Stability of superplasticizer and shrinkage-reducing admixtures Stability of superplasticizer and shrinkage-reducing admixtures in high basic media, Materiales de Construcción; Vol 54, No 276 (2004)DO - 10.3989/Mc.2004.V54.I276.256. (2004). http://materconstrucc.revistas.csic.es/index.php/materconstrucc/article/view/256/302.

[29] B.-G. Kim, S.P. Jiang, P.-C. Aïtcin, Slump improvement mechanism of alkalies in PNS superplasticized cement pastes, Materials and Structures. 33 (2000) 363–369. https://doi.org/10.1007/BF02479645.

[30] Y. Nakajima, K. Yamada, The effect of the kind of calcium sulfate in cements on the dispersing ability of poly β-naphthalene sulfonate condensate superplasticizer, Cement and Concrete Research. 34 (2004) 839–844. https://doi.org/10.1016/j.cemconres.2003.09.022.

[31] Y. Zhang, X. Kong, Correlations of the dispersing capability of NSF and PCE types of superplasticizer and their impacts on cement hydration with the adsorption in fresh cement pastes, Cement and Concrete Research. 69 (2015) 1–9.

[32] J. Cheung, A. Jeknavorian, L. Roberts, D. Silva, Impact of admixtures on the hydration kinetics of Portland cement, Cement and Concrete Research. 41 (2011) 1289–1309.

[33] F. Winnefeld, S. Becker, J. Pakusch, T. Götz, Effects of the molecular architecture of comb-shaped superplasticizers on their performance in cementitious systems, Cement and Concrete Composites. 29 (2007) 251–262.

[34] F. Ridi, E. Fratini, P. Luciani, F. Winnefeld, P. Baglioni, Tricalcium silicate hydration reaction in the presence of comb-shaped superplasticizers: boundary nucleation and growth model applied to polymer-modified pastes, The Journal of Physical Chemistry C. 116 (2012) 10887–10895.

[35] A. Zingg, F. Winnefeld, L. Holzer, J. Pakusch, S. Becker, R. Figi, L. Gauckler, Interaction of polycarboxylate-based superplasticizers with cements containing different C 3 A amounts, Cement and Concrete Composites. 31 (2009) 153–162.

[36] A. Zingg, F. Winnefeld, L. Holzer, J. Pakusch, S. Becker, L. Gauckler, Adsorption of polyelectrolytes and its influence on the rheology, zeta potential, and microstructure of various cement and hydrate phases, Journal of Colloid and Interface Science. 323 (2008) 301–312. https://doi.org/10.1016/j.jcis.2008.04.052.

[37] A. Zingg, L. Holzer, A. Kaech, F. Winnefeld, J. Pakusch, S. Becker, L. Gauckler, The microstructure of dispersed and non-dispersed fresh cement pastes—new insight by cryo-microscopy, Cement and Concrete Research. 38 (2008) 522–529.

[38] R. Cook, H. Ma, A. Kumar, Mechanism of tricalcium silicate hydration in the presence of polycarboxylate polymers, SN Applied Sciences. 1 (2019) 145. https://doi.org/10.1007/s42452-018-0153-1.

[39] G. Artioli, L. Valentini, M. Voltolini, M.C. Dalconi, G. Ferrari, V. Russo, Direct Imaging of Nucleation Mechanisms by Synchrotron Diffraction Micro-Tomography: Superplasticizer-Induced Change of C–S–H Nucleation in Cement, Crystal Growth & Design. 15 (2014) 20–23.

[40] L. Valentini, M. Favero, M.C. Dalconi, V. Russo, G. Ferrari, G. Artioli, Kinetic Model of Calcium-Silicate Hydrate Nucleation and Growth in the Presence of PCE Superplasticizers, Crystal Growth & Design. (2016) 646–654.

[41] W. Meng, P. Lunkad, A. Kumar, K. Khayat, Influence of Silica Fume and Polycarboxylate Ether Dispersant on Hydration Mechanisms of Cement, The Journal of Physical Chemistry C. 120 (2016) 26814–26823.

[42] G. Gelardi, N. Sanson, G. Nagy, R.J. Flatt, Characterization of comb-shaped copolymers by multidetection SEC, DLS and SANS, Polymers. 9 (2017) 61.

[43] D. Marchon, P. Juilland, E. Gallucci, L. Frunz, R.J. Flatt, Molecular and submolecular scale effects of comb-copolymers on tri-calcium silicate reactivity: Toward molecular design, Journal of the American Ceramic Society. 100 (2017) 817–841.

[44] D. Marchon, U. Sulser, A. Eberhardt, R.J. Flatt, Molecular design of comb-shaped polycarboxylate dispersants for environmentally friendly concrete, Soft Matter. 9 (2013) 10719–10728.

[45] J.J. Biernacki, J.W. Bullard, G. Sant, K. Brown, F.P. Glasser, S. Jones, T. Ley, R.A. Livingston, L. Nicoleau, J. Olek, F. Sanchez, R. Shahsavari, P.E. Stutzman, K. Soblev, T. Prater, Cements in the 21st century: Challenges, perspectives, and opportunities, 100 (2017) 27.

[46] E. Gartner, T. Sui, Alternative cement clinkers, Cement and Concrete Research. 114 (2018) 27–39. https://doi.org/10.1016/j.cemconres.2017.02.002.

[47] E. Worrell, L. Price, N. Martin, C. Hendriks, L.O. Meida, Carbon dioxide emissions from the global cement industry 1, Annual Review of Energy and the Environment. 26 (2001) 303–329.

[48] E. Gartner, H. Hirao, A review of alternative approaches to the reduction of CO2 emissions associated with the manufacture of the binder phase in concrete, Cement and Concrete Research. 78, Part A (2015) 126–142. https://doi.org/10.1016/j.cemconres.2015.04.012.

[49] M. Schneider, Process technology for efficient and sustainable cement production, Cement and Concrete Research. 78, Part A (2015) 14–23. https://doi.org/10.1016/j.cemconres.2015.05.014.

[50] J. Lapeyre, A. Kumar, Influence of pozzolanic additives on hydration mechanisms of tricalcium silicate, Journal of the American Ceramic Society. 101 (2018) 3557–3574. https://doi.org/10.1111/jace.15518.

[51] A. Kumar, T. Oey, G. Falzone, J. Huang, M. Bauchy, M. Balonis, N. Neithalath, J. Bullard, G. Sant, The filler effect: The influence of filler content and type on the hydration rate of tricalcium silicate, Journal of American Ceramics Society. 100 (2017) 3316–3328.

[52] W.A. Gutteridge, J.A. Dalziel, Filler cement: the effect of the secondary component on the hydration of Portland cement: part I. A fine non-hydraulic filler, Cement and Concrete Research. 20 (1990) 778–782.

[53] W.A. Gutteridge, J.A. Dalziel, Filler cement: the effect of the secondary component on the hydration of Portland cement: part 2. fine hydraulic binders, Cement and Concrete Reseach. 20 (1990) 853–861.

[54] V. Rahhal, R. Talero, Early Hydration of Portland Cement With Crystalline Mineral Additions, Cement and Concrete Reseach. 35 (2005) 1285–1291.

[55] R.L. Sharma, S.P. Pandey, Influence of Mineral Additives on the Hydration Characteristics of Ordinary Portland Cement, Cement and Concrete Reseach. 29 (1999) 1525–1529.

[56] K. De Weerdt, M.B. Haha, G. Le Saout, K.O. Kjellsen, H. Justnes, B. Lothenbach, Hydration mechanisms of ternary Portland cements containing limestone powder and fly ash, Cement and Concrete Research. 41 (2011) 279–291.

[57] A.R. Jayapalan, B.Y. Lee, S.M. Fredrich, K.E. Kurtis, Influence of Additions of Anatase TiO2 Nanoparticles on Early-Age Properties of Cement-Based Materials, Transportation Research Record. 2141 (2010) 41–46.

[58] J.J. Thomas, H.M. Jennings, J.J. Chen, Influence of nucleation seeding on the hydration mechanisms of tricalcium silicate and cement, Journal of Physical Chemistry C. 113 (2009) 4327–4334. https://doi.org/10.1021/jp809811w.

[59] M. Bellotto, A. Gualtieri, G. Artioli, S.M. Clark, Kinetic Study of the Kaolinite-Mullite Reaction Sequence. Part I: Kaolinite Dehydroxylation, Physics and Chemistry of Minerals. 22 (1995) 207–217. https://doi.org/10.1007/BF00202253.

[60] K. Scrivener, R. Snellings, B. Lothenbach, A Practical Guide to Microstructural Analysis of Cementitious Materials, CRC Press, 2016. https://books.google.com/books?hl=en&lr=&id=yJ2mCwAAQBAJ&oi=fnd&pg=PP1&dq=bazzoni+scrivener&ots=nOQBctXmro&sig=O5lraGrWf4btRVtZqrKkL8TcTuk (accessed May 26, 2016).

[61] K.L. Scrivener, P. Juilland, P.J. Monteiro, Advances in understanding hydration of Portland cement, Cement and Concrete Research. 78 (2015) 38–56.

[62] A. Bazzoni, Study of early hydration mechanisms of cement by means of electron microscopy, (2014). http://infoscience.epfl.ch/record/200217/ (accessed May 26, 2016).

[63] A. Bazzoni, S. Ma, Q. Wang, X. Shen, M. Cantoni, K.L. Scrivener, The Effect of Magnesium and Zinc Ions on the Hydration Kinetics of C3S, Journal of the American Ceramic Society. 97 (2014) 3684–3693.

[64] J.W. Bullard, A determination of hydration mechanisms for tricalcium silicate using a kinetic cellular automaton model, Journal of the American Ceramic Society. 91 (2008) 2088–2097.

[65] J.W. Bullard, G.W. Scherer, J.J. Thomas, Time dependent driving forces and the kinetics of tricalcium silicate hydration, Cement and Concrete Research. 74 (2015) 26–34.

[66] S. Garrault, T. Behr, A. Nonat, Formation of the C-S-H Layer During Early Hydration of Tricalcium Silicate Grains with Different Sizes, The Journal of Physical Chemistry B. 110 (2006) 270–275.

[67] K.O. Kjellsen, H. Justnes, Revisiting the microstructure of hydrated tricalcium silicate—a comparison to Portland cement, Cement and Concrete Composites. 26 (2004) 947–956.

[68] K.L. Scrivener, A. Nonat, Hydration of cementitious materials, present and future, Cement and Concrete Research. 41 (2011) 651–665.

[69] S. Bishnoi, K.L. Scrivener, Studying nucleation and growth kinetics of alite hydration using µic, Cement and Concrete Research. 39 (2009) 849–860.

[70] E. Gallucci, P. Mathur, K. Scrivener, Microstructural development of early age hydration shells around cement grains, Cement and Concrete Research. 40 (2010) 4–13.

[71] P.C. Mathur, Study of cementitious materials using transmission electron microscopy, Doctoral Thesis, École Polytechnique Fédérale de Lausanne, 2007.

[72] A.M. Ley-Hernandez, J. Lapeyre, R. Cook, A. Kumar, D. Feys, Elucidating the Effect of Water Content on Hydration Mechanisms of Cement, ACS Omega. 3 (2018) 5092–5105. https://doi.org/10.1021/acsomega.8b00097.

[73] A. Ouzia, K. Scrivener, The needle model: A new model for the main hydration peak of alite, Cement and Concrete Reseach. 115 (2019) 339–360.

[74] J.J. Thomas, J.J. Biernacki, J.W. Bullard, S. Bishnoi, J.S. Dolado, G.W. Scherer, A. Luttge, Modeling and simulation of cement hydration kinetics and microstructure development, Cement and Concrete Research. 41 (2011) 1257–1278.

[75] W.A. Johnson, R.F. Mehl, Reaction Kinetics in Processes of Nucleation and Growth, Transactions of the American Institute of Mining. 195 (1939) 416–442.

[76] M. Avrami, Kinetics of phase change. I General theory, The Journal of Chemical Physics. 7 (1939) 1103–1112.

[77] M. Avrami, Kinetics of Phase Change. II Transformation-Time Relations for Random Distribution of Nuclei, The Journal of Chemical Physics. 8 (1940) 212–224.

[78] M. Avrami, Granulation, phase change, and microstructure kinetics of phase change. III, The Journal of Chemical Physics. 9 (1941) 177–184.

[79] A.N. Kolmogorov, On the statistical theory of the crystallization of metals, Bull. Acad. Sci. USSR, Math. Ser. 1 (1937) 355–359.

[80] A.J. Allen, J.C. McLaughlin, D.A. Neumann, R.A. Livingston, In situ quasi-elastic scattering characterization of particle size effects on the hydration of tricalcium silicate, (2004).

[81] P.W. Brown, J. Pommersheim, G. Frohnsdorff, A Kinetic Model for the Hydration of Tricalcium Silicate, Cement and Concrete Reseach. 15 (1985) 35–41.

[82] A. Damasceni, L. Dei, E. Fratini, F. Ridi, S.-H. Chen, P. Baglioni, A Novel Approach Based on Differential Scanning Calorimetry Applied to the Study of Tricalcium Silicate Hydration Kinetics, The Journal of Physical Chemistry B. 106 (2002) 11572–11578. https://doi.org/10.1021/jp020211l.

[83] S.A. FitzGerald, D.A. Neumann, J.J. Rush, D.P. Bentz, R.A. Livingston, In situ quasi-elastic neutron scattering study of the hydration of tricalcium silicate, Chemistry of Materials. 10 (1998) 397–402.

[84] S.A. Grant, G.E. Boitnott, C.J. Korhonen, R.S. Sletten, Effect of temperature on hydration kinetics and polymerization of tricalcium silicate in stirred suspensions of CaO-saturated solutions, 36 (2006) 672–677. https://doi.org/10.1016/j.cemconres.2005.10.001.

[85] N. Tenoutasse, A. De Donder, The kinetics and mechanism of hydration of tricalcium silicate, Silicates Ind. 35 (1970) 301–307.

[86] J.J. Thomas, H.M. Jennings, Effects of D2O and mixing on the early hydration kinetics of tricalcium silicate, Chemistry of Materials. 11 (1999) 1907–1914.

[87] D.R. Vollet, A.F. Craievich, Effects of temperature and of the addition of accelerating and retarding agents on the kinetics of hydration of tricalcium silicate, The Journal of Physical Chemistry B. 104 (2000) 12143–12148.

[88] I.G. Richardson, Tobermorite/jennite-and tobermorite/calcium hydroxide-based models for the structure of CSH: applicability to hardened pastes of tricalcium silicate, β-dicalcium silicate, Portland cement, and blends of Portland cement with blast-furnace slag, metakaolin, or silica fume, Cement and Concrete Research. 34 (2004) 1733–1777.

[89] A.J. Allen, R.C. Oberthur, D. Peasrson, P. Schofield, C.R. Wilding, Development of the fine porosity and gel structure of hydrating cement systems, Philosophical Magazine B. 56 (1987) 263–288. https://doi.org/10.1080/13642818708221317.

[90] A. Nonat, The structure and stoichiometry of C-S-H, Cement and Concrete Research. 34 (2004) 1521–1528. https://doi.org/10.1016/j.cemconres.2004.04.035.

[91] J.W. Cahn, The Time Cone method for Nucleation and Growth Kinetics on a Finite Domain, MRS Proceedings. 398 (1995) 398–425. https://doi.org/10.1557/PROC-398-425.

[92] E. Villa, P.R. Rios, Transformation kinetics for surface and bulk nucleation, Acta Materialia. 58 (2010) 2752–2768. https://doi.org/10.1016/j.actamat.2010.01.012.

[93] A. Kumar, S. Bishnoi, K.L. Scrivener, Modelling early age hydration kinetics of alite, Cement and Concrete Research. 42 (2012) 903–918.

[94] V.K. Peterson, M.C.G. Juenger, Hydration of tricalcium silicate: effects of CaCl2 and sucrose on reaction kinetics and product formation, Chemistry of Materials. 18 (2006) 5798–5804.

[95] V.K. Peterson, A.E. Whitten, Hydration processes in tricalcium silicate: application of the boundary nucleation model to quasielastic neutron scattering data, The Journal of Physical Chemistry C. 113 (2009) 2347–2351.

[96] G.W. Scherer, J. Zhang, J.J. Thomas, Nucleation and growth models for hydration of cement, Cement and Concrete Research. 42 (2012) 982–993.

[97] J.J. Thomas, H.M. Jennings, J.J. Chen, Influence of nucleation seeding on the hydration mechanisms of tricalcium silicate and cement, The Journal of Physical Chemistry C. 113 (2009) 4327–4334.

[98] J.W. Cahn, The kinetics of grain boundary nucleated reactions, Acta Metallurgica. 4 (1956) 449–459.

[99] C. Naber, F. Bellmann, T. Sowoidnich, F. Goetz-Neunhoeffer, J. Neubauer, Alite dissolution and C-S-H precipitation rates during hydration, Cement and Concrete Reseach. 115 (2019) 283–293. https://doi.org/10.1016/j.cemconres.2018.09.001.

[100] L. Nicoleau, A. Nonat, A new view on the kinetics of tricalcium silicate hydration, Cement and Concrete Reseach. 86 (2016) 1–11. https://doi.org/10.1016/j.cemconres.2016.04.009.

[101] M.A. Etzold, P.J. McDonald, A.F. Routh, Growth of sheets in 3D confinements — a model for the C–S–H meso structure, Cememt Amd Concrete Research. 63 (2014) 137–142. https://doi.org/10.1016/j.cemconres.2014.05.001.

[102] E.M. Gartner, A proposed mechanism for the growth of C-S-H during the hydration of tricalcium silicate, 27 (1997) 665–672. https://doi.org/10.1016/S0008-8846(97)00049-5.

[103] E.M. Gartner, K.E. Kurtis, P.J.M. Monteiro, Proposed mechanism of C-S-H growth tested by soft X-ray microscopy, Cement and Concrete Reseach. 30 (2000) 817–822. https://doi.org/10.1016/S0008-8846(00)00235-0.

[104] T. Honorio, B. Bary, F. Benboudjema, S. Poyet, Modeling hydration kinetics based on boundary nucleation and space-filling growth in a fixed confined zone, Cement and Concrete Research. 83 (2016) 31–44. https://doi.org/10.1016/j.cemconres.2016.01.012.

[105] E. Masoero, J.J. Thomas, H.M. Jennings, A Reaction Zone Hypothesis for the Effects of Particle Size and Water-to-Cement Ratio on the Early Hydration Kinetics of C3S, Journal of the American Ceramic Society. 97 (2014) 967–975.

[106] C. Rößler, F. Steiniger, H.-M. Ludwig, Characterization of C–S–H and C–A–S–H phases by electron microscopy imaging, diffraction, and energy dispersive X-ray spectroscopy, Journal of the American Ceramic Society. 100 (2017) 1733–1742. https://doi.org/10.1111/jace.14729.

[107] G.W. Scherer, Models of Confined Growth, Cement and Concrete Research. 42 (2012) 1252–1260.

[108] J. Lapeyre, H. Ma, A. Kumar, Effect of particle size distribution of metakaolin on hydration kinetics of tricalcium silicate, 102 (2019) 5976–5988. https://doi.org/10.1111/jace.16467.

VITA

Rachel Elizabeth Cook was born in Madison, WI USA on October 26, 1993. She attended Alfred University in western New York state from August 2012 to May 2016, earning a Bachelor of Science in Ceramic Engineering. During her time at Alfred University, she completed her undergraduate thesis, which was focused on the hydrothermal synthesis of copper aluminum oxide powders, under the direction of Dr. Yiquan Wu.

In August 2016, Rachel started as a PhD student in the Materials Science & Engineering department at Missouri University of Science and Technology. In December 2020, she received a Doctor of Philosophy in Ceramic Engineering under the direction of Dr. Aditya Kumar from Missouri University of Science and Technology.